Department of Applied Geology

Hyperspectral Sensing of Acid Sulphate Soils and Their Environmental Impacts in South Yunderup, Western Australia

Xianzhong Shi

This thesis is presented for the Degree of

Doctor of Philosophy

of

Curtin University

February 2014

Declaration

To the best of my knowledge and belief this thesis contains no material previously published by any other person except where due acknowledgement has been made. This thesis contains no material which has been accepted for the award of any other degree or diploma in any university.

Signature: Xianzhong Shi

Date: Feb 18th, 2014

ABSTRACT

Acid sulphate soils (ASS) occur along coastal areas, certain inland areas and mine waste sites and can be detrimental to the environment and infrastructure due to their ability to produce and host strong acidity and produce toxicity due to the release of metals. The occurrence of ASS along the coastline of Australia has become a significant environmental issue, with the Peel Harvey region of Western Australia in general, and South Yunderup township in particular, being severely affected by the development of ASS due to natural and urbanisation activities. The widespread occurrence of ASS makes it imperative to explore new methods to assess the spatial occurrence and severity of ASS so as to assist in the development of sound land management practices. In the research presented in this thesis, visible to shortwave infrared (400-2500 nm) hyperspectral reflectance techniques, using the HyMap sensor for remote sensing and the HyLogger sensor and FieldSpec3 analytical spectral device for proximal sensing, were applied to study the reflectance properties of ASS in the study area.

To establish a framework to the field-based application of hyperspectral sensing to map and study ASS, two laboratory experiments with sulphidic material from the study area were conducted to test the oxidation of the sulphidic material under oxidising drying and wetting conditions of differing durations (weekly, monthly and three monthly). The results of the experiments revealed the overall processes of the sulphide oxidation and the evolution of the ASS involved mineral transformations, geochemical and spectral changes. The material that was subjected to a weekly cycle formed stable secondary iron oxides and hydroxide minerals (goethite, hematite), and exhibited a lower storage of actual acidity. The materials that were subjected to monthly and three monthly cycles were only partially oxidised and formed iron hydrolysis products (jarosite), and had a greater storage capacity for acidity. The variations in formation of secondary minerals that were detected spectrally could be explained due to the greater amount of oxidation via the higher frequency of wetting

by oxygenated water for the weekly cycle as opposed to the lesser oxidation in the drier and less frequent wetting cycles. The pH of the extracted pore waters of the oxidising sulphidic material remained acidic (<4) with a concomitant release in SO_4^{2-} due to sulphide oxidation, and release of Al^{3+} and Si^{4+} due to the dissolution of aluminosilicates, with the release of aluminium (Al) being critical due to its toxicity.

In another experiment to simulate surface mineralogical changes in the sulphidic materials that occurred in the wetlands and surface stockpiles in the study area, due to subtle variations in the landforms, minor surface variations were created on the homogenised sulphidic material which was then subjected to weekly drying and wetting cycles for five weeks. The surface of each landform displayed the presence of distinct secondary iron mineralogy indicative of the acidic and drainage conditions on the surface and immediately underlying the micro-landform. The micro-landform with the best drainage promoted high evaporation, favouring the precipitation of the mixed valence mineral copiapite, which was indicative of extremely low pH (pH<2). The micro-landform with moderate drainage revealed the initial presence of copiapite, but with increasing duration of oxidation and saturation; the environment shifted from one of evaporation to one favouring ferric hydrolysis, resulting in the formation of jarosite and minor goethite and copiapite, with jarosite presence indicative of low pH (<4). In the third micro-landform, with moderate drainage, oxidation and ferric hydrolysis was favoured, resulting in the formation of goethite with minor jarosite, with pH >4. The mineral paragenesis indicated by reflectance spectra – copiapite to jarosite to goethite dominance with increasing pH and saturation – was similar to that observed in sulphide weathering environments.

In the study area, the floodplain and delta hosted wetlands and constructed drains and the oxidised land-disposed dredged sulphidic material from estuaries were the main landform sites showing acute visual and surface pH signatures of ASS development. Field sampling, X-ray diffraction and visible to shortwave infrared (400-2500 nm) reflectance spectra of the surface of soils from the field areas, including ASS-affected sites, indicated the following soil surface-pH relations: jarosite dominated in pH <2.8, schwertmannite in pH range of 2.8-4.5, ferrihydrite in pH 6-7, goethite in pH <6, hematite formed when pH was in the range of 7-8, and the assemblage of jarosite + goethite and jarosite + ferrihydrite in a pH range of 2.9-4.5. These relationships were similar to those established for acid mine drainages.

The field-established relationship between the presence of secondary iron and Al oxides, hydroxides and sulphates, and pH was used to map the extent and severity of ASS in the study area, using two methods. In the first method, the HyMap data were utilised to make mineral maps using diagnostic absorption features of the indicative minerals, which were then linked to the mineral or mineral assemblage pH range to produce an interpreted pH map. In the second method, the direct relationship between the spectral features and soil chemical properties (pH) were established by partial least squares regression (PLSR) modelling and the robustness of the predicted model was proved by comparing the results of the PLSR method to those from the distribution of indicative iron-bearing minerals. The comparison between the two methods used to map the surface acid ranges found approximately 94% of the pixels in the pH classification maps deduced from the two different methods to be highly similar. Both of the pH maps produced using different methods with the HyMap data showed that the distribution and severity of the ASS varied according to the landform: the exposed and oxidised sulphidic dredge spoils from canals displayed the most intense ASS formation, while the constructed drains and shallow wetlands that are subjected to seasonal drying displayed moderate ASS formation but only in dry summer months due to the falling water table that exposed underlying sulphidic materials.

One of the main environmental damage issues linked to the acidity produced by ASS is the release of mobile Al in the soil pore waters and into hydrologically connected waterways, thereby causing Al toxicity and damaging ecosystems. The reason for Al release in acid environments is the reaction of aluminosilicates with acid pore waters to buffer the acid, with kaolinite dissolving only at pH <4.5. To study the potential to remotely map Al toxicity in the study area, a surface map of aluminium-bearing secondary minerals was constructed by identifying the diagnostic absorptions of kaolinite and gibbsite in the reflectance spectra of the HyMap data. The secondary aluminosilicate mineral map was combined with the pH map generated by the indicative minerals and PLSR modelling methods to derive five categories of possible Al toxicity across the area, with the highest toxicity level being represented by very low pH (<4) and abundance of kaolinite and gibbsite and negligible toxicity category represented by neutral pH and low kaolinite presence.

To assess the hyperspectral method to map the subsurface ASS occurrence as well as to assess the link between surface and subsurface ASS occurrence and

intensity, eight soil cores from the study area were investigated via the HyLogger proximal hyperspectral sensor. The common secondary soil minerals that could be detected and mapped were kaolinite, goethite and gypsum, which existed through most depths of the soil profiles. Other secondary minerals that were detected, namely jarosite, hematite, gibbsite and montmorillonite, were only observed in some cores, with the oxidised sulphidic material soils showing the highest presence of the acid indicator mineral, jarosite, and the neutral pH soils being composed mainly of kaolinite and montmorillonite (smectites).

The results of the research demonstrated success with the application of multiple-sourced hyperspectral sensing technology and conventional methods in studying, identifying and mapping ASS in a coastal area. The main findings of the laboratory oxidation of sulphidic material were the spectral characterisation of pH indicator secondary iron-bearing minerals on the surface of an evolving ASS and also the release of toxic elements in pore waters. The field studies successfully demonstrated the mapping of pH indicator minerals using airborne hyperspectral remote sensing as well as PLSR modelling of the pH, including the mapping of potential Al toxicity and subsurface mineralogy.

ACKNOWLEDGEMENTS

I would like to thank my supervisor Dr. Mehrooz Aspandiar, of Curtin University, for his patient teaching, guidance and support in my study and research. Dr. Aspandiar not only gave me helpful comments, suggestions and ideas to guide me in research and thesis and paper writing, but also helped me in the field work, data collecting and experimental design. I also want to thank my co-supervisor, David Oldmeadow. He helped me considerably with incubation experimental design and geochemical measurements, and provided valuable comments and guidance. My associate supervisor, Dr. Ian C Lau, gave me great help with hyperspectral remote sensing, spectral geology and mapping, and he also provided valuable comments on the thesis and manuscripts prepared. In addition, Dr. Lau provided HyMap data and facilities, including software, laboratory and apparatus, to support this research. I greatly appreciate Dr. Lau for his numerous assistance and support.

I would thank my colleagues who provided a lot of support with my study and research. The staff of Miss Alexandra Stevens and Giada Bufarale, gave a lot of help with map making and figures, and fellow PhD students, including Clinton Roga, Hamed Arosi, Tubagus Solihuddin, Sira Tecchiato and Kong-Yang Zhu gave me lots of help and comfort with my study and research.

A great thank you to the Head of Department, Associate Professor Pete Kinny and the Chairperson of thesis committee, Professor Zheng-Xiang Li, for their caring attitude and guidance. And I also appreciate Professor Lindsay Collins and Associate Professor Ron Watkins for their support and access to their laboratory facilities.

AS sponsors, Chinese Scholarship council (CSC) and Curtin International Postgraduate Research Scholarship (CIPRS) offered funding to support my study and research at Curtin University to whom I am grateful for their financial support.

Last but not least, I want to thank my family, who gave me endless and selfless support. Special thanks to my parents, they continuously cared about me wherever I

went. Special thanks to my wife, Mrs Xiuying Shi, as well, she always accompanies me and supports me, having no complaints no matter how difficulty the conditions are. Particularly, I want to thank my dearest daughter, Miss Xinyue Shi. She has given me the most powerful strength to overcome difficulties in my study and research with her cutest smile and warmth. I began to write my thesis when my daughter was born, and lots of words and chapters were typed when I held my baby, she has witnessed the progresses of my research and thesis writing and been a fountain of hope and joy during the preparation of the thesis. Therefore, I would like to dedicate this thesis to my dearest daughter.

TABLE OF CONTENTS

ABSTRACT II

ACKNOWLEDGEMENTS VI

TABLE OF CONTENTS VIII

LIST OF FIGURES XIII

LIST OF TABLE XXII

CHAPTER 1 INTRODUCTION AND OBJECTIVES 1

1.1 ENVIRONMENTAL IMPACT OF ACID SULPHATE SOILS 1

1.2 FORMATION OF ACID SULPHATE SOILS 3

1.2.1 Definition and classification of acid sulphate soils *3*
1.2.2 Formation of acid sulphate soils *3*
1.2.3 Neutralisation reactions in acid sulphate soils *4*
1.2.4 Main minerals related to acid sulphate soils *5*
1.2.5 Minerals indicative of acidity and toxicity *6*

1.3 AVAILABILITY OF HYPERSPECTRAL SENSING FOR ACID SULPHATE SOILS 7

1.3.1 Advantage of hyperspectral sensing *7*
1.3.2 Spectral features of the main minerals related to ASS *8*

1.4 PREVIOUS STUDIES ON ASS AND THEIR MAPPING LIMITATIONS 9

1.5 MAIN OBJECTIVES OF THIS STUDY 11

1.6 MAIN CONTENTS OF THIS THESIS 12

CHAPTER 2 METHODOLOGY AND DATA ACQUISITION 14

2.1 FIELD INVESTIGATION 15

2.1.1 Surface soil sample collection *15*
2.1.2 Soil coring *15*

2.2 HYPERSPECTRAL DATA ACQUISITION 15

2.2.1 HyMap data acquisition *15*
2.2.2 Proximal ASD hyperspectral data *16*
2.2.3 HyLogger™ scanning *16*

2.3 CHEMICAL MEASUREMENTS 16

2.3.1 pH measurement *16*
2.3.2 Soil solution analysis *17*
2.3.3 Titratable actual acidity and titratable potential acidity measurements *17*

2.4 MINERALOGY VERIFICATION (SPECTRAL GEOLOGIST, X-RAY DIFFRACTION AND SCANNING ELECTRON MICROSCOPY) 17

2.5 SPECTRAL MAPPING METHODS 18

2.6 PLSR MODELLING 21

2.7 INCUBATION EXPERIMENT 22

CHAPTER 3 SETTING OF THE STUDY AREA 23

3.1 LOCATION OF THE STUDY AREA 23

3.2 SETTING OF GEOLOGY AND GEOMORPHOLOGY 23

3.3 CLIMATE 26

3.4 HYDROLOGY 28

3.5 SOILS AND VEGETATION 28

3.6 SAMPLE SITES 32

CHAPTER 4 OBSERVATIONS ON THE OXIDATION OF IRON SULPHIDE-RICH MATERIAL DURING INCUBATION EXPERIMENTS AND POTENTIAL ENVIRONMENTAL CONSEQUENCES 34

4.1 INTRODUCTION 34

4.2 EXPERIMENTAL SETTINGS AND MEASUREMENTS 36

4.2.1 EXPERIMENTAL SETTINGS *36*
4.2.2 SAMPLE PREPARATION *37*
4.2.3 OPERATIONAL PROTOCOLS FOR INCUBATION CELLS *39*
4.2.4 CHEMICAL MEASUREMENTS *39*
4.2.5 TAA, TPA AND TOTAL SULPHUR CONTENT MEASUREMENT *40*
4.2.6 MINERALOGY *40*

4.3 RESULT AND INTERPRETATION 41

4.3.1 CHANGES IN REFLECTANCE SPECTRAL CHARACTERISTICS *41*
4.3.2 MINERALOGY CHANGES *44*
4.3.3 ACIDITY CHANGES *46*
4.3.4 COMPOSITION CHANGES *47*
4.3.5 SULPHATE RELEASE CHANGES *48*
4.3.6 ENVIRONMENTAL IMPACTS *51*
4.3.6.1 pH and EC *51*
4.3.6.2 Trace metal release *53*

4.4 DISCUSSION 55

4.4.1 MINERALOGICAL EVOLUTION DURING OXIDATION OF SULPHIDIC MATERIAL *55*
4.4.2 POTENTIAL HAZARDS CAUSED BY CLIMATE CHANGE *56*

4.5 CONCLUSION 57

CHARTER 5 OBSERVATION OF SPECTRAL VARIATION IN THE OXIDATION OF IRON SULPHIDE MATERIALS BY PROXIMAL SENSING 61

5.1 INTRODUCTION 61

5. 2 INFLUENTIAL FACTORS OF THE SPECTRAL CHANGES OF THE ASS 62

5.2.1 MINERAL COMPOSITION *62*
5.2.2 ORGANIC CONTENT *63*
5.2.3 PARTICLE SIZE *63*

5.2.4 MOISTURE CONTENT *64*

5.3 SPECTRAL CHANGES OCCURRING DUE TO OXIDATION OF IRON SULPHIDE-RICH MATERIAL **65**

5.3.1 EXPERIMENTAL SETTINGS AND MEASUREMENTS *65*
5.3.1.1 Sample preparation *65*
5.3.1.2 Spectral measurements *66*

5.4. RESULTS AND INTERPRETATIONS **66**

5.4.1 MATERIAL CHANGES WITHIN DIFFERENT MINIATURE LANDFORMS *66*
5.4.2 SPECTRAL CHANGES WITH THE OXIDATION TIME *71*
5.4.2.1 Changes in the mid-dark material with oxidation *71*
5.4.2.2 Spectral changes in the dark-brown material with oxidation *74*
5.4.2.3 Spectral changes in the around-light material with oxidation *74*

5.5 DISCUSSION OF MINERALOGICAL CHANGES DURING OXIDATION OF SULPHIDIC MATERIAL **78**

5.6 CONCLUSION **80**

CHAPTER 6 MINERALOGY AND SPECTRAL CHARACTERISATION OF ACID SULPHATE SOILS **82**

6.1 INTRODUCTION **82**

6.2 MAIN MINERALS RELATED TO ASS **84**

6.3 MINERAL DISTRIBUTION IN THE STUDY AREA **85**

6.4 SPECTRAL CHARACTERISATION OF ASS IN THE STUDY AREA **90**

6.4.1 SPECTRAL CHARACTERISTICS OF ACTUAL ACID SULPHATE SOIL *90*
6.4.1.1 Spectra of the soil with pH less than 4 ..... *91*
6.4.1.2 Spectral of the soil with pH in range of 4.0-6.0 ..... *97*
6.4.1.3 Soil pH in the range of 6.0-7.5 ..... *99*
6.4.2 SPECTRAL CHARACTERISTIC OF THE UNAFFECTED SOIL *100*

6.5 DISCUSSION **102**

6.5.1 SOIL MINERALOGY AND PH *102*
6.5.2 IDENTIFICATION OF SECONDARY MINERALS VIA REFLECTANCE SPECTROSCOPY *102*

6.6 CONCLUSION **103**

CHAPTER 7 ASSESSMENT OF SOIL PH OF THE SURFACE ACID SULPHATE SOIL BY PLSR MODELLING AND INDICATIVE MINERAL MAPPING OF AIRBORNE HYPERSPECTRAL IMAGERY **105**

7.1 INTRODUCTION **105**

7.2 METHODOLOGY AND DATA ACQUISITION **106**

7.2.1 HYMAP DATA *107*
7.2.2 SOIL SAMPLE COLLECTION *107*
7.2.3 PROXIMAL HYPERSPECTRAL DATA *107*
7.2.4 PH MEASUREMENT *107*
7.2.5 MINERALOGY VERIFICATION *107*

7.3 IMAGE PRE-PROCESSING **108**

7.4 PLSR PROCEDURES **109**

7.4.1 Training dataset preparation *109*
7.4.2 Spectral processing *109*
7.4.3 Cross-validation *109*
7.4.4 Determination of the optimum factors *110*
7.4.5 Sample and spectral outlier *110*
7.4.6 Final regression coefficient output *110*

7.5 RESULT AND DISCUSSION **111**

7.5.1 Acidity map deduced from predictive model *111*
7.5.1.1 Optimum factors *111*
7.5.1.2 Relation between actual and predicted value *112*
7.5.1.3 Final regression coefficient output *112*
7.5.1.4 Applying the PLSR model to map pH distribution *115*
7.5.2 Soil acidity deduced from iron-bearing mineral mapping *118*
7.5.2.1 Iron-bearing minerals mapping *118*
7.5.2.2 Soil acidity map deducted from HyMap mineral classification map *119*
7.5.3 Comparison of the predicted pH values deduced from the PLS model with the ground truth *125*

7.6 CONCLUSION **125**

CHAPTER 8 MAPPING OF NON-IRON BEARING MINERALS AND THE POTENTIAL ALUMINIUM TOXICITY **128**

8.1 INTRODUCTION **128**

8.2. DATA ACQUISITION AND PRE-PROCESSING **130**

8.3 MAPPING AND CLASSIFICATION OF ALUMINIUM-BEARING MINERALS, CARBONATES AND SULPHATES **130**

8.3.1 End-member selection *130*
8.3.2 Mapping of aluminium-bearing minerals *131*
8.3.2.1 Al-OH clay minerals *131*
8.3.2.2 Gibbsite *131*
8.3.3 Carbonates map *135*
8.3.4 Sulphates map *135*
8.3.5 Main soil matrix mineral classification *138*

8.4 DISTRIBUTION OF SOIL PH **138**

8.5 ALUMINIUM TOXICITY MAPPING **138**

CHAPTER 9 ASSESSMENT OF ACID SULPHATE SOILS IN SUBSURFACE BY PROXIMAL HYPERSPECTRAL SENSING **145**

9.1 INTRODUCTION **145**

9.2. DATA ACQUISITION **147**

9.2.1 Soil coring *147*
9.2.2 HyLogger scanning *149*

9.3 RESULTS AND DISCUSSION **150**

9.3.1 Soil profile characteristics *150*
9.3.2 Spectral characteristics in the subsurface *154*
9.3.3 Mineral identification *159*
9.3.4 Mineral distribution in the subsurface *163*
9.3.5 Separation of AASS and PASS *166*

9.3.6 Correlation between soil pH and reflectance spectra by PLSR modelling 169
9.3.7 Application of the model to predict the pH distribution in soil profiles 171
9.3.8 Comparison of the pH at the top of the cores with the pH on the surface soil .. 173
9.4 CONCLUSION 175
CHAPTER 10 CONCLUSIONS 177
10.1 MAIN RESULTS AND FINDINGS 177
10.2 CORRELATIONS AMONG THE RESULTS 181
10.3 NOVELTIES OF THE STUDY 183
10.4 FUTURE WORKS 184
REFERENCES 186
APPENDIX 1. XRD PLOT OF THE SOIL SAMPLES COLLECTED FROM THE SURFACE OF THE STUDY AREA 205
APPENDIX 2: REFLECTANCE SPECTRAL MEASUREMENTS OF THE SOIL SAMPLES COLLECTED FROM THE SURFACE OF STUDY AREA 215
APPENDIX 3: FIELD IMAGES OF THE SAMPLE SITES IN THE STUDY AREA 226
APPENDIX 4: PARTS OF PHOTOS OF SOILS SAMPLES COLLECTED FROM THE SURFACE OF THE STUDY AREA 230
APPENDIX 5: THE MEASUREMENTS OF THE SOLUTION FROM THE INCUBATION EXPERIMENT DESCRIBED IN CHAPTER 4 235
APPENDIX 6: PHOTOS AND SPECTRAL MEASUREMENTS OF THE IRON SULPHIDES MATERIALS IN THE EXPERIMENT DESCRIBED IN CHAPTER 5 237
APPENDIX 7: THE REFLECTANCE SPECTRAL MEASUREMENTS OF THE SAMPLES EXTRACTED FROM SOIL CORES 242
APPENDIX 8: THE SAMPLE PICTURES EXTRACTED FROM SOIL CORES 249
APPENDIX 9: THE DESCRIPTION OF THE SOIL CORES AND THE MEASUREMENTS OF PH AND EC OF THE SAMPLE EXTRACTED FROM DIFFERENT DEPTH OF SOIL CORES 256
APPENDIX 10: THE MEASUREMENTS OF MAIN ELEMENTS INTERESTED OF THE SAMPLES EXTRACTED FROM DIFFERENT DEPTH OF SOIL CORES 258

LIST OF FIGURES

Figures		Page
Figure 2. 1	Comparison of two spectral vectors between the test spectrum and reference spectrum	19
Figure 2. 2	Spectral absorption features. Left image: spectral characterisation; Right image: spectral characteristics after continuum removal	20
Figure 3. 1	Location of the study area (modified from Google map)	24
Figure 3. 2	Geomorphic elements of the Swan Coastal Plain – R (Ridge Hill Shelf), P (Pinjarra Plain), B (Bassendean dunes), S (Spearwood dunes), Q (Quindalup dunes)	26
Figure 3. 3	Mean maximum temperature from 1994 to 2011 and in 2011 (Bureau of Meteorology, Year)	27
Figure 3.4	Mean rainfall (mm) from 1993 to 2011 and in 2011(Bureau of Meteorology, Year)	27
Figure 3. 5	Aerial image of the South Yunderup area showing the main landforms – wetlands (W), drains (D), exposed floodplains (F), compacted dredged material flats (S), canals (C) and urban construction and townships (U).Modified from Google earth	29
Figure 3. 6	Images showing selected landforms as represented in Figure 3.5 aerial image. A. A constructed drain in August (winter) and B. the same drain in February (summer). The drain surface is exposed with grey (sulphidic) layers showing including oxidised reddish to yellow surfaces in summer. C. Compacted dredge spoil surface with yellowish-brown and grey surface with newly constructed housing in the background. D. Inactive floodplains. E. Wetlands in winter. F. Wetlands in summer showing oxidised surfaces (orange-yellow)	30

Figure 3. 7	HyMap imagery of the study area of South Yunderup township including surrounding area (green labels refer to the soil coring sites; red labels refer to the surface sampling sites)	32
Figure 4. 1	Set-up of the incubation experiment	36
Figure 4. 2	Residual material after 12 weeks' oxidation (a) the material from group 1 (weekly drying), displaying top surface; (b) the material from group 1, displaying side surface and bottom surface; (c) the material from group 2 (monthly drying); (d) the material from group 3 (three month drying). The images show visual oxidation signs of yellow-brown on the top and side surface with ugly colours in the inner	41
Figure 4. 3	Reflectance spectra of the material (a) the spectral characteristic of the initial material before oxidation; (b) the spectral characteristic of the material in group 1(weekly) after oxidation; (c) the spectral characteristic of the material in group 2 (monthly) after oxidation; (d) the spectral characteristic of the initial material in group 3 (three month) after oxidation. For b, c, and d, the black spectra is from the inner material, the green spectra is from the top surface, and the red spectra is from the side surface of the material	43
Figure 4. 4	XRD results of the different parts of material in different groups; I-001 the sample from initial material; in the sample name, G1, G2, G3 represent samples from group 1, group 2 and group 3, respectively, and TS, SS and M represent the top surface, side surface and middle part, respectively; for the mineral identification, K - kaolin group, G - goethite, J - jarosite, Q - quartz, GY - gypsum, P- pyrite, M -microcline, H - halite, F – ferrihydrite. In XRD plot, X axis is the two theta (deg) and the Y axis is the intensity (counts)	45
Figure 4. 5	Change of SO42- release (the unit for SO4 release was ppm, and the unit for the $SO4^{2-}$ release rate was ppm/day)	51
Figure 4. 6	Correlation between H+ deduced from pH and estimated release $SO4^{2-}$	51

Figure 4. 7	pH and EC changes with oxidation days. EC scale on the right in ms/cm	52
Figure 4. 8	Selected trace metal changes with duration of oxidation (X axis is the oxidation days, the right Y axis is for Ba, the left Y axis is for other metals; the unit of the concentrations is ppm)	53
Figure 4. 9	Correlation between Al^{3+} and Si^{4+} from measurement of the two cells of group 1	54
Figure 5. 1	Reflectance spectra of some minerals in soil (spectra were continuum to be removed)	63
Figure 5. 2	Comparisons of the spectra from different grain size – the spectra of Y-008-05 (green) was from coarse material, the spectra of Y-008-05P (red) was from the material after it was milled to powder.	64
Figure 5. 3	Reflectance spectra of soil with similar composition but with different moisture content.	65
Figure 5. 4	Photo and spectra collected on 26 April 2013, 5 weeks after the start of the experiment (a) Photo of three landforms in the cell, M: mid-dark; D: dark-brown; A: around-light;(b) Reflectance spectra of different micro-landforms of material;(c) Reflectance spectra of different micro-landforms after continuum removal	69
Figure 5. 5	Comparison of the spectra collected weekly in the same part of the of mid-dark region (red = week 5, green = week 4, blue= week 3; purple = week 2, black = week 1) (a) Reflectance spectra measured in different times, before continuum removed; (b) Spectral range near 0.9 μm; (c) Spectral range near 2.265 μm; (d) Spectral range near 1.17 μm; spectra shown in b-d are after removal of continuum	72
Figure 5. 6	Comparison of the spectra collected weekly in the same part of the dark-brown region (red = week 5, green = week 4, blue= week 3; purple = week 2, black = week 1) (a) Reflectance spectra measured at different times, before continuum removal; (b) Close-up of the spectra around 0.9 μm; (c) Close-up of spectra around 2.265 μm; (d) Close-up of spectra around 1.17	74

μm (Spectra shown in b-d are after removal of continuum)

Figure 5. 7 Comparison of the spectra collected weekly in the same part of the of around-light region (red = week 5, green = week 4, blue= week 3; purple = week 2, black = week 1). (a) Reflectance spectra measured at different times, before continuum removal; (b) Close-up of spectra around 0.9 μm; (c) Close-up of spectral near 2.265 μm; (d) Close-up of spectra near 1.17 μm (spectra shown in b-d are after removal of continuum) 76

Figure 6. 1 Location of sampling sites (red labels initialled with Y- are the surface sampling sites, and green labels initialled with “core” are the coring sites) 87

Figure 6. 2 XRD patterns (above) and continuum-reflectance spectra of sample Y-002-160212-02; the diffraction peaks of minerals are labelled in the XRD patterns and the absorption peaks of minerals are labelled in the spectra (In the XRD plot, Q: quartz; CA: calcite; H: halite; J: jarosite; GY: gypsum) 92

Figure 6. 3 XRD patterns(above) and VNIR-SWIR spectra (continuum-removed) of sample Y-011-160212-02(floc).The mineral diagnostic XRD peaks are labelled and so are the spectra absorption peaks (In the XRD plot, Q: quartz; B: bassanite; G: goethite; H: halite; P: pyrite; C: copiapite; J: jarosite) 93

Figure 6. 4 XRD patterns (above) and continuum-removed reflectance spectra of sample Y-007-221111-02. The diffraction peaks of minerals are labelled in the XRD patterns and the absorption peaks of minerals are labelled in the spectra; the sample contained jarosite and goethite (In the XRD plot, Q: quartz; G: goethite; H: halite; J: jarosite) 94

Figure 6. 5 XRD patterns (above) and continuum-removed reflectance spectra of sample Y-007-160212-04. The diffraction peaks of mineral are labelled in the XRD patterns and the absorption peaks of minerals are labelled in the spectra (In the XRD plot, J:jarosite, SC: schwertmannite, GY:gypsum, H:halite, Q:quartz) 95

Figure 6. 6	XRD patterns (above) and continuum-removed reflectance spectra of sample Y-007-2211-3. The diffraction peaks of mineral are labelled in the XRD patterns and the absorption peaks of minerals are labelled in the spectra (In the XRD plot, J: jarosite, SC: schwertmannite, G:goethite, Q:quartz, H: halite)	96
Figure 6. 7	XRD patterns (above) and continuum-removed reflectance spectra of sample Y-008-2211-05. The diffraction peaks of minerals are labelled in the XRD patterns and the absorption peaks of minerals are labelled in the spectra; the sample contains goethite (In the XRD plot, Q: quartz, G: goethite)	98
Figure 6. 8	XRD patterns (above) and continuum-removed reflectance spectra of sample Y-008-2211-02. The diffraction peaks of mineral are labelled in the XRD patterns and the absorption peaks of minerals are labelled in the spectra (In the XRD plot, Q: quartz, G: goethite, H: halite, K: kaolinite, GY: gypsum, F: ferrihydrite)	99
Figure 6. 9	XRD patterns (above) and continuum-removed reflectance spectra of sample Y-008-160212-05(ct). The diffraction peaks of mineral are labelled in the XRD patterns and the absorption peaks of minerals are labelled in the spectra (In the XRD plot, H: halite, GY: gypsum, F: ferrihydrite)	100
Figure 6. 10	XRD and reflectance spectrum plot (continuum-removed) of the sample from the background soil (In the XRD plot, Q: quartz)	101
Figure 6. 11	XRD and spectral plot (continuum-removed) of the soil core sample C6-01c showing features for kaolinite and gibbsite	102
Figure 7. 1	PRESS, SEP and F-test plot and factors	111
Figure 7. 2.	Scatter plots of the relation between actual pH and predicted pH	112
Figure 7. 3	Final regression coefficient compared to continuum-removed spectra of related ASS minerals; the X axis is the spectral wavelength in micrometers, Y axis on the left is the FRC; Y axis on the right is the reflectance response for the mineral	114

Figure 7. 4	PLSR pH classification map of acidity deduced from applying the PLSR model to the HyMap data	116
Figure 7. 5	Surface images of the main landforms that display surface acid conditions. A. Oxidised dredged spoil material showing yellow (jarosite/goethite) and grey surface with urban development in the background; B. Close-up of the surface of the dredged spoil showing yellow mottles (Y), brown mottles and nodules (Br) and dark grey clay-sand material (Sul) which is the original oxidised sulphidic material from the inlet; C. Semi-dried surface of a constructed drain showing orange to reddish surface coatings and flocs in the water; D. A dried wetland surface showing yellow (jarosite) and orange (schwertmannite) flocs with the halophyte vegetation.	117
Figure 7. 6	Spectral characteristic of the end-members of iron-bearing minerals resampled to HyMap wavelengths (All spectra have had their continuum removed)	118
Figure 7. 7	HyMap mineral classification map of the main iron-bearing minerals related to ASS	120
Figure 7. 8	HyMap soil acidity map derived from mineralogy deduced from the distribution of indicative minerals listed in Figure 7.7	121
Figure 7. 9	Differences in pH between the HyMap soil acidity map derived from mineralogy and the PLSR pH classification map of acidity (The proportion of each difference grade is shown in brackets)	124
Figure 8. 1	Reflectance spectra of the end-members of surrounding minerals related to ASS (from USGS Spectral Library)	130
Figure 8. 2	Kaolin mineral distribution map using the spectral indices method at 2.2 μm	132
Figure 8. 3	Gibbsite mineral distribution map produced using the SFF method focusing on three wavelength regions	133
Figure 8. 4	Carbonate mineral distribution map produced using the SFF method at 2.33 μm	132
Figure 8. 5	Sulphate (mainly gypsum) distribution map using spectral indices method at 1.75 μm	136

Figure 8. 6	Mineral classification result of the main non-iron-bearing soil matrix minerals related to ASS	138
Figure 8. 7	Soil pH map deduced from the PLSR model (from Chapter 7, Figure 7.4)	139
Figure 8. 8	Potential Al toxicity map as constructed from soil from the distribution of soil pH and main Al silicate and Al hydroxide-bearing minerals in the area (some soluble Al sulphates were found on site Y-005)	143
Figure 8.9	Two samples collected from the bed of a creek in site Y-005 were identified by XRD that contain soluble Al sulphate namely tamarugite and potasiumalum	144
Figure 9. 1	Location of soil coring on HyMap image	148
Figure 9. 2	Images of 8 soil cores collected from the study area	152
Figure 9. 3	Slice spectrum with corresponding intensity of 900, 1400, 1900 and 2200 nm absorption and abundance of Al-OH and FeOx for core 1 to core 3	157
Figure 9. 4	Slice spectrum with corresponding intensity of 900, 1400, 1900 and 2200 nm absorption and abundance of Al-OH and FeOx for core 4 to core 6	158
Figure 9. 5	Slice spectrum with corresponding intensity of 900, 1400, 1900 and 2200 nm absorption and abundance of Al-OH and FeOx for core 7 to core 8	159
Figure 9. 6	Reflectance spectra of soil cores; (Left) Image of core from 30 cm (below) showing reddish hues in a pale grey matrix with minor pale yellow fine mottles and spectra from same depth (Core 7, sample C7-07C) – the absorption features indicated the presence of kaolinite and hematite; (Right) Image of core from 60 cm (below) showing pale yellow mottles in brownish and grey matrix, and spectra from the same depth (above) (sample c7-05c) – the absorption features indicated kaolinite, jarosite and goethite (The reflectance spectra were collected from the centre line from top to bottom of the soil pictures and were continuum removed hull corrected)	160

Figure 9. 7 Reflectance spectra of soil cores (Left) Image of core from 65 cm (below) showing pale yellow/straw-coloured fine mottles and spectra from the same depth (Core 7, sample C7-03C) – the spectral absorption features indicated jarosite and kaolinite (Right) Image of core from ~30 cm depth with reflectance spectra (above) showing features diagnostic of kaolinite and likely gibbsite (sample equivalent to C5-04C) (The reflectance spectra were collected from the centre line from the top to bottom of the soil pictures and were continuum-removed hull corrected) 161

Figure 9. 8 Reflectance spectra of soil cores (Left) Image of the core (below) of loam texture with spectra (above) (sample C4-06C) – the spectra indicate montmorillonite and gypsum (Right) Image of core ~ 35 cm depth with spectra (above) showing the presence of gypsum and deep water feature (sample equivalent C8-04C) (The reflectance spectra were collected from the centre line from top to bottom of the soil pictures and were continuum-removed hull corrected) 162

Figure 9. 9 Minerals confirmed by SEM and XRD. (a) SEM image of yellow-grey parts of the core (C7-05C) showing aggregates of kaolinite plates and goethite grains (b) SEM image of yellow parts of core (C7-03C) showing ephedra rhomboidal crystal morphologies typical of jarosite (c) SEM image of yellow part of core (C7-03C) showing typical ephedra rhomboidal individual jarosite grains on a matrix of fine-grained kaolinite (d) SEM image of the red parts of core (C7-07C) showing aggregates of hematite grains over a dense matrix of grey kaolinite (Re the letters in the image – K represents kaolinite, J represents jarosite, H represents hematite, G represents goethite).(e) XRD plot indicate the existence of gibbsite and kaolinite in sample C6-09C 164

Figure 9. 10 Distribution of main secondary minerals and mineral assemblages as interpreted from the HyLogger data of the 165

studied soil profiles
Figure 9. 11 Separation of AASS and PASS in 8 cores 168
Figure 9. 12 Soil profile of core 5 (left) and core 6 (right) 169
Figure 9. 13 Relation between actual pH and predicted pH for soil profiles 170
Figure 9. 14 Final regression coefficient compared to continuum-removed spectra of ASS-related minerals; the X axis is the spectral wavelength in micrometers, the Y axis on the left is the FRC; the Y axis on the right is the reflectance response for the mineral spectra 172
Figure 9. 15 Comparison of the pH measurements and pH values predicted by the PLSR model (a) Measured pH values for core samples (b) pH values of the cores predicted by the PLSR model 173
Figure 9. 16 Comparison of the pH measurement of the soil in the top 5 cm of cores (marked by red dashed line) and pH map of the soil surface in the study area with core locations (reproduced from Figure 7.7) 174

LIST OF TABLE

Table		page
Table 1.1	Comparison between HyMap, ASD and HyLogger	8
Table 4. 1	Summary of the main measurements taken during the experiments	41
Table 4. 2	Comparison of the mineral composition of the different groups	47
Table 4. 3	Soil acidity measurement from different groups of material	48
Table 4. 4	Comparison of total sulphur contents in different parts and groups	49
Table 4. 5	Sulphate release estimation	51
Table 4. 6	Main chemical measurements of the solution from the material in different groups	60
Table 4.1	Main chemical measurements of the solution from the material in different groups	61
Table 5.1	Description of three miniature landforms	68
Table 5.2	Minerals identified by reflectance spectra in different landforms and different oxidation stages	79
Table 6.1	Listing of secondary minerals dominant in the acid sulphate soil environments	85
Table 6.2	Mineral composition of soil samples collected from surface of study area (identified by XRD analysis)	89
Table 6.3	Mineral composition of the samples collected from the subsurface (identified by reflectance spectra)	91
Table 7. 1	Reflectance spectral features and XRD d values of main indicative minerals	109
Table 7. 2	Relationship between indicative minerals and pH values	123
Table 7. 3	Result of the comparison between measured pH and predicted pH values deduced from the PLSR model	128
Table 8.1	Potential toxicity categories interpreted from the presence of aluminosilicates (kaolinite) and Al hydroxides (gibbsite) and soil pH	143
Table 9.1	Geographical data and landform location of the soil cores	150

Table 9.2 Selected physical and chemical properties of the soil profiles in the cores 154
Table 9.3 Comparison of the pH ranges of the soil in the top layer of the cores with the surface soil at the same location 176

Chapter 1 Introduction and Objectives

1.1 Environmental Impact of Acid Sulphate Soils

The Swan Coastal Plain, located along the coastal strip in south-western Australia, possesses a wide range of wetlands which play a significant role in supporting the hydrology and environment sustainability of the Plain, preserving rare animal and plant species, and creating a natural attraction for the tourism industry (Environmental Protection Authority, 1993a;1993b; 2004). In recent years, some wetlands, including estuarine, inlets, swamps, river floodplains and marshes have been facing several serious environmental issues. According to the estimation of the World Wildlife Fund (WWF), up to 80% of the wetlands on the Swan Coastal Plain have been destroyed and those remaining are facing constant environmental problems (Environmental Protection Authority, 2004). The environmental issues faced by these wetlands include the decline of the wetland areas, wetland eutrophication and wetland acidification. Of these environmental issues, the phenomenon of wetland acidification is mainly due to the occurrence of acid sulphate soils (ASS).

The occurrence of ASS is one of the most important factors contributing to wetland acidification and the consequent damage to aquatic ecosystems and overall wetland degradation. In addition, ASS also occurs in low-lying coastal areas impacted by urban development, as documented in the Mandurah region of south-eastern Australia (Semeniuk and Semeniuk, 1990; Degens, 2006; 2009; Singh and Wong, 2010). In Australia, ASS mainly occurs in the sediments formed in the Holocene geological period during the last 10,000-6,000 years after the last major sea level rise (Department of Environment and Conservation, 2004; 2011; Degens, 2006; 2009). It was estimated that there are more than 90,000 square kilometres of ASS in Australia, of which approximately 30% (27,500 square kilometres) are located in coastal Western Australia (Western Australian Planning Commission, 2003; 2008). Acid sulphate soils are spread widely throughout Western Australia and are commonly found in low-lying coastal wetlands and tidal flats, and have also been observed in inland areas in the south-west region (Western Australian Planning Commission, 2003; 2008). The Swan Coastal Plain has a large area of sediments formed during the Holocene geological period (McArthur and Bettenay, 1974;

Semeniuk and Semeniuk, 1990; Gozzard, 2007, Degens, 2009), and due to much of the area lying at geographically low elevation (lakes, swamps, floodplains and inlets), the plain is a locus for the formation of AAS. This kind of soil is widely distributed in inundated wetlands, seasonally or saturated or inundated floodplains, swamp lands, shallow estuarine areas, tidal swamps and artificial lakes (Fitzpatrick et al., 2003; Fitzpatrick et al., 2008; 2009; Singh and Wong, 2010; Prakongkep et al., 2011).

Acid sulphate soils become harmful when they are disturbed. Once these soils are exposed to the atmosphere, encountering oxygen and water, the contained sulphides (mainly pyrite) will be oxidised, resulting in the production of sulphuric acid (H_2SO_4). The production of sulphuric acid and acid conditions in general, in turn negatively impact the surrounding environment and infrastructure. These negative impacts can be described as follows:

(1) Soil and wetland acidification – The sulphuric acid decreases the soil pH value to below 3.5, resulting in damage to the soil structure. The acid flows into the wetlands with runoffs and, thus, makes the wetlands acidic (Fitzpatrick et al., 2008; Semeniuk and Semeniuk, 1990; Sommer, 2006).

(2) Release of harmful trace metals into the surrounding environment – The decrease in the pH of the soils and water results in the dissolution of the primary and secondary minerals in the soils, leading to the release of major and trace elements from the minerals. Furthermore, acidic pH causes some trace metals, such as iron, aluminium, copper and arsenic, to become more soluble. The increased dissolved major and trace metals due to acid conditions flow into drains, streams, floodwater and groundwater, and may cause fish kills (aluminium toxicity) and severe damage to the aquatic system, including polluting the groundwater system (Fitzpatrick, et al., 2003).

(3) Corrosion of infrastructure – Due to the release of strong acids, infrastructure assets such as roads, bridges, concrete and steel pipes, buildings, housing estates and tourism assets are gradually corroded resulting in a reduction in their strength and other long-term damage (Fitzpatrick, et al., 2003).

(4) Damage to buildings constructed on ASS – The buffering reactions to acid conditions from carbonates results in the formation of gypsum. The gypsum generated in ASS has a greater volume than the initial material and thus leads to the soil swelling beneath constructions, resulting in wall cracks and door and window frame distortions (Sammut et al., 2000).

The formation of ASS therefore has a negative effect on the environment, and the Swan Coastal Plain is increasingly becoming a region across which ASS are being identified.

1.2 Formation of Acid Sulphate Soils

1.2.1 Definition and classification of acid sulphate soils

The term "acid sulphate soils" refers to the soils or sediments that contain sulphides (mostly pyrite) and sulphuric acid, or that have the potential to generate sulphuric acid when the sulphides are exposed to the atmosphere (Fitzpatrick, et al., 2003; Fitzpatrick et al., 2008; Sullivan et al., 2002; 2004; 2006). Depending on whether the soils have been exposed to the atmosphere and oxidised, AAS can be classified into two subtypes: (1) potential acid sulphate soils (PASS) or sulphidic material which contains sulphides but has not been oxidised – these typically exist in waterlogged landforms (Dent, 1986; Fitzpatrick et al., 1998; Ahern et al., 2004); and (2) actual acid sulphate soils (AASS) or sulphuric horizons where sulphides have already been oxidised and sulphuric acid has been produced. In AASS, sulphides may have been depleted or may still be observable in the soil profiles (Fitzpatrick, 1998; Ahern et al., 2004). Based on the geographical settings, ASS can also be grouped into coastal acid sulphate soils (CASS), inland acid sulphate soils (IASS) and mine-site sulphate soils or acid mine drainage (AMD) (Fitzpatrick et al., 1998). These three subtypes represent the range of weathering situations from relatively stable (CASS) to non-stable (IASS) to rapid weathering (AMD), but the most striking differences among these three subtypes are reflected in the sulphide sources and iron mineralogy (Fitzpatrick et al., 1996).

1.2.2 Formation of acid sulphate soils

Acid sulphate soils form due to the oxidation of sulphides, most commonly from pyrite (FeS_2), although the soil may contain some other sulphides in lesser amounts, such as pyrrhotite, chalcopyrite, arsenopyrite, greigite and iron monosulphides (Bush and Sullivan, 1997). Pyrite is usually chosen as an example to demonstrate the formation of ASS. The precondition of the occurrence of pyrite oxidation is the presence of oxidant, including oxygen or ferric iron, and water. The oxidation process is complex and in most cases involves chemical, biological and electrochemical reactions, but the chemical reaction can be simplified and described as follows (Blowes et al., 2003):

$$FeS_2 + 3.75O_2 + 3.5H_2O \rightarrow Fe(OH)_3 + 2SO_4^{2-} + 4H^+ \quad (1.1)$$

This reaction can be divided into several steps. Initially, pyrite is oxidised by dissolved oxygen in neutral pH conditions, oxygen is the predominant oxidant in this stage, and usually operates without the participation of bacteria because the weak acidity is not conducive to the activity of bacterial (Blowes et al., 2003; Bigham and Nordstrom, 2000). The oxidation in this stage is slow. It can be described by the following formula:

$$FeS_2 + 3.5O_2 + H_20 \rightarrow Fe^{2+} + 2SO_4^{2-} + 2H^+ \quad (1.1.1)$$

With the pH decreasing, the activity of bacteria, such as *Thiobacillus ferrooxidans* and *Leptospirillum* ferro-oxidants begin to play an important role in catalysing the transformation of ferrous iron to ferric iron (Bigham and Nordstrom, 2000) which can be described as:

$$Fe^{2+} + 0.25O_2 + H^+ \rightarrow Fe^{3+} + 0.5\ H_2O \quad (1.1.2)$$

With the increasing concentration of ferric iron, it replaces oxygen to become the predominant oxidant; it greatly accelerates the pyrite oxidation rate and results in the production of more acidity which, in turn, is more conducive to the activity of the bacteria in transforming the ferrous iron to ferric iron. The oxidation of pyrite by ferric iron can be represented as:

$$FeS_2 + 14Fe^{3+} + 8H_20 \rightarrow 15\ Fe^{2+} + 2SO_4^{2-} + 16\ H^+ \quad (1.1.3)$$

The ferrous iron produced from reaction (1.1.3) will also be oxidised to ferric iron by reaction (1.1.2), and step by step all the ferrous iron would gradually convert to ferric iron. The ferric iron stays in the solution when the pH is less than 4. When the pH is above 4, the ferric iron hydrolyses and forms ferric hydroxide (or equivalents) (Ahern et al., 2004), which can be described as:

$$Fe^{3+} + 3H_2O \rightarrow Fe(OH)_3 + 3H^+ \quad (1.1.4)$$

Equation 1.1.4 shows the final products of pyrite oxidation. From the above sequence of reactions via the formulas it is clear that the formation of acid sulphate soils mainly involves two processes: (1) pyrite oxidation by oxygen and then by ferric iron; and (2) hydrolysis of Fe (III) and the subsequent precipitation of ferric oxyhydroxides or oxyhydroxide sulphates (Dold, 2000).

1.2.3 Neutralisation reactions in acid sulphate soils

The overall acidity of the ASS is not only dependant on the H^+ produced by the oxidation of pyrite (Equation 1.1), but also depends on the balance between the acid

production and acid consumption during neutralisation and the drainage conditions (Harries, 1997). Once the AAS forms, the products of acids may react with the surrounding carbonate and silicate minerals and this leads to acid neutralisation, with an increase in soil pH and consequent precipitation of metal-bearing oxyhydroxide and oxyhydroxide sulphate minerals (Dold, 2000). The buffering reactions are the dissolution of the carbonates, metal hydroxide and aluminosilicates (Blowes et al., 2003; Dold, 2000), of which the most significant is the dissolution of the carbonates, including calcite, dolomite and siderite (Blowes et al., 2003). The representative dissolution of calcite can be described as follows：

$$CaCO_3 + H^+ \leftrightarrow Ca^{2+} + HCO_3^- \qquad (1.2)$$

Or at low pH, as:

$$CaCO_3 + 2H^+ \leftrightarrow Ca^{2+} + CO_2 + H_2O \qquad (1.3)$$

The released Ca^{2+} will react with SO_4^{2-} to generate gypsum or bassanite:

$$Ca^{2+} + SO_4^{2-} \leftrightarrow CaSO_4 \qquad (1.4)$$

When carbonates are depleted, metal hydroxides, such as gibbsite, would participate in the neutralisation.

1.2.4 Main minerals related to acid sulphate soils

There are two phases of development of ASS which involve different minerals and organics, namely, the reduction phase and oxidation phase. The reduction phase (often referred to as PASS) mainly involves iron sulphide minerals. These sulphides mainly include pyrite (FeS_2) and sometimes iron monosulphides which are generally represented as FeS and vary in form and include the amorphous sulphides with general stoichiometry, mackinawite and greigite (Smith and Melville, 2004). For the oxidation stage, jarosite and natrojarosite are the most common sulphur-bearing minerals. Gypsum is common if carbonates are present in the sediments (Doner, and Lynn, 1989). Copiapite, schwertmannite and jarosite form and can be observed during rapid oxidation and in low pH conditions. Goethite is observed in a wide range of pH conditions, while ferrihydrite and hematite typically form in near neutral conditions. Some extremely soluble Fe-sulphate-hydrate species, such as melanterite and coquimbite may form as efflorescent crusts and contribute to high acidity and toxic metal concentrations (Crowley et al., 2003).

A part of the acids produced from the oxidation may be washed away by runoff; however, the remainder will react with soil minerals, mainly clay minerals, and liberate the dissolved aluminium, iron, manganese and heavy metals (Fitzpatrick et al., 1998). Kaolinite, the most common aluminium-bearing clay mineral, is an important source of Al^{3+} released to the AAS environment. The aluminium-bearing products generated from the process of the formation of AAS include soluble Al sulphates, such as halotrichite, pickeringite and alunogen, insoluble hydroxysulphates such as alunite and basaluminite, and Al hydroxides such as amorphous Al hydroxide or gibbsite (Blowes et al., 2003).

1.2.5 Minerals indicative of acidity and toxicity

Mineralogical studies of the secondary minerals formed in ASS indicate a link between the presence and persistence of specific secondary minerals and the pH of the environment (Bigham, 1994; Bigham et al., 1990, 1994; Bigham and Fitzpatrick, 2002). Generally, copiapite forms when pH < 1.5, jarosite forms when pH is in the range of 1.5 to 2.8, schwertmannite forms when pH is in the range of 2.8-4.5, goethite forms when pH < 6, while hematite generates when pH is in the range from 7 to 8, and the formation of ferrihydrite requires pH > 5 (Bigham, 1994; Alpers et al., 1994; Anderson, 1994; Fitzpatrick et al., 2003; Montero et al., 2005). Thus, these secondary iron-bearing minerals can be used as indicators of pH conditions when they are formed. Meanwhile, some aluminosilicate minerals in soils, such as k-feldspar and kaolinite, may also participate in the neutralisation process, consuming H^+ and releasing Al^{3+} (Blowes et al., 2003), and generating some aluminium-bearing minerals under different pH conditions. For instance, gibbsite forms in the primitive state of aluminosilicate neutralisation in near neutral conditions (Bigham and Nordstrom, 2000) and dissolves by reacting with sulphuric acid when pH further decreases in the range of 5-4. When the pH drops to below 4, soluble Al sulphates, such as halotrichite, pickeringite and alunogen may form (Bigham and Nordstrom, 2000). The insoluble hydroxysulphates, such as alunite and basaluminite, would form when the pH increases to 5 (Bigham and Nordstrom, 2000). Similar to the presence of iron-bearing secondary minerals, aluminium-bearing minerals also can be regarded as good indicators of pH conditions and various concentrations of Al^{3+}.

1.3 Availability of Hyperspectral Sensing for acid sulphate soils

The formation and evolution of ASS involve different kinds of mineral transformations. Firstly, ASS are generated by the oxidation of sulphidic minerals (pyrite, mono-sulphides) and the formation of secondary minerals such as iron oxyhydroxides (goethite, ferrihydrite) and iron sulphate minerals (jarosite, schwertmannite) (Fitzpatrick, et al., 2003; Sullivan and Bush, 2004). Secondly, the occurrence and severity (pH values) of ASS can be expressed by the presence of the type and amount of secondary minerals (Bigham and Nordstrom, 2000; Bigham et al., 2002). Therefore, to detect and map ASS and their severity rapidly and effectively, it is crucial to spatially detect the presence of the secondary minerals that are indicative of pH. Numerous studies have conducted to use hyperspectral sensing to rapidly identify and map the distribution of minerals on the surface (Burns, 1993; Farrand, 1997; Berman et al., 1999; Swayze et al., 2000; Rockwell, 2004; Cudahy et al., 2005). The following two sections describe the advantages of using hyperspectral sensing and the diagnostic spectral features of the main minerals related to ASS which could be potentially used to detect ASS.

1.3.1 Advantage of hyperspectral sensing

Hyperspectral sensors can acquire spectral data in narrow contiguous bandwidths, therefore providing a continuous spectra curve in a specified wavelength range, which allows the identification of diagnostic spectral features for mineral and soil identification with sufficient spectral and spatial resolution (Goetz et al., 1985). The hyperspectral sensing tools used in the present study included an airborne hyperspectral instrument called the hyperspectral mapper (HyMap) and proximal hyperspectral instruments (the ASD FieldSpec 3 and HyLogger^{TM} 2). HyMap, operated by HyVista Corporation, Australia, has 128 contiguous bands in the VNIR and SWIR range from 0.45 to 2.5 µm, with bandwidths between 15-20 nm, and pixel resolution between 2-10 m; ASD FieldSpe 3, developed by ASD Inc, USA, has a full spectral range in 0.35-2.5 µm, with sampling interval of .0014 µm (1.4 nm) in the range of .350-1.0 µm and .002 µm (2 nm) in the range of 1.00-2.50 µm, and with spectral resolution of 3 nm@ 700 nm, 10 nm @1400 nm and 10 nm @2100 nm; Hylogger^{TM} 2, developed by CSIRO, Australia, using ASD spectrometer in the spectral range of 0.45 to 2.5 µm, provides rapid, robotic scanning of drill core, chips and powder. The comparison between HyMap, ASD fieldSpec 3 and HyLogger^{TM} 2 was summarised as Table 1.1.

Table 1.1 Comparison between HyMap, ASD and HyLogger

	Spectral range	Spectral resolution
HyMap	0.45 to 2.5 µm	.010-.020 µm
ASD fieldSpec 3	.35-2.5 µm	3 nm@ 700 nm, 10 nm @1400 nm 10 nm @2100 nm
HyLogger™ 2	0.40 to 2.5 µm	.004 µm

In contrast to the traditional sensors, the advantages of hyperspectral instruments can be summarised as follows:

(1) Hyperspectral sensing usually has hundreds of contiguous bands compared to multispectral sensors, which typically consist of less than 10 bands that are often not continuous;

(2) The spectral resolution of hyperspectral data typically ranges from .001 to .20 µm in contrast to the resolution of multispectral data, which typically ranges from .050-.120 µm in bandwidth. Commonly, a .020 µm bandwidth is sufficient to distinguish the diagnostic absorption features of the majority of spectrally responsive minerals.

(3) Hyperspectral sensing (airborne or spaceborne) has the ability to acquire not only an image with high spatial resolution, but also a complete reflectance spectral for each pixel in the image, providing an image cube with a 3D pattern, with X, Y for space and Z for the spectra.

(4) Hyperspectral sensing is very sensitive to the changes in chemical composition and physical structure of the object. The variations in material composition often cause changes in the wavelength and depth of the spectral absorption; this allows us to probe subtle changes of the objects and identify similar objects in the natural environment (Clark, 1999). In addition, hyperspectral sensing has an advantage of being sensitive to both crystalline and amorphous materials, compared to the method of X-ray diffraction which usually requires the minerals to have good crystallinity (Clark, 1999).

1.3.2 Spectral features of the main minerals related to acid sulphae soils

Acid sulphate soils are dominantly composed of two main groups of minerals: non-iron or sulphate-bearing minerals (e.g., clay minerals such as kaolinite and illite and

other silicates such as quartz and feldspars), and secondary iron and sulphate-bearing minerals (e.g., schwertmannite, jarosite, goethite) (Fitzpatrick et al., 1996). The secondary iron-bearing minerals, including iron oxides, iron hydroxides and oxyhydroxides and iron sulphates, have diagnostic spectral absorption features in the reflectance range of 0.35-2.5 μm due to both electronic and vibrational processes. The main absorption features of these minerals, however, are concentrated on the visible and near infrared (VNIR) range (0.25-1.3 μm) due to the crystal field effects and charge transfer absorption. The common ferric iron absorption features mainly include the absorption centered in the ultraviolet region near 0.25 μm due to the charge transfer, a strong absorption edge between 0.4 and 0.6 μm which may be due to the paired excitations, and three absorptions near 0.45, 0.55 to 0.65, and 0.75 to 0.95 μm due to the crystal transition. The ferrous iron exhibits crystal transition absorption in the range of 0.9 to 1.1 μm (Crowley et al., 2003).

In contrast to the other minerals present in ASS, such as clay minerals, carbonates and sulphates, their main diagnostic absorption features occur in the short wave and infrared (SWIR) range (1.3 to 2.5 μm) and are caused by the molecular vibrations of H_2O, OH-, Al-OH, Mg-OH, Fe-OH and CO_3^{2-} (Clark, 1999). Generally, water molecules have a strong absorption at 1.4 μm due to the first overtones of the water O-H stretching, and another absorption at 1.9 μm related to the combination of the H–O–H bending (Crowley et al., 2003). Hydroxyl shows an overtone absorption near 1.4 μm, while Al-OH shows absorption in the range of 2.16-2.2 μm, Mg-OH shows absorption near 2.3-2.36 μm and Fe-OH shows absorption in the range of 2.23-2.295 μm (Gupta, 2003; Crowley et al., 2003); thus, the region of 2.1-2.4 μm is usually used to diagnose clay minerals (Gupta, 2003). Carbonates show diagnostic vibrational absorptions in the range of 2.30-2.35 μm (Crowley et al., 2003).

1.4 Previous Studies on ASS and their Mapping Limitations

A voluminous amount of research has been done in the field of AAS (or acid rock drainage) which is subject to a similar formation mechanism as acid sulphate soils (actually AMD is one kind of ASS). The studies on AMD have mainly focused on the mineralogical and chemical aspects of AMD and only a selected few studies have looked at the relationship between some indicative minerals and the pH value. Bigham (1994), Alpers et al. (1994), Crowley (2003), Montero et al. (2005) and Fitzpatrick et al. (2008) all examined the relation between the indicative mineral

species or assemblages and pH values in AMD areas. Some studies have investigated a new method to monitor and assess the extent and severity of AMD by utilising hyperspectral sensing to characterise and identify the indicative minerals (Anderson, 1994; Farrand, 1997; Anderson and Robbins, 1998; Swayze et al., 2000; Crowley et al., 2003; Rockwell, 2004). Other studies have tried to directly relate the reflectance spectral features to soil properties by establishing a mathematical model. Ong et al. (2003) used partial least squares regression (PLSR) to model the relationship between the pH value and reflectance spectral features in an AMD area.

Compared to the research on AMD, less work has been done on ASS in general, with seminal works carried out in Australia on the formation, classification, mineralogy and characterisation of ASS (Fitzpatrick et al., 1996; 1998; 2009; Sullivan and Bush, 2004), and other studies carried out on the environmental impacts of ASS (Bigham and Nordstrom, 2000; Johnston et al., 2011). Most studies to date have concentrated on the investigation, monitoring and mapping of ASS by conventional field sampling and laboratory chemical measurements (Fitzpatrick et al., 2003; 2008; Degens, 2009; Sullivan et al., 2009), and some works have also been done on the management and reclamation of ASS (Department of Environment and Conservation, 2011). However, much less work has been done on the mapping of ASS and monitoring the environments affected by ASS using remote sensing. The studies conducted on mapping and monitoring of ASS have only focused on mineral identification related to ASS on the surface of the area and tried to deduce some potential risks based on the mineral distribution and the relationship between the minerals and soil acidity. For example, Lau (2008) mapped associated iron-bearing secondary minerals, carbonates and sulphates using HyMap in South Yunderup, Western Australia, and produced a risk map based on the mineral distribution. A review of studies conducted on ASS and AMD in terms of environmental monitoring and mapping by remote sensing indicates that there still exist problems and knowledge gaps which are demonstrated as follows:

- Few studies have been done on the quantitative analysis of the relationship between soil properties and soil spectral features related to ASS, although numerous studies have been conducted on the qualitative linking between the presence of secondary iron minerals and pH;
- Very few studies have looked at identifying trace metal toxicity arising from ASS by remote sensing. For example, little work has been done on studying the

relation between aluminium-bearing minerals and the release of Al^{3+}, and none on the mapping of the surface distribution of Al toxicity, an effect arising from ASS that is extremely harmful to the environment.

- Little work has been conducted on using proximal hyperspectral sensors to observe the environment and routinely monitor the environmental changes caused by ASS.
- There is a dearth of knowledge on the subsurface mineral mapping of soils and ASS, and in particular the use of new rapid spectral mapping methods such as the Hylogger™.
- Although a large amount of work has been conducted on pyrite and sulphide oxidation and related effects, even in ASS (Bigham et al., 1990; Evangelou, 1995; Smith and Melville, 2004; Burton et al., 2006), little work has been done to investigate sulphidic material oxidation and the resulting mineralogical, chemical and spectral changes under natural drying and wetting cycles. Furthermore, little work has been done to investigate the transformation of minerals and their spectral responses within natural and artificial landforms underlain by oxidizing sulphidic material.
- Little systematic work has been done to characterize different subtypes of ASS based on their reflectance spectra.

The identification of these gaps in knowledge due to few or no studies on particular aspects of ASS, and in particular the application of hyperspectral remote sensing to ASS, formed the basis of the investigation in this thesis.

1.5 Main Objectives of this Study

The main aim of this research was to investigate the effectiveness of hyperspectral sensing to characterise, map and monitor ASS and the effects of the resulting acidity and toxicity on the environment in the South Yunderup area located on the Swan Coastal Plain. To achieve this aim, this research had the following specific objectives:

- To review and understand the mechanism of the occurrence of acid sulphate soils and its harmful effects on the environment.
- To investigate the mineralogical, geochemical and spectral changes occurring during the controlled oxidation of sulphidic materials that mimic natural wetting and drying cycles, and are therefore critical to the effective application of

hyperspectral sensing.

- To characterise the reflectance spectra of ASS and related minerals.
- To identify and map the main minerals related to ASS in the study area, including the minerals distributed on the surface and in the subsurface.
- To establish the relationship between indicative secondary iron mineral species and pH ranges, and then use this relationship to deduce the soil pH distribution based on the map of minerals.
- To mathematically model the relationship between the soil properties and spectral features, and then use the predictive model on HyMap to predict the extent and severity of the ASS directly.
- To map the extent and severity of potential Al toxicity based on the distribution of soil pH and the distribution of the main Al bearing minerals such as kaolinite in the soil.
- To investigate the effectiveness of the HyLogger (proximal hyperspectral sensing) to identify and map the subsurface soil mineralogy in soil cores, and combine this spectral data with the chemistry of the soil to establish a model to distinguish actual acid sulphate soils (AASS) and potential acid sulphate soils (PASS).

1.6 Main Contents of this Thesis

The thesis is organised as follows:

- Chapter 1 has introduced the project and its objectives.
- Chapter 2 deals with the methodology and data acquisition.
- Chapter 3 introduces the setting of the study area.
- Chapter 4 reports the investigation of the evolution of sulphidic materials under controlled drying (oxidation) and wetting (reduction) cycles (incubation experiment). Investigations into the oxidation rate of iron sulphides in the sulphidic material including mineralogical, compositional and acidity changes during different wetting and drying conditions were examined and assessed, and these results underpinned the application of the hyperspectral mapping of the ASS.
- Chapter 5 reports the investigation of the spectral changes occurring during the development of AAS. The aim was to observe the spectral changes that occur

due to lying on different landforms and spectral changes over time as ASS develops.

- Chapter 6 explains the spectral characterisation of the ASS and related mineralogy in the study area. This chapter details the characteristics of the reflectance spectra of the ASS which include several subtypes with different soil pH and containing different mineral assemblages. The relationship between specific minerals and surrounding pH is examined.
- Chapter 7 reports the examination of the soil acidity estimation via PLSR modelling of the HyMap data. Surface soil pH maps produced by PLSR modelling of spectral data and maps produced by pH indicative minerals were compared and the benefits of each were assessed.
- Chapter 8 reports the investigation of the surface mapping of the main non-iron minerals using the HyMap dataset, and presents the estimates of the distribution and severity of Al toxicity in the study area, based on the soil pH distribution and the distribution of the main aluminium-bearing minerals.
- Chapter 9 looks at the effectiveness of HyLogger in identifying spectrally responsive pH indicator minerals in the subsurface and combining geochemical data from the soil cores to assess ASS in the subsurface.
- The conclusions of the main aims of the study are presented in Chapter 10.

Chapter 2 Methodology and Data Acquisition

In this study, the application of hyperspectral sensing made use of three instruments: an airborne hyperspectral instrument, HyMap; a portable proximal hyperspectral analytical spectral device (ASD), FieldSpec3; and the proximal HyLogger system. Airborne HyMap sensor data were used to remotely map the minerals related to ASS, and were further used to remotely map the soil pH of ASS by utilising the relationship between the minerals and pH or by applying the model established by PLSR which reflected the relationship between the spectral features and soil pH. The HyMap data were also used to map the Al toxicity. ASD FieldSpec3 was used to measure spectra in the field and laboratory, with spectra being used to select suitable end-members for the HyMap data, and also to provide some spectral training datasets for predictive modelling of the relationship between spectra and chemical properties. The ASD was also used to observe the spectra variations during an incubation experiment which was designed to simulate the formation of ASS. The HyLogger system was used to scan the soil cores and thereby assess the occurrence and severity of ASS in the subsurface.

Conventional methods, such as soil sampling, soil coring, X-ray diffraction (XRD), scanning electron microscopy (SEM) with energy dispersive X-ray analysis (EDXA) and chemical measurements were also applied in this study. Soil sampling and soil coring were used to collect soil samples to take to the laboratory for further hyperspectral data measurements and chemical measurements. The XRD and SEM/EDXA were used to confirm the mineral identification and mineral composition of the samples collected from the field which could be used to establish the relationship between the confirmed mineral species and to choose end-members for further mapping. The results of XRD and SEM were used to verify the results of the mineral identification and mineral mapping by spectral sensing. Chemical measurements, particularly soil pH measurements, were used as training data to establish the relationships of the minerals and soil chemistry (mainly soil pH) and to model the relationship between spectral features and soil chemistry (mainly soil pH), and were also used to assess the ASS and verify the corresponding results.

To further understand and assess ASS, an incubation experiment was conducted as a supplement to examine the pyrite oxidation rate and resulting pH changes and

release of metals which could create potential environmental hazards in different climatic conditions. The details of these methods and tools are described in the following sub-sections.

2.1 Field Investigation

2.1.1 Surface soil sample collection

The aims in collecting the surface samples were threefold. One aim was to investigate the mineral distribution in the study area, one was to choose end-members for mineral mapping, and one was to verify the mineral mapping results.

Twelve sites were selected within the field area, based on the preparatory iron content mapping results from HyMap and visual observations of ASS occurrences. Several field datasets from Lau (2008) were also referenced. At each site, 4-5 samples were collected within a 10 m radius and surface samples measuring approximately 10×5 by 1 cm depth were carefully extracted and placed in an enclosed plastic box and then placed in an insulated cool box for transport back to the laboratory, where they were refrigerated at 5^{o}C. Care was taken not to disturb the surface of the samples until laboratory spectral measurements were obtained. The samples were collected during late November in 2011 and January in 2012 (summer months) to coincide with the seasonal collection of the HyMap data. The soil sample collection was mainly involved in the research activities reported in Chapter 6, Chapter 7 and Chapter 8.

2.1.2 Soil coring

The aim of the soil coring was to investigate the mineral distribution and soil properties in the subsurface. The work related to the soil coring is reported in Chapter 9 and the detailed method is described in that chapter.

2.2 Hyperspectral Data Acquisition

2.2.1 HyMap data acquisition

The remotely-sensed hyperspectral imagery used in this study was acquired via the airborne HyMap sensor operated by HyVista Corporation, Australia. Detailed information about the HyMap imagery used in this study is presented in Chapter 7.

2.2.2 Proximal ASD hyperspectral data

An ASD FieldSpec3 spectrometer was used in the laboratory to measure the reflectance spectra of the surface of the soil samples. These proximal hyperspectral data were used for three purposes. The first purpose was to characterise the acid sulphate soils and related minerals in reflectance spectra; the second purpose was to use the data as training data to establish the relationship between the spectral features and soil properties by PLSR modelling; and the third purpose was to select end-members to map the distribution of the related minerals. The ASD FieldSpec3 was also used to observe the spectral changes in the incubation experiment. The use of the ASD in this study to measure the reflectance spectra is described in Chapters 4, 5, 6 and 7.

2.2.3 HyLogger^{TM} scanning

HyLogger scanning was performed on the soil cores with the aim to acquire the hyperspectral data of the soil in the subsurface. Then, the hyperspectral data were used to identify and map the mineral distribution in the subsurface according to the analysis of the spectral characteristics. A detailed description of this method is provided in Chapter 9.

2.3 Chemical Measurements

2.3.1 pH measurement

The pH measurements involved the soil samples collected from the surface of the study area and the samples extracted from the soil cores at different depths. The aims in measuring the soil pH included four aspects. One was to establish a link between the surface mineralogy and the soil pH; one was to create training data to establish the relationship between the spectral features and pH values in PLSR modelling; one was to verify the soil pH results and the severity of ASS; and one was to form an important index with which to separate the potential acid sulphate soils and actual acid sulphate soils.

The pH values of the soil samples were measured in the laboratory using a TPS WP-80D dual pH-MV meter, which provides a pH resolution of 0.01 pH. The pH values of the soil materials were measured using the standard soil method of mixing soil and deionised water at the weight ratio of 1:5 (Rayment and Lyons, 2010). The

pH meter was regularly calibrated with pH 7 and pH 4 buffers at every 10 measurements. The pH measurements are reported in Chapters 4, 5, 6, 7, 8 and 9.

2.3.2 Soil solution analysis

The soil solution analysis in this study mainly involved the solution from the controlled incubation experiments on the sulphidic materials. The soil solution analysis is reported in Chapter 4 and the methods of the measurements are described in that chapter.

2.3.3 Titratable actual acidity and titratable potential acidity measurements

Titratable actual acidity (TAA) and titratable potential acidity (TPA) tests were used to measure the soil acidity. The TAA test considers the actual acidity of the ASS, which is readily soluble and exchangeable in materials. The TPA test considers the potential acidity of the ASS, which has not yet been produced due to the incomplete oxidation of the sulphides.

To perform the TAA and TPA tests, firstly, the soil material needed to be dried at a temperature of 38 ^{0}C for 48 hours, and then milled to a fine powder (<5 microns). The measurements of the TAA and TPA are described briefly here as follows:

- For TAA, firstly, pH_{kcl} was measured by reacting the soils/sediments with 1 M KCl solution for 4 hours and allowing the mixture to stand overnight. TAA was then determined by titration of the suspensions to pH 6.5 (Ahern et al., 2004).
- TPA was measured based on the measurement of pH_{ox} which uses 30% hydrogen peroxide to fully oxidise all the sulphides present in the material to produce sulphuric acid. After peroxide decomposition and extraction of KCl, TPA was determined by titration of the suspensions to pH 6.5 (Ahern et al., 2004).

TAA and TPA test was done in Chapter 4.

2.4 Mineralogy Verification (Spectral Geologist, X-Ray Diffraction and Scanning Electron Microscopy)

All the surface ASS samples for which pH values were determined were submitted for XRD analysis and four of the subsurface samples were studied using SEM and EDXA to verify the spectral interpretation results. For XRD, the samples were milled to a fine particle size (<5 microns) and random powder mounts were prepared. The diffraction data were collected with Bruker D8 Advance X-ray diffractometer and the diffraction patterns were analysed to identify minerals using Eva software.

Undisturbed surface samples were gently placed onto stubs and Pt-coated for observation with a Zeiss Evo 40XVP SEM. The surface composition of the samples was examined using the Link energy dispersive X-ray analysis system attached to the SEM. Spectral feature analysis and the use of the Spectral Assistant (TSA) (Berman et al., 1999), from the Spectral Geologist (TSG) software, was used to assist in choosing suitable end-members for the spectral mineral mapping.

2.5 Spectral Mapping Methods

The principle of the feature mapping for hyperspectral sensing is generally a two-step process involving characterisation of the spectral features of the unknown pixel, and then comparing the spectral features of the unknown material with the spectral features of the known material which are from a spectral library such as the US Geological Survey (USGS) spectral library, or from ground truth (Gupta, 2003). Several mapping methods have been established, and the methods for hyperspectral data include pixel-based mapping methods, including spectral feature fitting (SFF), spectral angle mapper (SAM) and spectral indices, and sub-pixel-based mapping methods, including complete linear spectral un-mixing and partial un-mixing.

In the pixel-based mapping methods, there are differences in the comparison between known spectra and unknown spectra. The spectral angle mapper is an algorithm based on a hypothesis that the spectra can be treated as a vector in a space with dimensions equal to the number of bands. This method determines the spectral similarity between pixel spectra and reference spectra by calculating the angle between these two vectors (Figure 2.1). The smaller the angle between two spectra, the closer the two spectra are, and the more likely that the target material (as indicated by the reference spectra) lies in the pixel (Boardman and Kruse, 1994; Kruse et al., 1993).

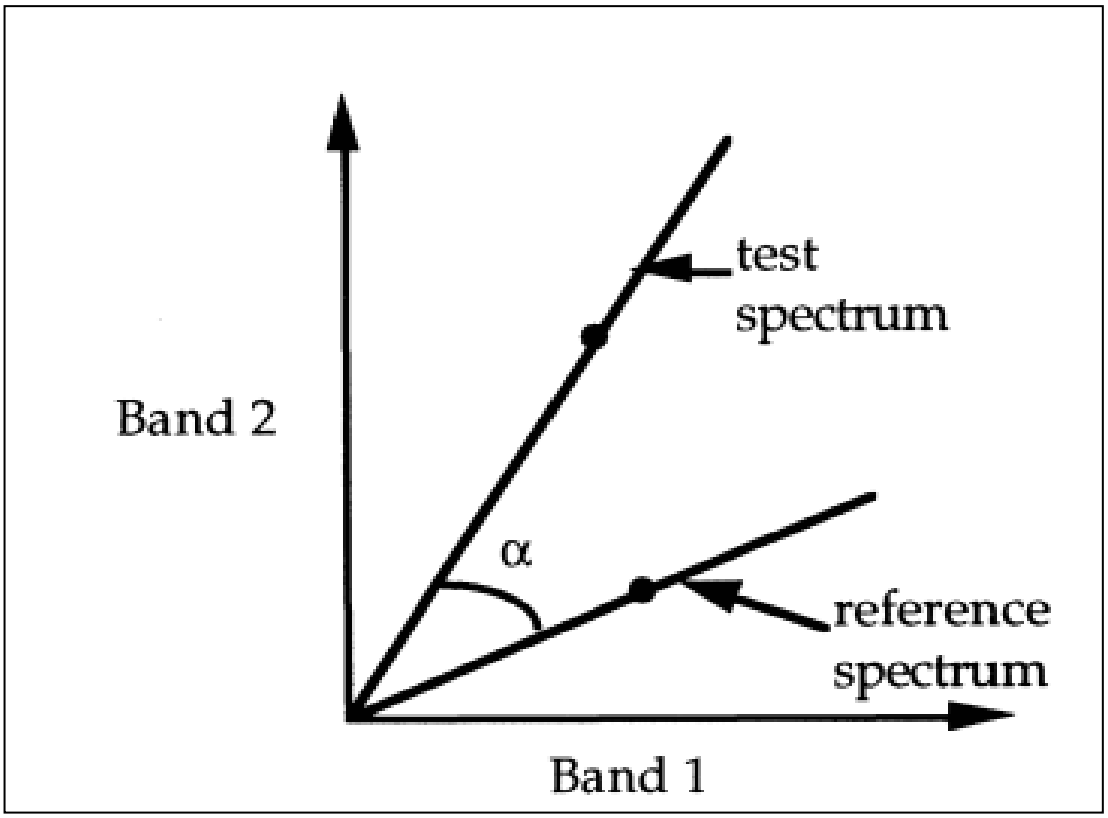

Figure 2.1: Comparison of two spectral vectors between the test spectrum and reference spectrum (Kruse et al., 1993)

Spectral feature fitting is an absorption feature-based detection algorithm to match the image spectra to selected reference spectra using a least squares technique (Kruse et al., 1988; Clark et al., 1990; Clark and Swayze, 1991). This method is based on the analysis of the characteristics of the spectral absorption which could be described according to its absorption position, absorption depth, absorption width (for which the full width of half maximum (FWHM) is used), and absorption asymmetry (Kruse et al., 1988) (Figure 2.2). Spectral feature fitting requires the data to be reduced to reflectance and the continuum which always corresponds to a background signal to be removed from the reflectance data prior to further analysis. Common spectral feature fitting uses the complete spectra in the comparison, while multi-spectral feature fitting is an advanced spectral feature fitting technique which allows the user to define multiple and specific wavelength ranges to extract the absorption feature for each end-member. The multi-spectral feature fitting technique also allows the user to define optional weights for each spectral range in order to emphasise the importance of certain features, and so is considered to produce relatively more accurate results than simple spectral feature fitting.

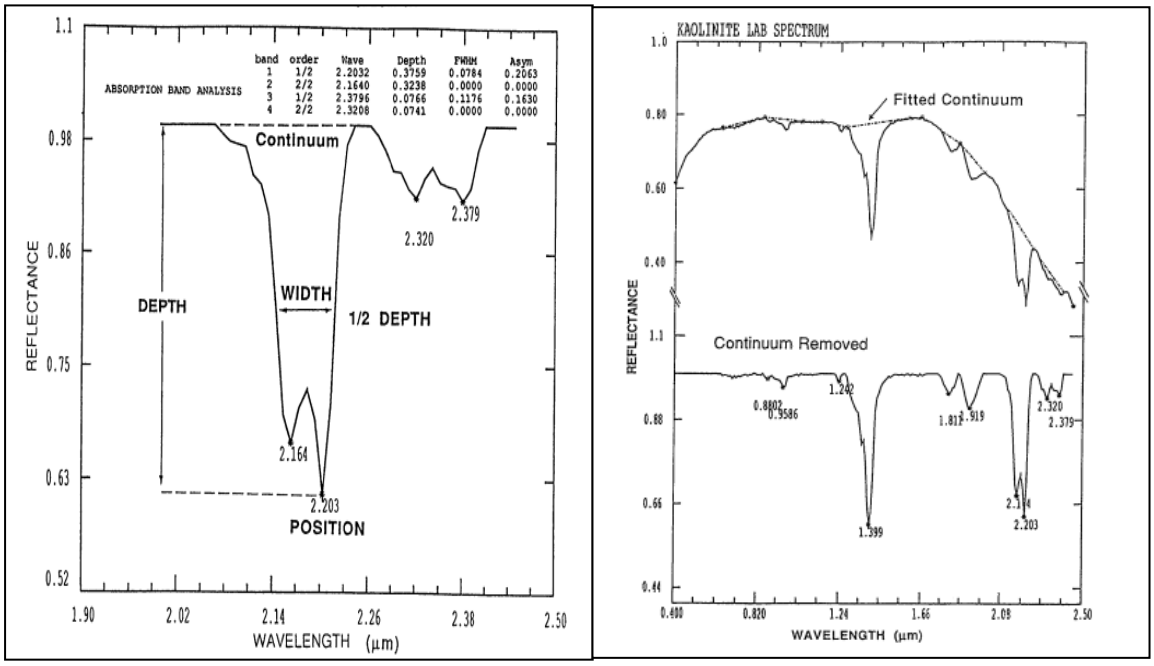

Figure 2.2: Spectral absorption features. Left image: spectral characterisation; Right image: spectral characteristics after continuum removal (Kruse et al., 1988)

The spectral indices method was developed by the CSIRO, as a component of their proprietary software called MMTG A-list (Hewson and Cudahy, 2010). The spectral indices method focuses on analysing and extracting the spectral features of specific absorption, including the absorption centre, relative depth or relative area of the absorption.

Complete linear spectral un-mixing is a sub-pixel mapping method that is based on the hypothesis that all end-members are mixed in reflectance in each pixel with a linear model in the pixel (Drake et al., 1999). The problem with this method is that it requires the use of all the end-members in the image and these are not easy to extract completely. Matched filtering is a method which only targets specific end-members in the pixel spectra; thus, it is commonly referred to as partial un-mixing. This method maximises the response of the target object and suppresses the response of the background (Chen and Reed, 1987; Stocker et al., 1990; Yu et al., 1993; Harsanyi and Chang, 1994).

In this project, the spectral feature fitting and spectral indices methods were mainly used to map the abundance and distribution of the minerals, although the SAM and spectral un-mixing methods were also applied in the mineral mapping with unsatisfactory results. The work related to the mapping was mainly involved in the results reported in Chapters 7 and 8.

2.6 PLSR Modelling

Partial least squares regression (PLSR) is a quantitative multivariate regression method developed by Herman Word (Wold, 1966a, 1966b), combining the features of principal component analysis (PCA) and multiple linear regressions (MLR). It allows for the analysis of data with strong correlations in the predictor variables, and is effective when the number of training samples is far smaller than that of predictor variables (Wold et al., 2001). Typically, the partial least squares (PLS) model consists of two outlier relations in the predictor matrix X and response matrix Y, respectively, and an inner relation between X and Y. The outer relation for the X block is written as:

$$X= t_1p_1^{'}+t_2p_2^{'}\ldots.+t_mp_m^{'}+E_m =\sum t_mp_m'+ E_m= TP'+ E$$

where T is the score matrix, P is the loading matrix, P' is the transpose of P, E is error matrix for block X, and the final factors number is m. The outer relation for the Y block can be written as:

$$Y= u_1q_1^{'}+u_2q_2^{'}\ldots.+u_mq_m^{'}+F_m^{=} \sum\mu mq_m'+F_m= UQ'+ F$$

where U is the score matrix, Q is the loading matrix, Q' is the transpose of Q, F is the error matrix for block Y and the final factors number is m. Reaching the aim of PLSR requires minimising the norm of F but maintaining a useful relation between X and Y. The simple model for this relation is linear between the score matrixes U and T and can be written as:

$$U=BT$$

where B is a regression coefficient. Then, the non-linear iterative partial least squares (NIPALS) algorithm is needed to improve the inner relation between X and Y because the inner relation calculates the X and Y blocks separately but does not relate X and Y to each other strongly. There are two types of PLS algorithms, namely, PLS1 and PLS2, in which PLS1 is regarded as simpler but suitable for the case when there is a need to only predict one response variable, such as soil pH. It is also believed that PLS1 provides better results than PLS2 if PLS1 is only applied separately to each column of the Y matrix. Therefore, PLS1 as provided in the TSG software was used in this research.

The procedures of PLSR include preparation of the training data, spectral processing which is used to remove some unwanted spectral variability, cross-validation which is used to assess the performance of the predictive model,

determination of the optimum factors to keep a good balance between robustness of the model and the minimum number of residual, sample and spectral outliers, and final regression coefficient output to show the influential weight of the different spectral predictors. The PLSR modelling conducted in this study is discussed in detail in Chapter 7 and Chapter 9.

2.7 Incubation Experiment

An experiment to test the mineralogical and chemical changes occurring during the controlled oxidation of sulphidic materials was conducted. There were two parts of the incubation experiment undertaken in this study. One part was to observe the spectral changes of the sulphidic materials when they lay in different landforms and to observe the spectral changes of the same material over time (temporal spectral changes). This part of the experiment involved weekly spectral measurements and image acquisition.

The second part was more complicated and aimed to observe the mineralogy, chemistry, material composition changes and spectral characteristics of the test material in different drying and rewetting conditions, thereby simulating the ASS evolution in different climatic conditions (weekly cycles of wet and drying, and seasonal cycles). This part of the experiment divided the homogenous sulphidic test material into three groups and subjected each group to different drying-rewetting cycles (weekly, monthly and three monthly). Each cycle commenced with draining pore water until the material was dry and then rewetting it with deionised water. The duration of these cycles varied from weekly to monthly to three monthly. For each duration, the pore water extracted was analysed for its pH, EC and composition (cations and anions). After the final drying phase, the different parts of the materials in the three different groups, including the surface and inner parts, were extracted to do XRD, TAA, TPA and total sulphur and total carbon content analyses. The incubation experiments are reported in Chapter 4 and Chapter 5 and the detailed setting of the experiments is illustrated in Chapters 4 and 5.

Chapter 3 Setting of the Study Area

3.1 Location of the Study Area

The study area is located within the township of South Yunderup, which is approximately 80 km south of the City of Perth, the capital of Western Australia. South Yunderup is located in the area of the Peel Inlet in Peel-Harvey Estuary (Figure 3.1). The Peel-Harvey Estuary and surrounding low-level landscapes lie on the western part of the Swan Coastal Plain, which is part of the Quaternary surface of the Perth Basin (Semeniuk and Semeniuk, 1990; Gozzard, 2007).

The area surrounding the estuary is underlain by the mid-Pleistocene Bassendean Dune System, which is composed of deep leached sands, and the late Pleistocene Spearwood Dune System, which is composed of aeolinite capped by a calcrete and underlain by quartz sand (Gozzard, 2007). The estuary is part of a shallow basin which has limited exchange with the sea and is fed by several rivers draining from the east. The study area has the Murray River flowing from the east into the estuary, forming a delta consisting of a main channel flanked by levees, lakes and flats that are dominated by interbedded sands and muds (Semeniuk and Semeniuk, 1990). The soils present in the wetlands and the recent alluvial landforms are mainly dominated by muds and sandy muds. Much of the landscape around South Yunderup is low lying and below 5 m on the Australian height datum (AHD), varying between 6 and 9 m in relief. South Yunderup is located on the south bank of the Murray River within the Shire of Murray, close to the Murray River and Peel Inlet junction with a network of recently constructed artificial canals.

3.2 Setting of Geology and Geomorphology

The study area is located on the Swan Coastal Plain which is part of the Perth region. The Perth region is mainly composed of two geological areas which are separated by the Darling Fault, namely, the Darling Plateau (or Darling Range) and the Swan Coastal Plain. The Darling Fault is one of the major fractures in the Earth's crust which extends 1000 km from the east of Shark Bay to Point D'Entrecasteaux on the south coast. The Darling Plateau has an average elevation of about 300 m AHD. It lies to the east of the Darling Fault and forms part of the Yilgarn Craton. The

bedrock of the plateau is dominantly Archean granite-greenstone and is covered by weathering products of lateritic materials and associated sands and gravels.

Figure 3.1: Location of the study area(modified from Google map)

The Swan Coastal Plain lies to the west of the Darling Fault, it extends westwards from the Darling Fault and the Gingin Scarps to the Indian Ocean. Commencing from the Ordovician, sediments from eroded continental rocks started to accumulate to the west of the Darling Fault with fluvial sediments deposited gradually built up through to the Late Jurassic and earliest Cretaceous periods. A large thickness of marine sediments was deposited as the sea over the Perth Basin grew wider and deeper (Gozzard, 2007). Uplift and erosion during the late Cretaceous to Paleogene periods favoured carbonate sedimentation that was followed by clastic sedimentation, and the development of weathering profiles over the basement rocks of the plateau (Gozzard, 2007). Due to the rise and fall of sea levels during the Neogene and Quaternary periods, sediments consisting mainly of sands, limestone, silts, clays and gravel of marine, estuarine and aeolian origin were deposited (Gozzard, 2007).

The Swan Coastal Plain includes several geomorphological elements trending approximately parallel to the present coastline. The sediments underlying these geomorphic elements were mainly deposited by rivers in the east and the wind to the west, giving rise to the following units from east to west: Ridge Hill, Pinjarra Plain and three dune systems, namely, the Bassendean Dune System, Spearwood Dune System and Quindalup Dune System (McArthur and Bettenay, 1974; Gozzard, 2007) (Figure 3.2).

Ridge Hill Shelf lies in the most eastern part of the Swan Coastal Plain, forming the foothills of the Darling Scarp with a narrow strip of 1.5 to 3 km width along the scarp (McArthur and Bettenay, 1974; Gozzard, 2007; Rivers, 2009). Pinjarra Plain lies on shoreline deposits and coastal dunes which were developed in several dune-building events 240,000 to 100,000 years ago during an interglacial period. The dunes consist of low hills of quartz sand interspersed with sand flats and seasonal swamps (Gozzard, 2007; Rivers, 2009). Further to the west, the Spearwood Dune System comprises two stratigraphic units: a foundation lower limestone formation called the Tamala Limestone which is composed largely of broken fossil shell fragments and various amounts of quartz sand; and its overlying cover of yellowish-brown sands (Gozzard, 2007; McArthur and Bettenay, 1974; Bastian, 1996).

The Quindalup Dune System is the most western dune system of the Swan Coastal Plain bordering the current coastline. The Quindalup Dune System consists of recent unconsolidated aeolian deposits of calcareous sands, exhibiting a linear arrangement parallel to the present coastline, and each individual dune in it shows a

gentle windward and steep lee slope because of the prevailing south-west wind (Gozzard, 2007; Rivers, 2009).

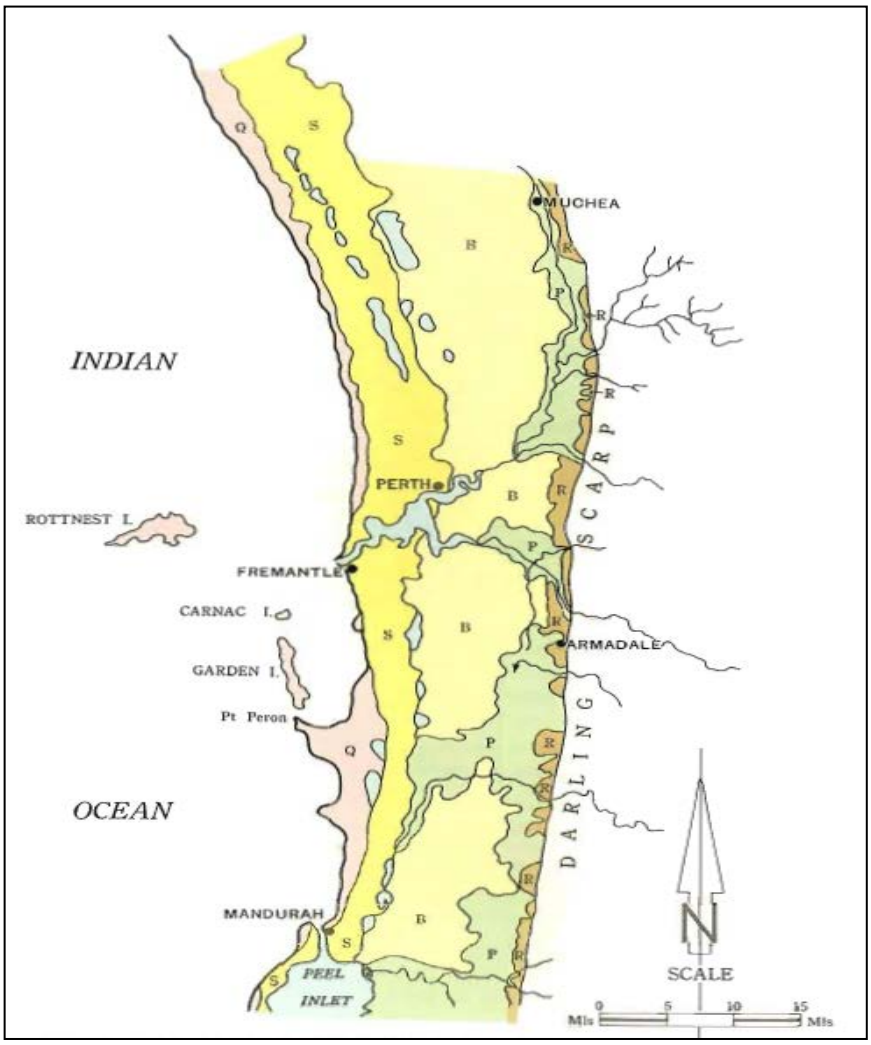

Figure 3.2: Geomorphic elements of the Swan Coastal Plain – R (Ridge Hill Shelf), P (Pinjarra Plain), B (Bassendean dunes), S (Spearwood dunes), Q (Quindalup dunes) (McArthur and Bettenay, 1974)

3.3 Climate

The Perth region has a typical Mediterranean climate. It is hot and dry in summer, and wet and warm in winter. Summer generally commences in December and lasts to late March, with an average temperature of 29 degrees Celsius during the day and 17 degrees Celsius at night. Generally, the hottest month is February. Winter falls from June to August, with an average temperature of 18 degrees Celsius during the day, and 9 degrees Celsius at night, and the coldest days are in July. The maximum temperatures from 1994 to 2011 and in 2011 are shown in Figure 3.3.

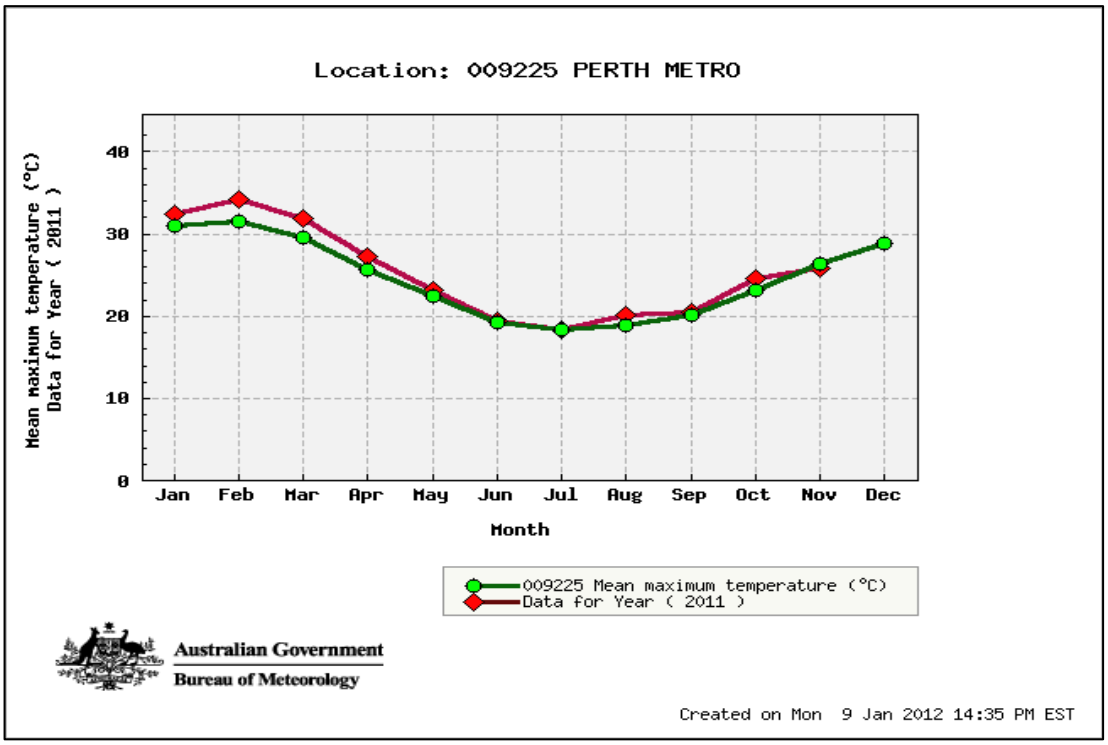

Figure 3.3: Mean maximum temperature from 1994 to 2011 and in 2011 (Bureau of Meteorology, Year 2011).

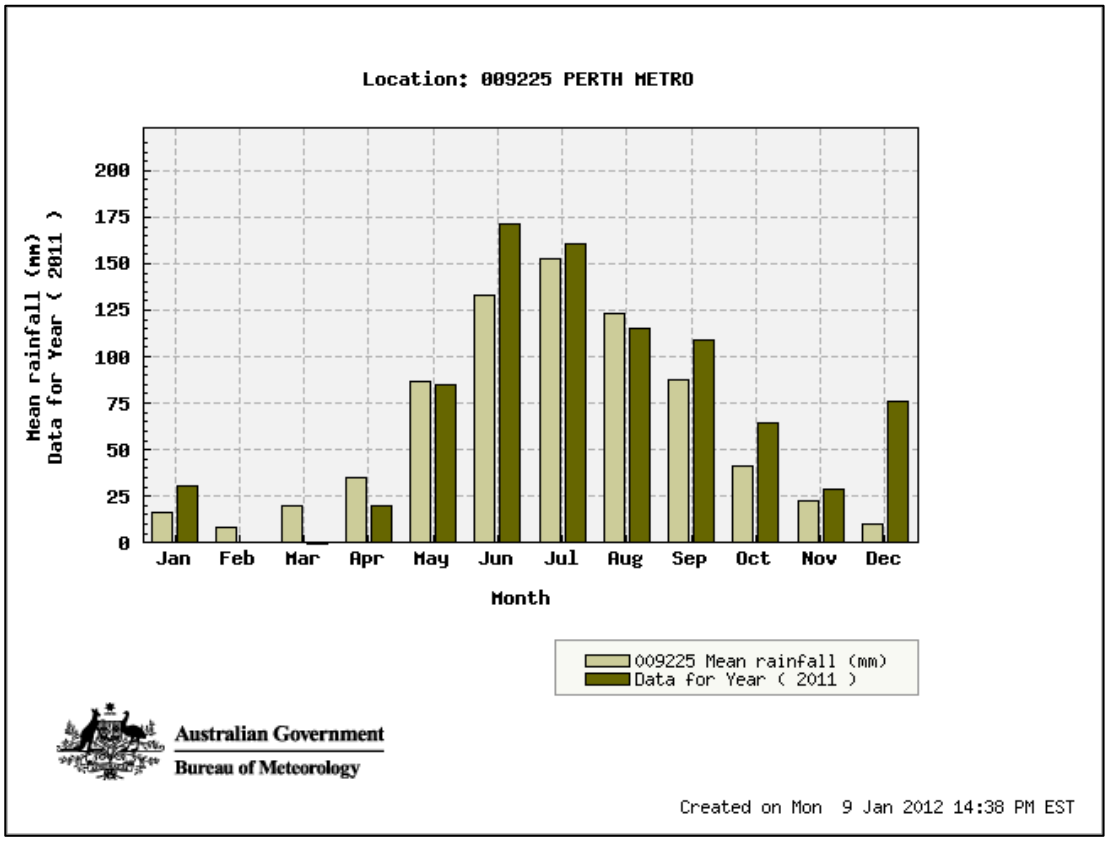

Figure 3.4: Mean rainfall (mm) from 1993 to 2011 and in 2011(Bureau of Meteorology, Year, 2011).

The average rainfall in the Perth region is 880 mm, and it mainly falls in the period between May and September, and especially concentrates in the winter season from June to August, with the wettest days in July. The mean rainfall figures from 1993 to 2011 and in 2011 are shown in Figure 3.4.

3.4 Hydrology

The Perth region includes two basins, namely, the Swan Coastal Basin and the Murray Basin. South Yunderup lies in the Murray Basin. The Murray Basin covers an area of 2018 km^2, crossing the Darling Range and Swan Coastal Plain and finally discharging into Peel-Harvey Estuary near Mandurah. The major tributaries are the Hotham River, Williams River and North and South Dandalup Rivers (CSIRO, 2009).

The Peel-Harvey Estuary is considered to be a shallow basin estuary, with limited tidal exchange with the sea. It has been gradually accumulating sediments since the Late Holocene period (Degens, 2009). Several rivers feed into the Peel-Harvey Estuary, having been forming deltas and floodplains with clay and silt-rich deposits (Semeniuk and Semeniuk, 1990; Degens, 2009). There are two main rivers flowing into the Peel Inlet: the Serpentine River which flows from the north travelling between the Spearwood and Bassendean Dune Systems, and the Murray River which flows from east and transects the Pinjarra Plain and upper Guildford formation. Before discharging into the Peel Inlet, both the rivers form a large area of delta which merges together as the Murray-Serpentine Delta. This delta complex consists of levees, lakes, abandoned channels and flats underlain by a complex series of interlayered muds and sands (Semeniuk and Semeniuk, 1990; Degens, 2009).

Waterlogging is a common phenomenon throughout the Peel-Harvey area during the winter wet season and early spring when the level of rainfall is more than evaporation. The drainage in the low relief areas is severely restricted, leading to the development of waterlogged conditions in these seasons (Rivers, 2009).

3.5 Soils and Vegetation

The Ridge Hill Shelf has residual laterite developed on the surface including yellow sands that are likely to be derived from the laterite. The vegetation on the shelf area comprises *Eucalyptus marginata-E.calophylla* forest, *Banksia grandis, Casuarina fraserianna* and *Persoonia longifolia* (McArthur and Bettenay, 1974). The Pinjarra Plain consists of unconsolidated alluvial deposits with successive layers formed from

the erosion of material from the Darling Scarp, consisting of pale-grey and blue clays through to brown silty and sandy clays with lenses of conglomeritic and shelly sands (McArthur and Bettenay, 1960; Davidson, 1995; Bolland, 1998). The Bassendean Dune System contains iron podzols and iron-humus podzols, and the soils have low fertility and are susceptible to leaching (McArthur, 1991; Rivers, 2009). The vegetation in this area mainly includes *Banksia menziesii*, *B. attenuata*, *B.ilicifolia*, *Casuarina freaseriana*, and *Xylcmelum occidentale* as codominants (McArthur and Bettenay, 1974).

The Spearwood Dune System consists of yellowish-brown siliceous sands overlying limestone at varying depths (Rivers, 2009). The sands appear red/brown, yellow and pale yellow/grey and are coated with both iron and Al oxides (Bollan, 1998). The vegetation on this system includes *E.gomphocephala* forest and *E.calophylla* which is only in the transition zone from this system to the Bassendean Dunes (McArthur and Bettenay, 1974).

The Quindalup Dune System usually consists of the most recent unconsolidated aeolian deposits (Rivers, 2009), which are mainly composed of quartz sands and shell fragments made up of calcium carbonate which makes the sands alkaline (Bollan, 1998). The vegetation on Quindalup Dunes is different from the other two dune systems in that the main species are *Acacia rostellifera* and other *Acacia spp.*, *Callitris robusta*, *Melaleuca huegelii* and *Mpubescens* in a scrub formation (McArthur and Bettenay, 1974).

3.6 Landform Elements of Study Area

The study area consists of several natural and artificially constructed landforms. The landforms are linked to the development and occurrence of ASS. The main landforms are (Figures 3.5 and 3.6):

- Wetlands (lakes) – These occur as permanent to seasonally saturated water bodies along the Murray River as well on the floodplains of the river. Most of the wetlands are hydrologically connected to the river and inlet. Many of these wetlands gradually dry in summer months and display orange to yellow surfaces, which are indicative of ASS (Figures 3.5 and 3.6 E, F).
- Inactive floodplains – These are flat areas adjacent to the Murray River and are underlain by silts and clays (Figure 3.6 D). They are largely exposed but are prone to waterlogging during intense rainfall events.

- Constructed drains – Drains, 2-20 m wide and 1-2 m deep, were constructed to allow the flow of water from inland waterlogged areas (lakes and floodplains) to the inlet. Many of the drains in the region were constructed in the early 1900s. Similar to that of the wetlands, the water level of the drains is seasonally affected.
- Canals – Canals were dredged in 1990-2000 to build marinas (Figure 3.5).
- Compacted flats – The artificially constructed flats are adjacent to the dredged canals and have been compacted for urban development. These flats are often 1-2 m higher than the surrounding areas and some are immediately adjacent to the canals (Figures 3.5 and 3.6 C). The flats are underlain by 1-2 m of dredged material. Much of the dredged material was sulphidic-bearing; therefore, these flats are sites of severe ASS development.
- During winter and spring, the drain surfaces are submerged, but during the end summer months, the drain surfaces are exposed and show grey to orange to reddish surface layers, all of which are visual signatures indicative of ASS (Figure 3.6 A, B).

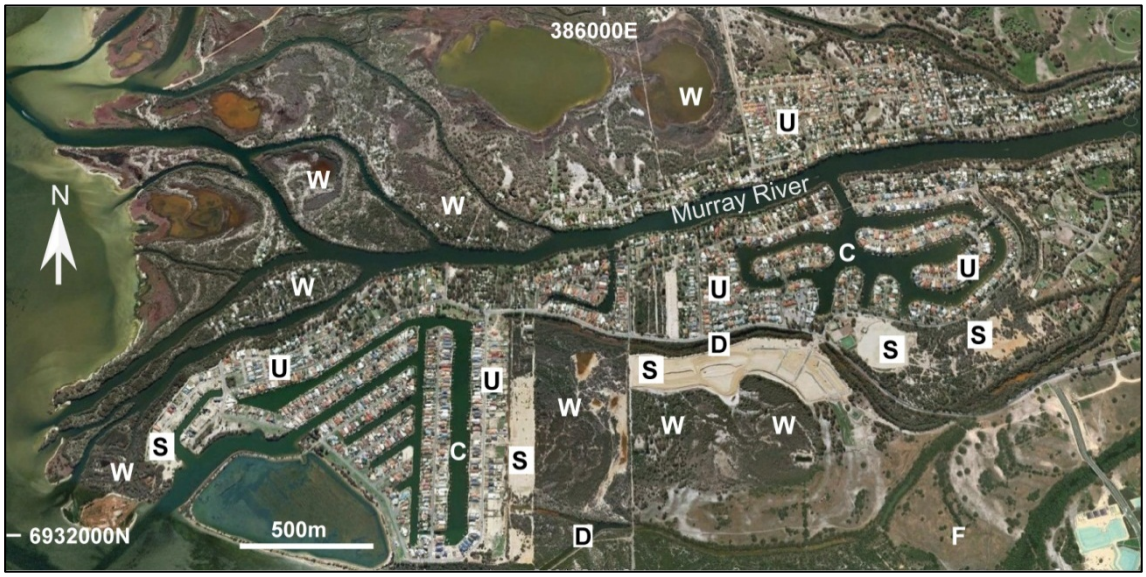

Figure 3.5: Aerial image of the South Yunderup area showing the main landforms – wetlands (W), drains (D), exposed floodplains (F), compacted dredged material flats (S), canals (C) and urban construction and townships (U).Modified from Google earth.

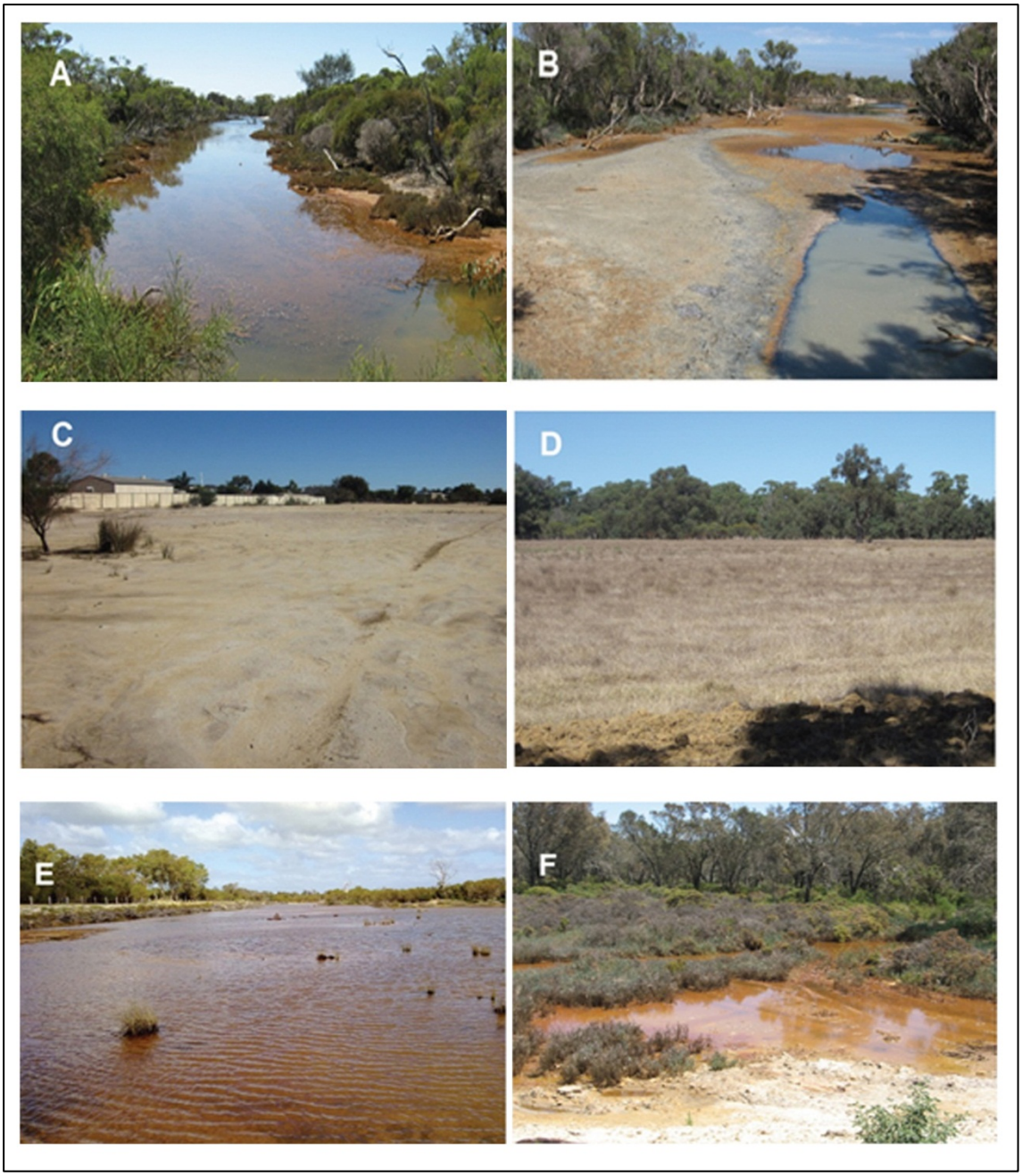

Figure 3.6: Images showing selected landforms as represented in Figure 3.5 aerial image. A. A constructed drain in August (winter) and B. the same drain in February (summer). The drain surface is exposed with grey (sulphidic) layers showing including oxidised reddish to yellow surfaces in summer. C. Compacted dredge spoil surface with yellowish-brown and grey surface with newly constructed housing in the background. D. Inactive floodplains. E. Wetlands in winter. F. Wetlands in summer showing oxidised surfaces (orange-yellow)

3.6 Sample Sites

The study area showed severe visible signs of exposed ASS materials that have arisen due to natural and anthropological activities. Presently, waterlogged and shallow groundwater areas, including natural wetlands and floodplains and constructed drains (Figures 3.5 and 3.6), have a hydrological connection with the estuarine and river waters. The pore waters of the estuary sediments have Fe monosulphides (FeS) that have precipitated during the mineralisation of organic C (Morgan et al., 2012) and these reactive monosulphides may transform to pyrite (Fe_2S). These reduced sulphide minerals reside within the upper layers of the estuarine sediments, as well as the lowland saturated soils of the wetlands and drains. Natural drying of the uppermost wetland and drain sediments and soils, due to the lowering of the water table during the summer months, causes the sulphidic materials to oxidise, resulting in the formation of ASS and the generation of acidity. Furthermore, the area has experienced widespread urban development, resulting in the dredging of the estuary and subsequent draining of the low-lying landforms (wetlands). This in turn has resulted in the exposure of the semi-saturated sediments and stockpiled dredged estuarine sediments to oxidising conditions, thereby forming widespread ASS in the urban areas (Singh and Wong, 2010). The sites for surface sampling were selected according to the areas affected by ASS activity (shown as red labels in Figure 3.7). Several sites showed visible signs of acidic conditions, such as reddish-brown-yellow surface precipitates, reddish coatings on the sands, brownish-yellow mottles in a grey matrix and grey scalded surfaces. These sites were categorised into specific landforms for the convenience of investigation and mapping.

The sites selected for coring are shown as green labels in Figure 3.7. The sampled landform sites fell into the categories of wetlands, excavated drains and adjoining spoils, and disturbed and undisturbed low-lying marshy lands. The wetlands were either natural (core 1 and core 8), or artificially created by dredging sediment (core 2 and core 3). The dredged sediment was rich in sulphidic materials and had been piled on adjacent banks and either left undisturbed for natural regrowth or flattened for urban construction. The sulphidic piles on the banks had since oxidised and weathered to form profiles of materials showing typical properties of ASS, such as brown-yellow jarosite and goethite mottles and red mottles in a grey matrix.

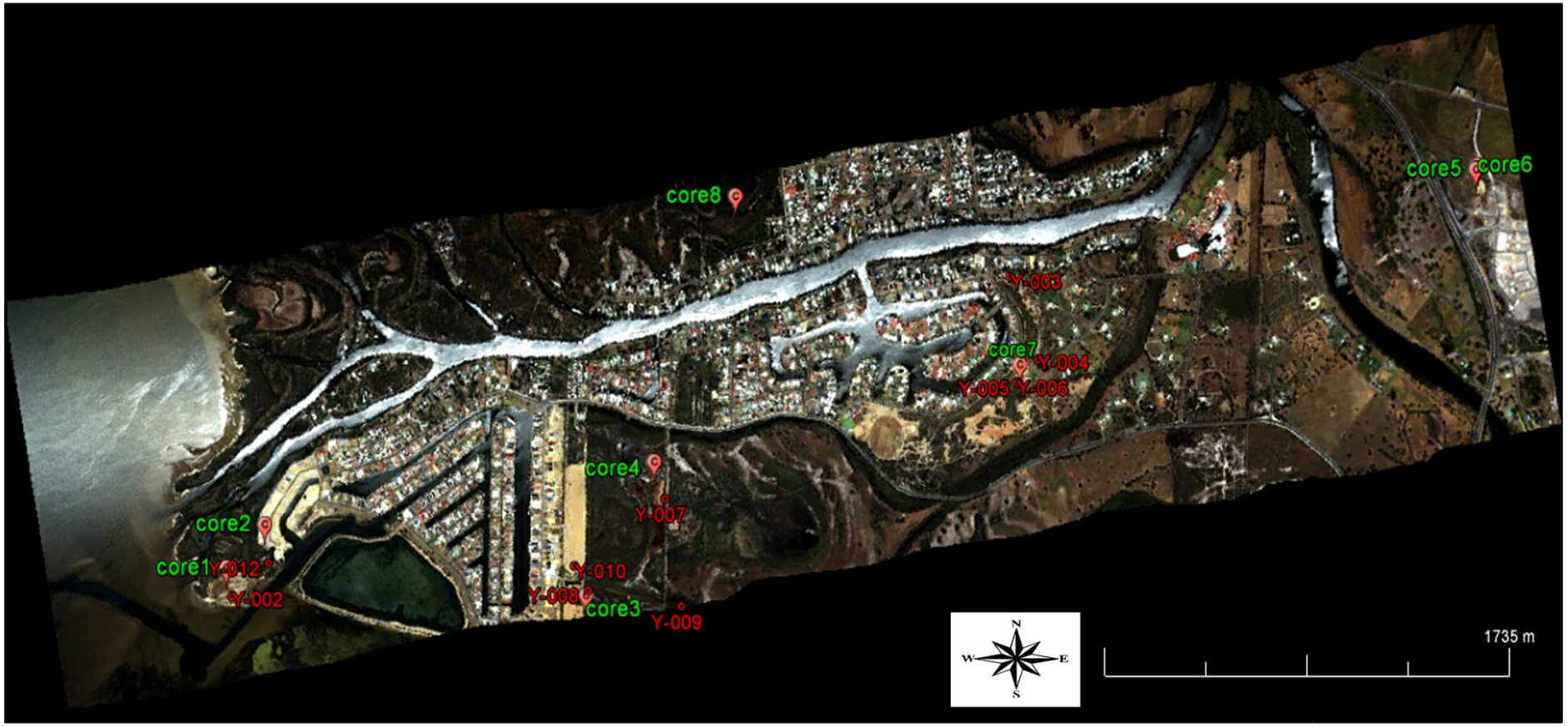

Figure 3.7: HyMap imagery of the study area of South Yunderup township including surrounding area (green labels refer to the soil coring sites; red labels refer to the surface sampling sites)

Chapter 4 Observations on the Oxidation of Iron Sulphide-Rich Material during Incubation Experiments and Potential Environmental Consequences

4.1 Introduction

The formation of acid sulphate soils originates from sulphide (mainly pyrite) oxidation which involves complex processes including mineralogical transformations and chemical, biological and electrochemical reactions (Blowes et al., 2003) resulting in the generation of acidity and often trace metal release. Most remote sensing methods relying on reflectance phenomena (VNIR-SWIR range), can only detect and identify composition and mineralogical changes occurring at the surface of the ASS, and any inferences about the immediate and deeper subsurface need to be justified by establishing links between the surface and subsurface mineralogy and composition. The main aim of the present study was to test the use of hyperspectral remote sensing to detect the occurrence and severity of ASS spatially on the surface and subsurface. To achieve this aim, it was also necessary to study the processes that resulted in the formation of ASS in the study area so a better understanding of the links between hyperspectral detection and the resulting mineralogical and chemical processes could be established for materials from the study area. In this chapter, the investigation of the chemical and mineralogical changes that accompany the oxidation of sulphidic material subjected to simulated natural conditions is discussed. The experiment and results provided a basis for applying hyperspectral remote sensing to detect, map and interpret the ASS in the study area.

All ASS form due to the oxidation of sulphidic materials. Sulphidic materials are soil and sediments that have accumulations of iron sulphides, mainly pyrite and iron monosulphides (Lamontagne et al. 2004). In Chapter 1, the common formation mechanisms of ASS were reviewed, but more detailed processes of the formation of ASS from natural sulphidic materials remain unclear. Furthermore, as every specific ASS area has its own unique soil characteristics and processes, it is necessary to understand the specific processes by which particular sulphidic materials oxidise and the concomitant mineralogical and chemical changes that proceed in that material under natural conditions.

Previous studies have demonstrated the processes of sulphidic material oxidation. Smith and Melville (2004) conducted a 60 day oxidation experiment on iron monosulphide-rich sediments and found the oxidation on sulphides resulted in the production of acidity with pH dropping from 6.7 to < 3. Ward et al. (2004) observed the oxidation of sulphides in a 36 day incubation experiment, which mainly focused on the speciation of sulphur, including sulphur content changes and various sulphur-bearing secondary minerals. Sommer (2006) conducted an incubation experiment for 49 days to investigate the geochemical effects in the period of drying and rewetting, by measurements of pH, Eh, EC, Fe^{3+}, Ca^{2+}, SO_4^{2-} and PO_4^{2-}, focusing on the potential for eutrophication and/or acidification on the organic sediments of a wetland. Sullivan et al. (2009) conducted an incubation experiment to observe the acidification behaviour and the oxidation rate of sulphidic material within an 8 week period. These examples of incubation experiments to simulate the sulphidic material oxidation processes are good reference points, but most of them were not conducted for a sufficiently long time, and only one of them was done to observe the potential for environmental impacts under natural seasonal conditions. Also, most of the previous incubation studies using sulphidic materials focused on the rate of oxidation and subsequent acidification, rather than on the trace metal release and the relation between acidity and metal release. None of the previous incubation studies simultaneously measured the changes in chemistry and mineralogy when sulphidic material was subjected to the natural seasonal conditions of wetting and drying.

In the experiment conducted in this study, fresh sulphidic material collected from an anoxic estuarine site in the field area was divided into three groups undergoing three different drying and rewetting regimes. The three groups were set up to simulate three wet-dry duration weather conditions: wet conditions (weekly rainfall), semi-dry conditions (monthly rainfall), and dry conditions (seasonal changes). These three wet-dry cycle durations were selected to observe the difference in oxidation rate and related acidity production, mineralogy changes and trace metal release from the sulphidic material under simulated natural conditions. Specifically, there were five main aims for this experiment, including:

(1) To determine the degree of oxidation of sulphidic material in different climatic conditions by observing changes in the sulphate release in the extracted pore waters.

(2) To quantify the release of acidity in different weathering scenarios by measuring the pH of extracted solutions, as well as measuring the TAA and TPA of the initial sulphidic material and the same material after oxidation.
(3) To observe the mineralogical transformation occurring during the process of oxidation and acidification, and the corresponding spectral changes.
(4) To observe the compositional changes by measuring the total sulphur content of the initial material and the material after oxidation.
(5) To assess the potential environmental impacts of oxidation and acidification by measuring the concentration of specific metals of environmental concern, such as Al, in the pore waters from the oxidising sulphidic materials, and to predict the potential environmental risk due to potential drying climate (climate change).

The chemical changes in the sulphidic material were monitored by periodically measuring the solutions extracted from the incubation cells for major anions, including SO_4^{2-},Cl^-, Br^- and F^- , major cations, including major and trace metals, pH, EC, TAA, TPA, and total sulphur. Mineralogical identification by XRD and measurement of reflectance spectra were also conducted on the solid materials both before and after the experiment.

4.2 Experimental Settings and Measurements

4.2.1 Experimental settings

The apparatus for the experiment included three parts: an oxidation cell, a filter between the top and bottom part of the oxidation cell, and solution control systems. The oxidation cell was made up of two parts. The upper part held the sulphidic material, and the lower part collected the solution leached from the sulphidic material. A 60 μm nylon filter mesh was used to hold the material in place and ensure the solutions generated could penetrate into the bottom whilst retaining the fine clay soil particles. The water control system contained three parts, namely, a hanging bottle with a volume of 1000 ml, a plastic hose connected between the bottom of the oxidation cell and hanging bottle, and a stopcock. The water control system was used to control the rise and fall of water, to create conditions whereby the soil materials were submerged to simulate wet conditions, or to drop the water table below the top cell exposing the material to drying, oxidative conditions. There was also an exit port

at the bottom of each oxidation cell which was used to remove the solution for measurement. The configuration of the experiment is shown in Figure 4.1.

Figure 4.1: Set-up of the incubation experiment

4.2.2 Sample preparation

(1) Sample collection. Sulphidic materials are rich in iron sulphides and usually form and persist in eutrophic conditions which have a supply of reactive iron, dissolved sulphate and organic matter (Berner, 1970; 1984). These environmental conditions conducive to the formation of sulphidic materials can be found in eutrophic depositional environments on the beds of rivers, lakes, swamps and other aquatic systems. Sulphidic materials can be a mixture of micro-pyrites and a variety of iron monosulphides which include amorphous FeS, mackinawite (tetragonal FeS_{1-x}) and greigite (Fe_3O_4) (Morse et al., 1987). Many of these sulphidic sediments, due to their dark colour and clay gel texture are referred to as “monosulphidic black oozes”.

Sulphidic materials in this study were collected from the bed of a tidal estuarine basin, which is inundated year round, and lies in the interface between the estuarine water and terrestrial surface, with thick vegetation in the east of the water body, providing rich organic material to the estuary bed. Recent studies on the estuarine sediments such as those collected in this study found that the SO_4^{-2} reduction with

high carbon was an ongoing process forming the monosulphide-rich sulphidic material (Morgan et al., 2012). The sulphidic materials collected in this study were clay textured. The sulphidic materials were similar to those that had been dredged from estuaries to construct canals and the materials stockpiled and often spread and compacted for housing development. The sulphidic samples were transferred to a sealable plastic bag from which all air was expelled, and then placed into the field ice-box before transportation to the laboratory to ensure that the sample could not be oxidised.

(2) Sample preservation. The sulphidic materials were stored at 4°C until further treatment to suppress microbial activity.

(3) Sample homogenisation. Past studies on incubation experiments have differed in mixing of the sulphidic materials, with some favouring homogenization of the material while other using the natural occurrence (Smith, 2004). In this study, homogenization was considered a better option because of the setup of the incubation experiment and the dredging and stockpiling activity that exposed the sulphidic sediments in the study area also had a mixing effect on the material. Samples were removed from cold storage and placed into a cleaned plastic bucket and mixed using an industrial mortar mixer to ensure sample homogeneity. Prior to stirring, the bucket and the stirrer were cleaned with acid solutions and then rinsed using pure water to clean them to ensure the material was not contaminated. The mixing would have resulted in some oxidation of reactive sulphides (iron monosulphides), although this oxidation was insignificant as shown by little manifestation of oxidation, such as yellow-brown mottled colours nor in the change in pH of the starting material.

(4) Sample division. The homogenous sulphidic material was divided into three groups, with each group being further duplicated, for a total of six equal samples. Each of the six incubation cells was filled with the samples to make a 30 cm thick layer of sulphidic material in the cell.

(5) Sample preparation for analysis. After stirring, a representative sample was extracted from the homogeneous mixture and oven dried for 48 hours at 38°C. The dried sample was then milled to a powder using a ceramic mortar and pestle and divided into four parts; one for XRD analysis, one for pH and EC measurement, one for compositional analysis, and one for TAA and TPA measurements.

4.2.3 Operational protocols for incubation cells

Drying and rewetting conditions were created by controlling the water table by adding water into and drawing water out from oxidation cells. For each wetting cycle, 1000 ml of deionised water was added from the hanging bottle to the bottom cell to maintain submerged conditions for 24 hours to ensure all the soluble metals and acidity were released into the water. After this time, all the solution was drawn out from the bottom part of the cell and collected for analysis.

The materials in different groups experienced different periodic wetting/drying conditions. The groups were separated according the following wetting-drying cycles.

- Group 1. The drying period is 6 days, with wetting phase after every 6 days (weekly wetting).
- Group 2. The dry period is 27 days, with sample in cell wetted after 27 days (monthly wetting).
- Group 3. The drying period is 83 days (three month wetting to mimic seasonal change)

4.2.4 Chemical measurements

(1) Measurement of initial material. The pore water from the mono-sulphidic black ooze material was extracted by centrifuge, and its pH and EC values were measured to determine the initial acidity and salinity conditions before oxidation. A quantity of fresh solid material was put into the oven to dry. After calculating the moisture ratio, the dried material was analysed for total sulphur. These measurements provided a baseline constituent to compare the initial conditions with the conditions after oxidation to ascertain the differences and changes in constituents.

(2) Solution measurement. Solutions were extracted from the material in the different groups by washing them at different frequencies. The solutions from group 1, group 2 and group 3 were acquired weekly, monthly (4 weeks) and seasonally (12 weeks), respectively, after inundation. In each case, when the solution was extracted, a 20 ml aliquot was extracted for immediate measurement of the pH and EC. The remainder was stored in a plastic bottle, in a refrigerator at <4°C to preserve them for further analysis. After extraction of the final solutions, all the collected solutions were analysed to measure the concentration of trace metals, such as Fe, Al, Cu, As,

Mg, Zn, Cr, Ni, Co Mn via ICP-MS, and major cations, such as K^+, Na^+, Mg^{2+} , Si^{4+} and Ca^{2+} via ICP- AES. Major anions, such as F^-, Cl^-, Br^-, NO_3^2-, PO_4^2-, SO_4^{2-}, were measured by High Performance Ion Chromatography (HPIC) using a Dionex® ICS-1000 ion chromatograph equipped with Dionex AS-14, 4x250 mm anion column and AG-14 guard column. The isocratic run used an eluent of 3.5 mM $NaCO_3$ and 1.0 mM $NaHCO_3$ at a flow rate of 1.5 ml /min. The HPIC method employed electronic suppression and conductivity detection.

(3) Residual soil measurement. After several periodic drying and rewetting cycles, the residual sulphidic material from the different groups was processed by removing it from the cell and cutting, photographing, drying and separating. Representative subsamples were taken for subsequent analysis corresponding to those performed on the initial materials, i.e XRD, pH, EC, TAA.

4.2.5 TAA, TPA and total sulphur content measurement

The initial material and the residual material after 12 weeks' oxidation and flushing, were analysed for TAA, TPA and total sulphur. TAA measures the actual acidity of the ASS, which is readily soluble and exchangeable in materials. TPA measures the potential acidity of the ASS, from the oxidation of residual sulphides. The methods of measuring TAA and TPA were introduced in Chapter 2. Total sulphur content was measured using an Eltra 2000 C and S determinator in a Leco-type furnace.

4.2.6 Mineralogy

Mineral identification was undertaken on the initial material and residual soil samples, with the aim to compare the mineralogical changes between the initial material and the material after 12 weeks' oxidation. Firstly, mineral identification was done by analysing the reflectance spectral features using an ASD FieldSpec3, and then XRD was utilised to confirm the mineral composition. The design and measurement for the experiment are listed in Table 4.1.

Table 4.2: Summary of the main measurements taken during the experiments

Sample type	Groups	numbers of samples	Measurements
Initial material	Soil sample	2	(1) Mineralogy: reflectance spectra and XRD (2) Acidity: TAA, TPA (3) Composition: total S
	Pore water	3	(1) EC, pH (2) SO_4^{2-}concentration (3) Main cations: Al, As, Ba, Fe, Co, Mn, Pb, U, Zn (4) Main anions: Cl^-, Br^-, F^-, NO_3^{2-},PO_4^{2-}, Si^{4+}
Solution	Group 1	12(week)x2=24	(1) EC, pH (2) SO_4^{2-}concentration (3) Main cations: Al, As, Ba, Fe, Co, Mn, Pb, U, Zn (4) Main anions: Cl^-, Br^-, F^-, NO_3^{2-},PO_4^{2-}, Si^{4+}
	Group 2	3(month)x2=6	
	Group 3	1(season)x2=2	
Residual soil sample	Group 1	2	(1) Mineralogy: reflectance spectra and XRD (2) Acidity: TAA, TPA (3) Composition: total S
	Group 2	2	
	Group 3	2	

4.3 Result and Interpretation

4.3.1 Changes in reflectance spectral characteristics

The residual oxidized sulphuric material from each cell from all three groups was scanned using an ASD after 12 weeks of the experiment. The top surface (TS), the side surface (SS) and the inner part (IN) of the material from each group were scanned. The images of the materials from three different groups and the location of the TS, SS and IN are shown as Figure 4.2.

The initial material was also measured to obtain the reflectance spectra. The reflectance spectra of the initial material showed a low response over the whole spectrum (Figure 4.3 a), displaying a slight absorption at 2.205 μm which suggested the presence of Al-OH content and usually relates to the presence of kaolinite. After 12 weeks' oxidation, with the exception of the inner material in all the groups which retained low reflectance with indistinct absorption features, the reflectance responses of the other parts of the material were much higher than that of the initial material, with stronger and distinct absorption features near 0.667 and 2.205 μm, as well as near 0.9, 1.4, 1.9 μm and some absorptions in the range of 2.1-2.5 μm, which varied in different parts of the different groups. All the materials in the top surface showed

distinct gypsum which has a diagnostic absorption at 1.75 μm due to vibrational bending and stretching of the H_2O/OH in the mineral (Cloutis et. al., 2006). The material on the top surface in group 2 and group 3 showed absorption at 2.265 μm which is indicative of the presence of jarosite, as jarosite has a diagnostic peak at 2.265 μm (Cloutis, et al., 2006). The material from the side surface, regardless of group (group 1, 2, 3), showed absorption features at 2.265 and 1.75 μm but these are not explicit. The detailed comparison of the reflectance spectra is shown as figure 4.3

Figure 4.2: Residual material after 12 weeks' oxidation (a) the material from group 1 (weekly drying), displaying top surface; (b) the material from group 1, displaying side surface and bottom surface; (c) the material from group 2 (monthly drying); (d) the material from group 3 (three month drying). The images show visual oxidation signs of yellow-brown on the top and side surface with gley colours in the inner part.

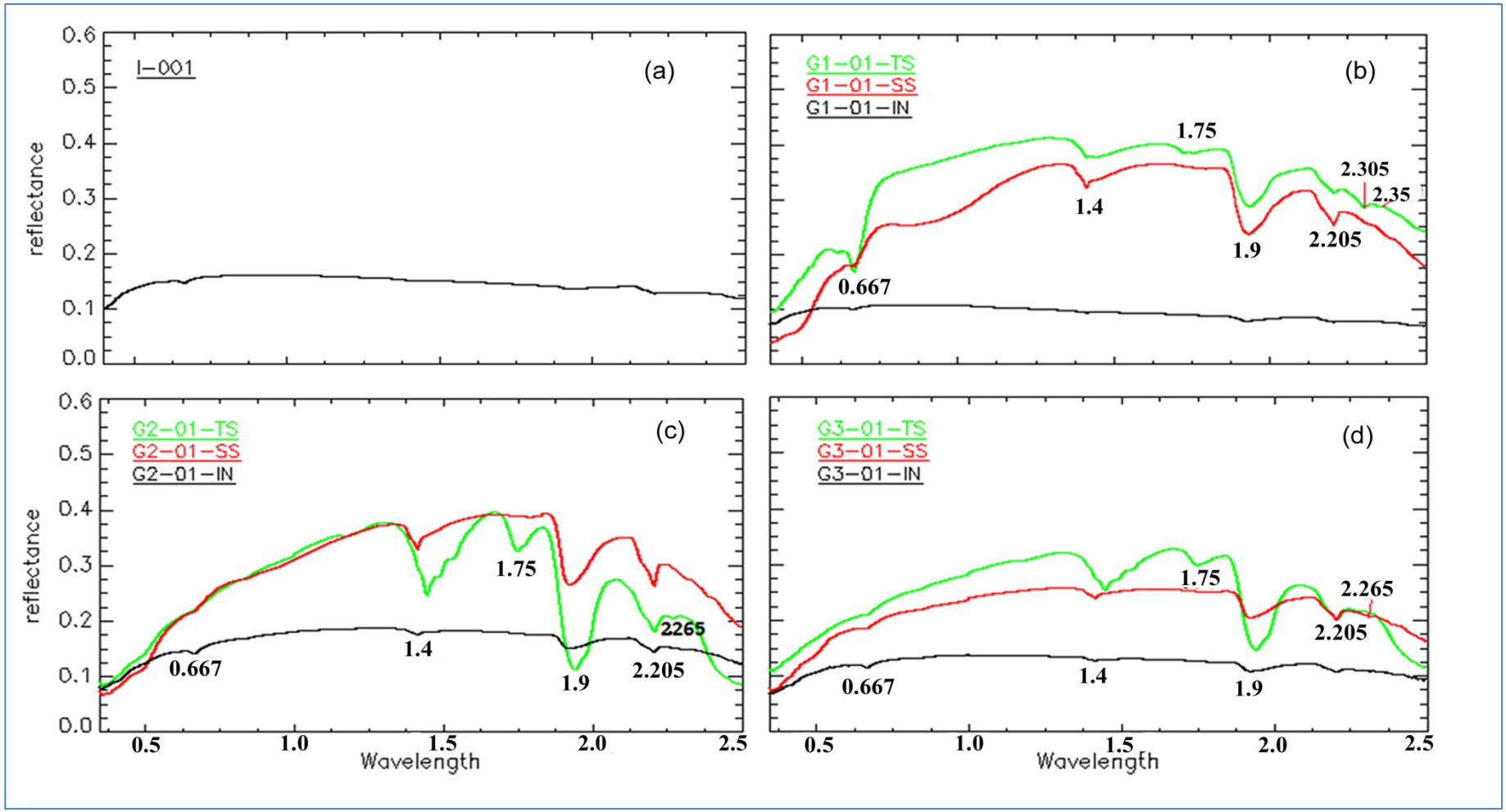

Figure 4.3: Reflectance spectra of the material (a) the spectral characteristic of the initial material before oxidation; (b) the spectral characteristic of the material in group 1 (weekly) after oxidation; (c) the spectral characteristic of the material in group 2 (monthly) after oxidation; (d) the spectral characteristic of the initial material in group 3 (three month) after oxidation. For b, c, and d, the black spectra is from the inner material, the green spectra is from the top surface, and the red spectra is from the side surface of the material

4.3.2 Mineralogy changes

XRD analysis identified abundant quartz and kaolinite, primary aluminosilicates, such as microcline, and considerable pyrite in the initial material (Figure 4.4, I-001). After 12 weeks' oxidation, the mineral composition of the material varied in different parts in three groups. In group 1, the top surface contained minor goethite and ferrihydrite, and abundant gypsum (Figure 4.4, G1-1-TS01). Around the side surface, abundant goethite, minor hematite and a trace of jarosite existed. Both the top surface and side surface no longer contained pyrite. In the middle of the material, the composition was very similar to the initial material, but also contained a trace of goethite which the initial material did not have. In group 2, goethite and gypsum were present on the top surface, but also contained some jarosite that was not been found on the top surface in group 1 (Figure 4.4, G2-1-TS01). Around the side surface of group 2, there mainly existed goethite, but also a trace of jarosite (Figure 4.4, G2-1-SS01). It was noteworthy that both the top surface and side surface still retained some residual pyrite. For inner materials in group 2, there existed small quantities of goethite and jarosite (Figure 4.4, G2-1-M01).

The material on the top surface in group 3 mainly contained jarosite and minor pyrite together with the other dominant minerals (Figure 4.4, G3-1-TS01). Around the side surface in group 3, jarosite was more abundant than on the top surface, while pyrite concentrations were lower than on the top surface (Figure 4.4, G3-1-SS01). In the middle section of group 3, jarosite was also present, together with abundant pyrite and other dominant minerals (Figure 4.4, G3-1-M01). The comparison of the mineral composition in the different groups is summarised in Table 4.2.

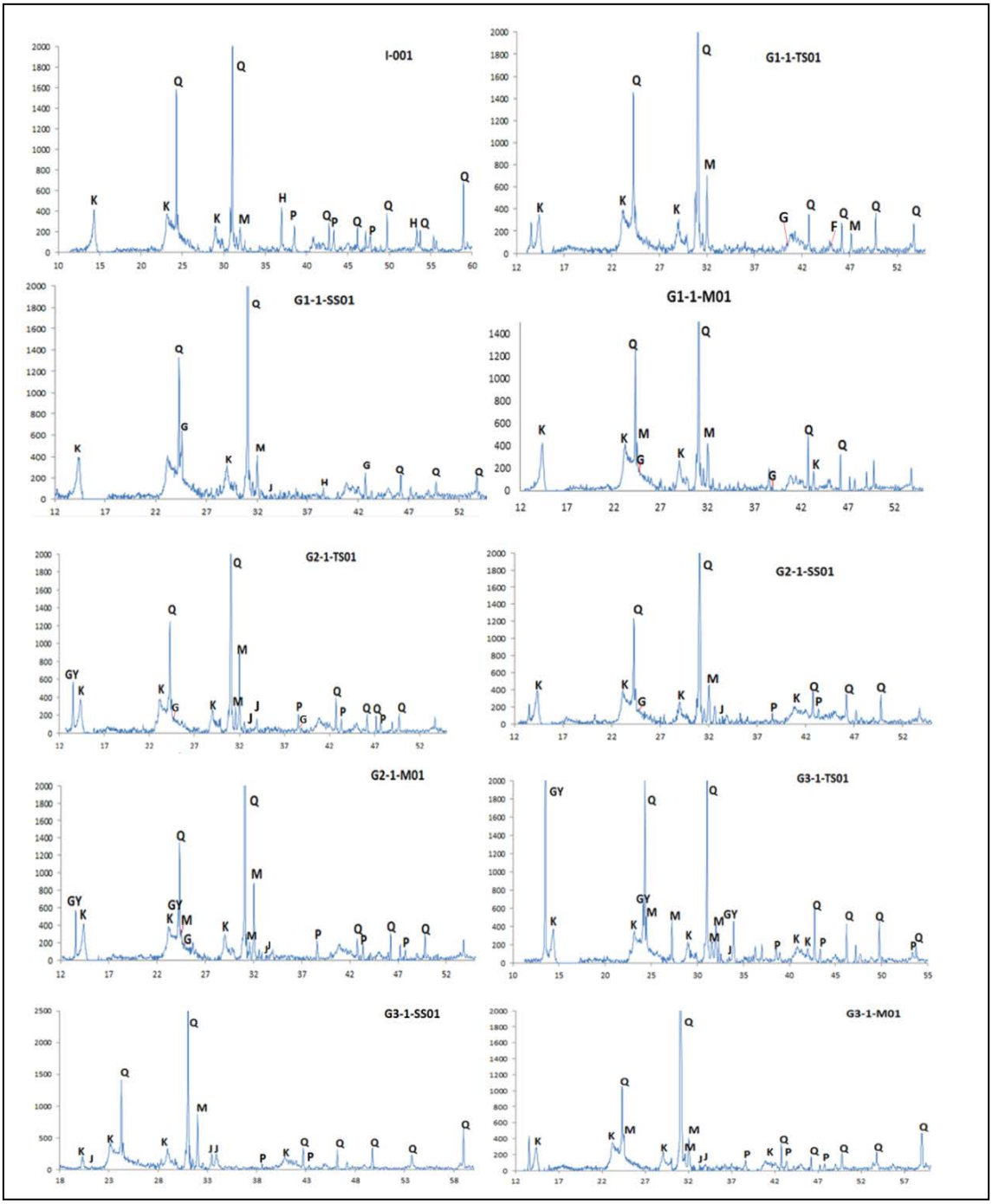

Figure 4.4: XRD results of the different parts of material in different groups; I-001 the sample from initial material; in the sample name, G1, G2, G3 represent samples from group 1, group 2 and group 3, respectively, and TS, SS and M represent the top surface, side surface and middle part, respectively; for the mineral identification, K - kaolin group, G - goethite, J - jarosite, Q - quartz, GY - gypsum, P- pyrite, M -microcline, H - halite, F – ferrihydrite. In XRD plot, X axis is the two theta (deg) and Y axis is the intensity (counts)

Table 4.3: Comparison of the mineral composition of the different groups

Source	Sample	Minerals identified by reflectance spectra	Minerals confirmed by XRD
Initial material	Mixed	Kaolinite	Major: quartz, halite, kaolin, microcline, pyrite
Residual material in group 1	Top surface	Kaolinite, gypsum	Major: quartz, kaolin, microcline, Minor: goethite, ferrihydrite, gypsum
	Side surface	Kaolinite, goethite	Major: quartz, kaolinite, microcline, goethite Minor: hematite Trace: jarosite
	In the middle	Kaolinite	Major: quartz, kaolin, microcline, pyrite Trace: goethite
Residual material in group 2	Top surface	Kaolinite, jarosite, gypsum	Major: quartz, kaolin, microcline, pyrite, gypsum Minor: jarosite, goethite,
	Side surface	Kaolinite, goethite, jarosite	Major: quartz, kaolin, microcline, pyrite Minor: goethite Trace: jarosite
	In the middle	Kaolinite	Major: quartz, kaolin, microcline, pyrite, gypsum Minor: jarosite, goethite
Residual material in group 3	Top surface	Kaolinite, jarosite, gypsum	Major: quartz, kaolinite, microcline, gypsum, pyrite Minor: jarosite
	Side surface	Kaolinite, jarosite	Major: Quartz, kaolin, microcline, jarosite Minor: pyrite
	In the middle	Kaolinite	Major: quartz, kaolin, microcline, pyrite Minor: jarosite

4.3.3 Acidity changes

With respect to TAA and TPA (Table 4.3), the initial material had the lowest TAA value which meant it had the lowest existing acidity, and the highest TPA value which meant it had the largest potential acidity as expected for fresh un-oxidised material. The TAA of the residual materials showed an expected trend of highest

TAA in the more heavily oxidised Group 1 material with decreasing TAA in group 2 and group 3. This demonstrated that the increased rate of flushing increased oxidation, and that the acidity produced was being retained in the material, most likely as dehydrated acidic pore solutions and soluble iron sulphate minerals which would generate secondary acidity upon dissolution.

Table 4.4: Soil acidity measurement from different groups of material

Group	Sample ID	pH_{KCl}	pH_{ox}	TAA	TPA	TAA average	TPA average
Initial material	I-002	4.7	2.2	60	1227.5	60	1197.5
	I-001	4.7	2.22	60	1167.5		
Group 1	G1-1-01	3.8	2.25	150	1090	153.125	1113.75
	G1-1-02	3.8	2.2	156.25	1137.5		
Group 2	G2-1-02	3.7	2.19	137.5	1005	137.5	1027.5
	G2-1-01	3.7	2.14	137.5	1050		
Group 3	G3-1-01	3.8	2.23	125	1077.5	125	1051.25
	G3-1-02	3.8	2.1	125	1025		

4.3.4 Composition changes

The total sulphur contents were analysed to observe the changes of the composition of the materials before and after oxidation. The measurements are shown in Table 4.4. It was clear that the samples which experienced more frequent washing had lower total sulphur contents because the sulphate released during sulphide oxidation was washed away. With respect to the changes occurring in different parts, the material on the top surface usually had lower total sulphur content than the side surface, and the side surface had lower content than the inner material, with an exception that: in group 2 and group 3, the total sulphur content of the material on the top surface was surprisingly higher than in the other two parts; and in group 3, the total sulphur content of the material on the top surface was even higher than in the initial material. This was very likely due to the long drying times experienced and movement of sulphate released to the surface by evaporative

forcing. This was confirmed by the XRD measurements which identified gypsum present on the surface of groups 2 and 3 (Figure 4.4, G2-1-TS01 and G3-1-TS01).

Table 4.5: Comparison of total sulphur contents in different parts and groups

Material from	Part of cell	Total sulphur (%)
Initial material		3.12
Group 1	Top surface	1.2065
	Side surface	1.4615
	Inner part	2.2305
Group 2	Top surface	3.0262
	Side surface	1.8466
	Inner part	2.6573
Group 3	Top surface	3.7
	Side surface	1.6498
	Inner part	2.6046

4.3.5 Sulphate release changes

The measurement of total sulphate concentration represents the sulphate released during the oxidation, and residual sulphate from the estuarine water remaining in the material. How to separate these two contributions of sulphate is crucial for the determination of sulphate release due to sulphide oxidation. There is a simple but effective way to tell apart these two parts of sulphate. The method is based on the assumption that F^-, Cl^-, Br^- and SO_4^{-2} have a relatively fixed mole percentage in the sea water, and that the percentage does not change in the residual pore water in the material when washed periodically with pure water. Based on this assumption, we could calculate the sulphate contribution from sea water remaining in the material, and thus deduce the sulphate released due to the pyrite oxidation. The estimation of the sulphate released by pyrite oxidation is presented in Table 4.5.

Although there are some intermediate sulphur states, such as $S_4O_6^{2-}$, SO_3^{2-}, that may be produced during the first stage of oxidation, they will be oxidised to SO_4^{2-} in the long run. Thus, once we know the amount of SO_4^{2-} released by pyrite oxidation and the time of the pyrite oxidation, it is easy to calculate the sulphate release rate

which can be used to approximate the oxidation rate by dividing the released amount by the oxidation days. The sulphate release rate thus calculated based on the preceding assumption is shown in Figure 4.5.

From Figure 4.5 and Table 4.5, it can be seen that the peaks of the estimated sulphate release and release rate in group 1 were on days 21, 72 and 94 which was consistent with the pH measurements which had nadirs on days 21, 72 and 94(the detailed pH measurements were list in following session 4.36.1). To some extent, this consistency suggested the relative accuracy of the estimation of the sulphate release and reflected the condition of sulphide (pyrite) oxidation approximately. However, as we see in Figure 4.6, the correlation between H^+ which was deduced from the pH measurement and the estimated SO_4^{2-} was not as good as we expected. Logically, the released SO_4^{2-} and the released H^+ should be proportional according to the reaction equation of pyrite oxidation and thus there should be a very good correlation between them. The moderate correlation index suggested the complexity of the release of sulphate and hydrogen ions. The K^+ dissolved from the surrounding minerals and the Fe^{3+} and SO_4^{2-} released from the pyrite oxidation would react and generate relatively insoluble jarosite, the existence of which was proved by XRD in conditions where the pH was between 1.5 and 2.8 by the reaction as follows (Dold, 2000):

$$3Fe^{3+} + K^+ + 2SO_4^{2-} + 6\,H_2O \leftrightarrow KFe_3^{3+}(SO_4^{2-})_2(OH)_6 + 6H^+ \quad (4.1)$$

Although jarosite can dissolve and transform to goethite and release SO_4^{2-} back in the reaction expressed below, the dissolution capability is very slow with a reaction expressed as follows (Dold, 2000):

$$KFe_3(SO_4)_2(OH)_6 \rightarrow 3FeO(OH) + K^+ + 2SO_4^{2-} + 3H^+ \quad (4.2)$$

These two reactions indicate that for the sulphate released by the pyrite oxidation, a proportion of the sulphate was transformed to relatively insoluble jarosite, and furthermore, during the generation of jarosite, a sizeable amount of H^+ was produced. All of these resulted in relatively low correlation between the H^+ and SO_4^{2-}, and therefore, the estimation of the sulphate release was only approximate to the real sulphate release, and thus the sulphate release rate reflected the pyrite oxidation rate only approximately.

Table 4.6: Sulphate release estimation

Ac-days	Ox-days	SO_4^{2-} measurements (ppm)	SO_4^{2-} release estimation (ppm)	SO_4^{2-} release rate estimation (ppm/day)
0		5741.030	0	0
7	6	1008.659	395.96	65.99
14	6	1029.981	489.26	81.54
21	6	1305.477	725.18	120.86
28	6	963.12	600.86	100.14
34	5	857.144	579.65	115.93
42	7	850.387	632.07	90.30
49	6	763.494	598.47	99.74
56	6	760.424	611.87	101.98
63	6	700.604	573.50	95.58
72	8	1062.088	924.40	115.55
79	6	794.78	648.90	108.15
86	6	632.557	550.83	91.80
94	7	791.503	732.51	104.64
101	6	487.461	487.46	81.24
108	6	520.075	489.98	81.66

(1)This estimation was based on the average value of group 1. The measurement of the day 0 was for the pore water from the sulphide material.

(2)The unit of all the measurements was ppm.

(3)Ac-days means accumulated days in the experiment, Ox-days means actual days when the material was exposed to air (usually one day less than the interval of measurements).

For group 2 and group 3, the limited measurements suggested a much lower sulphate release rate than that of group 1 (Figure 4.5). This was likely due to differences in the volumes of water supplied. Although the materials in group 2 and group 3 were constantly exposed to the atmosphere, water was added to them monthly and seasonally, respectively – much less frequently than the group 1 materials which were washed weekly. Thus, the lack of water in group 2 and especially in group 3, made the oxidation in these two groups much lower, and the low oxidation rate consequently influenced the corresponding sulphate release rate.

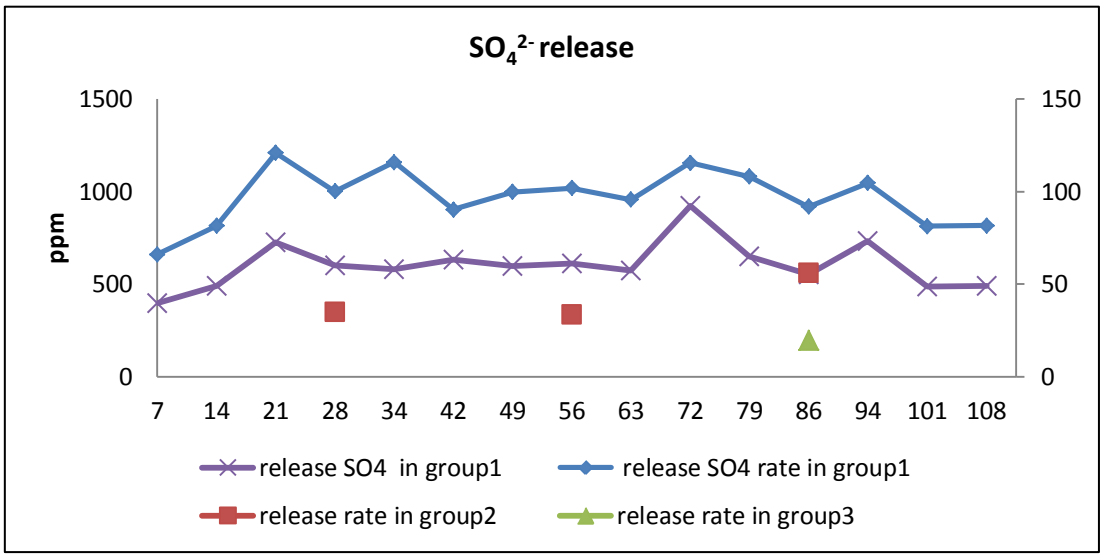

Figure 4.5: Change of SO_4^{2-} release (the unit for SO_4^{2-} release was ppm, and the unit for SO_4^{2-} release rate was ppm/day). Horizontal scale is ppm/day.

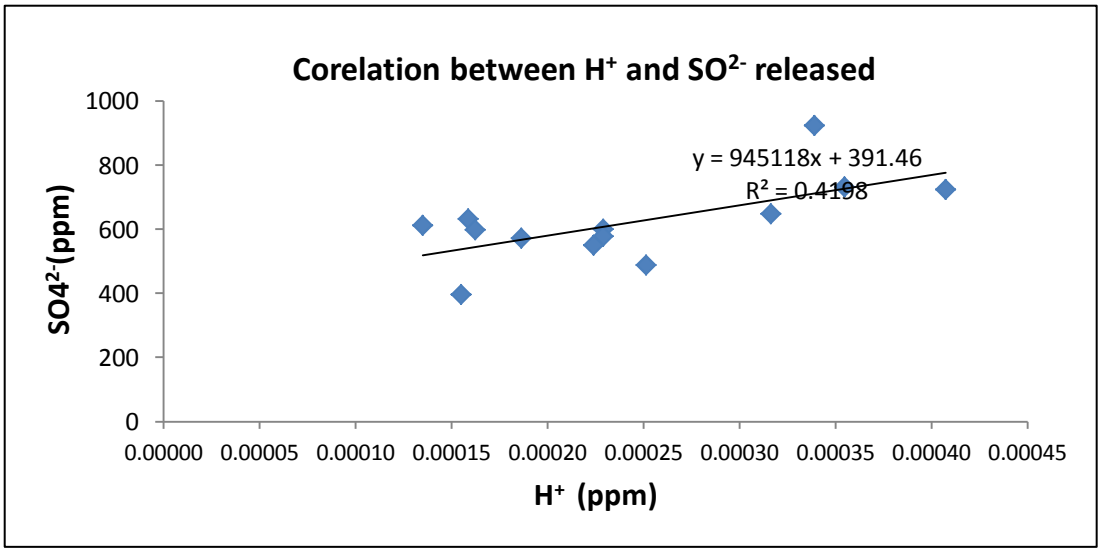

Figure 4.6: Correlation between H^+ deduced from pH and estimated released SO_4^{2-}

4.3.6 Environmental impacts

The main chemical measurements of the solutions generated in the incubation cells are shown in Table 4.6.

4.3.6.1 pH and EC

The measurements of the pH and EC of the solutions acquired from washing the materials periodically are shown in Figure 4.7. Initially, all the pH values of the

solutions from all the groups were below 4, with average values of approximately 3.5, much lower than that of the pore water of the initial material which was near to 7. This suggested that large amounts of acidity were produced during the pyrite oxidation, and this strong acid condition would influence the structures and productivity of the soil and also would affect the surrounding environment. For the salinity, the EC maintained high values during the experimental period even after regular washing with pure water, with an average value of 5.77 ms/cm, although much lower than the sea water comparing the EC of the pore water of the initial materials. It suggested that large amounts of salinity were produced during the evolution of the test ASS, and that the salinity would also influence the soil conditions and surrounding environment. With respect to the change pattern of the pH and EC, group 1which experienced the most frequent inundation, exhibited a trend of decreasing EC with time, while the pH did not display an apparent trend but remained less than 4. Noticeably, the pH of the material in group 1 decreased significantly on days 21, 72 and 94, with EC displaying two peaks on days 21 and 94. This may represent the dissolution of iron sulphate minerals with a commensurate increase in EC due to the release of salts and increased acidity through ferric hydrolysis. A difference in the pH among the three groups was not

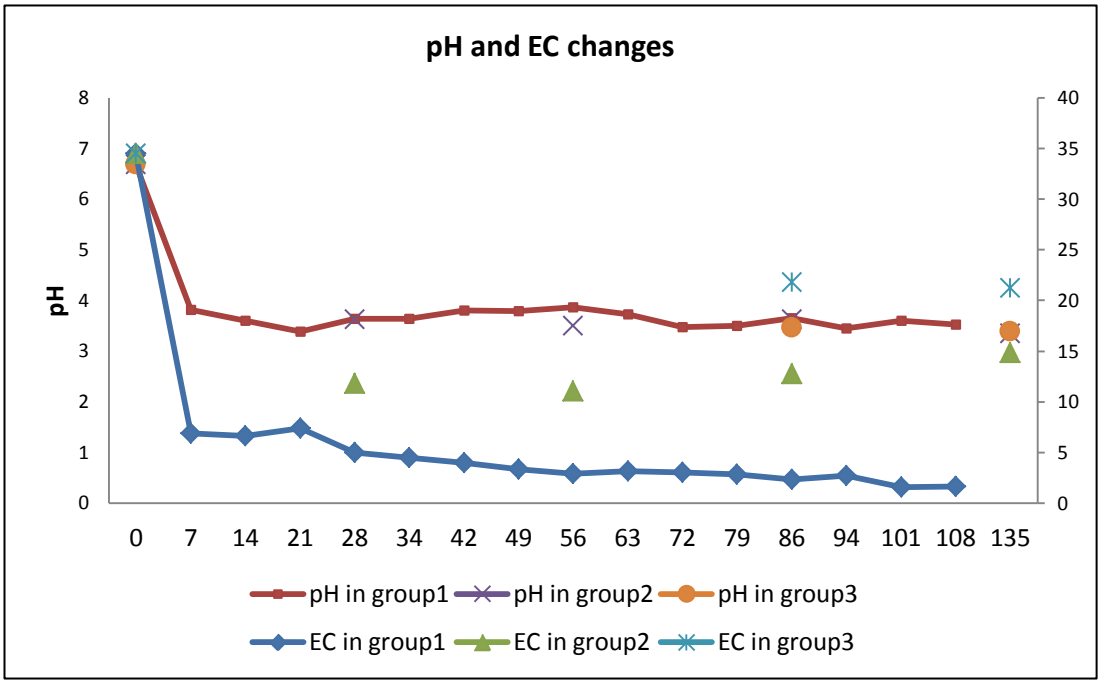

Figure 4.7: pH and EC changes with oxidation days. EC scale on the right in ms/cm

apparent, but the EC values varied with the order that group 1<group 2<group 3.

This can be explained by the differences in the washing frequency, in that the more often washed groups had lower EC values.

4.3.6.2 Trace metal release

Metal release has environmental significance, and the low pH conditions usually facilitate trace metal release (Bigham and Nordstrom, 2000; Degens et al., 2008). Al, As, Fe, Ba, Mn, U, Pb, and Co were selected to observe their concentration changes as the oxidation experiment progressed, and Al and As were selected as the critical elements in terms of toxicity issues facing coastal ASS (Ljung et al., 2009). Figure 4.8 shows the concentrations of the selected trace metals in solution extracted weekly from the oxidizing material. Most of the trace metals in the extracted solutions were higher than in the initial pore water. The higher releases of the metals were due to the low pH conditions being created by sulphide oxidation in the material, except for Ba and As. In the initial pore water, Al, Pb and Fe were not detected, while Ba had high concentration. Generally, due to weekly washing of the sulphidic material with deionized water, the metal concentrations in solutions should decrease if the metals are not being released due to sulphide weathering. Therefore, the decrease of the concentration of Ba in extracted solutions is understandable, but the decrease and the final disappearance of arsenic in the solutions appear more complicated. Arsenic was detected in the pore water of the

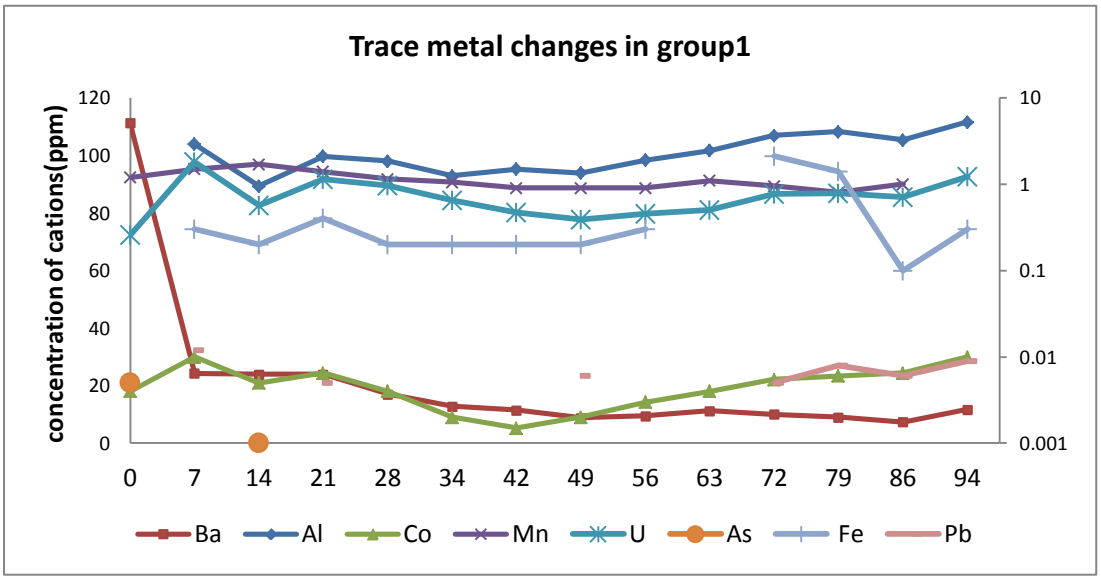

Figure 4.8: Selected trace metal changes with duration of oxidation (X axis is the oxidation days, the right Y axis is for Ba and U, the left Y axis is for other metals; the unit of the concentrations is ppm)

initial materials, but was observed in solutions only on day 14 and then was not detected in subsequent weeks. It was very likely that, due to the generation of secondary iron-bearing minerals, such as goethite, hematite and jarosite, the Asc was absorbed by these iron-bearing minerals. The ability of As to be retained due to adsorption and co-precipitation on iron oxides and iron hydroxysulphate is well documented (Garcia et al., 2009; Mamindy-Pajany et al., 2009).

Aluminium is the ion of most environmental concern in the study area because the soil and estuarine materials are rich in Al-bearing minerals such as kaolinite. Aluminium is phytotoxic and thus represents a threat to aquatic and terrestrial flora (Ljung et al., 2009). Aluminium ions were not detected in the pore water of the initial material, but increased in the solution over experimental time. The high concentration of Al^{3+} was due to the material being rich in aluminium-bearing minerals, such as kaolinite and microcline, the presence of which was confirmed by XRD, and from which Al is released through contact with acidic solutions. Figure 4.9 shows that the release of Al^{3+} had a good relationship with that of Si^{4+}. The measurements from both oxidation cells in group 1 showed that total Al^{3+} correlated with total Si^{4+}, with coefficients of 0.6527 and 0.788 for oxidation cells G1-1 and G1-2, respectively. The robust relationship between the ions of Al and Si suggested that the soluble Al^{3+} was derived mainly from aluminosilicate minerals, which contain both Al and Si. Previous studies on kaolinite dissolution found release of Al and Si due to kaolinite dissolution in acidic conditions of pH < 4.5 (Carroll and Walther, 1990; Cama et al., 2002). As the pH decreases, Al^{3+} and Si^{4+} would be

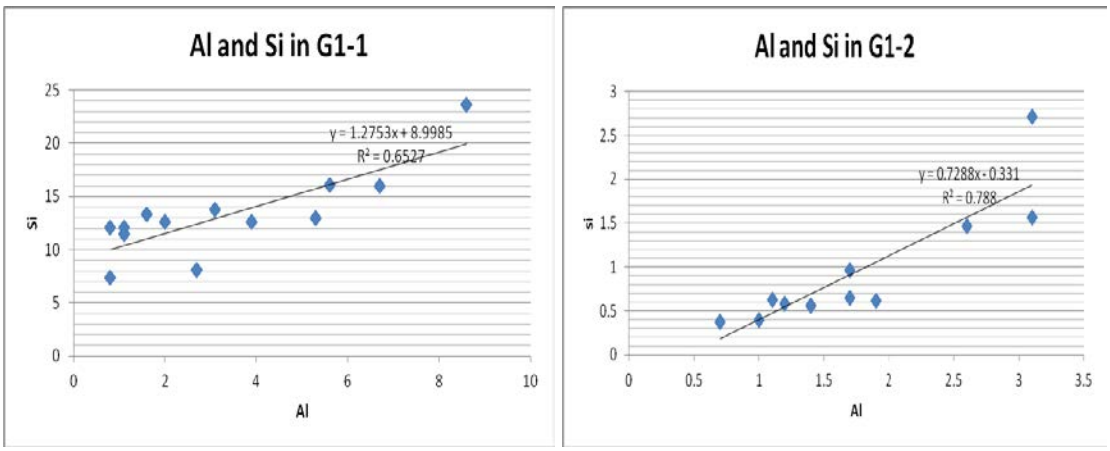

Figure 4.9: Correlation between Al^{3+} and Si^{4+} from measurement of the two cells of group 1

released from the minerals and the concentration of these soluble cations should be proportional with each other.

Moreover, it was noteworthy that there was a strong correlation between low pH and higher concentrations of major elements on days 21, 72 and 94.

4.4 Discussion

4.4.1 Mineralogical evolution during oxidation of sulphidic material

The yellow-brown to reddish coloured material on the surface of the oxidized sulphidic material is composed of secondary iron oxides and hydroxides and some sulphates and is representative of ASS surfaces as seen in the field (Fitzpatrick et al., 2008). In contrast, the inner part of the material in group still retained the initial mineralogical composition due to retention of saturated anoxic conditions in the interior preventing appreciable oxidation to occur.

The controlled oxidation of natural sulphidic material resulted in the formation of new secondary iron bearing minerals which provide a valid hypothesis that hyperpsectral sensing can detect these minerals and therefore it is important to discuss their significance. The main sulphide detected in the sulphidic material was pyrite, but volatile, reactive monosulphides could also be present, which are difficult to detect via spectral and XRD methods. The main mineralogical changes are summarized in table 4.2.

The majority of mineralogical changes occurring during the oxidation of sulphide minerals in the sulphidic material at different oxidation durations involved iron bearing minerals, and mainly occurred at the surface and to some extent at the sides of reaction or incubation cells. The material in group1 which were wetted weekly for 12 weeks, received appreciable amount of oxygen bearing water which in turn promoted significant iron sulphide oxidation with subsequent complete hydrolysis of oxidized Fe^{3+} within the surface of the sulphidic material (Bigham et al., 2002; Sullivan and Bush, 2004). The presence of stable end members such as goethite, ferrihydrite and hematite indicate that the inundation regime was also sufficient to dissolve intermediary iron sulphate salts such as jarosite that may have formed and the final pH of the surface materials is likely to be > 5. The presence of goethite and hematite, which are stable secondary iron minerals (Bigham et al., 2002) does not necessarily imply that intermediate mineralogical products did not form

(intermediate products are covered in experiment in chapter 5), but that at the end of oxidation cycle of 12 weeks, the main products were stable iron oxides and hydroxides on the surface. It is likely that iron sulphates – jarosite and schwertmannite, that are common secondary minerals in ASS environments, may have formed but due to the continuing and complete oxidation and hydrolysis of Fe^{3+} at the surface, and these meta-stable minerals gradually transformed as surface pore water pH increased due to higher frequency of rewetting. The sulphate released from the dissolution of iron sulphates resulted in precipitation of gypsum. Support for the likely formation of iron sulphates as intermediate minerals during early stages of oxidation is seen in the trace presence of jarosite at the edge material (Table 4.2).

In group 2 and group 3, because of longer durations between wetting cycles which translated to insufficient water supplies to the entire material, the material on the top surface and around the side surface oxidized at a slower rate than that in group 1. Accordingly, the transformation from pyrite and iron monosulphides to other secondary iron bearing minerals is also slower than that in group 1. The secondary mineral assemblages observed are mostly intermediary products of partially oxidized sulphides, such as jarosite, formed as acidic Fe and SO_4^{2-} rich solutions dried out between inundation events. Pyrite is still present on the surface in group 2 and group 3. Therefore the ASS evolving on the surface in group 2 and group 3, which had longer wet-dry cycles, likely stored additional acidity in the form of hydrolysable iron sulphate salts. For example, Sullivan and Bush (2004) indicated that the type of secondary mineral that forms due to sulphidic material oxidation is important for the storage of acidity. When the hydrolysis of Fe^{3+} occurring due to oxidation of sulphides results in the formation of goethite or ferrihydrite then 3 moles of H^+ is formed for every mole of Fe^{3+} hydrolysed. In contrast, if the hydrolysis of Fe^{3+} is incomplete, jarosite forms resulting in around 2.6 moles of H^+ being released. Therefore, presence of jarosite (and/or schwertmannite) results in the greater storage of acidity within the oxidizing sediments and soils as compared to when goethite and hematite form.

4.4.2 Potential hazards caused by climate change

A drying climate could cause a decrease in rainfall and the occurrence of higher temperatures in the south-west region of Western Australia (Pearce and Feng, 2007; Stephens et al., 2009) where the study area lies. A drying or lower annual

precipitation trend in the south-west could subsequently could result in the exposure of the material containing rich iron sulphides in the beds of the wetland systema and shallow estuaries for a longer duration than that in a wetter period. The depth of the oxidised layer of the experimental material in group 1, which experienced 12 weeks of oxidation, was about 1 mm on the top surface, and 1.5 mm around the side surface (as shown above in Figure 4.2) and the diameter of the cell was about 60 mm; thus, we calculated the volume of the oxidised material was about 85786 mm^3 accounting for about one-tenth of the total volume of the material which was 847800 mm^3. The whole material had released an accumulated amount of Al^{3+} of about 201.6 mg when it was immersed into low pH solutions. The thickness of the material on the top of the bed of the estuary where the material was collected was about 400 mm; thus, we calculated that the oxidation of the material could last 400*12 weeks (about 90 years) in the ideal conditions whereby the material could peel away when oxidised and expose the deeper layers to the air in a stepwise manner. During the oxidation, the pH condition of the surrounding environment remained low (less than 4) because of the constant supply of iron sulphides for gradual oxidation. As indicated in the experiment, the acidic pH would facilitate the dissolution of kaolinite and other aluminionsilicates which would in turn accelerate the release of Al^{3+} and Si^{4+}. If these large amounts of Al^{3+} and other trace metals are released to the wetland, it could kill fish and other aquatic animals and even damage the aquatic system.

When the large amounts of Al^{3+} and other trace metals are released to the wetlands and estuaries, the resulting damage to the ecosystems and indirectly to human health could be severe (Powell and Martens, 2005; Ljung et al., 2009). Aluminium is known to be harmful to fish because increased levels of Al cause gill damage leading to reduced ability to regulate oxygen, salt and water uptake, resulting in large fish kills (Ljung, et al., 2009). Considering the study area is on a coastal strip with wetlands hydrologically connected to the estuarine system, the oxidation of sulphidic materials in wetlands, stockpiles and even shallow estuarine beds could result in the release of appreciable and harmful concentrations of Al thereby severely affecting land and marine aquatic ecosystems.

4.5 Conclusion

The simulated sulphidic material experiment reveals significant changes and potential environmental impacts during the formation and development of AAS.

Firstly, the controlled experiment demonstrated the processes of the sulphide oxidation and evolution of ASS, revealing the mineral transformation and associated chemical changes under different duration wetting and drying conditions, and it successfully estimated the sulphate release rate which may be used as a proxy for oxidation rate. Secondly, the results of the incubation experiment reiterate that the occurrence of pyrite oxidation and the formation of acid sulphate soil need both water and oxygen. Sufficient oxygenated water inundation or flushing by regularly washing in group 1 (weekly flushing) greatly facilitated the oxidation of sulphidic material and development of ASS and produced stable iron oxides minerals. Material experiencing less oxidized water interaction showed less oxidation and lower hydrolysis of Fe^{3+} and produced mainly intermediary iron hydroxysulphate minerals such as jarosite. This suggests that exposed surface soil or sediments in the high rainfall conditions could be much more rapidly oxidized and transformed than those in arid to semi-arid conditions or for those landform sites less subjected to constant drying and wetting. Long-term drying such as that revealed by group 2 and 3, may however promote desiccation cracking facilitating pyrite oxidation deeper in the soil or sediment which are dependent on grain size and depositional facies of the sediment. The onset of acid conditions (pH < 4) due to iron sulphide oxidation in the sulphidic materials, results in the dissolution of aluminosilicate minerals present in sulphidic materials, thereby facilitating the release of Al^{3+} and other metals whose solubility is linked to pH. Dissolution of aluminosilicates could provide significant quantities of aluminum in acidic discharges to the surrounding environment especially the waterways and estuaries. Furthermore, the potential increase in lowering of rainfall to the southwestern Australia could result in lower water tables and greater exposure of the submerged anoxic sulphidic material to air, resulting in greater oxidation.

Table 4.7: Main chemical measurements of the solution from the material in different groups

	days	EC	Ph	Al	As	Ba	Co	Fe	Mn	Pb	Si	U	F	Cl	Br	SO4
Group 1 Cell-1	0	34.5	6.68	BD	0.005	111.2	0.004	BDL	3.3	BDL	9.8	0.26	2.6895	10275.	62.37	5741.0
	7	6.88	3.81	2.7	BDL	20.7	0.01	0.3	1.1	0.012	8.1	0.89	0.44	1829.9	6.657	1008.6
	14	6.64	3.6	0.8	0.001	20.2	0.004	0.2	1.3	BDL	7.4	0.51	0.22	1685.3	5.875	1029.9
	21	7.41	3.39	1.1	BDL	24.9	0.006	0.4	1.8	0.005	12.1	0.72	0.373	1807.4	6.305	1305.4
	28	5	3.64	1.1	BDL	17.2	0.003	0.2	1.4	BDL	11.5	0.46	0.372	1182.4	3.936	963.12
	34	4.51	3.64	0.8	BDL	13.3	0.002	0.2	1.3	BDL	12.1	0.35	0.333	1017.4	3.015	857.14
	42	3.98	3.8	1.6	BDL	11.4	0.002	0.2	1.2	BDL	13.3	0.38	0.501	760.28	2.372	850.38
	49	3.33	3.79	2	BDL	8.6	0.003	0.2	1.1	0.006	12.6	0.41	0.926	562.42	1.793	763.49
	56	2.91	3.87	3.1	BDL	9.1	0.004	0.3	1.1	BDL	13.8	0.54	0.845	459.85	1.614	760.42
	63	3.13	3.73	3.9	BDL	10.9	0.005	BDL	1	BDL	12.6	0.61	0.748	410.31	1.381	700.60
	72	3.04	3.47	5.6	BDL	8.8	0.008	2.1	1.2	0.005	16.1	0.9	0.99	428.82	1.496	1062.0
	79	2.87	3.5	6.7	BDL	8.7	0.009	1.4	1.1	0.008	16	1.01	1.667	253.60	1.585	794.78
	86	2.32	3.65	5.3	BDL	6.2	0.009	0.1	0.9	0.006	13	0.83	0.751	173.74	0.888	632.55
	94	2.71	3.45	8.6	BDL	13.2	0.017	0.3	1.2	0.009	23.6	1.82	1.252	171.16	0.641	791.50
	101	1.571	3.6										0.605	83.182		487.46
	108	1.634	3.52										0.636	68.715	0.327	520.07
Group 1 Cell-2	0	34.5	6.68	BD	0.005	111.2	0.004	BDL	3.3	BDL	9.8	0.26	2.6895	10275.	62.37	5741.0
	7	9.82	3.62	3.1	BDL	27.9	0.01	2	1.3	0.026	9.3	2.71	0.535	2492.6	9.506	1411.6
	14	8.72	3.73	1.1	BDL	27.8	0.006	BDL	1.7	0.007	11.5	0.63	0.678	2424.1	8.276	1351.6
	21	7.07	3.46	3.1	BDL	23	0.007	0.2	1.6	0.009	14	1.57	1.247	1912.8	8.614	1201.1
	28	5.43	3.57	2.6	BDL	17	0.005	BDL	1.4	0.009	15.2	1.47	0.701	1391.6	4.599	988.07
	34	4.1	3.71	1.7	BDL	12.4	0.002	BDL	1	BDL	13.8	0.96		909.79	5.092	723.64
	42	3.97	3.7	1.4	BDL	11.5	0.001	BDL	0.9	BDL	16	0.56	0.597	334.01	1.266	689.94
	49	3.02	3.72	0.7	BDL	9	0.001	BDL	0.7	BDL	13.2	0.37	0.267	561.98	1.711	571.86
	56	2.74	3.81	0.7	BDL	9.9	0.002	BDL	0.7	0.005	15.2	0.37	0.343	500.08	1.764	606.78

Table 4.8: Main chemical measurements of the solution from the material in different groups

	63	3.1	3.68	1	BDL	11.6	0.003	0.1	0.8	BDL	15.7	0.4	0.401	397.47	1.302	607.57
	72	3.07	3.43	1.7	BDL	11.4	0.003	0.2	1	0.006	21.3	0.65	1.594	885.62	2.848	786.39
	79	3.3	3.5	1.4	BDL	9.3	0.003	BDL	0.8	BDL	19	0.56	0.652	198.64	0.811	528.24
	86	1.87	3.64	1.2	BDL	8.6	0.004	BDL	0.7	0.005	17.1	0.58	0.433	159.69	0.56	479.92
	94	1.95	3.69	1.9	BDL	10.2	0.003	BDL	0.8	BDL	21.8	0.61	0.75	149.57		513.76
	101	1.228	3.62										0.769	86.398	0.49	344.51
	108	1.458	3.57										0.418	80.874	0.27	376.6
Group 2 Cell-1	0	34.5	6.68	BD	0.005	111.2	0.004	BDL	3.3	BDL	9.8	0.26	2.6895	10275.	62.37	5741.0
	28	9.91	3.76	5.4	BDL	20.9	0.013	0.7	2.7	0.006	11.4	1.18	0.72	2366.9	8.868	1817.1
	56	10.97	3.36	13.	0.002	31.4	0.026	0.6	2.7	BDL	14.2	4.57	2.752	2665.2	13.26	1815.9
	86	16.26	3.79	6.6	0.005	22.3	0.105	42	4.1	0.026	13.6	1.94	1.094	3361.9	11.00	2263.1
Group 2 Cell-2	0	34.5	6.68	BD	0.005	111.2	0.004	BDL	3.3	BDL	9.8	0.26	2.6895	10275.	62.37	5741.0
	28	11.82	3.63	8.6	BDL	27.4	0.021	0.4	3.2	BDL	14.7	2.42	1.627	3167.4	14.03	2170.7
	56	11.05	3.5	6.4	BDL	17.3	0.007	0.3	2.8	0.007	13.4	2.27	0.922	2655.7	9.156	2055.9
	86	12.78	3.62	7	0.006	23.2	0.136	72.3	3.9	0.026	12.4	2.44	1.472	2338.8		1984.3
	86	26.3	3.41	25.	0.011	25.1	0.241	90.3	9.1	0.097	14.1	8.56	3.674	5452.5	17.54	3815.3
Group 3	0	34.5	6.68	BD	0.005	111.2	0.004	BDL	3.3	BDL	9.8	0.26	2.6895	10275.	62.37	5741.0
	86	26.3	3.41	25.	0.011	25.1	0.241	90.3	9.1	0.097	14.1	8.56	3.674	5452.5	17.54	3815.3
Group 3	0	34.5	6.68	BD	0.005	111.2	0.004	BDL	3.3	BDL	9.8	0.26	2.6895	10275.	62.37	5741.0
	86	21.8	3.46	23.	0.011	17.7	0.231	78.4	8.5	0.11	13.2	7.9	3.066	4381.3	19.18	2902.8

Note: (1) Days here mean the experiment lasting days, the concentration of day 0 means the concentration of pore water of initial material; (2) The unit for EC is ms/cm; (3) The unit for cations and anions is ppm; (4) The BDL in the cell means no value because it beyond the detectable limitation.

Charter 5 Observation of Spectral Variation in the Oxidation of Iron Sulphide Materials by Proximal Sensing

5.1 Introduction

Chapter 4 reported the experiments which were designed to simulate the oxidation of sulphidic material (material rich in iron sulphides, mainly pyrite and monosulphidic black ooze) in the natural environment. The experimental results revealed the formation of several secondary minerals due to mineral transformation processes (oxidation, dissolution, precipitation) during the oxidation of the sulphidic materials. Most of the secondary minerals produced as a result of sulphidic material oxidation had diagnostic spectral features (see the spectral review of secondary minerals in Chapter 1). Therefore, the mineral transformations occurring during the oxidation of the iron sulphides and associated reactions due to the drop in pH will result in the spectral variation of the sulphidic material on oxidation.

Furthermore, the activities of this research reported in Chapter 1 and Chapter 4 also demonstrated that the secondary indicative iron-bearing minerals had a nature that suggested the soil pH conditions, because many of these iron-bearing secondary minerals formed and were stable in a specific pH range. Thus, it was proposed that an understanding of the variations that occur in reflectance spectra during the oxidation of iron sulphide materials is critical to the detection of environmental changes affected by the detrimental AAS. The technique can also be used to provide a reference for using hyperspectral remote sensing to map the occurrence of ASS and the environmental impacts due to ASS. This technique could provide an alternative way to economically and conveniently assess environmental changes by measuring spectra routinely with portable field spectrometers, such as the ASD FieldSpec and corresponding comparative analysis, in contrast to the conventional remote sensing method which compares the different temporal remotely sensed imagery to identify the changes. This method could be particularly useful when remote sensing data are hard to acquire. Accordingly, the aim of the research reported in this chapter was to measure the changes in spectral responses occurring during the oxidation of sulphidic materials and thereby to establish a link between the mineral transformations accompanying sulphidic material oxidation under naturally simulated conditions and the corresponding spectral changes. The established links between mineral

paragenesis in controlled oxidation of sulphidic materials and reflectance spectra will be beneficial to an understanding of the formative processes of ASS and aid in the remote mapping of the spatial spread of acid conditions (as examined in Chapters 7-8).

5. 2 Influential Factors of the Spectral Changes of the ASS

There are several factors that affect the spectral features of soils in general and ASS in particular. The following section identifies the main factors that affect the overall spectral properties of ASS, such as inorganic mineral constituents, organic content, particle size and moisture content.

5.2.1 Mineral composition

Inorganic minerals comprise much of soils, usually accounting for 95% or more in dry weight and more than 50% of the volume (Fanning and Fanning, 1989). Different mineral species display different reflectance spectral features (Clark, 1999). The soil spectra acquired by remote sensing or a proximal spectrometer is the comprehensive superimposition of all mineral spectral in the field of view (FOV) area. While some minerals have no apparent spectral features in the VNIR and SWIR ranges, such as quartz and pyrite, some minerals have apparent spectral features that dominate these areas of the spectrum. For instance, iron oxides have absorption features in the ranges near 0.45 μm, 0.55 to 0.65 μm, and 0.75 to 0.95 μm due to the crystal field effects (Cowley et al., 2003). Clay minerals, such as kaolinite, have strong absorption features at 2.20 μm and less strong absorption features at 2.16 μm, and carbonates have diagnostic absorption features at 2.30-2.35 μm (Figure 5.1) (Clark, 1999). The reflectance spectra of soil would provide useful information about the identity (and composition) of these main soil minerals that are spectrally responsive.

Furthermore, the relative band depths (RBD) of the diagnostic absorption peaks of specific minerals could reflect the relative abundance of specific minerals. For example, Figure 5.1b shows the relative depth of spectral absorption at 2.265 μm in two soil samples containing variable amounts of jarosite. The respective XRD of these two samples showed relatively higher intensity diagnostic diffraction peaks of jarosite at d-values of 3.08 and 3.11. The corresponding increase in diffraction peak intensities and the relative depth increase in diagnostic absorption peaks suggested that the relative abundances of specific minerals can be estimated from spectra. The

abundances, however, are dependent on several factors, such as the presence of other spectrally responsive minerals and non-responsive minerals (e.g., quartz) and the scattering dynamics; therefore, the estimates can vary.

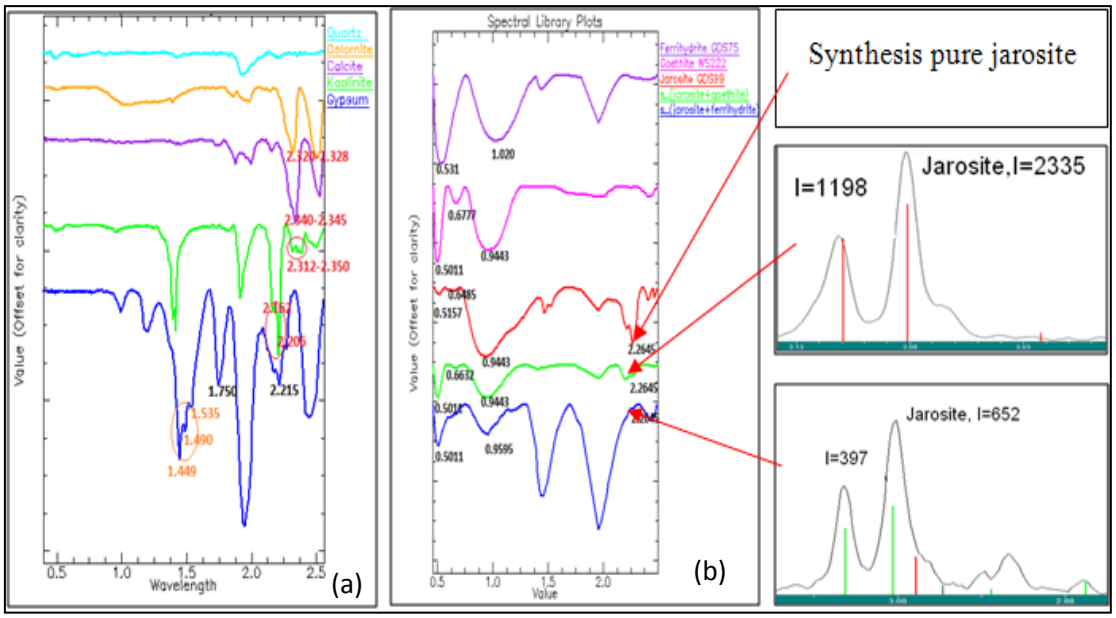

Figure 5.1: Reflectance spectra of some minerals in soil (spectra have continuum removed). (a) spectra of some non-iron minerals related to ASS; (b) spectra of some iron bearing minerals and the comparison of the absorption depth at 2.265 µm for different abundance of jarosite. Horizontal scale in µm.

5.2.2 Organic content

The organic content in soils also influences the reflectance spectra of the soils. If the organic matter present in soils exceeds a concentration of 20 g kg^{-1}, it results in a decrease in reflectance, particularly in the VNIR wavelength range, and this could mask the absorption features of other minerals (Baumgardner et al., 1985; Ben-Dor, 2002; Richter, 2010).

5.2.3 Particle size

Generally, soil particle size influences the albedo of the spectra. As the particle size increases, the overall reflectance decreases, while the absorption depth in the spectrum increases (Baumgardner et al., 1985). Thus, in the same or similar conditions in soil constituents and moisture content, under the same ambient soil conditions, the reflectance spectra of fine-textured soils usually are higher intensity than that of coarse-grained soils (Richter, 2010). Figure 5.2 shows the differences in the spectra of one of the samples taken in the present study; the spectra are from the same sample, but with different particle sizes. The red spectra of Y-008-05P was

measured after the material was milled to powder with a particle size of less than 50 µm, while Y-008-05 (green spectra) was measured before milling and as it occurred in nature. The two spectra represent the same material but with different particle sizes that are very similar in shape, nearly parallel to each other, having absorption features and peaks in the same position, but the reflectance response of the fine size particles was much stronger than that of the raw materials. These results demonstrate that the particle size affects the overall reflectance but has little effect on the absorption positions.

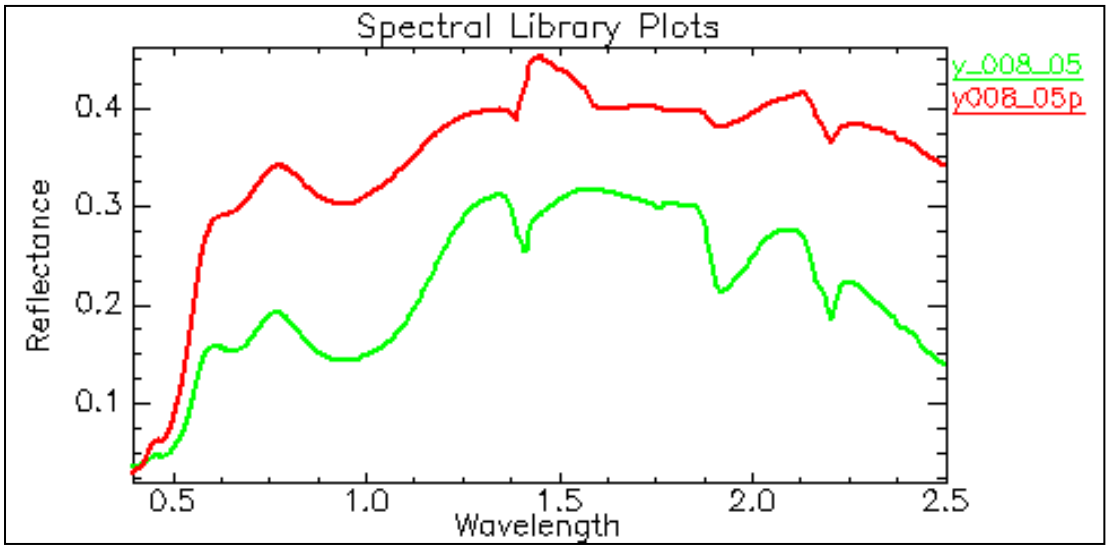

Figure 5.2: Comparisons of the spectra from different grain size – the spectra of Y-008-05 (green) was from coarse material, the spectra of Y-008-05P (red) was from the material after it was milled to powder.

5.2.4 Moisture content

Moisture content also influences the albedo of soil reflectance. Generally, wet soil has a lower overall reflectance than that of dry soil due to the water absorption, especially in the range of VNIR and SWIR (Richter, 2010).

Furthermore, in wet samples, the characteristic absorption caused by the vibration of water molecules, including two strong absorptions at 1.4 µm and 1.9 µm and two occasionally less strong absorptions at 0.9 µm and 1.2 µm, are deeper and wider than those of the dried soil samples having the same or similar constituents (Haubrock et al., 2008; Richter, 2010). Demattê et al. (2006) compared the spectra measured from soils containing different moisture content (percentages) and found that the drier soil spectra had higher reflectance (albedo) than that of the wetter soil (Figure 5.3).

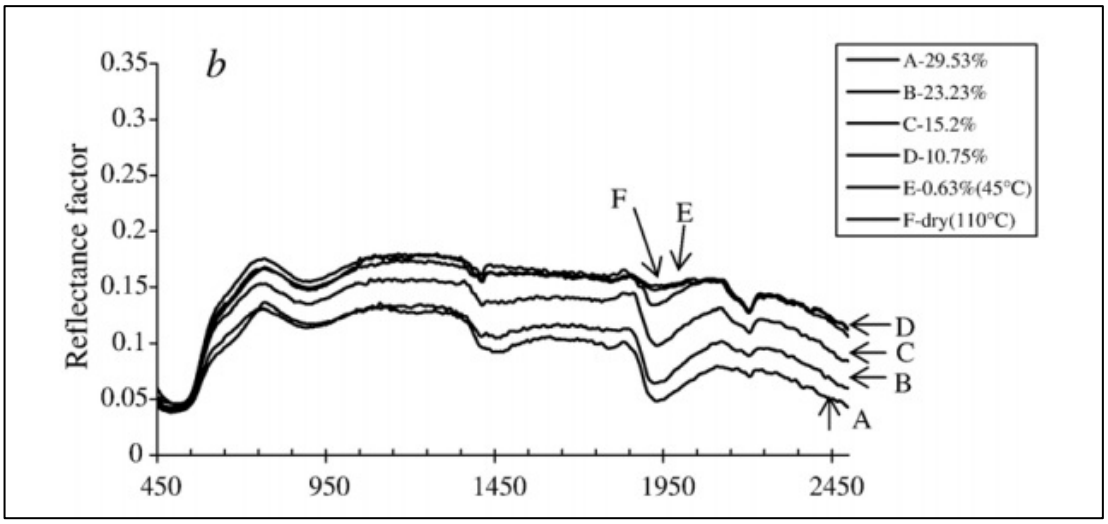

Figure 5.3: Reflectance spectra of soil with similar composition but with different moisture content (Demattê et al., 2006)

5.3 Spectral Changes occurring due to Oxidation of Iron Sulphide-Rich Material

5.3.1 Experimental settings and measurements

5.3.1.1 Sample preparation

The source of the material used for the experiment and the method used to prepare the sample are the same as those described in Chapter 4 (section 4.22). In addition, the surface of the sulphidic material was physically moulded to reflect natural topographic variations that occur when dredged material is dumped on the land surface. The surfaces of dredged material are gently undulating largely because of drying of materials in small areas with minor 6 inch depressions in places and in some areas had bench type topography due to difference in lateral dumping. To mimic these topographical or minor landform variations, the sulphidic material surface was gently moulded with a clean spatula to create subtle miniature topographic variations. The miniature relief variations were highest in the centre with steps on either side to make three topographical heights. These variations are described in detail later.

5.3.1.2 Spectral measurements

The homogeneous materials were put into acid washed plastic cells measuring 20 cm in diameter. The materials were washed weekly by adding deionised water from the top and extracting solution out from the bottom of the cell. Each water extraction stage represented a complete drying phase of the entire material. Subsequent to the extraction of the water from the material, deionised water was added to simulate a wetting phase. These cycles simulated natural drying and wetting cycles (rainfall events and seasonal changes) and the oxidation progressed further with each cycle. After extracting the solutions, the surface of the material was spectrally measured with an ASD FieldSpec3 spectroradiometer. For each part of the landform described in the following section, eight to ten spectral measurements were collected from around the surface of each representative part of the material, and then the measurements were averaged to generate a representation of the landform. The experiment was performed for 5 continuous weeks, and 5 batches of spectral data were acquired. These five measurements represented five oxidation sequences.

5.4. Results and Interpretations

5.4.1 Material changes within different miniature landforms

The visual observations described and the spectral measurements acquired were mainly from the surface of the material within the cell. As the drying (water extraction) and wetting cycles commenced (oxidation), in week 1 itself, the surface of the sulphidic material with the subtle relief variations or miniature or micro-landforms evolved to show different visible physical changes, with the main differences between micro-relief being expressed in colour variations. The final representation of these micro-landforms is shown in the image in Figure 5.4a. The following descriptions of the landforms are summarised in Table 5.1:

- *Mid-dark material.* In the centre of the cell, some part of the sulphidic material was pushed up from the surface, appearing dark in colour. For the purposes of this study, this was referred to as the mid-dark material. This part of the material had the highest elevation.

- *Dark-brown material.* From the centre of the mid-dark material outwards towards the perimeter of the cell, some of the materials appeared dark reddish. This part of material was referred to as the dark-brown material. This part of the material had relatively moderate relief.
- *Around-light material*. Between the edge along the cell wall and the middle part of the mid-dark material, the material appeared to be a light yellow to brown colour. This part of the material was referred to as the around-light material. This part of the material was relatively low in relief or near flat.

Table 5.1: Description of three miniature landforms

Micro-landform	**Location in cell**	**Colour**	**Relative elevation**	**Drainage condition**
Mid-dark	Toward the centre	Dark-yellow	Highest	Very good
Dark-brown	Around the mid-dark	Dark-brown	Moderate	Moderate
Around-light	Along the edge of cell wall	Light-brown	Lowest	Poor

The reflectance of the three materials at the end of the experiment (week 5) showed different characteristics. In the range of VNIR, the around-light material had the strongest reflective response, followed by the mid-dark material and then the dark-brown material. In the range of SWIR, the order of the reflectance was around-light>dark-brown>mid-dark (Figure 5.4b).

In the continuum-removed spectra (Figure 5.4c), the differences in the spectral features became more apparent. Firstly, the depths of the spectral absorptions near 1.4 μm and near 1.9 μm which were related to the water content in the around-light material were deeper than those of the dark-brown material, and the depths of the dark-brown material were deeper than those of the mid-dark material. This suggested that the water contents in these three parts in decreasing order were: around-light>dark-brown>mid-dark. This was consistent with the different micro-landforms in which the materials lay. The mid-dark material lay in the highest landform; thus, it had the best drainage conditions and consequently the lowest water content. The elevation of the dark-brown material was the second highest and had the second-best drainage conditions, with the second-lowest water content; while the around-light

materials lay in the lowest landform and had the relatively poorest drainage conditions and the highest water content.

Secondly, the spectral characteristics of the materials in the absorption near 0.9 μm also varied in these three landforms. The absorption near 0.9 μm was caused by the crystal effect of ferric iron and usually indicates ferric iron content (Crowley et al., 2003). The mid-dark material had the smallest depth in this absorption, while the dark-brown material had biggest depth and the around-light had the medium depth in this absorption. The absorption depth of the ferric iron feature suggested that the degree of the transformation of pyrite (FeS_2) and MBO to ferric iron was variable on the surface of an oxidising sulphidic material. The experimental observation showed the following sequence in the ferric contents: dark-brown>around-light>mid-dark.

In addition, the specific positions of the absorption near 0.9 μm in these three materials also changed. The mid-dark material had an absorption near 0.855 μm, an absorption near 1.17 μm and an absorption near 1.75 μm, implying the presence of copiapite rather than other ferric iron-bearing minerals. Copiapite is the dominant mineral in the copiapite group of minerals that are common in oxidised sulphide deposits and mine-waste environments (Jambor et al., 2000). Copiapite has a diagnostic absorption between 0.85-0.87 μm due to the Fe^{2+} crystal field transition (Crowley et al., 2003; Monterro et al., 2005; Cloutis et al., 2006), together with absorption near 0.54, 1.17 and 1.75 μm. It is noteworthy that hematite has an diagnostic absorption near 0.85 μm (very close to 0.855 μm), but hematite has not absorption near 1.17 and 1.75 μm. Hematite has also an absorption near 0.67 μm which copiapite does not possess. In the dark-brown material, the wavelength of the deepest absorption in the 0.9 μm region occurred near 0.94 μm, suggesting the dominant iron-bearing mineral was goethite. For the around-light material, the specific absorption near 0.9 μm occurred at 0.924 μm, which suggested the jarosite had become dominant.

Thirdly, for the depth of the absorption near 1.78 μm, which is usually regarded as a diagnostic feature suggesting the presence of sulphate minerals (such as gypsum), the sequence in these three materials was similar to the sequence for the water contents, namely, around-light>dark-brown>mid-dark. The existence of the absorption near 2.205 μm in all the spectra suggested the presence of Al-OH minerals in all three landform materials.

Fourthly, for the absorption near 1.17 μm which is caused by the crystal effect of ferrous iron and usually suggests the ferrous iron content, the around-light material had a distinct feature and the mid-dark material had a minor feature, while the dark-brown material had no evident absorption.

Finally, for the depth of the absorption near 2.265 μm, which is usually regarded as a diagnostic feature of jarosite, the depth of the absorption had the following sequence: dark-brown (deepest)>around-light>mid-dark (least). Therefore, the presence of jarosite appeared to be relatively more abundant in the dark-brown material and least in the mid-dark material.

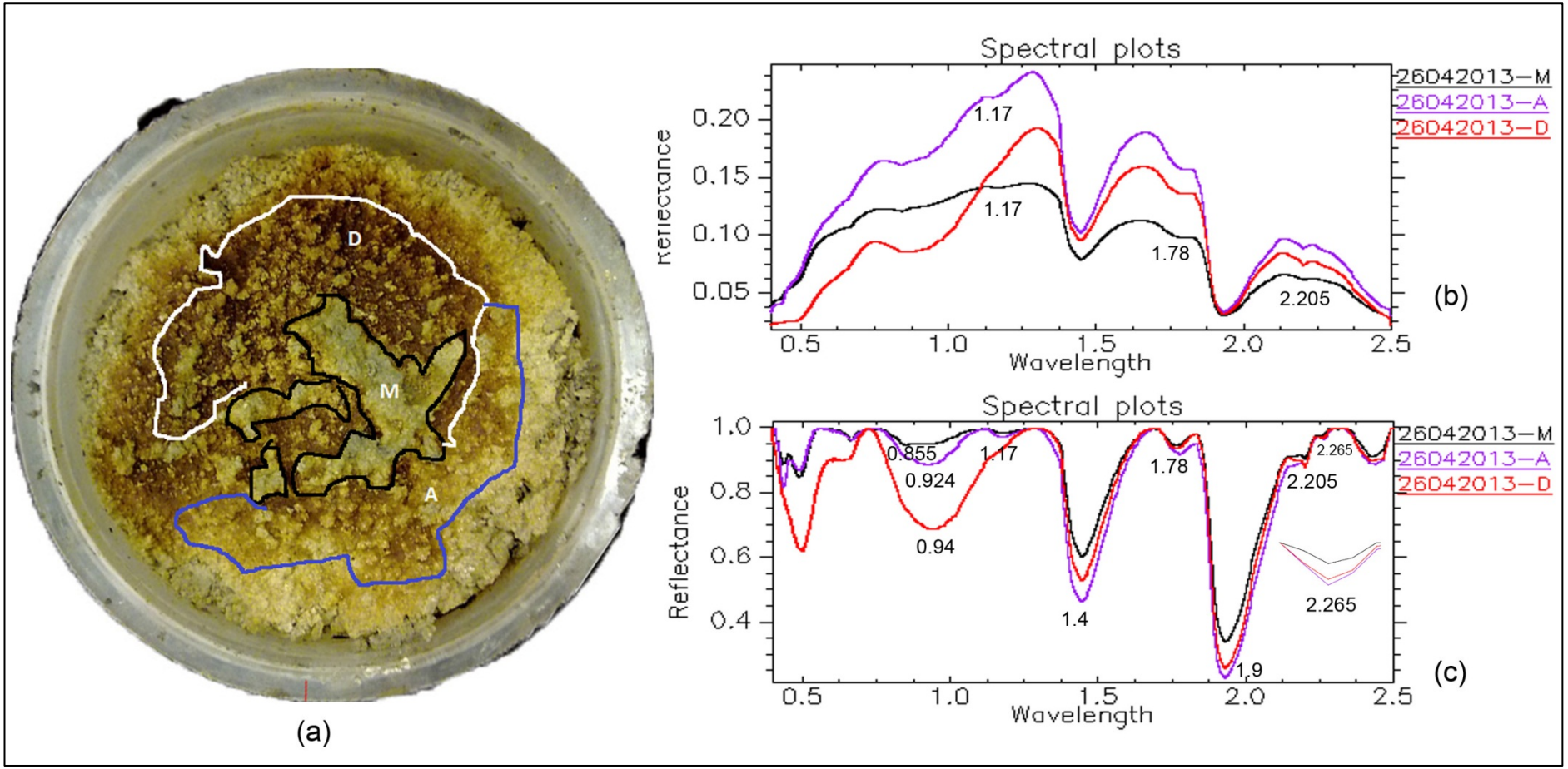

Figure 5.4: Photo and spectra collected on 26 April 2013, 5 weeks after the start of the experiment. (a) Photo of three micro-landforms in the cell, M: mid-dark; D: dark-brown; A: around-light; (b) Reflectance spectra of different micro-landforms of material; (c) Reflectance spectra of different micro-landforms after continuum removal. Horizontal wavelength scale is in µm.

5.4.2 Spectral changes with the oxidation time

The results reported in the preceding sections were from the final reflectance spectra at the end of the five week experiment. In addition to that, the reflectance spectra of the three different micro-landform materials seen in the cell after each solution extraction stage were also recorded and studied in order to assess the gradual changes on the surface of the sulphidic material over time due to oxidation. The spectral measurements were taken from the three different surface materials (micro-landforms) as the experiment progressed. The spectra at the different times of the experiment are shown in Figures 5.5-5.7. The spectra shown in red were the final spectra (in the most oxidised phase after week 5), followed by green (week 4), blue (week 3), purple (week 2) and the black spectra were those at the start of the experiment (week 1) and represented the earliest drying material.

5.4.2.1 Changes in the mid-dark material with oxidation

Figure 5.5a shows the overall reflective response of the mid-dark material increasing with time across almost all the recorded wavelengths. For the continuum-removed spectra, the presence of absorption within three specific wavelength ranges related to iron transformations were examined (Figure 5.5a, b, c). In the wavelength range of 0.8-0.95 μm, there existed a strong and broad absorption near 0.855 μm and relatively weaker absorption near 0.94 μm (Figure 5.5b). The depth of the broad absorption near 0.9 μm in the late stages of oxidation (red spectra, week 5) was the deepest, and the depths in the earliest stage of oxidation (black spectra) had the shallowest depth, showing the gradual increase in the presence of ferric iron content. The stronger absorptions at 0.855 μm rather than at 0.94 μm in all the spectra, together with the absorption near 1.17 μm, suggested that the dominant iron-bearing mineral was copiapite rather than goethite in the mid-dark material. Over time, the spectra for the material near 0.9 μm showed an increase in the depth of absorption with increasing oxidation time. This suggested that ferric iron was gradually formed from the ferrous-dominated sulphidic material, and this was manifested in the relatively minor presence of goethite at the end of week 5.

In the range near 2.265 μm, the depth of the absorption at 2.265 μm increased with time (Figure 5.5c). The increase in the 2.265 μm absorption was likely due to the increasing presence of jarosite formed from the oxidation of pyrite and MBO in the sulphidic material.

In the range near 1.17 μm that relates to the presence of ferrous iron and is commonly associated with the mineral copiapite (or copiapite group), the specific absorption position changed slightly from about 1.08 μm in the earliest oxidation phase (black spectra collected in the first week) to about 1.17 μm in the final oxidation phase (red spectra).

The change of the depth of the absorption near 1.17 μm was complex and difficult to explain (Figure 5.5d). Ferrous iron is unstable under natural conditions as it reacts readily with oxygen to produce ferric iron. This means that common ferrous-ferric iron-bearing mineral such as copiapite could transform to other ferric iron-bearing minerals. Ferrous iron can transform to ferric iron; therefore, the relative abundance of copiapite depends on the balance of the formation of copiapite and its dissolution due to the gradual increase in pH (pH>4) when it destabilises (Jambor et al., 2000). When it destabilises, it releases ferrous and ferric ions which hydrolyse and form new ferric iron sulphates and iron oxyhydroxides (Jambor et al., 2000). An increase in the depth of the absorption near 1.17 μm over time was observed, suggesting the formation of the copiapite was faster than its transformation into other ferric iron minerals.

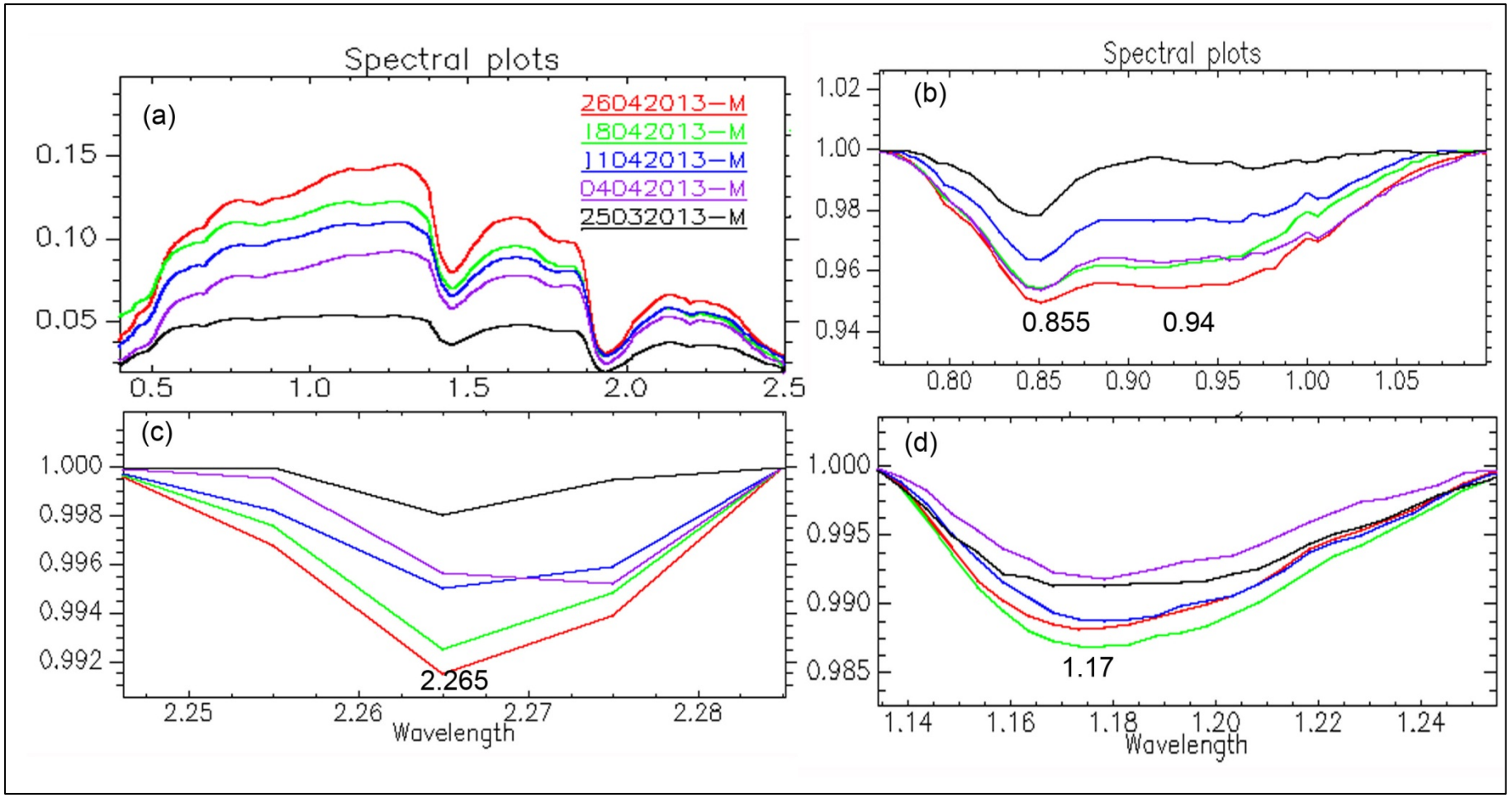

Figure 5.5: Comparison of the spectra collected weekly in the same part of the of mid-dark region (red = week 5, green = week 4, blue= week 3; purple = week 2, black = week 1) (a) Reflectance spectra measured in different times, before continuum removed; (b) Spectral range near 0.9 µm; (c) Spectral range near 2.265 µm; (d) Spectral range near 1.17 µm. Spectra shown in b-d are after removal of continuum. Horizontal wavelength scale is in µm.

5.4.2.2 Spectral changes in the dark-brown material with oxidation

The reflectance spectra collected from the dark-brown material at different oxidation phases or times displayed similar patterns to those of the mid-dark material, but was more complex (Figure 5.6a). In the range of 0.35-1.2 μm and 1.9-2.5 μm, the reflective response for the earlier oxidation phases (the green spectra in Figure 5.6a) was stronger than that seen in the final oxidation stage (black spectra). The overall reflectance of the other spectra increased with time. As shown in Figure 5.6b, the depth of the broad absorption near 0.9 μm increased with oxidation (from week 1 to week 5); for instance, the spectra from the final phase of oxidation (week 5) had greater depths of features representative of ferric iron as compared to the spectra from the early stages of oxidation. Furthermore, the main absorption peak of iron shifted from 0.855 μm in the earlist oxidation stage to 0.94 μm in the later oxidation stages. The presence of the 0.855 μm peak possibly persisted in week 5, but was much weaker as compared to the 0.94 μm feature. This shift suggested that the dominant ferric-bearing minerals changed from copiapite (mixed valence) to goethite with the possible persistence of copiapite. The gradual increase over time of the absorption at 0.67 μm, together with the occurrence of absorption at 0.94 μm, was indicative of goethite being the dominant ferric mineral in this micro-landform. In the 2.2-2.3 μm range, the depth of absorption of the 2.265 μm feature showed a similar increase in depth to that of the absorption near 0.9 μm over time (Figure 5.6c). This suggested the gradual increase in the presence of jarosite as the oxidation progressed. For the depth of the absorption near 1.17 μm, the spectra were similar to those of the mid-dark material and remained difficult to explain (Figure 5.6d).

5.4.2.3 Spectral changes in the around-light material with oxidation

The spectra of the around-light material were more complex than those of the dark-brown or the mid-dark materials. The overall reflective response of the spectra increased with oxidation(Figure 5.7a). In the range near 0.9 μm, the depths of the broad absorption increased with the duration of oxidation (weeks 1 to 5) which was similar to that observed for the other landforms, but the depth of the blue spectra (week 3) surprisingly had the greatest depth (Figure 5.7b). This suggested that the ferric contents in general increased with the duration of oxidation; however, the potentially highest content of ferric iron did not occur after the longest oxidation period but after week 3.

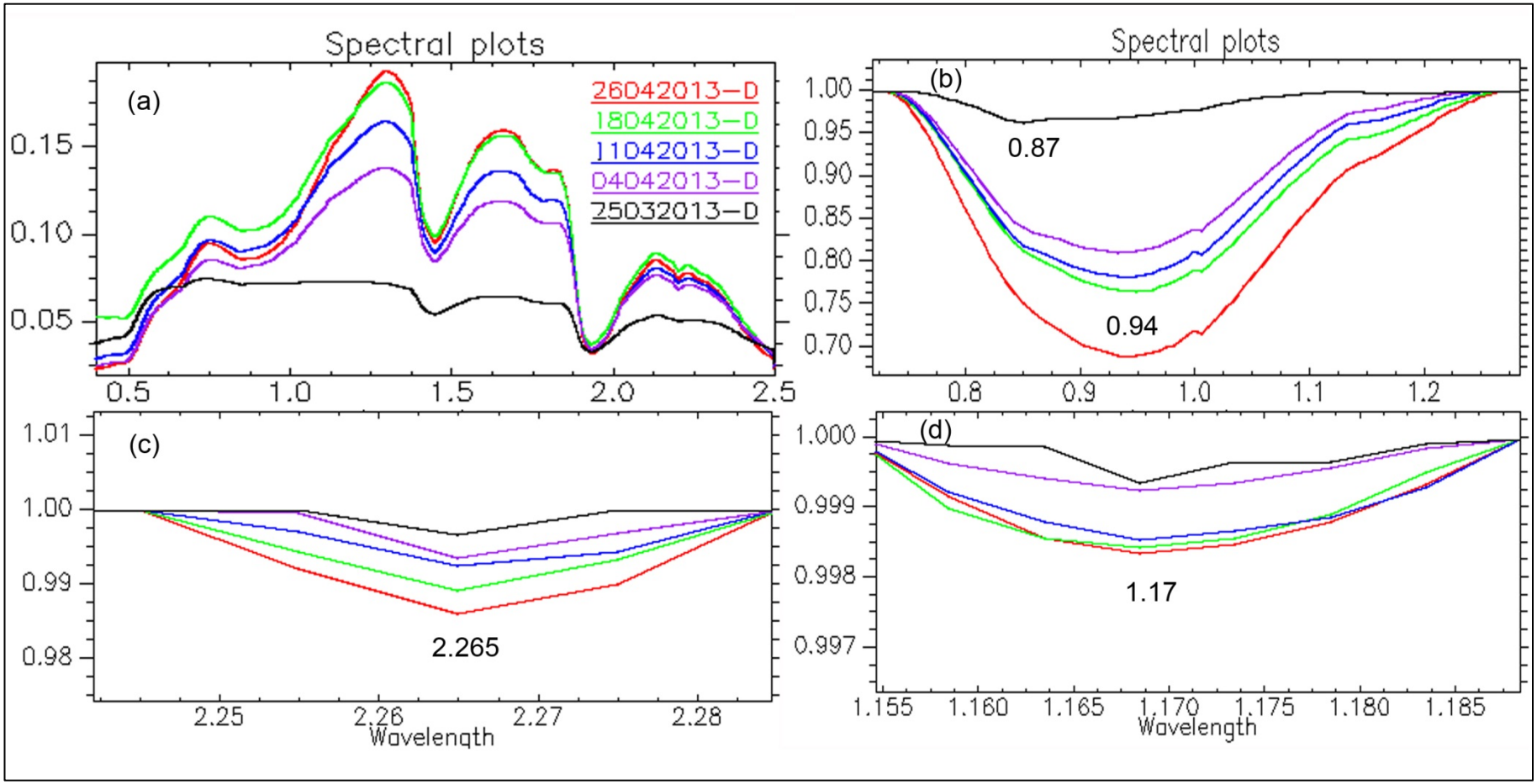

Figure 5.6: Comparison of the spectra collected weekly in the same part of the dark-brown region (red = week 5, green = week 4, blue= week 3; purple = week 2, black = week 1). (a) Reflectance spectra measured in different times, before continuum removal; (b) Close-up of the spectra around 0.9 µm; (c) Close-up of spectra around 2.265 µm; (d) Close-up of spectra around 1.17 µm. Spectra shown in b-d are after removal of continuum. Horizontal wavelength scale is in µm.

There were some differences in the specific position of the absorption near 0.9 μm. The spectra from the first oxidation phase (week 1) had absorptions centred near 0.85 μm and no absorption between 0.88-0.94 μm, thereby indicative of the presence of mainly copiapite. From week 2 onwards, with the gradual increase in oxidation, a broad peak at 0.92 μm appeared (week 2) and then the 0.92 μm peak shifted to a distinct absorption peak at 0.94 μm (weeks 3-5) (Figure 5.7b). The appearance of a slight absorption at 0.67 μm simultaneous with the appearance of the 0.94 μm absorption towards weeks 4-5 was indicative of the gradual formation of goethite with increasing oxidation. However, unlike the dark-brown material, the 0.85 μm absorption peak persisted in this material and was of equal depth to that of the 0.92 and 0.94 μm features (Figure 5.7b). The presence and possible persistence of the feature at 0.92 μm could have been related to the main ferric iron absorption of jarosite or could have been due to schwertmannite (Crowley et al., 2003). The absorption feature at 2.265 μm gradually increased with the duration of oxidation (weeks 2-5), being non-existent at week 1 when the strong 0.85 μm feature was present (Figure 5.7c). The increase in the 2.265 μm was indicative of the gradual formation of jarosite with oxidation in this material and also appeared with the 0.92 μm peak.

The absorptions near 0.85 μm (Figure 5.7b) and a slight absorption near 1.17 μm (Figure 5.7d) in the black spectra suggested that copiapite formation was dominant in the earliest stage (week 1) of this material. The absorption near 0.85 μm and the stronger absorption near 1.17 μm in the middle stages of the oxidation (second and third weeks; purple and blue spectra) suggested the greater presence of copiapite in the second and third weeks after the exposure of the pyrite material to the atmosphere. The decrease in the depth of the 0.85 μm feature and a simultaneous increase in the depth of the 0.94 μm and 2.265 μm features suggested that the dominant mineral had changed from copiapite to goethite and jarosite and goethite with oxidation, but the presence of copiapite persisted.

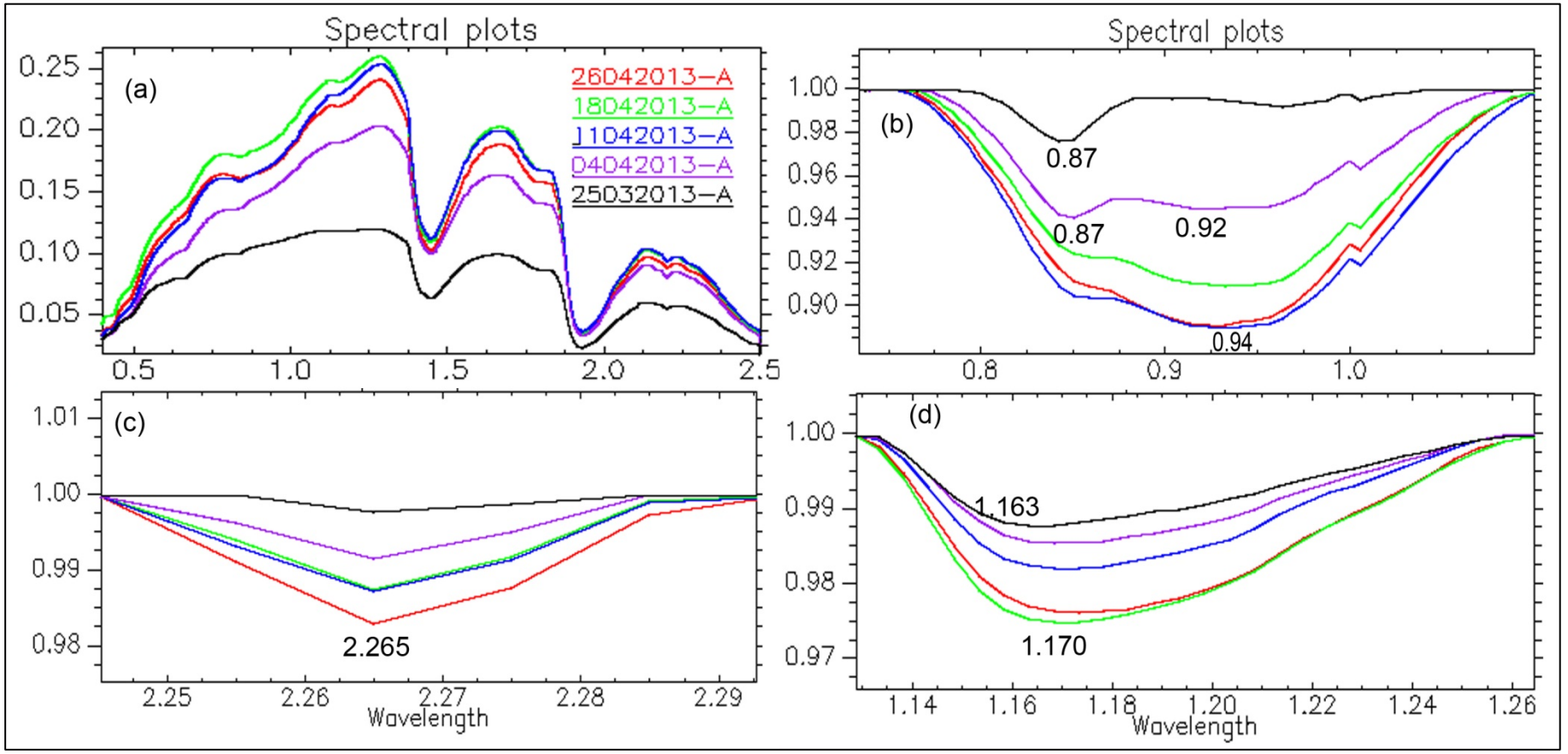

Figure 5.7: Comparison of the spectra collected weekly in the same part of the of around-light region (red = week 5, green = week 4, blue= week 3; purple = week 2, black = week 1). (a) Reflectance spectra measured in different times, before continuum removal; (b) Close-up of spectra around 0.9 μm; (c) Close-up of spectral near 2.265 μm; (d) Close-up of spectra near 1.17 μm. Spectra shown in b-d are after removal of continuum. Horizontal wavelength scale is in μm.

5.5 Discussion of Mineralogical Changes during Oxidation of Sulphidic Material

The results of the spectral changes during the controlled oxidative evolution of the sulphidic material facilitated the interpretation of the surface mineralogical changes occurring with the evolution of the oxidation of the sulphidic material. The near surface of the homogeneous sulphidic material experienced variable drying conditions resulting in the evolution of micro-reliefs each with different dominant secondary iron-bearing minerals that were typical of sulphide oxidation. The micro-landforms also suggested variable drainage and thereby variable drying conditions underlying the micro-landforms. The variable physical processes of drainage or drying could be linked to subtly different geochemical processes of oxidation, evaporation, hydrolysis and precipitation with changing pH and pore water chemistry. The combination of the oxidation-related geochemical and drainage factors underlying each micro-landform gave rise to the dominant secondary iron-bearing minerals that are similar to those found in natural sulphide oxidation environments such as abandoned mine sites or sulphide-rich mine-waste piles (Jambor et al., 2000; Buckby et al., 2003) and acid sulphate soils (Fitzpatrick et al., 1997; Sullivan and Bush, 2004). The results of the surface reflectance measurements are summarised in Table 5.2.

Table 5.2: Minerals identified by reflectance spectra in different landforms and different oxidation stages

Micro-landform	**Mineralogy @ 1 week**	**Mineralogy @ 3 weeks**	**Mineralogy @ 5 weeks**	**Drainage condition**
Mid-dark	Copiapite	Copiapite> jarosite~ goethite	Copiapite> jarosite ~ goethite	Very good
Dark-brown	Copiapite	Goethite > Jarosite>copiapite	Goethite > jarosite	Good
Around-light	Copiapite	Copiapite> jarosite ~goethite	Copiapite ~jarosite ~ goethite	Poor

Underlying the highest relief micro-landform (mid-dark), copiapite was the dominant mineral and remained the dominant mineral as oxidation progresses. In contrast, although copiapite appeared to be the first mineral to form at the other

micro-landforms, there was a change to the ferric iron minerals, jarosite and goethite, over time in the other two landforms which were comparatively poorly drained (due to longer saturation). The changes in the surface mineralogy of the three landforms could be explained by the geochemical conditions evolving on each micro-landform. Copiapite is known to form in environments adjacent to sulphide oxidation that experience high evaporation which results in the rapid precipitation of tri and di-valent iron sulphates at very low pHs of <2 (Alpers et al., 1994; Jambor et al., 2000; Buckby et al., 2003; Jamieson et al., 2005; Montero et al., 2005). The good drainage of the mid-dark material favoured rapid evaporation (or quick drying out of acid waters) resulting in the formation of copiapite from the Fe-SO_4 rich pore waters in the sulphidic material according to the following reaction:

$$Fe^{2+} + 4Fe^{3+} + 6SO_4^{2-} + 21H_2O + 0.5O_2 \rightarrow Fe^{2+}Fe_4^{3+}(SO_4)_6(OH)_2.20H_2O \quad (5.1)$$

The copiapite persisted in this environment as the drainage was good and high evaporation was favoured even though the oxidation continued. The evolution of the micro-landforms did not appear to alter the rapid draining and high evaporation conditions at least in the top microns of the mid-dark material.

In the relatively lower micro-relief site of the around-light material, copiapite formed first; however, with an increase in the oxidation duration, jarosite and goethite formed. This material also had poor drainage and indicated saturation for longer than in the mid-dark material. In the initial stages of oxidation, the micro-landform had not fully developed and extraction of the first water phase would have resulted in drying conditions similar to those for the mid-dark material, leading to the formation of copiapite similar to that for the mid-dark material. With an increase in the duration of oxidation and subsequent evolution of the micro-landform favouring longer saturation and more complete oxidation of Fe^{2+}, the resulting geochemical conditions promoted ferric iron hydrolysis and precipitation as compared to evaporation (which favours salt precipitation). The shift in conditions from evaporation to hydrolysis and precipitation (saturation) resulted in the formation of jarosite (and/or schwertmannite) and goethite (Bigham and Nordstrom, 2000):

$$3Fe^{3+} + 2SO_4^{2-} + K^+ + 6H_2O \rightarrow KFe_3(SO_4)_2(OH)_6 + 6H^+ \quad (5.2)$$

(Jarosite)

$$Fe^{3+} + 2H_2O \rightarrow FeOOH + 3H^+ \quad (5.3)$$

The pH immediately underlying the around-light landforms was likely to be <4.5 as jarosite forms and is stable at pH <4.5 (Bigham and Nordstrom, 2000; Murad and

Rojik, 2005). The persistence of copiapite with oxidation was suggestive of the existence of micro-environments where rapid evaporation caused copiapite formation and those conditions in that micro-environment persisted during experiment.

In the dark-brown material, copiapite formed first after the initial stage of oxidation largely because the micro-landforms had not developed completely, oxidation had not progressed and evaporation was uniform throughout the upper surface of the material. On further oxidation and development of the micro-landform, the duration of saturation was longer and conditions changed to those favouring hydrolysis of ferric iron and precipitation, which led to the formation of goethite and jarosite. The conditions in the dark-brown material evolved so that the initially formed copiapite was solubilised and either became a minor constituent or disappeared (Figure 5.6b). The conditions that would favour solubilisation of copiapite would be an increase in pH above 2 and saturation, both of which were likely considering the dominance of goethite in the dark-brown material because goethite forms in high water activity and slightly higher pH (Bigham et al., 2002).

Studies on the oxidation of mine-waste sites and acid drainage arising from abandoned mine sites (Bigham and Nordstrom, 2000; Jambor et al., 2000; Buckby et al., 2003; Hammarstrom et al., 2005) have indicated a mineral paragenesis of ferric iron-related secondary mineral evolution similar to the one noted in this experiment. The sequence of initial copiapite (mixed iron valence salt) to a change to jarosite (iron sulphate) to goethite is indicative of the gradual oxidation of the sulphidic material and changing hydration state of the material at the surface.

5.6 Conclusion

Spectral reflectance characteristics change with landforms. Landforms which have good drainage conditions have poor capability for water retention, which results in relatively low oxidation intensity and the formation of partially oxidised products such as copiapite. In this study, the typical spectra of such landforms had weak absorption near 0.9 μm, and the specific position of the absorption was centred near 0.85 μm. In a landform with poor draining conditions because of the low elevation, the oxidation intensity is also constrained, and the secondary iron-bearing minerals are dominated by jarosite. In this study, the spectra of the material in such a landform displayed medium-strong absorption near 0.9 μm, and the specific position of the absorption was centred at 0.924 μm. Meanwhile, a landform which has moderate

draining conditions has the most intensive oxidation, showing the most abundant presence of ferric iron contents. In this study, such a landform was dominated by fully oxidised products, such as goethite, and displayed distinct absorption near 0.94 μm.

There were two main observations of the landforms in this study with respect to the spectral changes over time. Firstly, the depths of the absorption near 0.9 μm usually increased with oxidation time, suggesting the iron ferric abundance was increasing with the oxidation time. A similar observation was also made of the absorption near 2.265 μm. Secondly, the specific absorption position near 0.9 μm shifted from 0.85 μm, to 0.924 μm or 0.94 μm, suggesting that the dominant secondary iron-bearing minerals changed from copiapite to jarosite or goethite.

Chapter 6 Mineralogy and Spectral Characterisation of Acid Sulphate Soils

6.1 Introduction

The previous chapters, including Chapter 1 which discussed the mechanisms of the generation of acid sulphate soils, and Chapter 4 and Chapter 5 which reported the simulation of the oxidation of iron sulphide material, revealed that the formation and evolution of AAS involve a wide range of minerals and mineral transformations. In this chapter, the investigation of the mineralogy of the ASS in the study area and the spectral characterisations of the different subtypes is reported. Understanding mineralogy and the spectral characterisation of ASS, as well as the relationship between them, was important in order to characterise and identify the ASS in the study area.

Minerals are the main components of most soils. Soils are dominated by minerals which include primary minerals mostly derived from parent rocks, including quartz, feldspar, mica, pyroxene, olivine, epidote, chlorite, tourmaline, zircon and rutile, and secondary minerals which are produced during the process of chemical weathering of primary minerals at different stages, such as kaolinite, illite, smectites and vermiculites (clay layer silicates or hydrous phyllosilicates), hematite and goethite (iron oxides and hydroxides), gypsum (sulphate), calcite (carbonate), gibbsite (aluminium hydroxide) and even opal-A, opal-CT and microcrystalline quartz (framework silicates) (White and Melville, 1993). The mineralogy of the soils, however, is mainly determined by the soil type, parent material and weathering processes that promote the mineral transformations during a long stage of soil development (White and Melville, 1993).

Representing one type of soil in a wide range of soil types, AAS have common soil evolution processes and controlling factors, and a similar composition of minerals and organics to other soils, but also have their own particular mineralogy, organics and individual chemical weathering processes promoting their development, and consequently ASS display some unique soil features. From the previous introduction to the formation of acid sulphate soils in Chapter 1, we can see that there are two phases of development of AAS which involve the formation of different minerals, including two different geochemical processes, namely, reduction and oxidation. The reducing stage (reduction process) mainly involves minerals such

as pyrite, and sometimes iron monosulphides. The oxidation phase, however, involves some minerals produced at different degrees of oxidation and in different pH conditions, including iron oxides, hydroxides/oxyhydroxies (such as hematite, goethite and ferrihydrite) and iron sulphates (such as jarosite and copiapite). The relationships between these mineral species and pH conditions were discussed in Chapter 1, Chapter 4 and Chapter 5.

Sulphuric acid reacts with the surrounding minerals. The reaction of sulphuric acid with soil silicate and carbonate minerals would lead to buffering and acid neutralisation reactions. The minerals available for acid neutralisation in the soils are carbonates, such as calcite, dolomite and siderite, clay minerals, such as kaolinite, framework silicates such as K-feldspar and Al hydroxides such as gibbsite. The neutralisation would result in sulphates, such as gypsum and bassanite, when Ca-carbonates are present.

The minerals which are associated with AAS usually have some diagnostic spectral features in the range of VNIR to SWIR. The secondary iron-bearing minerals, which include iron oxides, hydroxides and oxyhdroxides and iron sulphates, and the non-iron surrounding minerals, such as carbonates, sulphates, aluminosilicate and Al hydroxides, have some diagnostic spectral features in the range of 0.4-2.5 μm. The spectral characteristics of these secondary iron minerals were illustrated in Chapter 1.

The superimpositions of all the spectral features of the compositional minerals determine the spectral characteristics of ASS. Acid sulphate soils are composed of minerals from parent rocks and some secondary minerals produced from the pyrite oxidation; thus, the spectra of the soil are the superimposition of the spectra of the compositional minerals. Sulphides, such as pyrite and monosulphides, usually have no distinctive spectral features in reflection, and the dominant minerals, such as quartz, also have no distinctive spectral features in the reflectance range. Thus, these minerals have little influence on the spectral characteristics of ASS in the range of VNIR to SWIR. In contrast, the secondary products, such as iron oxides (i.e., hematite), hydroxides (i.e., goethite) and oxyhdroxides (i.e., ferrihydrite), iron sulphates (i.e., copiapite and jarosite) and sulphates (i.e., gypsum) have obvious diagnostic spectral features in the reflectance range. Therefore, the spectral features of these secondary minerals dominate the spectral features of ASS in the VNIR to SWIR range.

From the above, we can see it is important to understand the mineralogy and spectral characterisation of ASS. This mineralogy is indicative of the progress of the oxidation of ASS and its severity, and determines the spectral characteristic of ASS. Meanwhile, spectral characterisation is crucial to effectively identify ASS and map its extent by remote sensing. Accordingly, the investigation reported in this chapter focused on identifying the mineralogy and spectral characterisation of the ASS in the study area, so that the ASS could be identified and mapped via hyperspectral methods, and the resulting maps could be utilised to study the spread and severity of acid conditions and their harmful effects.

6.2 Main Minerals related to ASS

The main minerals related to acid sulphate soils, and their formation environment, their indicative pH range and their main spectral features are summarised in Table 6.1.

Table 6.1: Listing of secondary minerals dominant in the acid sulphate soil environments.

Mineral	Colour and environment	Indicative pH range	Reflectance spectral features*
Iron oxides and hydroxides			
Hematite (Fe_2O_3)	Bright red, oxidising, warm climates, good drainage	Neutral	$^6A_{1g} \rightarrow {}^4T_{1g}$ = 0.87 µm
Goethite (α-FeOOH)	Brown to yellow, poor drainage, wet and cooler climates	Acidic to neutral	$^6A_{1g} \rightarrow {}^4T_{1g}$ = 0.93 µm $^6A_{1g} \rightarrow {}^4T_{2g}$ = 0.67 µm
Ferrihydrite ($5Fe_2O_3.9H_2O$)	Reddish-brown, soils affected by rapid oxidation, good drainage	Neutral to alkaline	$^6A_{1g} \rightarrow {}^4T_{1g}$ = 0.91 µm
Lepidocrocite (γ-FeOOH)	Orange to reddish-purple, seasonally anaerobic, cool conditions	Acidic to neutral	$^6A_{1g} \rightarrow {}^4T_{1g}$ = 0.97 µm $^6A_{1g} \rightarrow {}^4T_{2g}$ = 0.67 µm
Iron sulphates and other sulphates			
Schwertmannite $Fe_8O_8(OH)_{4.6}(SO_4)_{1.7}$	Reddish-orange, sulphuric materials of acid drainages	Acidic	$^6A_{1g} \rightarrow {}^4T_{1g}$ = 0.915 µm $^6A_{1g} \rightarrow {}^4T_{2g}$ = 0.5 µm
Jarosite ($KFe_3(SO_4)_2(OH)_6$ Natrojarosite ($NaFe_3(SO_4)_2(OH)_6$	Pale yellow, sulphuric materials of acid environments	Acidic	$^6A_{1g} \rightarrow {}^4T_{1g}$ = 0.91 µm $^6A_{1g} \rightarrow {}^4T_{2g}$ = 0.5 µm & .63 µm $^6A_{1g} \rightarrow {}^4A_{1g}$ = .43 µm Fe-OH = 2.26 µm
Copiapite ($Fe^{2+}Fe_4^{3+}(SO_4)_6(OH)_2.20 H_2O$)	Pale yellow, sulphuric materials of acid environments	Extreme acidic	$^6A_{1g} \rightarrow {}^4T_{1g}$ = 0.855 µm $^6A_{1g} \rightarrow {}^4T_{2g}$ = 0.55 µm $^6A_{1g} \rightarrow {}^4A_{1g}$ = .43 µm Fe^{2+} transition = 1.17 µm

Table 6.1: Listing of secondary minerals dominant in the acid sulphate soil environments (continued).

Mineral	Colour and environment	Indicative pH range	Reflectance spectral features*
Gypsum ($CaSO_4.H_2O$)	Very pale brown, saline and saline acid soils	Neutral	OH = 1.75 μm
Layer silicates (phyllosilicates) & Al hydroxide			
Kaolinite ($Al_2Si_2O_5(OH)_4$)	White	Neutral	Doublet at 2.20 & 2.17 μm
Gibbsite ($Al(OH)_3$)	White	Neutral to alkaline	2.26 μm
Carbonates			
Calcite ($CaCO_3$) & Dolomite ($CaMgCO_3$)	White, calcareous horizons	Neutral to alkaline	2.35 μm
Sulphides			
Pyrite (FeS_2)	Black, strongly hydromorphic, reducing conditions	Neutral to alkaline	Subdued, none diagnostic
Iron monosulphides (FeS)	Black, strongly hydromorphic, reducing conditions	Neutral to alkaline	Subdued, none diagnostic
Primary minerals (framework silicates)			
Quartz (SiO_2)	White or transparent	-	None
Feldspars ($NaCaAl_3Si_4O_8$)	White to pale pink	-	None

* Data taken from Crowley et al. (2003) and Cloutis et al. (2006)

6.3 Mineral Distribution in the Study Area

Fifty samples from 12 different sites on the surface of the study area were selected for XRD analysis in order to identify the mineral composition. The mineral composition of 64 samples extracted from different depths of 8 soil cores was identified by their reflectance spectra acquired by HyLogger scanning. The surface sampling sites and coring sites are shown in Figure 6.1.

The samples collected from the surface of the study area and their main identified minerals are listed in Table 6.2. Most of the samples (45 of the 50) contained quartz and, based on the high intensity of quartz diagnostic peaks in the XRD pattern for the samples, quartz dominated the mineral composition in these samples. Sixteen of the 50 samples contained aluminium-bearing minerals, of which 14 contained kaolinite and/or microcline. Interestingly, from site Y-005, the sample Y-005-160212-05 contained three different Al phases (kaolinite, gibbsite and a soluble Al sulphate

tamarugite ($NaAl(SO_4)2\ 6H_2O$)), and the sample Y-005-160212-02 contained two soluble Al sulphates (including tamarugite ($NaAl(SO_4)_2.6H_2O$) and potassium alum ($KAl(SO_4)_2 2H_2O$)).

Forty-two of the 50 samples contained secondary iron-bearing mineral species, of which 26 contained jarosite or natrojarosite, 14 contained goethite, 11 contained ferrihydrite, 4 contained schwermannite, and 1 contained copiapite. There were also observations of some other iron-bearing minerals which are reported less frequently in acid sulphate soils, such as magnetite, maghemite, sideronatrite and magnesioferrite. Most of the identified jarosites did not exist alone, but occurred together with other iron-bearing minerals. The jarosite were mostly present together with goethite (i.e., jarosite + goethite), or schwertmannite (jarosite + schwertmannite, or jarosite + schwertmannite + goethite) or ferrihydrite (jarosite + ferrihydrite), while goethite and ferrihydrite were observed individually in the samples. Thirteen samples contained carbonates. In this study, only calcite ($CaCO_3$) was found, and carbonates were present in sites Y-02, Y-04, Y-05, Y-10 and Y-11 (Figure 6.1). Twenty samples contained sulphates, mainly gypsum (excluding jarosite) or bassanite, but also soluble Al sulphates, such as tamarugite and potassium alum, hexahydrite and blodite. These sulphates (excluding jarosite) were generally present with salts (halite).

The samples collected from the subsurface of the study area and their main mineral composition are listed in Table 6.3. The mineral composition in the subsurface was similar to that on the surface; both of them had abundant layer silicates (such as kaolinite), iron oxides and hydroxides (such as goethite) and iron sulphates (such as jarosite). Comparing the findings in Table 6.2 and Table 6.3, we can see that the number of minerals listed in Table 6.3 is much less than those in Table 6.3. It does not necessarily mean that the mineral composition of the subsurface soil was simpler than that of the surface soil; it is only because the minerals identified by the reflectance spectra were much less than those identified by XRD. For instance, quartz can be identified by XRD while it cannot be identified by reflectance spectra.

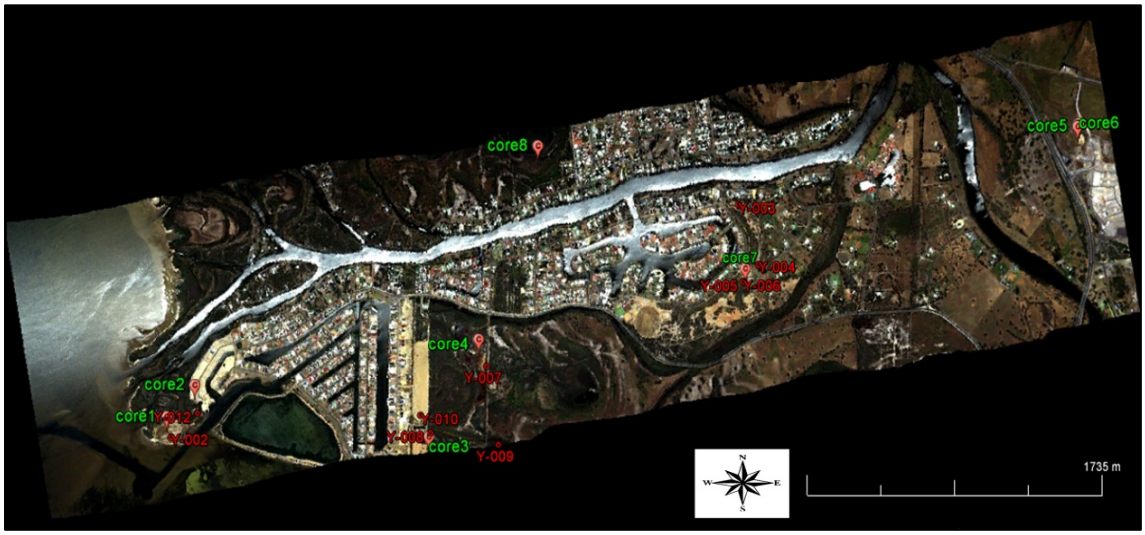

Figure 6.1: Location of sampling sites (red labels initialled with Y- are the surface sampling sites, and green labels initialled with “core” are the coring sites)

The ubiquitous presence of quartz in the study area soils samples was due to its dominance in the parent materials of the soil. South Yunderup lies between the Spearwood and Bassendean Dune Systems on a fluvial delta, and therefore the underlying sediments and parent materials for the ASS are dominated by quartz acquired mainly from the dune systems.

The presence of specific minerals and mineral groups in the surface and the subsurface of the sample sites suggested the following:

- The abundance of quartz usually influences the permeability and the structure of soils and therefore the predominantly quartz-bearing soils were likely to be permeable and prone to relatively easy draining and oxidation.
- The presence of iron-bearing minerals, such as iron oxides and iron hydroxides and iron sulphates, suggested the potential widespread occurrence of ASS in the area. The presence of acid indicative iron-bearing minerals in ASS such as jarosite, goethite and ferrihydrite indicated the existence of different acidity conditions in the different sites.
- The presence of secondary soluble Al sulphates (e.g., tamarugite) suggested the very likely strong release of Al^{3+} and therefore the susceptibility of the area to Al toxicity. In addition, the widespread occurrence of kaolinite and microcline suggested the potential capability for Al^{3+} release when these minerals are in low pH conditions.

- The presence in most of the samples of abundant jarosite, gypsum and other sulphates such as blodite provided further proof that the sample sites were affected by ASS.
- The combined presence of gypsum and halite (salt) in several sites was indicative of saline conditions in at least some soils. Saline acidic conditions are known to occur in several ASS (Fitzpatrick et al., 2008) and the occurrence of these mineral assemblages in the study area suggested the influence of ocean-derived or associated salinity within the soils.

Table 6.2: Mineral composition of soil samples collected from the surface of the study area (identified by XRD analysis).

Sample ID	Site	Mineral compositions	Ph
Y_002_160212_01	Y-002	goethite, loweite, blodite	5.13
Y_002_160212_02		quartz, jarosite, kaolinite, gypsum, halite, calcite	4.49
Y_002_160212_03		quartz, jarosite, ferrihydrite, kaolinite, halite, gypsum, calcite	4.32
Y_002_160212_04		quartz, jarosite, halite, gypsum, calcite	4.535
Y_002_160212_02(ct)		quartz, kaolinite, halite, gypsum, ferrihydrite, jarosite	4.21
Y_003_201011_01	Y-003	quartz, jarosite, microcline	5.23
Y_004_201011_01	Y-004	quartz, jarosite, calcite	3.79
Y_004_201011_02		quartz, jarosite, kaolinite, microcline, calcite	3.93
Y_004_201011_03		quartz, jarosite, ferrihydrite, kaolinite, microcline, calcite	3.4
Y_004_201011_04		quartz, natrojarosite, goethite, microcline, calcite	4.75
Y_005_160212_01	Y-005	quartz, natrojarosite, ferrihydrite, microcline, calcite	4.355
Y_005_160212_02		moganite, tamarugite, potassium alum, calcite	3.21
Y_005_160212_03		quartz, natrojarosite, microcline	4.44
Y_005_160212_04		quartz, goethite, kaolinite, calcite	4.735
Y_005_160212_05		quartz, jarosite, tamarugite, kaolinite, gibbsite, gypsum, calcite	3.17
Y_005_201011_01		quartz, natrojarosite, schwertmannite, kaolinite, microcline	3.81
Y_007_160212_01	Y-007	quartz, goethite, halite	4.215
Y_007_160212_02		quartz, ferrihydrite, goethite, halite, bassanite, gypsum	7.1
Y_007_160212_03		quartz, bernalite, natrojarosite, halite, gypsum	7.38
Y_007_160212_04		quartz, jarosite, schwertmannite, halite, gypsum	4.25

Table 6.2: Mineral composition of soil samples collected from the surface of the study area (identified by XRD analysis).

Sample ID	Site	Mineral compositions	Ph
Y_007_160212_05		quartz, jarosite, halite	3.865
Y_007_160212_07(sub)		quartz	6.345
Y_007_160212_07(top)		quartz, jarosite, ferrihydrite, gypsum, halite, calcite	4.315
Y_007_160212_08		quartz, halite	6.5
Y_007_160212_09(top)		quartz, jarosite, ferrihydrite, halite, gypsum	3.885
Y_007_201011_01		quartz, magnesioferrite, jasmundite, halite	5.59
Y_007_201011_02		quartz, magnesioferrite, goethite, halite	5.08
Y_007_201011_04		quartz, mag-hematite, magnetite, paramelaconite, halite	7.78
Y_007_221111_01		quartz, sideronatrite, natrojarosite, goethite, halite, gypsum	0
Y_007_221111_02		quartz, natrojarosite, goethite, berlinite, halite	3.1
Y_007_221111_03		quartz, natrojarosite, goethite, schwertmannite, halite	3.1
Y_007_221111_4		quartz	9.5
Y_008_160212_03	Y-008	quartz, gypsum, halite, hexahydrite	7.73
Y_008_160212_05		ferrihydrite, halite, gypsum	7.73
Y_008_221111_02		quartz, ferrihydrite, goethite, kaolinite, halite, gypsum	5.71
Y_008_221111_04		quartz, natrojarosite	4.5
Y_008_221111_05		quartz, goethite	4.9
Y_008_221111_06		quartz, jarosite, goethite	5.03
Y_008_221111_07		quartz, jarosite, goethite	4.54
Y_008_221111_08		quartz	4.19
Y_008_221111_09		quartz, jarosite, goethite	3.8
Y_009_160212_01	Y-009	halite, bassanite	7.92
Y_009_160212_02		gypsum, halite, bassanite	8.1
Y_010_160212_01	Y-010	quartz, goethite, kaolinite, calcite	5.58
Y_011_160212_01	Y-011	quartz, ferrihydrite, halite, gypsum	5.29
Y_011_160212_01(ct)		quartz, halite, gypsum blodite, calcite	7.2
Y_011_160212_02		quartz, pyrite, jarosite, copiapite, goethite, halite, bassanite	3.81
Y_011_160212_04		quartz, jarosite, schwertmannite, ferrihydrite, halite	3.795
Y_011_160212_05		quartz, ferrihydrite, jarosite, halite, bassanite	6.89
Y-012-240512-03	Y-012	quartz	7.45

Table 6.3: Mineral composition of the samples collected from the subsurface (identified by reflectance spectra)

Core	Sample	Depth (cm)	Minerals identified by reflectance spectra
Core 1	6	65	kaolinite, gypsum, goethite
Core 2	9	90	kaolinite, gypsum, goethite
Core 3	11	100	kaolinite, goethite
Core 4	7	70	kaolinite, montmorillonite, gypsum, smectite
Core 5	5	45	kaolinite, gibbsite, jarosite, kaolinite
Core 6	9	80	kaolinite, gibbsite, smectite
Core 7	11	75	kaolinite, goethite, jarosite, hematite
Core 8	6	60	kaolinite, gypsum, goethite

6.4 Spectral Characterisation of ASS in the Study Area

6.4.1 Spectral characteristics of actual acid sulphate soil

Among ASS, and in particular among actual acid sulphate soils (AASS), there exist differences in pH, Eh, EC, release of trace metals and the presence and abundance of typical secondary minerals due to different AASS being in different developmental stages. Different subtypes of ASS may experience different degrees of oxidation and may be located in different environments (such as landform settings, parent materials and drainage conditions). The formation mechanisms of AASS show the soil acidity to be generally correlated with the secondary mineral composition, especially with those secondary iron-bearing minerals produced during the oxidation of pyrite (mainly iron oxides/hydroxides and sulphates). Thus, in order to distinguish and characterise the differences among AASS, this study used soil pH as an index to classify the ASS of the study area into three groups:

- ASS with pH less than 4
- ASS with pH values in the 4-6 range
- ASS with pH values in the 6-7 range.

Subsequently, the different iron-bearing mineral compositions were used, together with carbonates which have the capability for acidity buffering, to further classify the three main groups into subtypes, as reported in the following sections.

6.4.1.1 Spectra of the soil with pH less than 4

Of the 50 soil samples collected from the surface of the study area, no sample had pH values less than 3.0, but 14 samples had relatively low pH values which were between 3.0 and 4.0, and all of these <pH 4 samples contained jarosite. As jarosite was the main secondary mineral in the samples, the ASS were subdivided into five subtypes according to the presence of associated secondary minerals with jarosite:

- ASS containing jarosite + carbonate
- ASS containing jarosite + pyrite + copiapite + goethite
- ASS containing jarosite + goethite
- ASS containing jarosite + schwertmannite
- ASS containing jarosite + goethite + schwertmannite

All these subtypes included jarosite in assembly with other minerals (usually assembled with other iron-bearing minerals), this suggested that jarosite was common in the study area. The spectral characterisation of these 5 subtype soils is discussed in more detail as follows.

(1) Jarosite + carbonate

The jarosite + carbonate subtype is represented by the presence of mineral jarosite together with carbonate, as well as kaolinite and gypsum. The appearance of the relevant sample in the present study is shown in Figure 6.2. There were six samples for this subtype with an average pH value of nearly 4. Sample Y-002-160212-02 was representative of this subtype. The pH of the sample which only contained jarosite should have had a pH less than 2.8 (Bigham, 1994; Montero et al., 2005), but the average pH value of this sample was nearly 4. The reason for the higher pH in this subtype was the additional presence of carbonate which has an acid buffering capability; carbonate could greatly buffer the soil acidity produced by pyrite oxidation. The dissolution of carbonates in response to acid conditions has been established with carbonate rapidly dissolved at <6 pH to buffer the acid conditions in this soil type. Generally, carbonate dissolution starts with near neutral conditions; for example, calcite starts dissolving at pH 6.5-7.5, while siderite follows at pH 5.0-5.5 (Dold, 2000).

The XRD data indicated the presence of jarosite, calcite, kaolinite, gypsum, halite and quartz, with the gypsum likely to have been formed by the reaction between sulphuric acidity and carbonate. Furthermore, this type of soil contains some

potential hazards due to the presence of kaolinite and the relatively low pH value, which would release Al^{3+} from the kaolinite.

The reflectance spectra of this sample showed the absorption feature of jarosite near 0.43 µm but it lacked another distinct absorption of jarosite near 2.265 µm. It also had a diagnostic spectral feature of carbonate at 2.35 µm and a diagnostic doublet of kaolinite at 2.2 µm and 2.17 µm, and the feature representative of gypsum at 1.78 µm. The spectra did show absorption features of goethite at 0.5 µm and 0.67 µm, but lacked the expected diagnostic feature of goethite at 0.94 µm (Figure 6.2). The broad absorption near 0.9 µm was complicated, showing features at 0.89 µm, 0.98 µm and 1.12 µm. These three features suggested the soil may contain a minor amount of copiapite, but this was not confirmed by XRD. The results of the mineral identification by the reflectance spectra and XRD were relatively consistent, except that halite and quartz were detected by the XRD but not by the reflectance spectra. Halite and quartz are not responsive in the VNIR-SWIR range and were therefore not detected by reflectance.

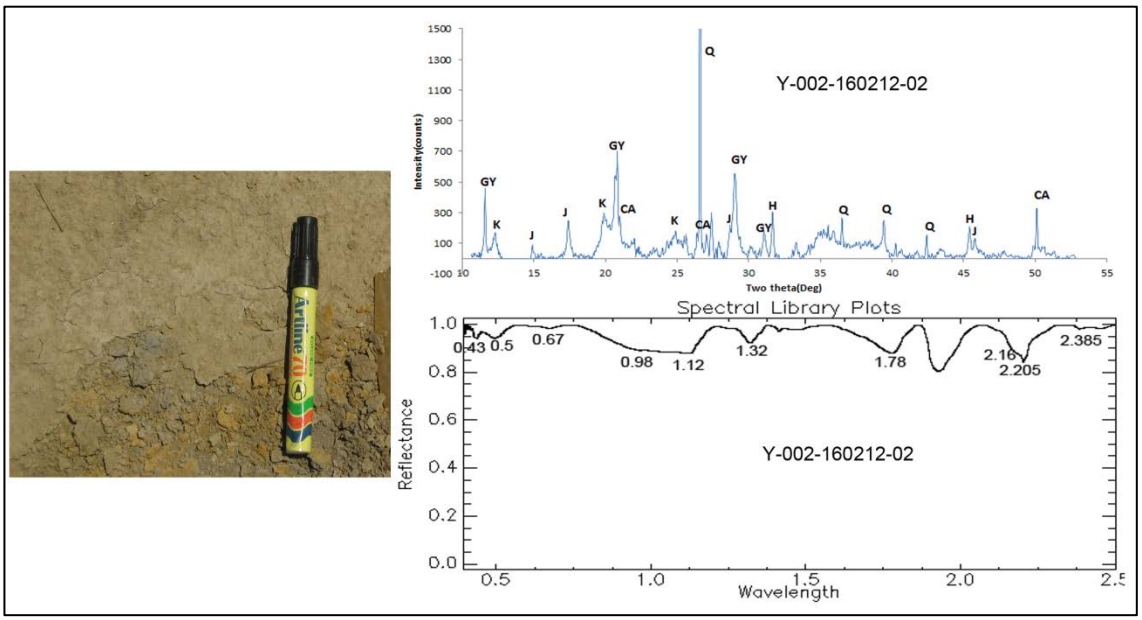

Figure 6.2: XRD patterns (above) and continuum-reflectance spectra of sample Y-002-160212-02. The diffraction peaks of minerals are labelled in the XRD patterns and the absorption peaks of minerals are labelled in the spectra (In the XRD plot, Q: quartz; CA: calcite; H: halite; J: jarosite; GY: gypsum). Wavelength units are in µm.

(2) Jarosite + pyrite + copiapite + goethite

The jarosite + pyrite + copiapite + goethite subtype is considered to represent the ASS in the early or nascent stages of development, within which some source materials of pyrite (sulphidic) and intermediate but metastable sulphidic oxidation products represented by mineral copiapite are present. This subtype also contains jarosite and mature and stable products of goethite (Figure 6.3).

Sample Y-011-160212-02 was representative of this ASS subtype. The XRD data showed that it contained minor pyrite, copiapite, jarosite and goethite (Figure 6.3). The pH value of this sample was approximately 3.81. It is likely that the pH would drop further for this type of material or soil subtype because the further oxidation of the remaining sulphide mineral (pyrite) and the gradual transformation of the meta-stable copiapite to jarosite and goethite will produce more H^+ (Bigham, 1994; Montero et al., 2005).

The reflectance spectra of this soil subtype showed a diagnostic absorption feature of goethite at 0.5 μm and 0.67 μm, and a diagnostic combination feature of copiapite at 0.43, 0.5, 0.87 and 1.17 μm, but the absorption near 0.87 μm was not distinct (Figure 6.3). Jarosite features were shown at slight absorption at 0.434 μm, but lacked the absorption at 2.265 μm. The broad absorption near 0.9 μm was centred at

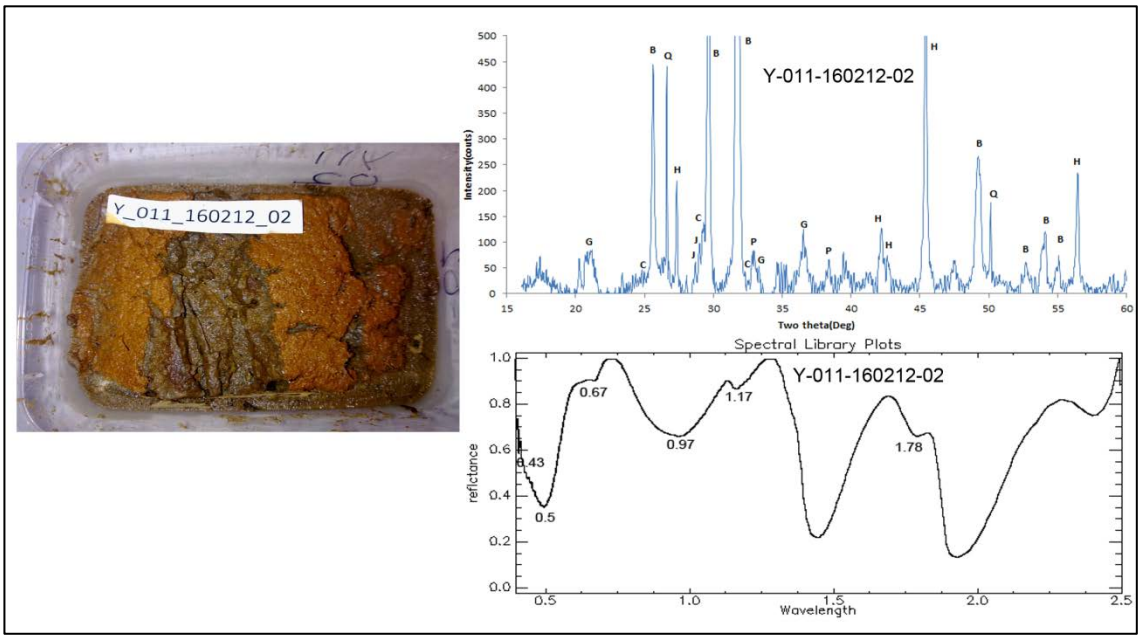

Figure 6.3: XRD patterns (above) and VNIR-SWIR spectra (continuum-removed) of sample Y-011-160212-02(floc). The mineral diagnostic XRD peaks are labelled and so are the spectra absorption peaks (In the XRD plot, Q: quartz; B: bassanite; G: goethite; H: halite; P: pyrite; C: copiapite; J: jarosite). Wavelength units are in μm.

0.97 μm. Pyrite has no apparent spectral feature in the reflectance range, thus it was not identified by the reflectance spectra of this soil subtype. The spectra also displayed the features of bassanite, which has similar chemical formula and spectral features to gypsum; these features were found in the range near 1.78 μm.

(3) Jarosite + goethite

The secondary mineralogy of this subtype is dominated by jarosite + goethite. Five samples in the present study displayed this mineralogical association. Previous studies indicated that the jarosite + goethite mineralogical combination represents a pH range of 2.9-3.5 (Swayze et al., 2000). The five samples representing this subtype in the present study had an average pH of close to 4 which was a little higher than that reported in previous studies of similar mineral assemblage. Sample Y-007-221112-2 was representative of this subtype, with a pH value of 3.1 which was consistent with the very low pH reported in previous studies. The colour and appearance of the sample are shown in Figure 6.4.

The XRD data of the samples showed them to contain jarosite and goethite including quartz and halite (Figure 6.4). The reflectance spectra showed the

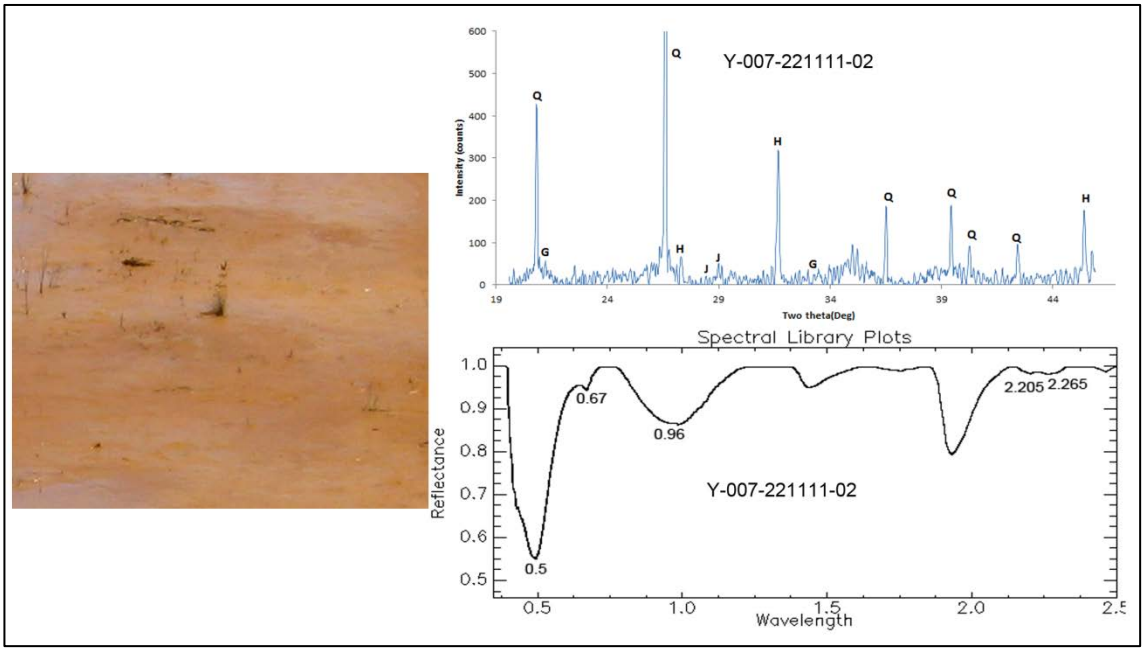

Figure 6.4: XRD patterns(above) and continuum-removed reflectance spectra of sample Y-007-221111-02. The diffraction peaks of minerals are labelled in the XRD patterns and the absorption peaks of minerals are labelled in the spectra (In the XRD plot, Q: quartz; G: goethite; H: halite; J: jarosite)

absorption feature of jarosite at 2.265 μm, and the absorption feature of goethite at 0.5 μm and 0.67 μm, but the diagnostic feature of goethite at 0.94 μm shifted to 0.96 μm. Interestingly, the broad absorption near 0.9 μm centred near 0.96 μm, and neither showed the diagnostic feature of jarosite at 0.92 μm, nor the diagnostic feature of goethite at 0.94 μm. The superimposition of the spectral features of these two minerals may be responsible for the complexity of the absorption near 0.9 μm. The identification results from the reflectance spectra were consistent with the results of the XRD in the iron-bearing mineral composition, although there were no spectral features of halite and quartz because these minerals do not have absorption features in the VNIR-SWIR range.

(4) Jarosite + schwertmannite

The jarosite + schwertmannite subtype had an average pH value of nearly 4. Sample Y-007-160212_04 was representative of this subtype of soil and had a pH value of nearly 4. The colour and appearance of the sample are shown in Figure 6.5. The XRD data showed the sample containing the iron-bearing minerals of jarosite and schwertmannite, and non-iron-bearing minerals of halite, gypsum and quartz (Figure

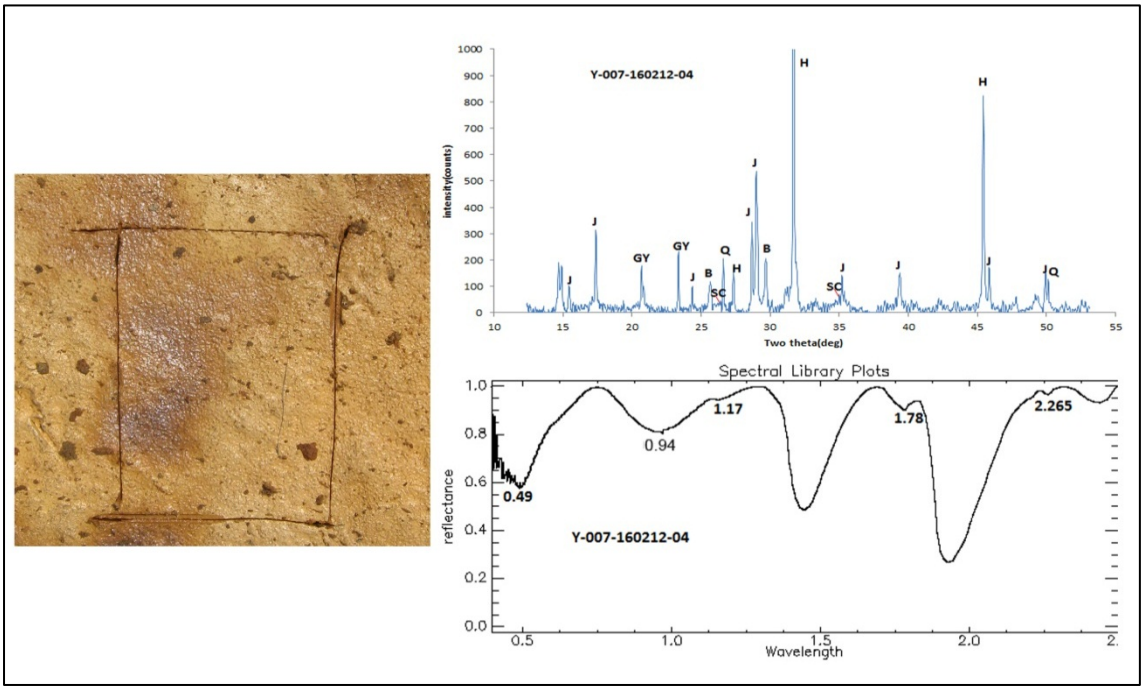

Figure 6.5: XRD patterns (above) and continuum-removed reflectance spectra of sample Y-007-160212-04. The diffraction peaks of mineral are labelled in the XRD patterns and the absorption peaks of minerals are labelled in the spectra (In the XRD plot, J: jarosite, SC: schwertmannite, GY:gypsum, H:halite, Q:quartz)

6.5). The reflectance spectra (Figure 6.5) showed absorption features at 0.5 μm and 0.94 μm, which goethite and schwertmannite commonly have. However, the reflectance spectra showed a lack of absorption at 0.67 μm, which suggested the presence of schwertmannite rather than goethite, because the difference between goethite and schwertmannite is the presence or absence of the absorption at 0.67 μm. The spectra also showed the features of jarosite near 2.265 μm. There was also an absorption at 1.78 μm which may have been related to the presence of gypsum.

(5) Jarosite + goethite + schwertmannite

The Y-007-2211-3 sample was representative of the jarosite + goethite + schwertmannite subtype soil which had the pH value of 3.1. It showed an orange and brown colour in appearance (a picture taken in the field is shown in Figure 6.6). The XRD data showed the sample to contain iron-bearing minerals of jarosite, goethite and schwertmannite, and also quartz and halite.

In the reflectance spectra, there was a distinct feature of jarosite at 2.265 μm, and also two characteristics of goethite at 0.49 μm and 0.67 μm. There were no diagnostic features of schwertmannite, the presence of which had been confirmed by

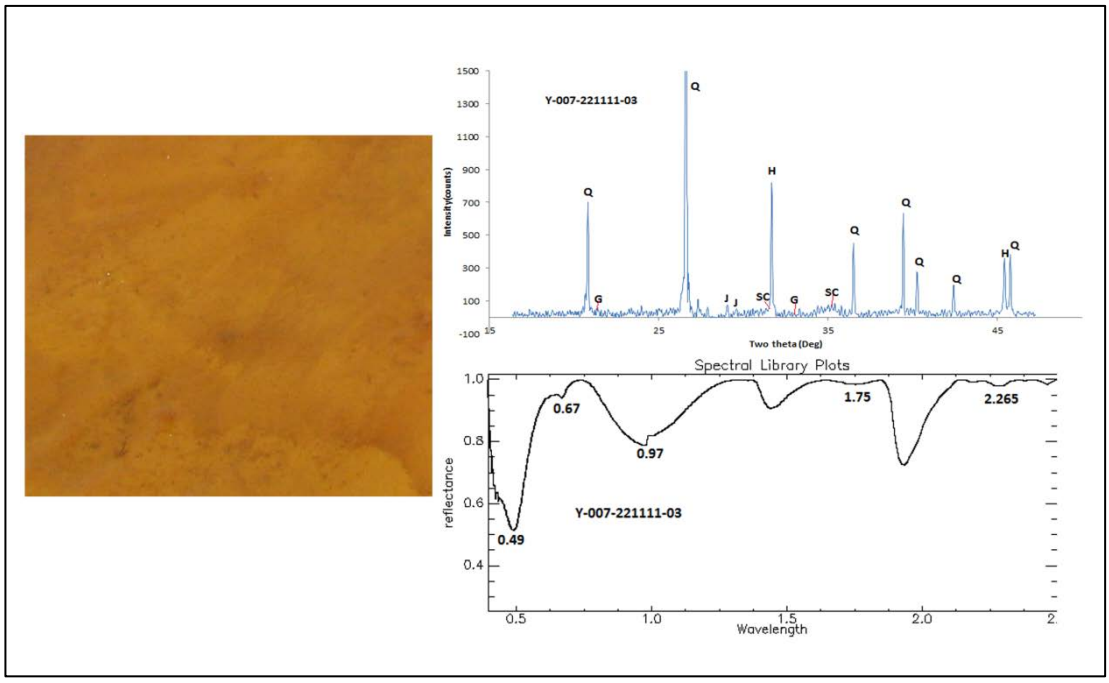

Figure 6.6: XRD patterns (above) and continuum-removed reflectance spectra of sample Y-007-2211-3. The diffraction peaks of mineral are labelled in the XRD patterns and the absorption peaks of minerals are labelled in the spectra (In the XRD plot, J: jarosite, SC: schwertmannite, G:goethite, Q:quartz, H: halite).

XRD analysis. There was broad and strong absorption from 0.75 μm to 1.2 μm but centred at 0.97 μm, which was likely to be related to the superimposition of the common absorption of schwertmannite and goethite centred at 0.94 μm and jarosite centred at 0.92 μm. There was also a shallow absorption of gypsum which was not observed by the XRD. Likewise, quartz and halite have no spectral features in the reflectance spectra and were not identified. Pictures of the sample, XRD plot and reflectance spectra of the sample are shown in Figure 6.6.

6.4.1.2 Spectral of the soil with pH in range of 4.0-6.0

The samples in the higher pH range of 4-6 represented two subtypes. One subtype only included goethite and the other subtype only included ferrihydrite as the main secondary mineral.

(1) Goethite

Soils and precipitates related to acid conditions that contain goethite usually have a pH of less than 6 (Bigham, 1994). Goethite can form in a wide range of pH conditions, existing alone or with other minerals, such as jarosite, ferrihydrite and hematite. In this study, when goethite existed alone, it usually had pH values in the range of 4-6. There were four samples that contained goethite only, with an average pH value of about 4.86. The representative sample of Y-008-2211-05 had two apparent and strong absorption features at 0.49 μm and 0.67 μm and a strong and broad absorption feature centred at about 0.98 μm which made it very like lepidocrosite, but the result of the XRD confirmed that the mineral was goethite. It was likely that the usual absorption feature of goethite at 0.94 μm was shifted to 0.98 μm. The reflectance spectra also showed features of a kaolinite doublet including a strong absorption at 2.2 μm and a slight absorption at 2.16 μm (Figure 6.7). The presence of kaolinite and the moderate low pH condition meant the ASS contained the potential risk of Al release.

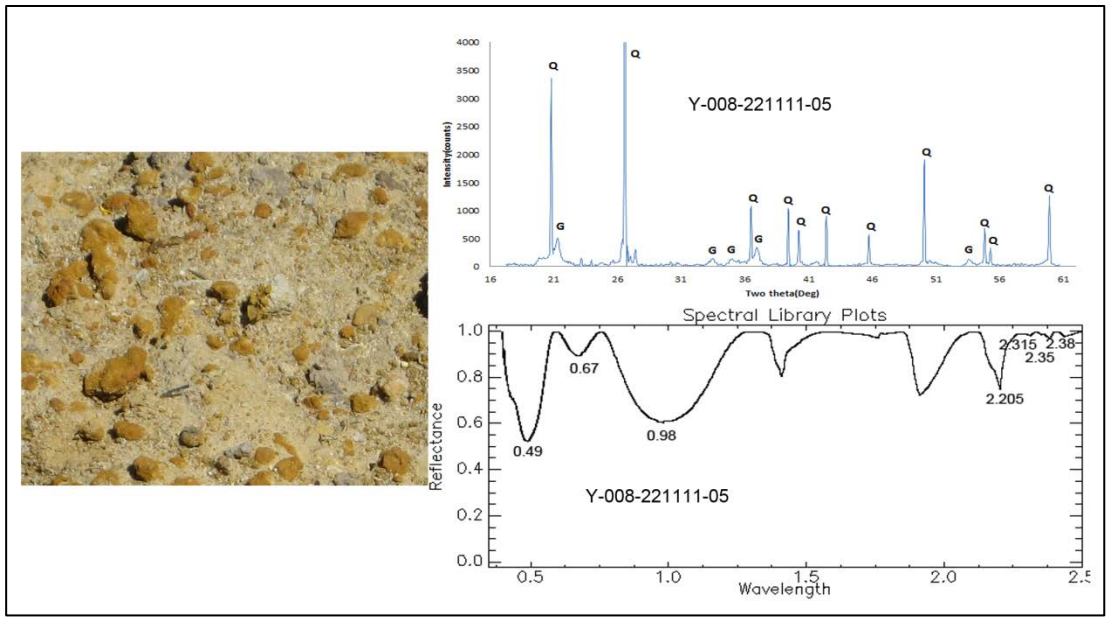

Figure 6.7: XRD patterns (above) and continuum-removed reflectance spectra of sample Y-008-2211-05. The diffraction peaks of minerals are labelled in the XRD patterns and the absorption peaks of minerals are labelled in the spectra; the sample contains goethite (In the XRD plot, Q: quartz, G: goethite). Wavelength units are in µm.

(2) Goethite + ferrihydrite

The XRD pattern showed the samples to be composed of goethite and ferrihydrite (broad peaks), and quartz and halite (Figure 6.8). The reflectance spectra dominantly showed the diagnostic features of goethite with strong absorption features at 0.49 µm and 0.67 µm. There was also a broad and shallow absorption centred at 0.98 µm which was very likely the superimposition of the absorption of goethite centred at 0.94 µm and the absorption of ferrihydrite centred near 1.02 µm. The spectral features of the non-iron-bearing mineral of kaolinite were distinct and occurred as the typical doublet at 2.2 µm and a slight absorption at 2.17 µm. The spectra also showed the absorption feature of gypsum at 1.78 µm.

Generally, ferrihydrite forms when pH is greater than 5 (Montero et al., 2005), and goethite forms when pH is less than 6 (Bigham, 1994). The soils containing both goethite and ferrihydrite in the study area were found in the pH range of 5-6. Sample Y-008-221111-02, as the representative of this subtype, had a pH value of 5.70 which was consistent with previous studies that reported the occurrence of both goethite and ferrihydrite (Swayze et al., 2000; Murad and Rojik, 2005).

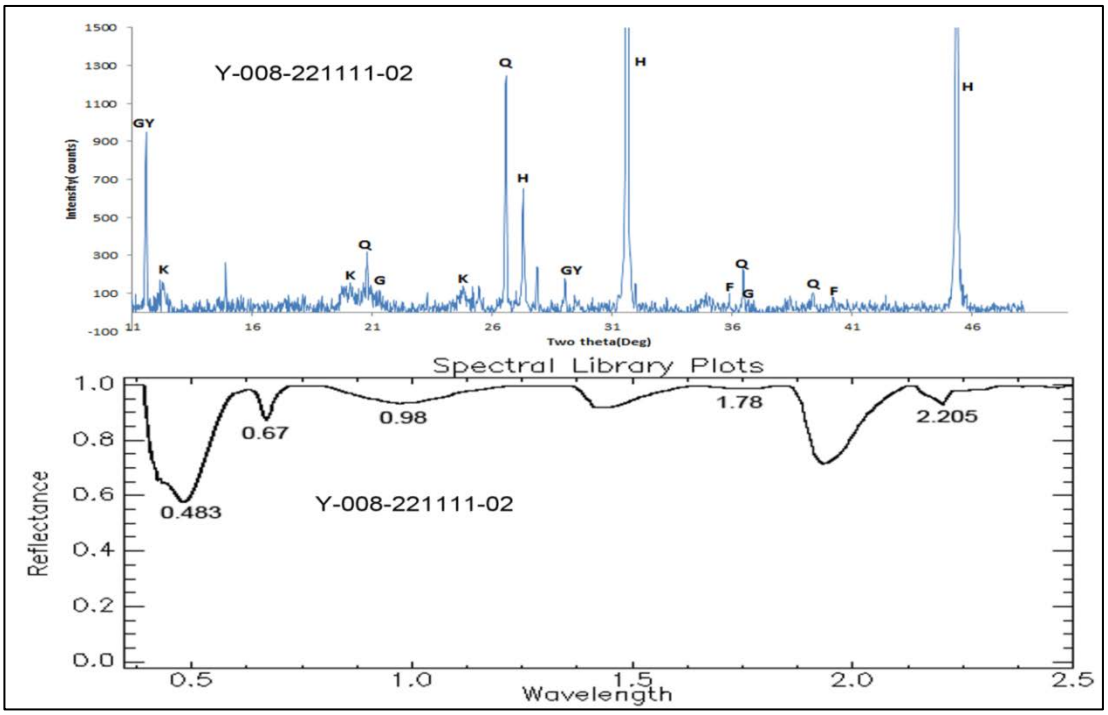

Figure 6.8: XRD patterns (above) and continuum-removed reflectance spectra of sample Y-008-2211-02. The diffraction peaks of mineral are labelled in the XRD patterns and the absorption peaks of minerals are labelled in the spectra (In the XRD plot, Q: quartz, G: goethite, H: halite, K: kaolinite, GY: gypsum, F: ferrihydrite). Wavelength units are in μm.

6.4.1.3 Soil pH in the range of 6.0-7.5

(1) Ferrihydrite

There were samples of this subtype with an average pH value of 6.9. The higher pH value and the presence of ferrihydrite as the only iron oxyhydroxide mineral were consistent with the observations of previous studies which illustrated that ferrihydrite usually forms when the pH is above 5 and generally in the range of 6-7 (Montero et al., 2005; Murad and Rojik, 2005). The sample Y-008-160212-05(ct) was the representative of this subtype. The XRD scan showed that the sample contained only ferrihydrite as the iron-bearing mineral, but also large amounts of halite and gypsum (Figure 6.9). The reflectance spectra of the sample showed diagnostic absorption features of ferrihydrite with strong absorption at 0.49 μm and slight absorption at 0.97 μm. It also showed hematite absorption features at 0.67 μm and a slight absorption at 0.87 μm (Figure 6.9). It was possible that minor amounts of hematite

could have been present in the sample and the minor quantity (<3%) was not detected by the XRD. The sample also displayed a feature of gypsum at 1.78 μm, but no features of halite.

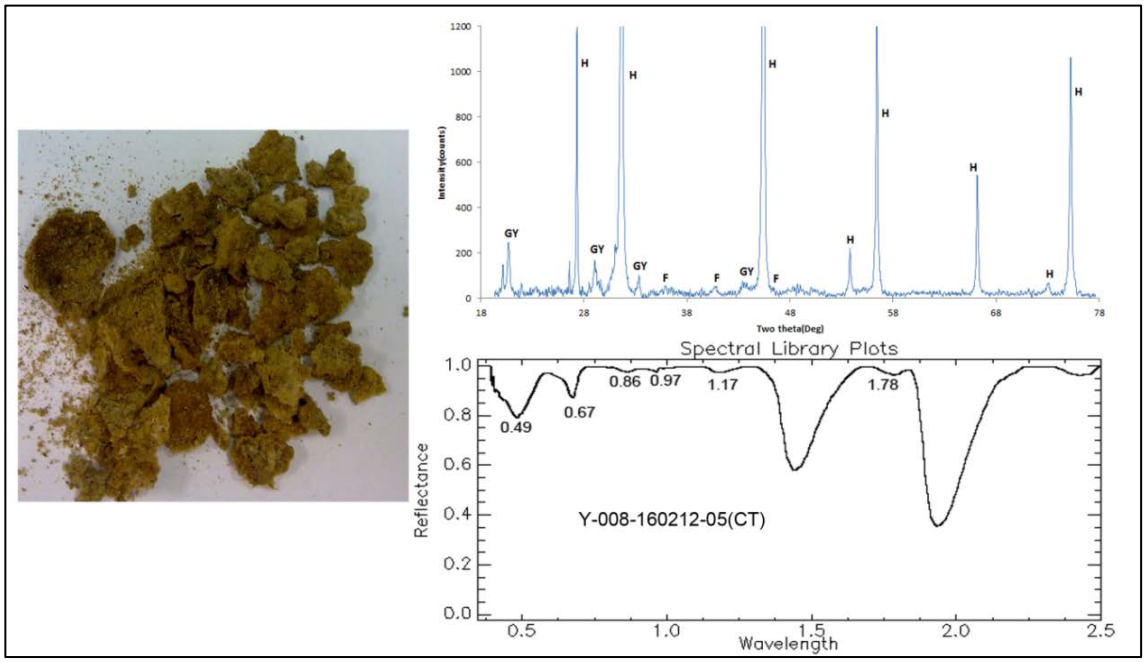

Figure 6.9: XRD patterns (above) and continuum-removed reflectance spectra of sample Y-008-160212-05(ct). The diffraction peaks of mineral are labelled in the XRD patterns and the absorption peaks of minerals are labelled in the spectra (In the XRD plot, H: halite, GY: gypsum, F: ferrihydrite)

6.4.2 Spectral characteristic of the unaffected soil

(1) Quartz + kaolinite

From the results of the mineral identification of the samples (Table 6.2), we can see that quartz was present in all the samples, and kaolinite and gypsum existed in most of the samples. Thus, we regarded these three minerals as being the dominant minerals in soils that are unaffected by sulphidic materials and ASS. (background soil). The representative background soil sample Y-012-240512-03 was collected at a site which had green vegetation cover and no visual signs of being affected by acid sulphate soil. The pH of this sample was 7.41, and the spectral measurement suggested the existence of kaolinite by the spectral absorption features at 2.205 and 2.305 μm, and the presence of gypsum by the spectral absorption at 1.75 μm. The presence of these two minerals was not confirmed by the XRD analysis, because the strong intensity of quartz hides the information of all the other minerals. The XRD and reflectance spectra are shown as Figure 6.10.

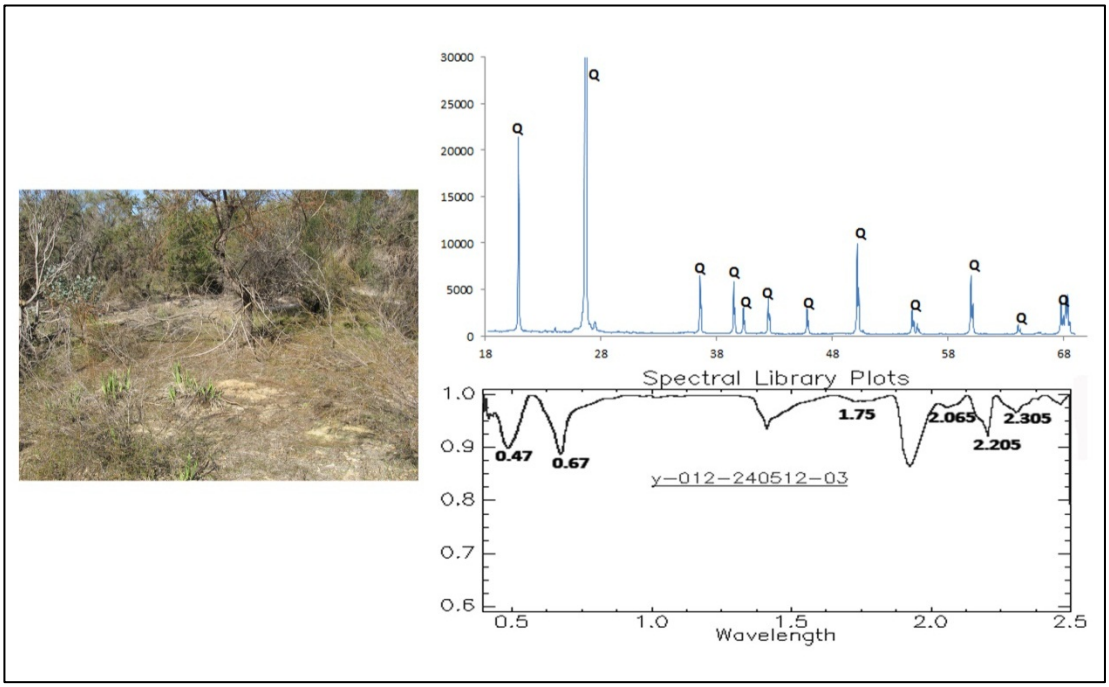

Figure 6.10: XRD plot (above) and reflectance spectrum plot (continuum-removed) of the sample from background soil (In the XRD plot, Q: quartz).

(2) Kaolinite + gibbsite

Gibbsite ($Al(OH)_3$) forms in the primitive state of aluminosilicate neutralisation, such as k-feldspar ($KAlSi_3O_8$) and kaolinite ($Al_2Si_2O_5(OH)_4$), in near neutral conditions (Bigham and Nordstrom, 2000), and will dissolve when pH is below 4 (Blowes et al., 2003*)*. The soil that contains gibbsite is usually in near-neutral conditions (pH range of 5-7). There were 5 samples from 2 soil cores that showed the presence of gibbsite and kaolinite, and therefore belonged to this subtype. These samples had an average pH value of 6.55. Sample C6-01C which was from soil core 6, was the representative of this subtype and had a pH value of 6.15, and the presence of gibbsite and the neutral pH was very consistent with previous studies.

The spectra of sample C6-01C had a strong absorption at 2.267 μm and doublet absorption at 1.412 μm and 1.452 μm (which are absent in jarosite). These features suggested the presence of gibbsite (Baptista et al., 1998; GMEX, 2008). The sample spectra also showed a doublet absorption in the 2.1-2.2 μm range which is typical of kaolin minerals (Clark, 1999). The image and reflectance spectra of this sample are shown in Figure 6.11.

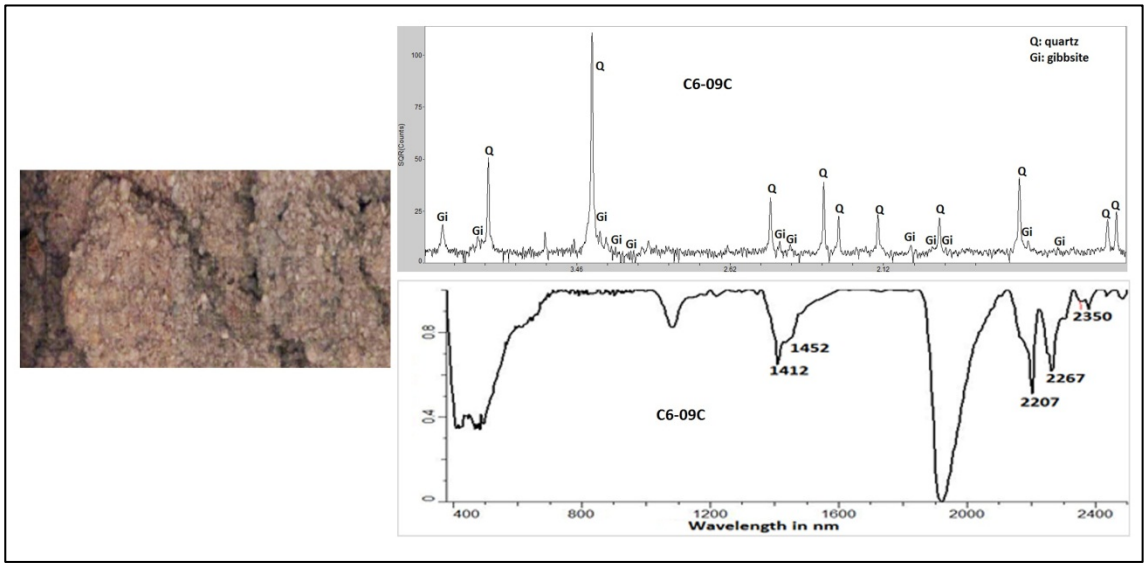

Figure 6.11: XRD plot (above) and spectral plot (continuum-removed) of the soil core sample C6-01C showing features for kaolinite and gibbsite

6.5 Discussion

6.5.1 Soil mineralogy and pH

The results of the mineralogy of the soil samples taken from the ASS sites in this study agreed with results from previous studies regarding the links between specific mineral assemblages and soil pH. The results of the XRD and spectral mineral identification of the 50 samples, and the respective pH of the samples, indicated the following mineral and soil subtype associations:

- Samples with dominantly jarosite assemblage with goethite and/or schwertmannite, and copiapite had pH values < 4.
- Samples with goethite, or goethite and ferrihydrite, had pH values between 4 and 6.
- Samples with ferrihydrite or gibbsite had pH values above 6.

Because the results established the occurrence of individual mineral or specific mineral assemblages, they allowed us to make interpretations based on the soil pH range for the study area.

6.5.2 Identification of secondary minerals via reflectance spectroscopy

Several studies have used hyperspectral reflectance spectra to identify specific secondary minerals and mineral assemblages and then map these minerals in acid environments (Swayze et al., 2000). To apply hyperspectral remote sensing for

mapping minerals on soil surfaces in ASS areas, it is imperative to first assess the capability of identifying the indicative minerals via hyperspectral methods. For example, are field and laboratory-acquired reflectance spectra from study area samples able to correctly identify the minerals in the soil? The results presented in the study area indicated that secondary mineral identification was possible and could be confirmed by XRD. Indicative minerals such as jarosite, goethite, schwertmannite and copiapite could be identified as well as other associated soil minerals such as kaolinite, gibbsite, gypsum and carbonates. Minerals that do not have absorption features in the VNIR-SWIR range, such as halite, quartz, feldspar and importantly sulphide minerals (pyrite and Fe monosulphides) could not be identified by reflectance spectra.

The comparison of the XRD and reflectance of the soils, although mostly consistent, did reveal some minor discrepancies. In some samples, a secondary mineral was detected in the reflectance spectra (e.g., goethite and hematite), but the mineral was not identified via XRD. This discrepancy can be explained based on the amount of minerals present. X-ray Diffraction can generally detect minerals present above 3% by volume (especially for fine-grained minerals, and most secondary minerals have characteristic nanometre grain sizes), while reflectance spectra can detect the absorption features of minerals in much smaller quantities. Therefore, for specific minerals such as iron oxides and hydroxides, the reflectance spectra results appear to be more sensitive than the XRD results.

6.6 Conclusion

This chapter firstly revealed the overall mineral composition of the AAS in the study area. The soil mineral composition of the selected sites in the study area was identified by reflectance spectral measurements and XRD analysis. The dominant minerals in the ASS samples in the present study were the inherited minerals of quartz, kaolinite, halite and calcite, and minerals formed as a result of ASS oxidative formation such as goethite, jarosite, schwertmannite, gypsum and copiapite. The reflectance spectra were capable of identifying specific iron oxides, hydroxides and sulphate minerals and kaolinite and gypsum, but could not identify spectrally non-responsive minerals such as quartz and sulphides.

This study focused on characterising the different groups and subtypes of acid sulphate soils in the reflectance spectra. Acid sulphate soils in the study area were

divided by the pH conditions of the soil, and it was found that the differences in spectra between the different groups and subtypes were mainly influenced by the spectral features of the present secondary iron-bearing minerals. Jarosite, which was wide spread in the study area, combining with copiapite, schwertmannite, goethite, ferrihydrite and sometimes carbonates, influenced the spectral characteristic of the type of ASS which had low pH values, while ferrihydrite, either alone or combined with goethite, influenced the spectral features of the type of ASS which had high pH values. This further established the link between the indicative soil mineral and mineral assemblages and soil pH.

The spectral characterisation of the different types of acid sulphate soils, and the establishment of the relationship between minerals or mineral assemblages and soil pH, can facilitate the use of hyperspectral remote sensing to map minerals across an area and thereby be used as a surrogate to broadly map soil pH.

Chapter 7 Assessment of Soil pH of the Surface Acid Sulphate Soil by PLSR Modelling and Indicative Mineral Mapping of Airborne Hyperspectral Imagery

7.1 Introduction

The basic principles of detecting acid sulphate soils by remote sensing consist of two aspects: 1) acid sulphate soils contain some minerals that are able to reflect the pH conditions at which they generate; 2) these indicative minerals have diagnostic spectral characteristics in their reflection spectra. The relationships between the secondary iron bearing mineral species or mineral assemblies and pHs were illustrated in Chapter 1, and the spectral characteristics of these indicative minerals were also demonstrated in Chapter 1 and Chapter 4. Therefore, the presence of specific minerals on the Earth's surface and subsurface can be used as an indicator of pH conditions, and such a relationship has been used in the past to map acidic variations arising from AMD (Swayze et al., 2000; Ong et al., 2003; Riaza and Muller, 2010).

Since surface soil and water pH are linked with the formation and persistence of specific iron oxyhydroxide and iron-sulphate oxyhydroxide-bearing mineral species, and these minerals have diagnostic spectral features in the VNIR-SWIR wavelength regions, logically, there is a justification to suggest that the pH values of soils have a direct influence on their spectral reflectance. In addition, if the pH and spectral response link does exist, it would facilitate the method of using spectral properties to rapidly and effectively map the distribution of surface acidity. To achieve this aim, proper modelling approaches are necessary. The PLSR technique is an effective modelling method, combining features of principal component analysis and multiple regressions (Wold, 1966a, 1966b; Thomas and Haaland, 1990). PLSR is particularly useful when the number of predictions exceeds the number of samples and when strong correlations exist between predictions (Haaland and Thomas; 1988; Wold et al., 2001). The method has been widely applied in numerous applications of hyperspectral remote sensing, which possesses hundreds of bands, to detect relatively limited properties. Examples of the use of PLSR in different geoscientific research include for acid mine drainage to predict pH (Ong et al., 2003), in soil science to estimate soil moisture, nitrogen content, organic matter and heavy metals (Li, 2006),

to detect and predict soil salinity (Farifteh et al., 2006), and in geology to determine mineralogical information in granitoid rocks (Hecker et al., 2012). In this study, PLSR was used to establish a relationship between pH values and reflectance spectral features measured in the laboratory on field samples from the study area, and then the relationship established was applied to airborne hyperspectral imagery to predict and map the distribution of pH extent and severity.

The discussion in this chapter focuses on the exploration of a new way to map the spread and severity of soil pH in ASS and the comparison of this method with established hyperspectral mineral mapping methods. The aims of this part of the research were to model the relationship between pH values and reflectance spectral features by PLSR and to apply the resultant predictive model to airborne hyperspectral imagery to deduce the soil pH distribution; to map the main indicative iron-bearing and sulphate-bearing minerals and subsequently to deduce maps of soil pH according to the relationship between the minerals and the pH. A final objective was to compare the two maps produced from the PLSR modelling and from the mapping of acid indicative minerals showing acid conditions, so the comparative effectiveness of the maps could be assessed.

7.2 Methodology and Data Acquisition

The strategy for this study included the systematic collection of spectral and physical ground surface data and the application of PLSR modelling to the datasets. Firstly, the pH measurements were collected on selected surface samples and the reflectance spectra of the same undisturbed samples were measured in the laboratory. Then, PLSR was used to establish the relationship between the collected spectra and the corresponding sample pH. Subsequently, the relationship between the mineral assemblages and pH values of the samples was established by validating the mineralogy with XRD. Finally, the soil surface acid maps were produced using two different methods. The first method was through applying a PLSR model to the airborne hyperspectral data to directly deduce the pH distribution, and the second method was the mapping of the distribution of pH indicative iron-bearing minerals in the airborne hyperspectral data and then the deduction of soil pH distribution by utilising the link between mineral species and pH. The second method has been extensively employed in other studies to map the acid arising from mine wastes (for example, Swayze et al. (2000); Riaza et al. (2011)).

7.2.1 HyMap data

The remotely sensed hyperspectral data for this study were acquired via the airborne HyMap sensor operated by HyVista Corporation. The data for South Yunderup were acquired for the Western Australian Department of Environment on the at 12:45 pm, 1st December, 2005 on a bearing of 258° and at an altitude of 1447 m ASL. This generated a pixel size of approximately 2.9 m at nadir for a swath width of 1.7 km and flight-line length of 7 km (Lau 2008). HyMap has 128 contiguous bands in the VNIR and SWIR range from 0.45 to 2.5 µm, with bandwidths between 15-20 nm, and pixel resolution of between 2-10 m varying with the flight height of the aircraft, and signal-to-noise ratio greater than 500:1 (Cocks et al., 1998). The resolution of the HyMap images for this study was 5 m and 10 nm for the spatial and spectral images, respectively.

7.2.2 Soil sample collection

The method used for the soil sample collection was described in Chapter 2.

7.2.3 Proximal hyperspectral data

An ASD FieldSpec3 spectroradiometer was used in the laboratory to measure the reflectance spectra of the surface of the soil samples. Four to five spectral measurements, each an average of 40 measurements, were collected from around the surface of each ASS sample using an ASD contact probe device, which housed a 15 watt halogen bulb. Each spectral measurement was ratioed against a LabSphere Spectralon 99% white reference standard. These multiple spectra were then averaged and resampled from 2151 bands to 128 bands in order to match the resolution of the HyMap images.

7.2.4 pH measurement

The method used in the pH measurements was described in Chapter 2.

7.2.5 Mineralogy verification

All the surface ASS samples were submitted for XRD analysis to verify the spectral results. Spectral feature analysis and the use of the Spectral Assistant (Berman et al., 1999), from the Spectral Geologist software, were used to assist in choosing suitable end-members for the spectral mineral mapping. The main XRD d values (interplanar

spacings) and reflectance spectral features of indicative iron-bearing minerals are listed in Table 7.1.

Table 7.1: Reflectance spectral features and XRD d values of main indicative minerals

Minerals	**XRD d values**	**Diagnostic absorption positions (µm)**
Copiapite	9.23, 18.4, 5.57	0.55,0.855,1.17,171
Jarosite	3.08, 3.11, 2.292	0.438,2.265
Schwertmannite	2.55, 3.39, 4.86	0.5,0.98
Ferrihydrite	2.45, 1.97, 2.25	0.53,1.03
Goethite	4.18, 2.69, 2.452	0.5,0.67,0.94
Jarosite + ferrihydrite	3.08, 3.11, 2.292,2.45, 1.97, 2.25	0.5,0.95,2.265
Jarosite + goethite	3.08, 3.11, 2.292, 4.18, 2.69, 2.452	0.5,0.67,0.94,2.265
Hematite	2.69, 1.69, 2.51	0.54,0.67,0.87

7.3 Image Pre-Processing

A radiative transfer model (AtComp, Rodger, 2011) was used to remove atmospheric effects and correct at-sensor radiance to apparent ground reflectance, as well as to provide a correction for wavelength shifts. An empirical line calibration, which included field spectral measurements, was applied to the AtComp reflectance product to further correct residual atmospheric and instrument effects. Anthropogenic objects within the imagery play a negative role in the processes of target object identification, mapping and interpretation of ASS, thus it was necessary to create a mask to exclude these objects. For the purposes of this study in particular, roof materials containing iron oxides would be very spectrally similar to iron-bearing minerals in soils or sediments, and would be likely to confuse the iron mineral mapping results. Roof materials, vegetation, water bodies (such as the sea, rivers, lakes and creeks) and roads were mapped in advance of information extraction. In addition, a mask was generated to exclude these pixels from further image processing and mapping, similar to the methods described by Cudahy et al. (2005).

7.4 PLSR Procedures

7.4.1 Training dataset preparation

The preparation of the training dataset is critical to establish a robust PLSR model. Therefore, care was taken to correctly prepare the training dataset. Firstly, the training dataset of spectral and pH measurements was required to strictly correspond one-to-one and efforts were made to ensure that the samples were measured accurately in a consistent manner. Secondly, the samples selected for the training dataset came from the same environment and location as the pixels that were locatable and identifiable in the HyMap dataset. Thirdly, a consistent procedure was followed to measure the reflectance spectra of the samples, using the same spectroradiometer with the same device settings. All the spectra measured on the training samples were done in as close to their natural condition as collected in the field as possible and not after drying or disturbance of their surfaces.

7.4.2 Spectral processing

A robust method to process the spectral data was required in order to acquire a good PLSR model because of the general presence of some unrelated spectral variability that obstructed the obtaining of a sound model. In this study, the acquired spectra were normalised by using individual spectral mean values to process the spectra of the training sample. The aim of the normalisation was to remove, where present, some unwanted spectral variability.

7.4.3 Cross-validation

Validation was used to assess the performance of the predictive model. The leave one out cross-validation method which is often used in PLSR and multiple linear regression (MLR) was used in this study. The robustness of the model is usually estimated by the cross-validation statistic R^2, which reflects the correlation between the actual value and predicted response and can be described as follows:

$$R^2=1- [\sum_i(Act_i-Pred_i)^2/\sum_i (Act_i-U_{act})^2]$$

where Act_i and $Pred_i$ are the actual and predicted responses, and U_{act} is the average actual response.

7.4.4 Determination of the optimum factors

The determination of the optimum number of factors was the key to establishing a robust PLSR model because too few factors can lead to insufficient modelling of the property being investigated, while too many factors can result in over fitting. Thus, it was crucial to choose an optimum number of PLSR factors to keep the response residual minimised and keep a good balance between the robustness of the model and the minimum of the residual. Usually, the prediction error sum of squares (PRESS) or standard error of prediction (SEP) are used as indicator values to determine the optimum number of PLSR factors. PRESS can be defined as:

$$PRESS=\sum(\hat{y}(i) - y_i)^2$$

where $\hat{y}(i)$ and y_i are the estimated and actual response values, respectively; while SEP can be described as:

$$SEP = Sqrt(PRESS / M)$$

where M is the number of samples. Every factor has its own PRESS or SEP, and the ideal number of factors is very likely the one where the PRESS or SEP approaches a minimum. To assess the goodness of fit between the predicted values against the observed values, other model performance parameters such as the coefficient of determination (R^2) were also calculated.

7.4.5 Sample and spectral outlier

The aim of PLSR modelling is to establish a relationship between the actual value and predicted value using cross-validation. When all the training reflectance data were used, the R^2 of the relationship between reflectance and pH was often unsatisfactory. Therefore, it was necessary to exclude sample outliers to obtain satisfactory R^2 values. Importantly, after exclusion of each outlier, the relationship was again cross-verified to update the relationship between the actual pH value, predicted value and the new final regression coefficient. Another case where there was a need for outlier exclusion was when some bands had negligible or zero influence on the response variable or contained noise which showed very low absolute values of the coefficient.

7.4.6 Final regression coefficient output

The final regression coefficient (FRC) can show the influential weight of different spectral predictors. In the research conducted in this study, FRC weights with

positive values influenced the response variable pH positively, while the FRC weights with negative values affected pH negatively. In addition, the bigger the absolute coefficient values, the more significant impact on the pH value. Compared to the model derived from MLR, which has limited independent variables, the PLSR model for hyperspectral sensing applications usually has hundreds of predictors. For example, for the South Yunderup dataset, the HyMap imagery has 128 bands or predictors. Therefore, the resulting model could be too complex and complicated to apply to the imagery, and thus it was necessary to reduce some predictors that had low absolute values in coefficients because they contributed insignificantly to the prediction. Accordingly, in making the model for the dataset, bands with low coefficients of determination values were removed. After the removal of these bands, cross-validation was conducted again to reallocate the coefficients to the remaining wavelengths.

7.5 Result and Discussion

7.5.1 Acidity map deduced from predictive model

7.5.1.1 Optimum factors

The PRESS and factors plot (Figure 7.1) showed that 8 was the optimum number of factors in the predictive model, as this number had the lowest PRESS value of 1.7153 and lowest SEP value of 0.2673. The number of optimum factors as indicated by PRESS was also supported by the F probability for the data. The F probability, which forms the statistical tool to determine probabilities called the F test, is another

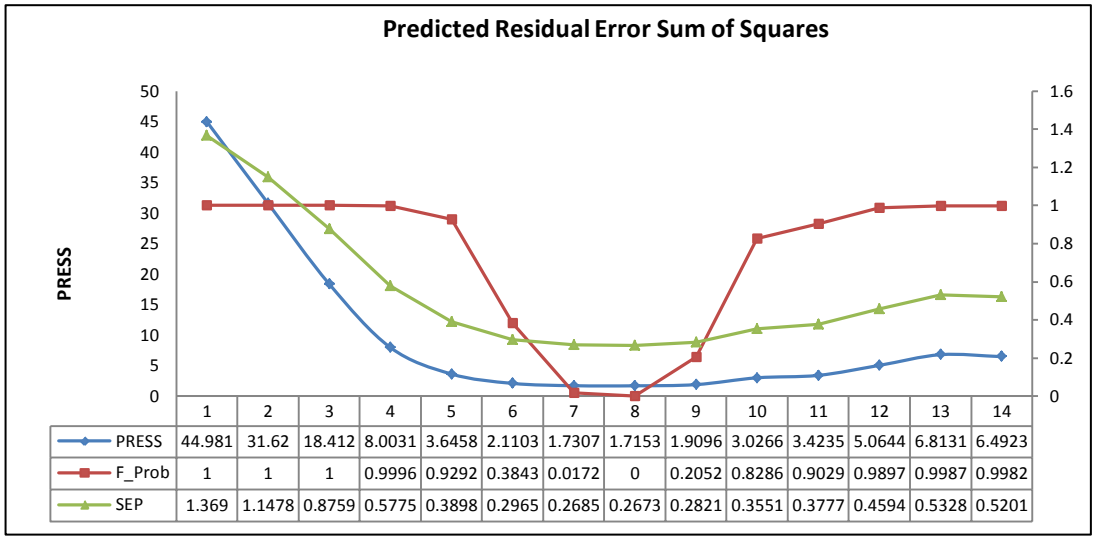

Figure 7.1: PRESS, SEP and F-test plot and factors.

variable that helps in deciding the optimum number of factors. Usually, the lower the F value, the better, and for the model calculated, the optimum factors were 8 when the F probability value was zero. Therefore, both PRESS and F probability pointed to 8 being the optimum number of factors for the dataset.

7.5.1.2 Relation between actual and predicted value

The coefficient of determination (R^2) is a measure of the statistical correlation between measured values and predicted values for the PLSR model. Thus, R^2 was an important indicator to demonstrate the model's capability to predict. In general, higher values of R^2 are an indication that there is a good prediction of the model. The plot of correlations between the actual pH and predicted pH showed a high R^2 value of 0.963 (Figure 7.2). High R^2 values such as this strongly suggested that the generated model had strong capabilities to predict the response variable (pH) from the spectral information.

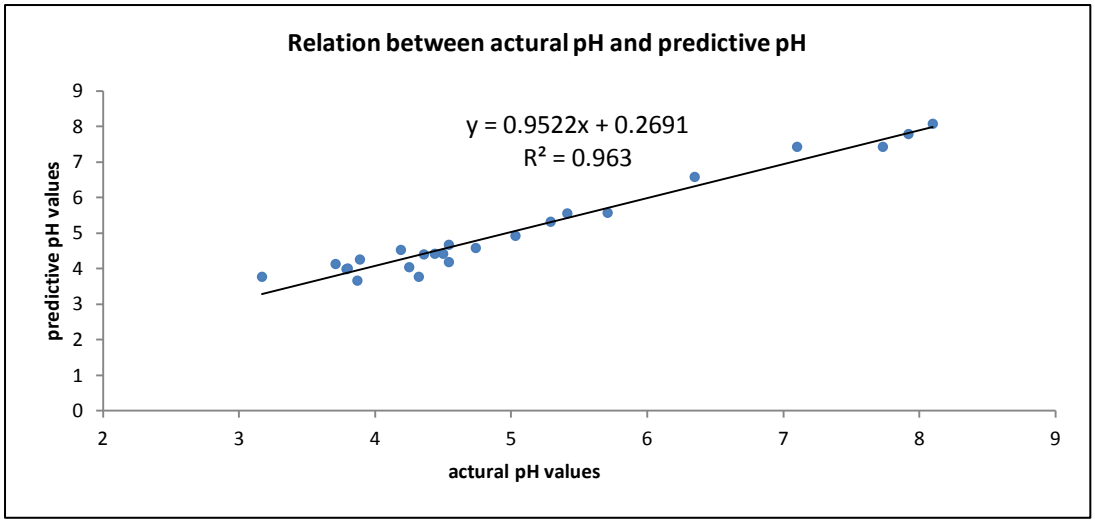

Figure 7.2: Scatter plots of the relation between actual pH and predicted pH.

7.5.1.3 Final regression coefficient output

The final coefficient of determination plot (Figure 7.3), which was reduced from 128 to 50 bands, showed significant troughs, which negatively influenced increases in pH value, including the bands from 0.457 to 0.5 µm, 1.123 µm, 1.292 to 1.462 µm, 2.247 µm and 2.463 µm. Among these, the bands in the range of 0.457-0.5 µm were likely to be related to the strong absorption edge which occurred between 0.4 and 0.6 µm caused by paired excitations between magnetically coupled ferric cations (Sherman & Waite 1985). This feature was present in ferric iron-bearing minerals, such as copiapite, jarosite, schwertmannite and goethite, which are commonly found in acid

conditions (Crowley et al., 2003). The absorption bands occurring in the range of 1.292 to 1.462 μm appeared to be related to the absorption feature of jarosite, which occurred in the 1.3 to 1.5 μm region and was centred at 1.404 to 1.448 μm due to OH. The feature at 2.247 μm was very likely related to the strong diagnostic absorption feature of jarosite near 2.265 μm and less strong absorption feature at 2.212 μm, with both bands related to the sulphate or OH combination and overtone bands. The point at 2.463 μm is related to another absorption feature of jarosite at 2.463 μm; but the less strong point of 1.123 μm is very possibly related to the absorption feature of copiapite near 1.123 μm. However, because copiapite was not as widespread as jarosite in the study area, it was likely to influence the pH of soil less than jarosite.

The reason why pH values are negatively related to the diagnostic absorptions of jarosite and copiapite is explained by these two minerals usually forming in low pH conditions (Bigham, 1994; Anderson, 1994). Jarosite forms when pH is less than 2.8, while copiapite forms at even lower pH, that is, below 1.5 (Bigham, 1994; Anderson, 1994).

There also existed significant peaks in the FRC plot which positively influenced the increases in pH value, including a peak at 0.678 μm, which was likely related to the absorption feature of goethite near 0.67 μm, a peak near 0.96 μm which was likely related to the superimposition of the absorption feature of ferrihydrite near 1.03 μm and the absorption of goethite at 0.94 μm, and a peak at 2.333 μm which was likely related to the absorption feature of carbonate near 2.333 μm. The feature at 1.663 μm was difficult to link to the diagnostic absorption features of the minerals known to occur in the field area. This feature could be associated with the absorption feature related to the combination of OH or S-O bending overtones of sulphate group minerals near 1.7 μm.

The reason why the pH values were positively related to goethite, ferrihydrite and carbonate could also be interpreted from the FRC. Ferrihydrite usually forms in neutral pH conditions when the pH is above 5, and the average pH value acquired from the study site samples was 6.7. Goethite can form and persist in a wide range of pH conditions, but the average pH of samples containing goethite in the study area

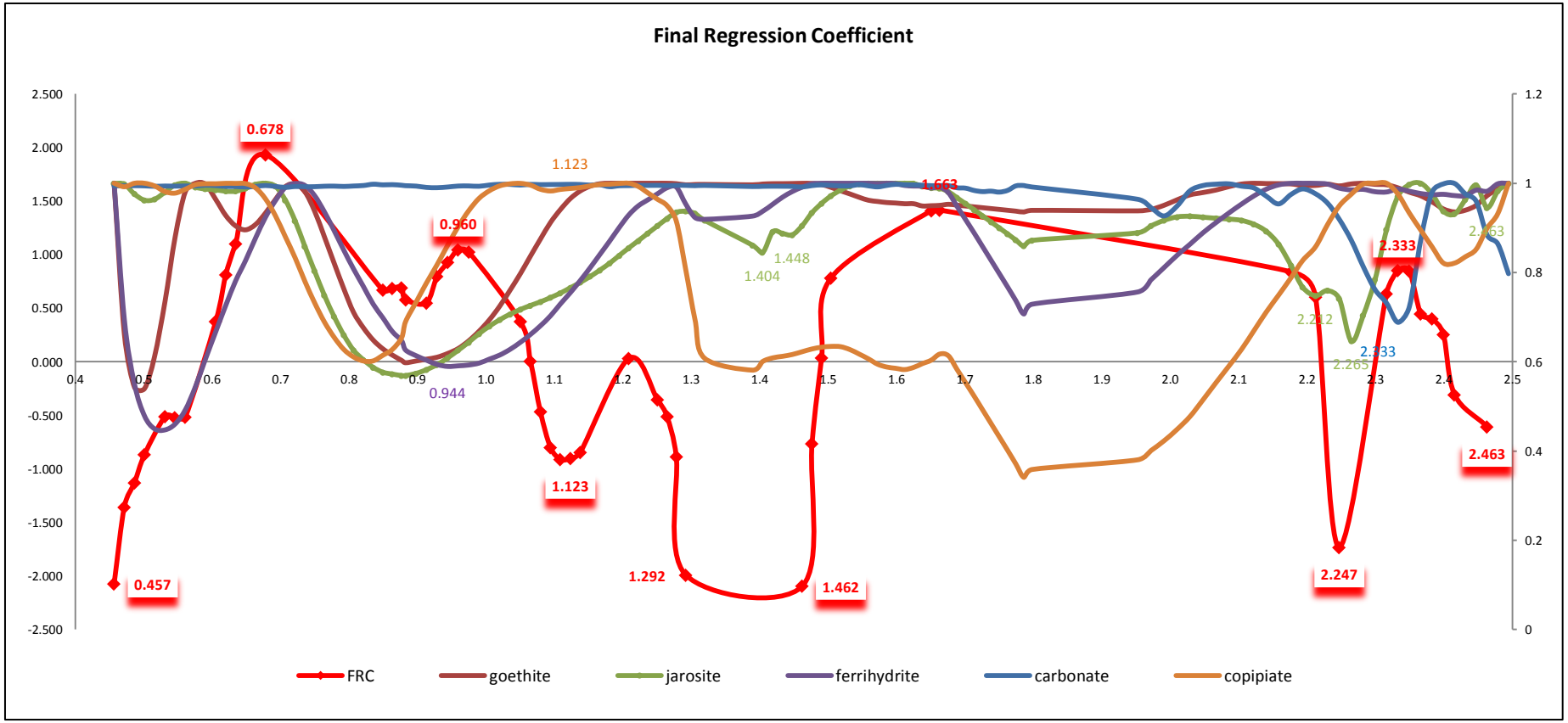

Figure 7.3: Final regression coefficient compared to continuum-removed spectra of related ASS minerals; the X axis is the spectral wavelength in micrometers, Y axis on the left is the FRC; Y axis on the right is the reflectance response for the mineral.

was 6. Therefore, both ferrihydrite and goethite are indicators of neutral pH, and jarosite and copiapite are indicators of acidic pH. The presence of carbonate minerals positively impacts the pH due to their ability to act as a buffer to the acidity produced by the oxidation of pyrite, thereby increasing the pH values of soils and waters (Blowes et al., 2003).

7.5.1.4 Applying the PLSR model to map pH distribution

The PLSR model established from the pH values and reflectance spectral measurements in the laboratory were applied to the HyMap imagery. The output of the model was a formula containing the result of the reflectance response of the chosen bands, multiplied by the final regression coefficients of corresponding bands, plus the residual. The resulting greyscale image, with pixel values reflecting soil pH predicted values within the pixel, was subjected to thresholds to extract pixels reflecting a pH range in a region of interest (ROI). In order to conveniently compare the results deduced from the indicative minerals, the pHs were classified into some ranges which indicative minerals usually suggest. The pH ranges distinguished were: (1) less than 2.8 (<=2.8); (2) 2.8-4.5 (>2.8 and <=4.5); (3) 4.5-6 (>4.5 and <=6); (4) 6-7 (>6 and <=7) and (5) 7-8 (>7 and <8). The pH classification image is illustrated in Figure 7.4.

The pH classification of the acidity map showed specific natural and constructed local landform elements (as shown in Figure 7.4 and Figure 7.5) to have acidic pH. The semi-dried wetlands and constructed drains and the surface of the exposed stockpiled dredge spoils were the regions represented by the lowest pH values (red and yellow colours). Fieldwork to validate these results found that all these geomorphic sites displayed visual signs of acid conditions and their acid nature was confirmed by several surface soil measurements. The seasonal nature of the surface conditions should be considered when interpreting the spatial extent of acid conditions. Although the exposed dredge material displayed a similar surface reflectance throughout most of the year because it was not flooded and therefore rarely underwater, the drains and wetlands were flooded during the winter months and gradually dried out to varying degrees during the summer months.

Accordingly, the distribution of the surface expression of the acid conditions in the wetlands and drains will be dependent on seasonal conditions.

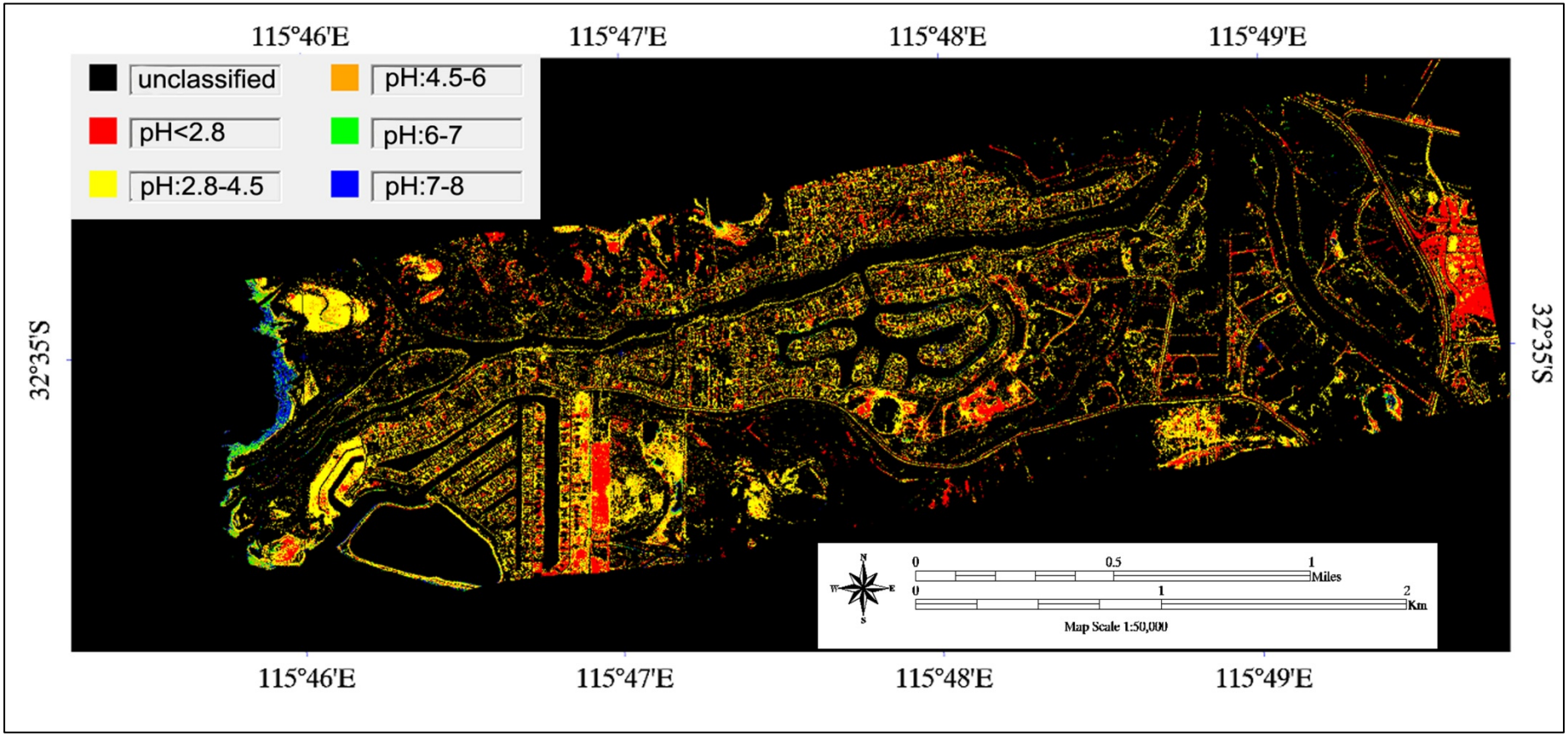

Figure 7.4: PLSR pH classification map of acidity deduced from applying the PLSR model to the HyMap data.

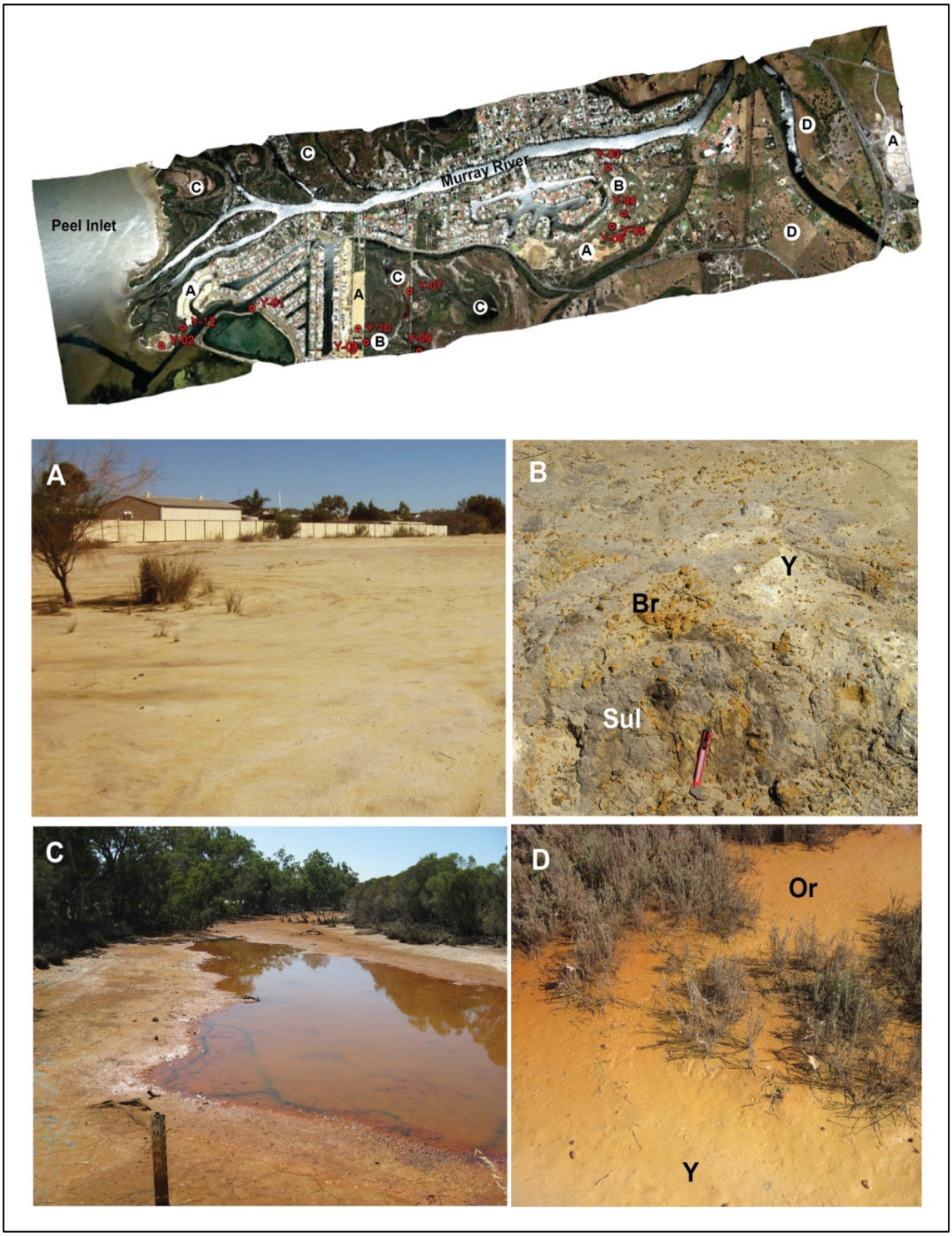

Figure 7.5: Surface images of the main landforms that display surface acid conditions – A. Oxidised dredged spoil material showing yellow (jarosite/goethite) and grey surface with urban development in the background; B. Close-up of the surface of the dredged spoil showing yellow mottles (Y), brown mottles and nodules (Br) and dark grey clay-sand material (Sul) which is the original oxidised sulphidic material from the inlet; C. Semi-dried surface of a constructed drain showing orange to reddish surface coatings and flocs in the water; D. A dried wetland surface showing yellow (jarosite) and orange (schwertmannite) flocs with the halophyte vegetation.

7.5.2 Soil acidity deduced from iron-bearing mineral mapping

7.5.2.1 Iron-bearing minerals mapping

7.5.2.1.1 Selection of end-members

Eight spectral end-members of the main indicative iron-bearing minerals were selected for mineral mapping, namely, jarosite, copiapite, goethite, ferrihydrite, schwertmannite, hematite, jarosite + goethite and jarosite + ferrihydrite. The former six were from the USGS Spectral Library (Clark et al., 2007), and the latter two were from spectral measurements of samples from the study area, with their mineral composition verified by XRD. The spectral features described above are shown in Figure 7.6.

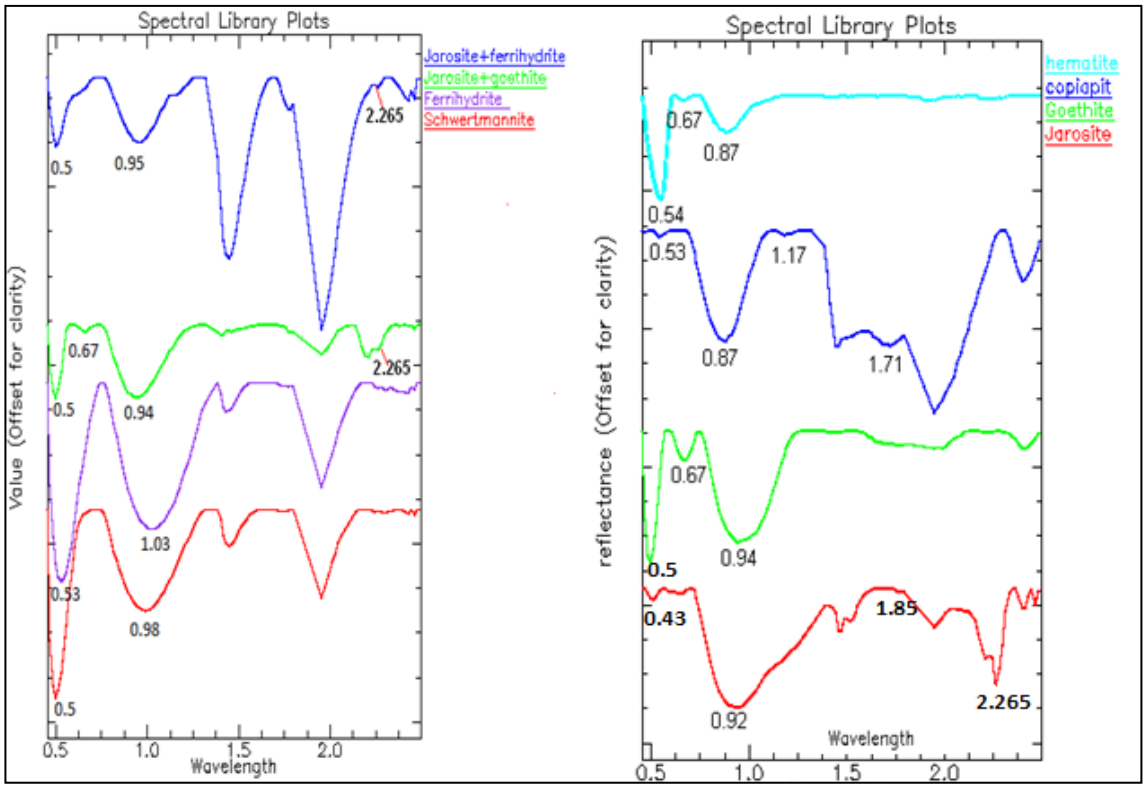

Figure 7.6: Spectral characteristic of the end-members of iron-bearing minerals resampled to HyMap wavelengths (all spectra have had their continuum removed).

7.5.2.1.2 Mapping and classification of indicative iron secondary minerals

Different mapping methods were used to map different iron-bearing mineral species. Hematite, goethite and jarosite have some distinguished absorption features, thus the spectral indices method was applied for these minerals using the relative depth of the corresponding absorption, focusing on the absorption near 0.87, 0.94 and 2.265 μm, respectively.

The abundance of other end-members was mapped using multi-spectral feature fitting (MSFF) which is one kind of spectral feature fitting (SFF) method (Clark et al., 1990; 1991) which allows the user to define specific wavelength ranges with optional weights to emphasise the importance of certain features. The matching operation for ferrihydrite was focused on the spectral regions near 0.53 μm and 1.03 μm, for schwertmannite the spectral ranges were focused on the regions near 0.53 μm and 0.98 μm, and for copiapite the spectral ranges were focused on the regions near 1.17 and 1.71 μm. Meanwhile, for the end-members of the mineral assemblages of jarosite + goethite and jarosite + ferrihydrite, common SFF was used to compare the whole spectral shape and features of the end-members to those of the HyMap pixels.

For each method, matching scores and matching errors were produced for each end-member, and then 2-D scatter plots were used to produce regions of interest by grouping pixels which had high matching scores but low matching error values. Then the regions of interest extracted for each end-member were regarded as training data and were put into classifications using the "image classification from ROI" function which is a kind of supervised classifier in ENVI 4.7 software. The mineral classification result using the HyMap imagery is shown in Figure 7.7.

7.5.2.2 Soil acidity map deducted from HyMap mineral classification map

The relationships between the pH values and indicative minerals are summarised in Table 7.2. The average pH values of soil consisting of different mineral species or mineral assemblages were consistent with the findings in previous studies (Bigham, 1994; Swayze et al., 2000; Crowley et al.,2003; Montero et al., 2005). Using the link between the presence of minerals and their formative pH values reported in previous studies and the results from the samples investigated in this study (Table 7.2), various ranges of pH values for each indicative mineral or mineral assembly were adopted to produce the HyMap soil acidity map (Figure 7.8). During the process of making the HyMap soil acidity map, the pH range of <1.5 and the range of 1.5-2.8 were merged into <2.8, and the range of 2.8-4.5 and range of 2.9-4.5 were merged into 2.8-4.5 (Table 7.2). The resultant HyMap soil acidity map (Figure 7.8) was deduced from the indicative minerals identified in the HyMap mineral classification map derived from mineralogy (shown in Figure 7.7) by utilising the link between the minerals and the pH values shown in Table 7.2.

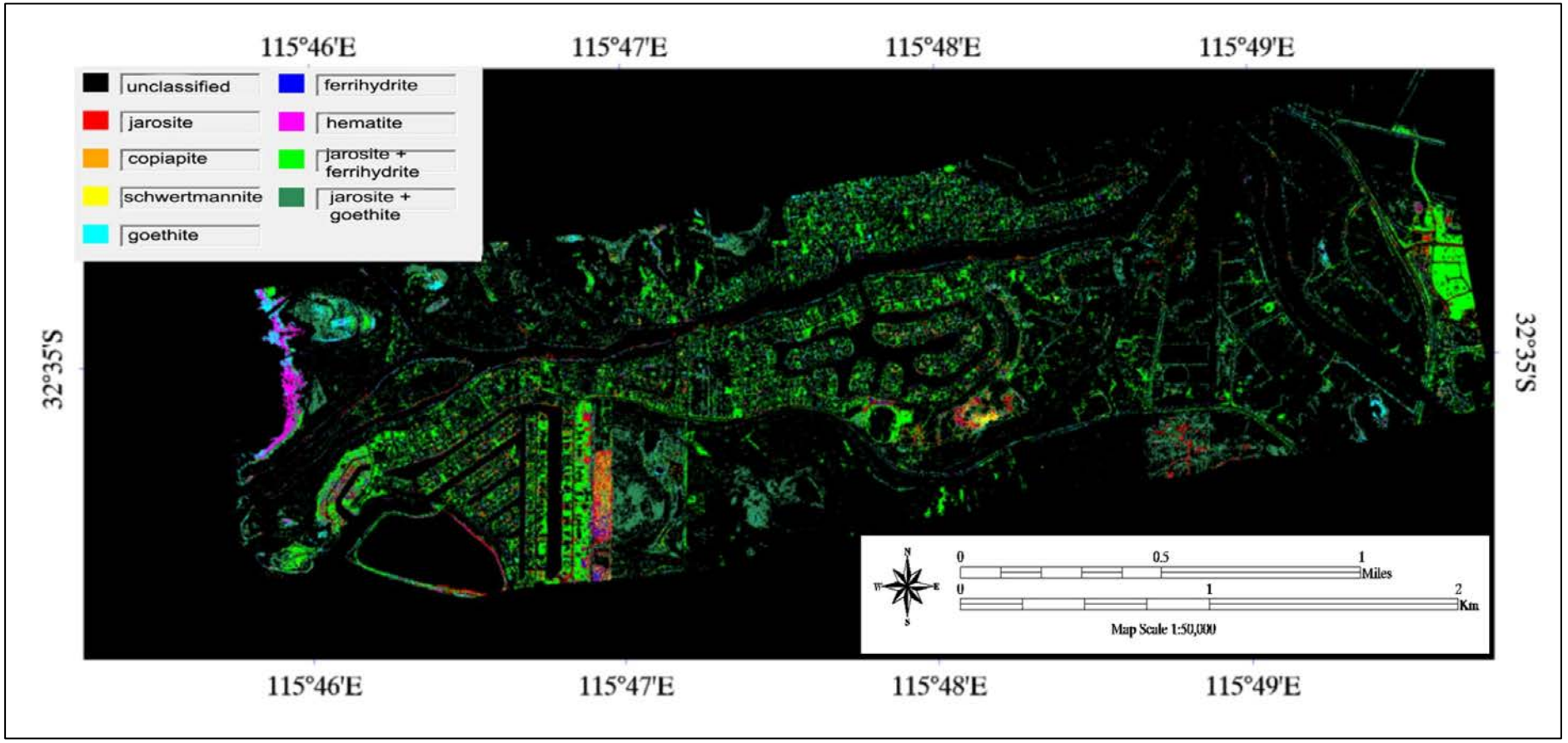

Figure 7.7: HyMap mineral classification map of the main iron-bearing minerals related to ASS.

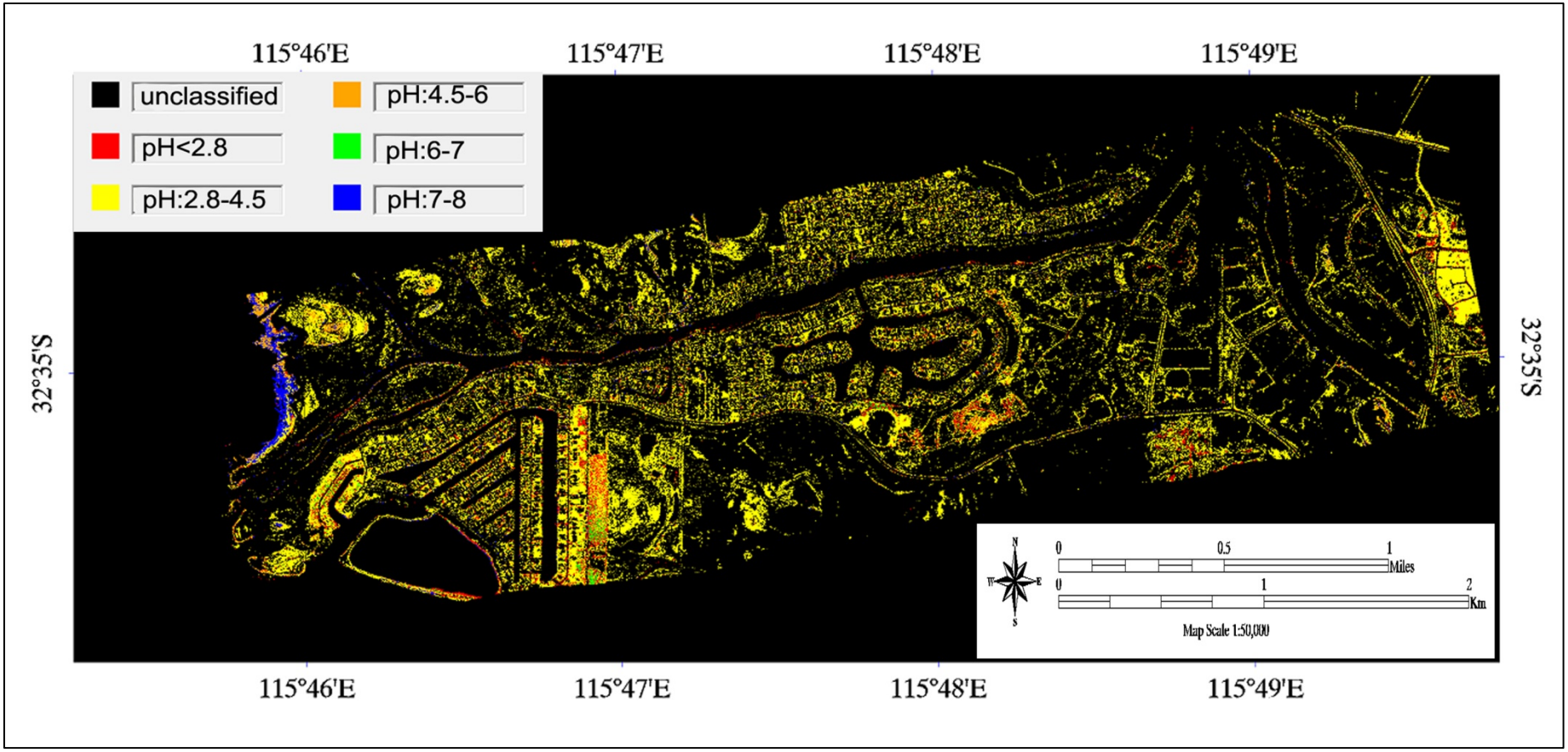

Figure 7.8: HyMap soil acidity map derived from mineralogy deduced from the distribution of indicative minerals listed in Figure 7.7.

Table 7.2: Relationship between indicative minerals and pH values

Minerals identified from samples	Number of samples for each mineral(s)	Average pH in this study for specific mineral	pH as reported in previous studies	Reference	pH range adopted in this paper
Copiapite			<1.5	Montero et al., 2005	<1.5
Jarosite			<2.8	Crowley et al.,2003; Murad & Rojiak, 2005	1.5-2.8
Schwertmannite	4	3.30	2.8-4.5 or 2.8 – 5.5	Crowley et al.,2003; Murad & Rojiak, 2005	2.8-4.5
Ferrihydrite	6	6.7	>5	Montero et al., 2005; Murad & Rojiak, 2005	6-7
Goethite	4	5.08	2.5 – 7.5	Bigham,1994; Murad & Rojiak, 2005	4.5-6
Jarosite + ferrihydrite	8	4.26			2.9-4.5
Jarosite + goethite	6	4.28	2.9-3.5	Swayze et al., 2000	
Hematite	2	5	7-8	Bigham, 1994	7-8
Other iron minerals	10	5.05			

7.5.3 Comparison of two resultant acidity maps

In this research, two acidity maps were produced using different methods. One used PLSR to predict pH from a model derived from field samples (Figure 7.4), while the other used mineralogy as an indicator of pH (Figure 7.8). Both Figure 7.4 and Figure 7.8 have the same colour classification system to represent the pH ranges. A comparison of the colour distributions between both the figures showed the pH classifications deduced from the PLSR model (Figure 7.4) and from the indicative minerals (Figure 7.8) were very similar. Both of the images were dominated by yellow and red colours in the same areas, which suggested that the soil pH in a large part of the study area, that had its surface exposed and not covered by urbanisation, was below 4.5. A subtraction operation between the two classification images was conducted to highlight the differences in each pixel between the two resultant classification images. The resulting image is shown in Figure 7.9. The red coloured pixels suggested no difference existed between the two classification images (dif=0), the green coloured pixels suggested one grade difference existed between the two classification images (dif=1), while the other colours suggested the corresponding

pixels had more than one grade of difference between the two classification images. Each grade difference between the two classification images was less than 1.7 pH units. The red coloured pixels accounted for 59% of the total classified pixels, the green coloured pixels accounted for 34.7%, and the pixels with other colours accounted for a negligible percentage, among which pixels with a difference of two grades (dif=2) accounted for 2%, pixels with a difference of three grades (dif=3) accounted for 1.4%, and pixels with a difference of more than 3 grades (dif=4 and dif=5) accounted 2.7%. This comparison of the two pH classification images suggested each image was being generated independently of the other, using different criteria. This confirmed that nearly 94% of the classified pixels had the same or similar pH values in both the images.

This high percentage of agreement between the two independently derived images provided support to the interpretation that the pH distribution interpreted from HyMap data correctly represented the ground data. Although the two resultant acidity maps were close, the acidity map deduced from the PLSR model appeared to be a better representation of the soil pH than the map deduced from the indicative minerals. The main reasons for this were: 1) the complexity of soil mineral compositions, so that several mineral species may have aggregated in a small area or even mixed together; and 2) the relationship between the pH values and iron and sulphate-bearing mineral species not being strictly defined – for example, although jarosite is restricted to pH <3, goethite appears to form and persist in a wide range of pH from 3-8, and schwertmannite between 3-6 (Rojiak and Murad, 2005). Therefore, the HyMap soil acidity map derived from mineralogy was semi-quantitative rather than quantitative. It should be mentioned that that PLSR model is just an empirical model and its availability is limited to the specific area. Although it can deduce more accurate results, the method of mapping using indicative minerals has been proven by numerous studies to be transferable to other areas and thus can be used elsewhere without the need for a prior knowledge, such as creating a PLSR model.

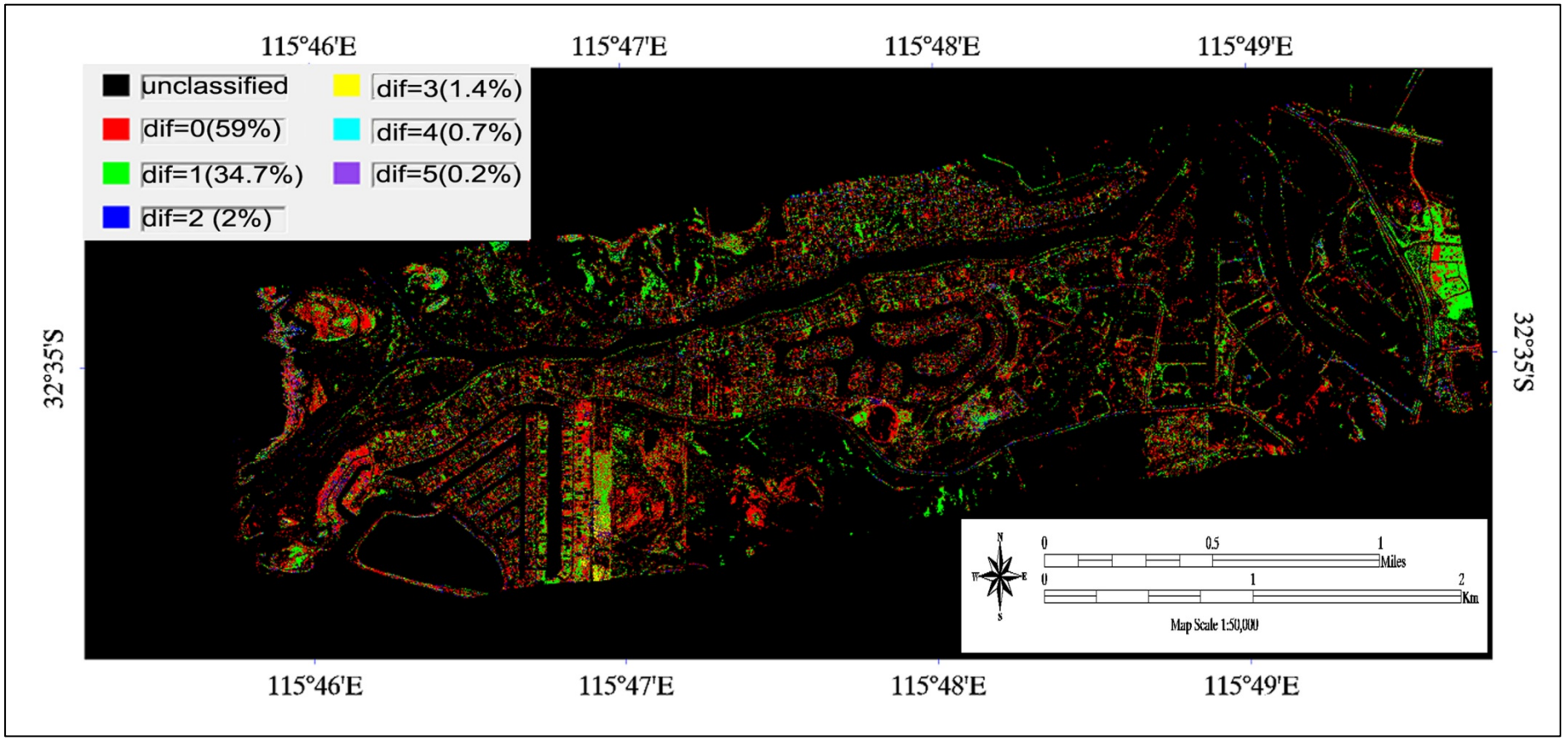

Figure 7.9: Differences in pH between the HyMap soil acidity map derived from mineralogy and the PLSR pH classification map of acidity (The proportion of each difference grade is shown in brackets).

7.5.3 Comparison of the predicted pH values deduced from the PLS model with the ground truth

During the process of model building, the relationship between the actual measured pH values and the predicted pH values was cross-verified to prove the robustness of the model, and the verification was confined to a limited training dataset. The effectiveness of the model applied to the HyMap data was tested by comparing the pH measurements of the soil samples to the values of the pixels in the resultant pH classification images deduced from the PLSR model that had the same location as the sample sites. Samples from eight different sites were selected and their pH data were compared to the corresponding pixel locations in the classified images deduced from the PLSR model (the PLSR pH classification map of acidity in Figure 7.4). The results of the comparison are listed in Table 7.3. The results varied from between 0.6 and 1 (perfect match), with an average confirmation of 0.67. The differences in the pH, as measured from the ground samples against those interpreted from the pH classification image deduced from the PLSR model, were likely due to the differences in the temporal aspects of the data collection for the two datasets. The HyMap data were acquired in December 2005, while the pH measurements were conducted in February 2012. Many of the sites chosen were from geomorphic locations, such as wetlands and constructed drains, which showed surface acid conditions expressed as indicative minerals or spectrally relating to their saturation state. Drying of the ASS caused the oxidation of near-surface sulphidic materials, which in turn generated acid, and therefore the local events of seasonal drying would have varied over the years.

7.6 Conclusion

This chapter presented the mapping of the soil surface pH values via two different methods using a HyMap dataset in a coastal area affected by ASS. The acidity map deduced from the distribution of the indicative minerals showed that jarosite, or a mixture of jarosite and another iron oxide/oxyhydroxide or iron oxysulphate (like schwertmannite), strongly indicated the presence of low pH surface conditions in the study area, while goethite and ferrihydrite appeared as indicators of higher soil pH conditions (closer to neutral). The acidity map deduced from the PLSR model (as pH ranges) produced using the HyMap imagery was consistent with the final regression

coefficients in the PLSR model derived from the laboratory spectral and pH measurements, which showed high negative coefficients for the wavelengths related to the absorption features of jarosite, which usually forms in low pH conditions, while also showing high positive coefficients for the wavelengths related to the absorption features of ferrihydrite and goethite, which usually form at higher pH conditions (goethite forms across a wide range of pH). The relationship between higher pH and the absorption of carbonates in the PLSR model was not reflected in the soil acidity map deduced from the indicative iron-bearing minerals. This was because the indicative mineral map only focused on iron-bearing minerals and neglected the buffering capability of carbonate minerals. This result indicated that the PLSR modelling method was useful for identifying what components of minerals were contributing to the FRC. Approximately 94% of the pixels in the pH classification maps deduced from the two different methods were found to be highly similar. This result allowed us to draw the following conclusions:

- The PLSR model established in this study was robust and suitable for predicting the soil surface acidity arising in response to ASS in the study area. Furthermore, the explanation of the FRC was reasonable; thus, this empirical predictive model could potentially be used in other coastal and inland areas affected by ASS.
- The relationships between indicative iron oxide/oxyhydroxide and iron sulphate-bearing minerals and pH values were reliable, but semi-quantitative, and could be applied to estimate the soil acidity conditions in the ASS.
- The highly similar pH mapping results deduced by the different methods, including the identification of low pH conditions across landforms that displayed severe surface acid conditions seasonally, suggested that the soil pH distribution was accurately mapped using the HyMap imagery.

Table 7.3: Result of the comparison between measured pH and predicted pH values deduced from the PLSR model

Site	Average pH of samples	Total numbers of samples measured for each site	Number of samples within the range of the predicted image of PLS	Ratio of measured to predicted
Y-002	4.588	5	3	0.60
Y-003	5.23	1	1	1.00
Y-004	3.9675	4	3	0.75
Y-005	3.95	6	4	0.67
Y-007	5.08	19	12	0.63
Y-008	5.37	13	10	0.77
Y-010	5.58	1	1	1.00
Y-011	5.39	5	3	0.60
		54	36	0.67

Chapter 8 Mapping of Non-Iron bearing minerals and the potential for Aluminium Toxicity

8.1 Introduction

In Chapter 7, the mapping of the distribution of the secondary iron-bearing minerals produced during the formation and evolution of AAS was presented, and the link between indicative minerals and pH to derive a soil pH map was demonstrated. The negative effects of ASS are not merely because of the direct effects of acidification, but also because of the release of trace metals, such as Al, As, Cr, Cu and Zn, due to the dissolution of carbonate and silicate soil minerals and due to the increase in solubility of cationic metals bound to soil organic matter at low pH (Nordstrom and Alpers, 1999; Bigham et al., 2000). These metals either remain as dissolved constituents in soil pore waters, wetlands and drains or form secondary soluble minerals such as salts due to evaporation. The presence of dissolved Al and Al as flocs enhances the toxicity of the soils and waters, especially causing toxicity to a range of aquatic fish and benthic organisms (Sparling et al., 1997; Ljung et al., 2009). In chapter 4 high concentrations of Al^{3+} released were observed during the oxidation of sulphidic material that was collected from the study area. The results of chapter 6 found widespread presence of aluminium-bearing minerals, such as kaolinite and microcline, in the study area. Furthermore, the surface pH maps derived from hyperspectral imagery and confirmed with ground data found large areas with low pH conditions. A combination of the presence of alumina-silicates in the soils and low pH conditions can result in the release of Al into solution as confirmed by reaction of kaolinite and feldspars with acidic solutions in laboratory experiments (Carroll and Walther, 1990; chapter 4). Accordingly, there is a potential Al toxicity risk in the study area. Thus, it is necessary to map the distribution of the surrounding minerals and the corresponding products of the reaction between the acidic environment and the surrounding minerals.

The sulphuric acid produced by oxidising ASS reacts with the surrounding minerals, mainly the carbonates and silicates, resulting in the dissolution of the soil minerals, the formation of new minerals and the buffering of acidity. The acid reacts with the carbonates present in the soil such as calcite, dolomite and siderite, resulting in acid neutralisation and the potential formation of gypsum. In addition, the gypsum

produced is capable of swelling due to its combination with water which makes the volume greater than the raw material, and this swelling could damage infrastructure built on these soils (Sammut et al., 2000). Therefore, the acid buffering ability of carbonates and the swelling capability of gypsum make it necessary to map these minerals.

More importantly, aluminosilicate minerals present in soils, such as the kaolin group of minerals, and Al hydroxyl, such as gibbsite, also participate in the acid neutralisation process (buffering) and would result in release of Al ions. Both these mineral groups, upon reaction with acid solutions, consume H^+ and release Al^{3+} (Blowes et al., 2003*)*, and result in the formation of secondary Al-bearing sulphates under different pH conditions. For instance, gibbsite forms in the primitive state of aluminosilicate neutralisation in near neutral conditions (Bigham and Nordstrom, 2000) and dissolves by reacting with sulphuric acid when pH further decreases in the range of 5-4. When pH drops to below 4, soluble Al sulphates, such as halotrichite, pickeringite and alunogen may form (Bigham and Nordstrom, 2000). The depletion of pyrite from the ASS results in the reduction of acidity production, eventually this will become lower than the buffering capability of the soils and will result in the formation of insoluble hydroxysulphates such as alunite and basaluminite when pH increases to 5 (Bigham and Nordstrom, 2000), on the condition that sufficient neutralising minerals are present. At a mine site, Kim et al. (2003) found that Al sulphate was precipitated in the pH range of 4.45 to 5.95, and Al ions were mostly removed from the mining drainage when pH >5. Similar to the presence of iron-bearing secondary minerals, Al-bearing minerals can also be regarded as indicators of pH conditions and various concentrations of Al^{3+}.

The bulk mineralogy of the soil samples from the study area indicated the widespread distribution of kaolinite, gibbsite and microcline, as well as minor amounts of berlinite and soluble Al sulphates (e.g., tamarugite) (Table 6.2 in Chapter 6). Therefore, it was possible to map the occurrence of these minerals using hyperspectral data, provided the minerals have diagnostic features. Due to the lack of distinct spectral features of berlinite, tamarugite,potassium alum and microcline, it was not possible at the time of this study to map them using the commercially available sensors. Therefore, it was only possible to map the kaolin group of minerals and gibbsite as the main sources of Al in this study.

The research steps reported in this chapter aimed to: (1) map the distribution of the main non-iron bearing minerals related to ASS, including carbonates, gypsum, and more importantly, aluminium-bearing minerals such as kaolinite and gibbsite; and (2) based on the distribution of the aluminium-bearing minerals and the soil pH distribution from the results presented in Chapter 7, attempt to map the distribution and severity of potential Al toxicity in the study area.

8.2. Data Acquisition and Pre-Processing

The remotely sensed HyMap imagery and the pre-processing procedures were described in Chapter 7.

8.3 Mapping and Classification of Aluminium-Bearing Minerals, Carbonates and Sulphates

8.3.1 End-member selection

The non-sulphidic soil matrix minerals related to acid sulphate soils mainly include aluminosilicates, Al hydroxides, carbonate and sulphates. The reflectance spectra of these minerals are illustrated in Figure 8.1. The kaolinite, as a representative of the kaolin group has diagnostic doublet absorption arising from the Al-OH overtone which contains a strong absorption near 2.206 μm and a lesser absorption near 2.162 μm. The kaolinite also has triplet water absorption features from 2.3-2.8 μm, including absorptions at 2.312, 2.35 and 2.38 μm. Gypsum, as the representative of

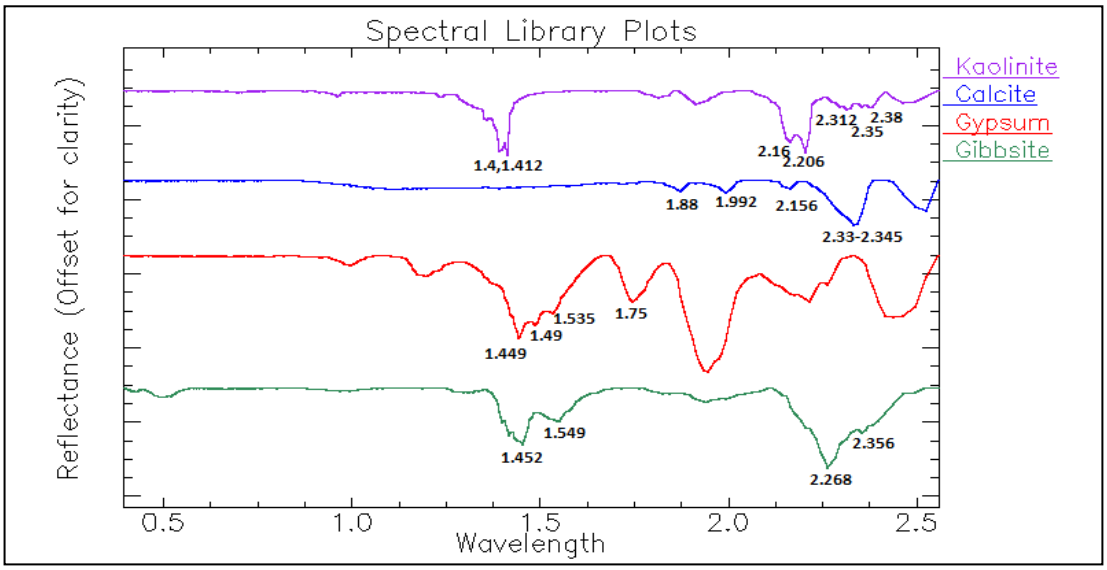

Figure 8.1: Reflectance spectra of the end-members of surrounding minerals related to ASS. From USGS Spectral Library (Clark et al., 2007).

triplet water absorption features near 1.449, 1.49 and 1.535 μm. Calcite, as the representative of carbonate, has a strong and distinctive absorption in the range of 2.33-2.45 μm which could be used to identify the carbonate by using the spectral index method. Gibbsite has a diagnostic absorption feature at 2.268 μm which persisted strongly in mixtures, and a series of diagnostic absorptions near 1.452, 1.521 and 1.549 μm. Comparing the absorption features of the non-iron minerals, it appeared that the spectral features of gibbsite were more complicated than those of the gypsum, kaolin and carbonate, and therefore an advanced SFF mapping method was chosen to map the content of the gibbsite, while the spectral indices method was used to map the content of the gypsum, kaolin and carbonate.

8.3.2 Mapping of aluminium-bearing minerals

8.3.2.1 Al-OH clay minerals

Aluminium hydroxyl (Al-OH) bearning clay minerals contain the kaolin group which includes kaolinite, dickite, nacrite and halloysite, while the white mica group includes paragonite, barmmallite, illite, muscovite, phengite, and the Al smectite group which includes montmorillonite and beidellite. All of these minerals have a common absorption feature near 2.2 μm related to Al-OH absorption. In the study area, kaolinite was the most common and widespread Al-OH clay mineral; thus, it was chosen as the representative end-member. To map the abundance of the Al-OH group clay minerals using the spectral indices method, the continuum of the collected spectra were removed and then the depth of the fourth-order polynomial was fitted between 2.12 and 2.245 μm. Using the 2.12-2.24 range to map kaolinite was appropriate because negligible amounts of micas were identified via XRD in the soils of the area, and therefore mica absorption peaks would not interfere in the selected wavelength range. The resulting kaolinite distribution map is shown in Figure 8.2. The map showed high kaolinite occurrence on the surfaces of the oxidised dredge spoils and negligible presence in the wetlands.

8.3.2.2 Gibbsite

Gibbsite has a strong absorption feature at 2.268 μm which is close to the absorption of jarosite at 2.265 μm, thus making it unsuitable to be identified and mapped via the spectral indices method. Gibbsite also has two less strong absorptions at 1.452 and 1.521 μm; this made it possible to use the multi-spectral feature fitting method to

map the gibbsite. Therefore, three spectral ranges were defined near 2.268, 1.452 and 1.521 μm, and the spectral feature fitting operation was focused on these wavelength ranges. The map produced using the SFF method using the three absorption features for gibbsite is shown in Figure 8.3. The map showed that the coastal ridges along the west appeared to be dominated by gibbsite. Surprisingly, gibbsite appeared negligible on the oxidised dredged materials. Prior to the mapping result being proved by the ground truth, it appeared that the distribution of the gibbsite was consistent with the pH conditions of its locations which had pH in the range of 7-8 (Figure 8.7).

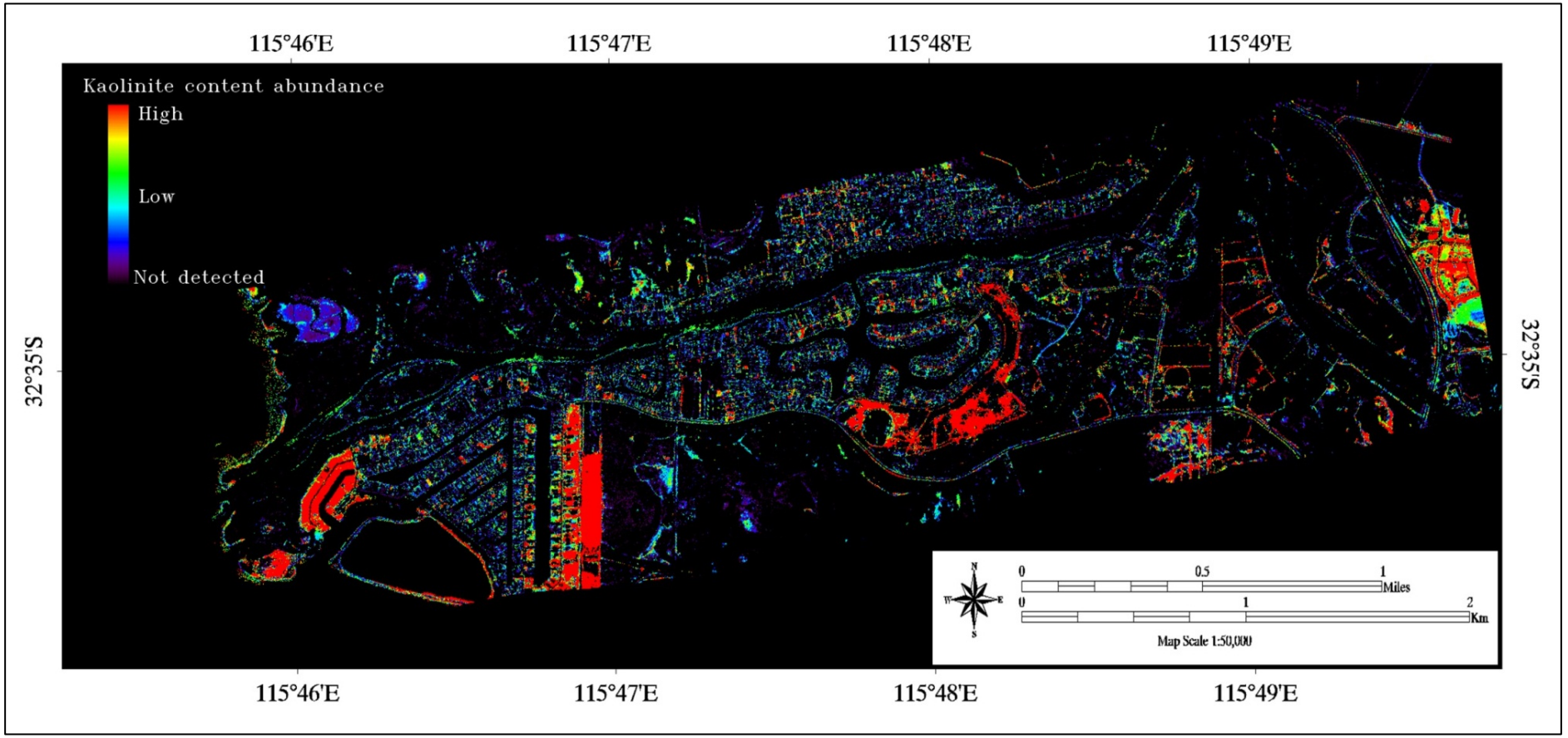

Figure 8.2: Kaolin mineral distribution map using the spectral indices method at 2.2µm.

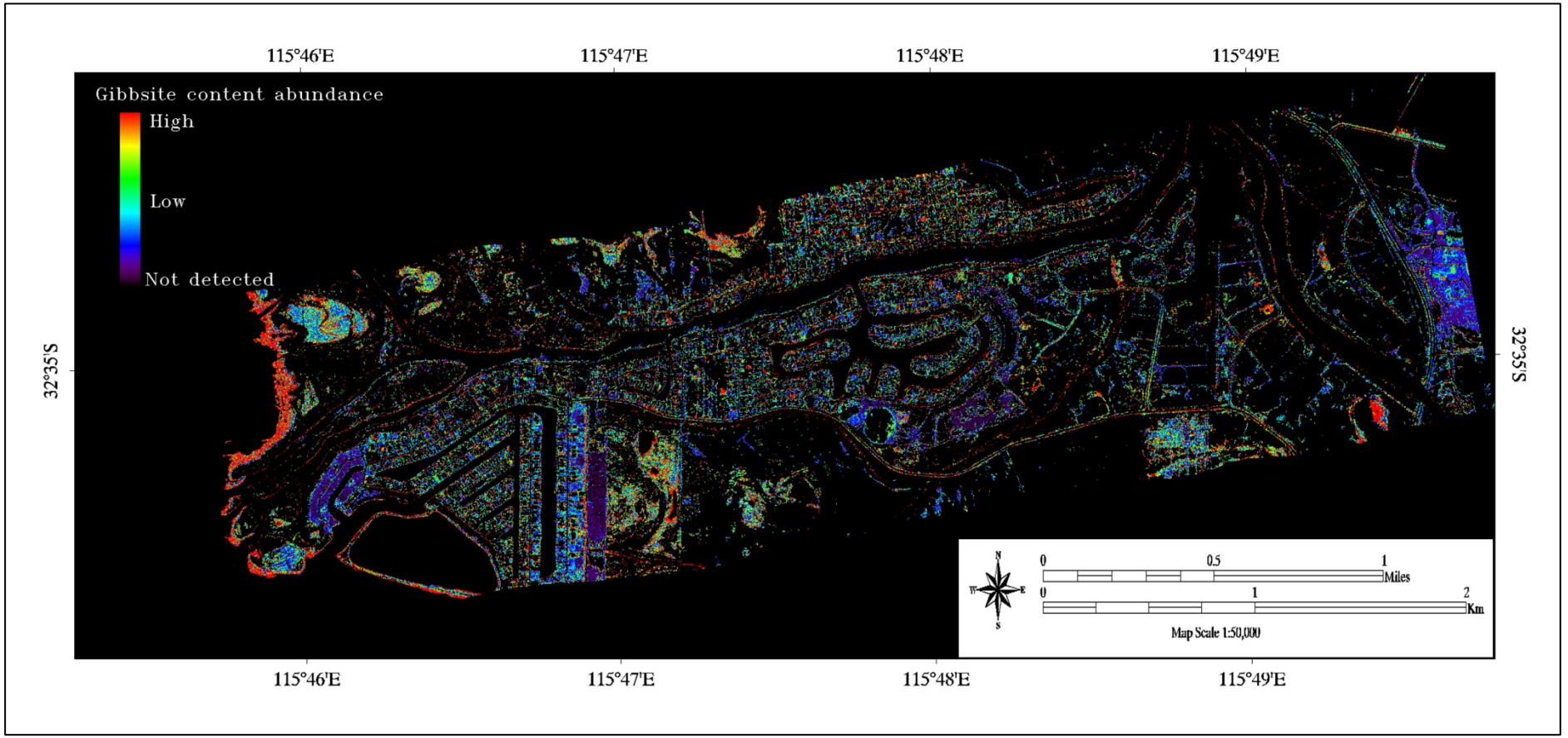

Figure 8.3: Gibbsite mineral distribution map produced using the SFF method focusing on three wavelength regions.

8.3.3 Carbonates map

Carbonates, including calcite, dolomite and siderite, have a common spectral feature near 2.33 μm. Calcite was selected as a representative end-member of carbonate. The continuum-removed depth of the fourth-order polynomial fitted between 2.25 and 2.36 μm was used to map the content of carbonate using the spectral indices method. The resulting map produced using the spectral indices method is shown in Figure 8.4. The map produced using the spectral indices method indicated carbonates to be moderately abundant along the coastal strip to the west, which was likely due to the presence of carbonate shell fragments. Small inland areas of the wetlands also showed the presence of carbonate. Carbonate was also linearly distributed along the lake, creek and river; this was likely due to the use of limestone materials in the artificial project.

8.3.4 Sulphates map

The group of sulphate minerals (excluding jarosite) has a common spectral absorption feature in the range of 1.7-1.8 μm and centred at 1.75 μm (Cloutis et al., 2006). In acid sulphate soil areas, the non-iron-bearing sulphates mainly include gypsum, and thus gypsum was chosen in this study as the representative of sulphates. The relative depth at 1.75 μm was used to map the distribution of gypsum in the study area using the spectral indices method. The sulphate distribution map is shown in Figure 8.5. The map showed gypsum to be dominant along the coastal strip to the west (similar to the gibbsite and carbonates) but also present in some drying wetlands and moderately present on oxidised dredge spoil surfaces (blue areas in Figure 8.5). In comparison to the gibbsite and carbonates, the gypsum was present at low pH sites.

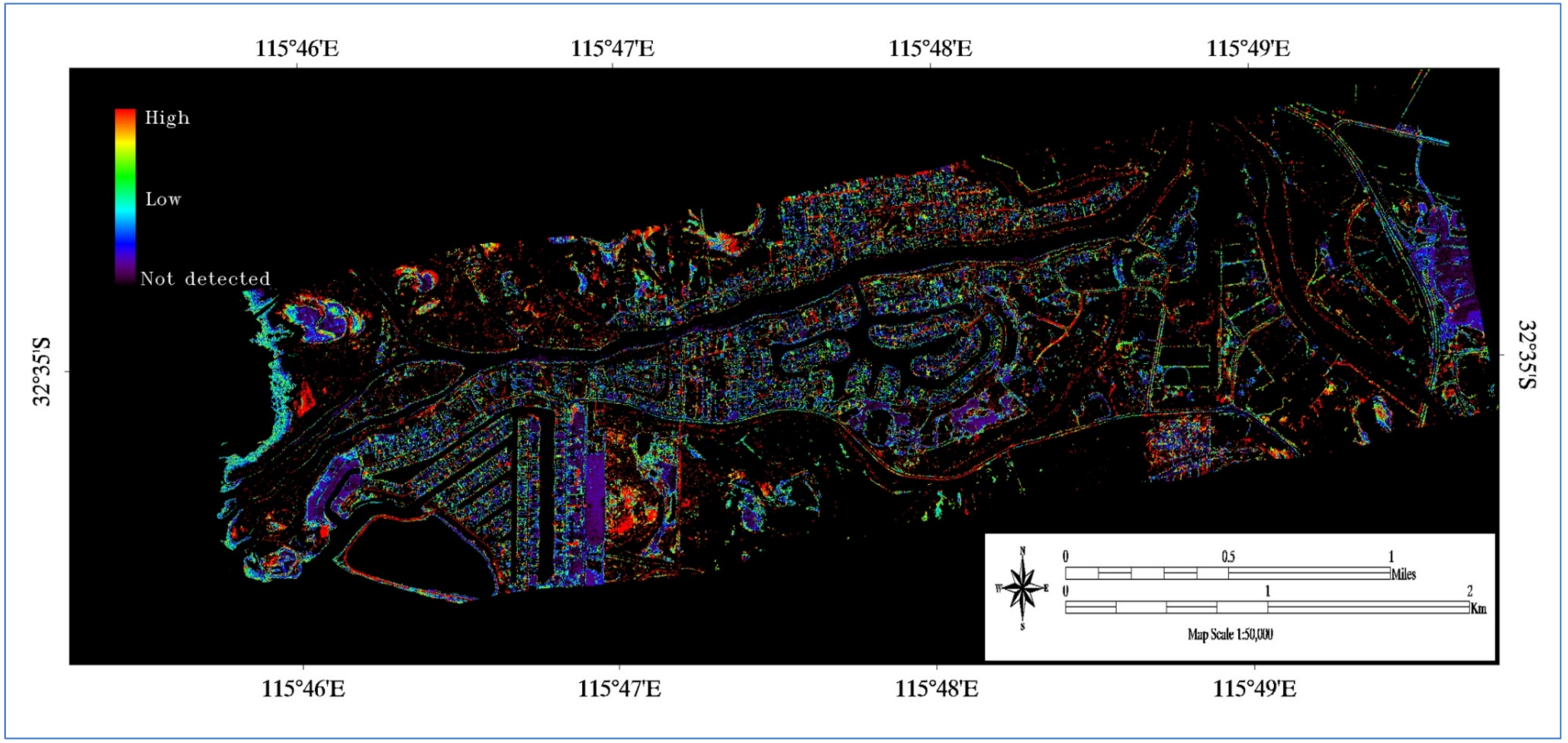

Figure 8.4: Carbonate mineral distribution map produced using the SFF method at 2.33µm.

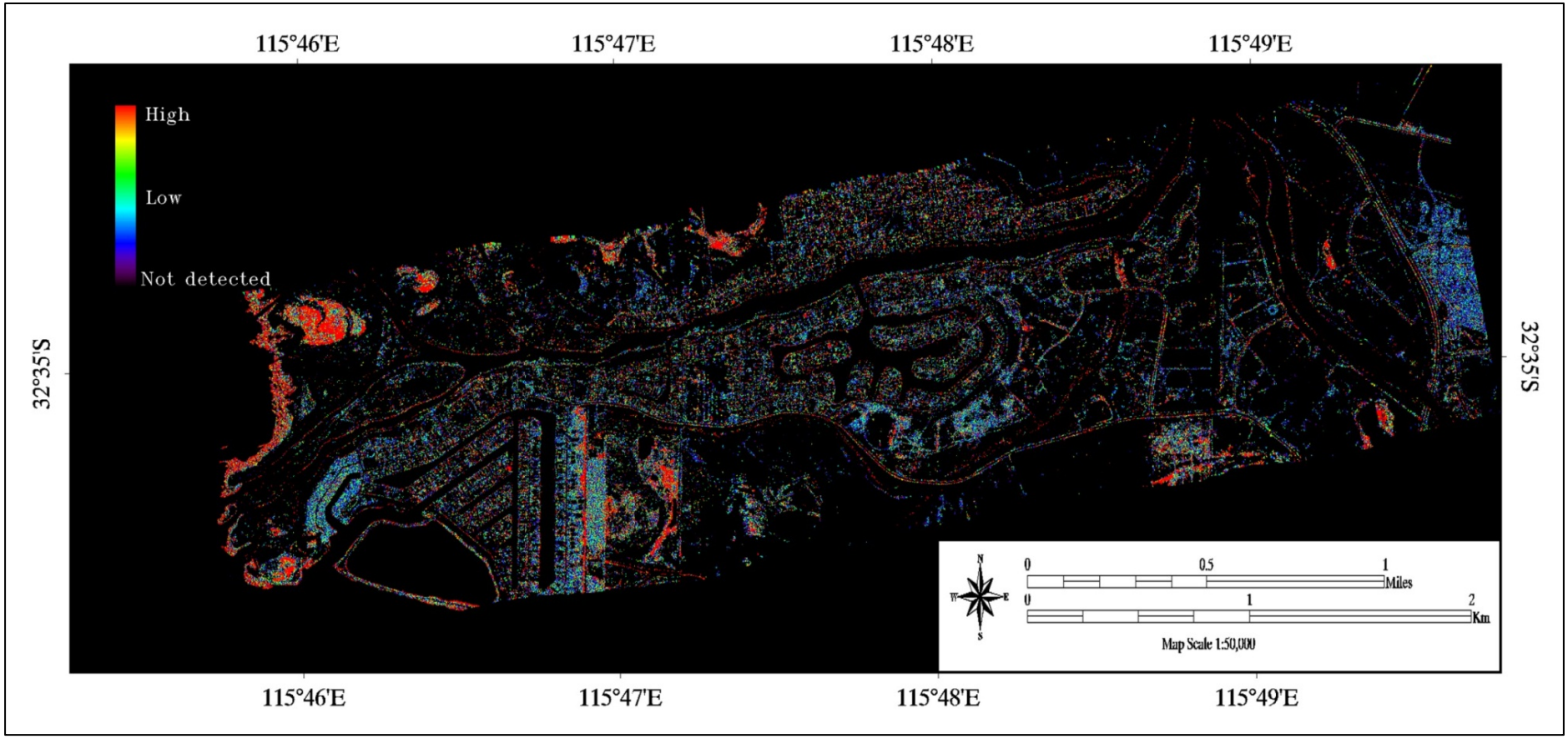

Figure 8.5: Sulphate (mainly gypsum) distribution map using spectral indices method at 1.75 µm.

8.3.5 Main soil matrix mineral classification

After the mapping of each non-iron soil matrix mineral, the 2-D scatter plot was used to extract the POIs (points of interest) for each end-member. Using the 2-D scatter plot, the pixels which had high matching scores and low matching errors were extracted and grouped into POIs for each non-iron-bearing end-member. These grouped pixels representing non-iron-bearing members were then used in the application of a method of image classification from ROIs in the ENVI software. The result of this classification process of the non-iron minerals is shown in Figure 8.6. The results of the classification showed kaolinite to be dominant in the exposed oxidised sulphidic dredge spoils (green areas in Figure 8.6), carbonates to be present in the minor drying wetlands (yellow areas in Figure 8.6) and gibbsite and gypsum to be present along the exposed coastal strip.

8.4 Distribution of Soil pH

Two soil pH maps were produced in the research, as presented in Chapter 7: one was deduced from the indicative iron-bearing minerals, and the other was deduced from the PLSR model. After comparing the resulting pH maps with the ground truth pH data, the pH map from the PLSR model was found to be closer to the ground pH data. Therefore, the pH map derived from the PLSR model was selected to map the Al toxicity (Figure 8.7).

8.5 Aluminium toxicity mapping

Similar to iron-bearing secondary minerals, Al-bearing secondary minerals in the soils also can be regarded as good indicators of different pH ranges and importantly, as indicators of the potential Al toxicity, because the dissolution of these aluminium-bearing minerals will release dissolved Al^{3+} in the pore and surface waters, thereby causing toxicity (Fitzpatrick and Shand, 2008).

Several studies on the dissolution rates of Al silicates and Al hydroxides have indicated a relationship between the solubility of kaolinite and gibbsite versus pH. Laboratory studies using a variety of acids have shown the increasing dissolution of kaolinite with pH <4 as indicated by Al^{3+} release into the reacting solution (Carrol and Walther, 1990; Camaetal, 2002). A relationship between pH and dissolved Al concentrations in over one hundred samples from acidic groundwater in the Yilgarn Craton goldfields, and surface in the lake and drain

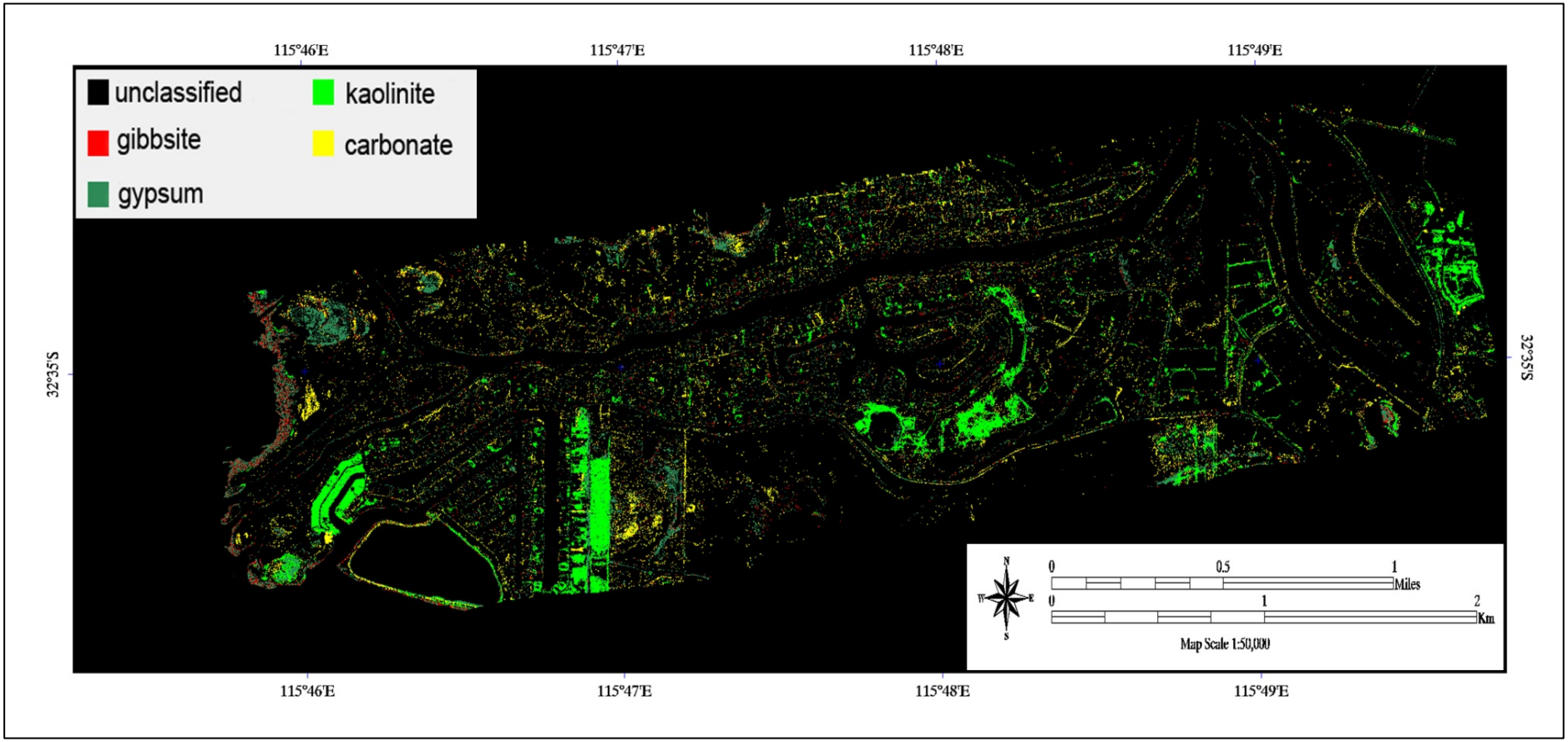

Figure 8.6: Mineral classification result of the main non-iron-bearing soil matrix minerals related to ASS.

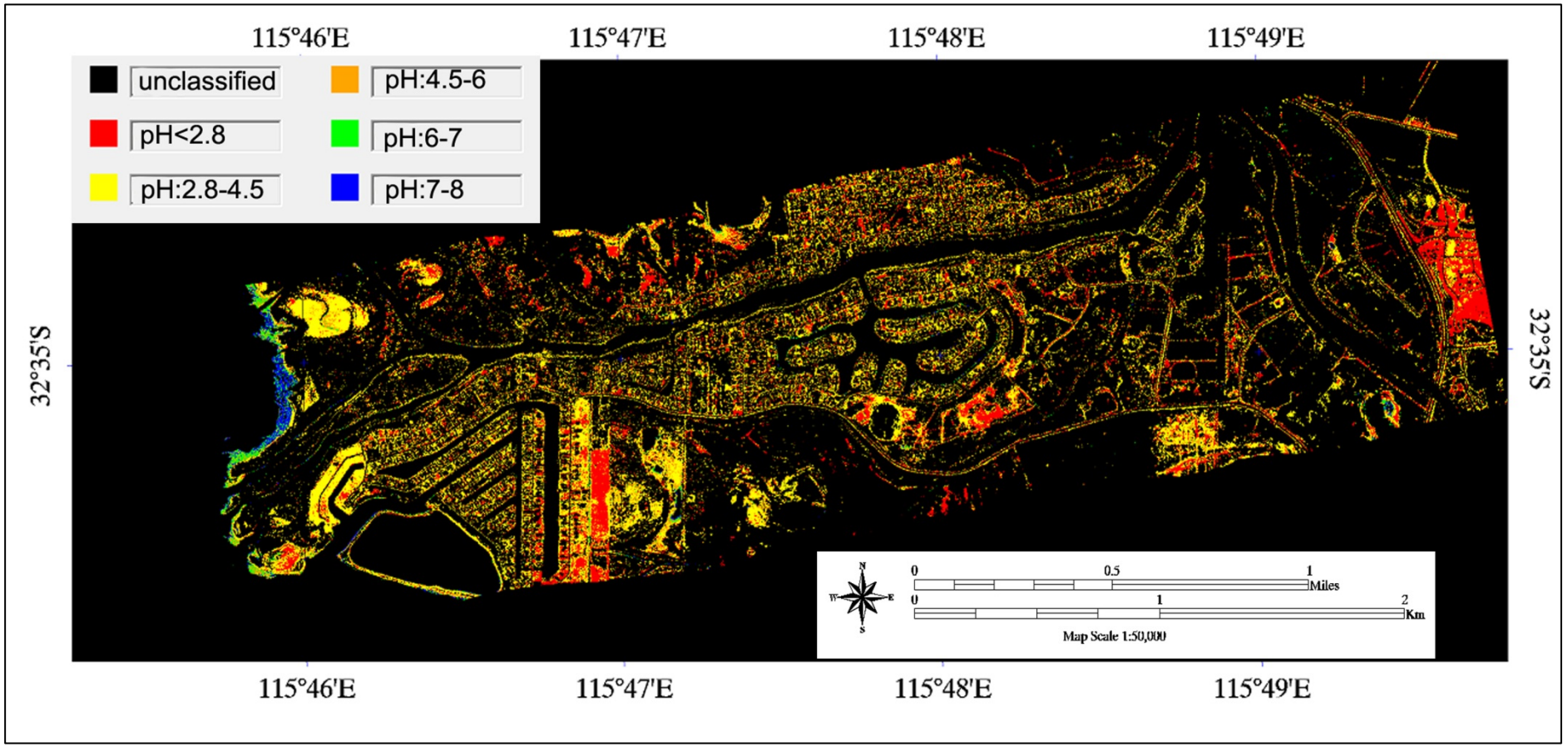

Figure 8.7: Soil pH map deduced from the PLSR model (from Chapter 7, Figure 7.4).

Water of the south-western Australian wheatbelt, indicated a strong linear relationship between lower pH and higher Al concentrations (Gray, 2001; Degens et al., 2008). The pH versus dissolved Al concentrations showed Al concentrations to be above 25 mg/L at pH <5 (Degens et al., 2008). The dissolution rate of gibbsite increases at low pH, and experiments using different acids have found that gibbsite dissolution increased by a factor of 6 to 30 times when SO_4^{2-} ions were used (Ridley et al., 1997; Dietzel and Bohme, 2005), indicating gibbsite was more easily dissolved in sulphuric acid as compared to other acids.

The data on kaolinite and gibbsite solubility allow Al toxicity ranges to be established according to the presence of minerals and the pH values of the soil (Cama et al., 2002; Dietzel and Bohme, 2005). When the soil pH is above 5, there is low abundance of dissolved Al^{3+} in the soil or sediments whether aluminium-bearing minerals exist in the environment or not, and therefore the soil would have potentially low toxicity. When the soil pH is less than 4, kaolin minerals and gibbsite will dissolve, often at varying rates but faster in sulphuric acid; thus, an environment containing kaolinite or gibbsite with pH of <4 is potentially a high toxicity zone. For soil pH values between 4 and 5, the concentration of Al^{3+} will be at a moderate level and will vary according to other environmental conditions, and therefore the potential toxicity will be moderate.

When the pH is below 2.8 in ASS, the acute sulphuric acid-related acidity will accelerate the reaction with kaolin and gibbsite to release more Al^{3+}, and almost all the gibbsite will be dissolved to release Al ions. Therefore, soils with pH <2.8 and the presence of kaolinite and gibbsite are the most susceptible to Al^{3+} toxicity.

Considering both pH conditions and the distribution of aluminium-bearing minerals at a particular site, five grades of toxicity related to the potential release of Al^{3+} were proposed (Table 8.1): potential very high toxicity, potential high toxicity, potential medium (or moderate) toxicity, low toxicity and negligible toxicity. The hyperspectral data-constructed mineral and pH maps were used to identify and classify the image pixels into one of the five potential toxicity categories. Considering the pH range adoped by the pH classification map (Figure 8.7), the same pH ranges were also used for deduction of Al toxicity. The intersections between the pixels containing the gibbsite and kaolinite and the pixels in each pH range presented in the pH classification were operated, then the results of the gibbsite zone intersecting with the zone of pH <2.8 and the kaolin zone intersecting with the zone

of pH <2.8 were merged to provide the category of potential very high toxicity. Likewise, the intersection result of gibbsite and kaolinite within the pH zone from 2.8 to 4.5 was merged to provide the category of potential high toxicity, and the intersection result within the pH zone from 4.5 to 6 was merged into the category of potential medium toxicity, and the intersection result within the pH zone more than 6 was merged to provide the category of low toxicity. The Al toxicity classification was summarized in Table 8.1.

The potential Al toxicity category distribution is illustrated in Figure 8.8. The map showed potentially high and moderate toxicity over the oxidised dredged sulphidic piles and low potential toxicity around some drying wetlands and the coastal strip. The presence of potentially high toxicity in the oxidised sulphidic material matched the lack of vegetation on most parts. Although most of the areas with low pH (<4) in the pH map also had high to moderate potential toxicity, there were some low pH areas that did not have the potentially high toxicity category, largely because of the lack of aluminium-bearing minerals in the soil matrix at that site or landform. The unclassified areas in the image (in black) were indicative of no toxicity threat as they did have high pH and low aluminium-bearing minerals.

The Al toxicity classification results have not been fully verified by the ground truth because of the timing of the project. Although the creek bed in site Y-005 was classified as a very high toxicity location in the classification image, some precipitation of soluble Al sulphates was found in two samples from this site, namely, tamarugite ($NaAl(SO_4)_2 \bullet 6(H_2O)$) and potassium alum ($KAl(SO_4)_2.12(H_2O)$) (Figure 8.9). The presence of tamarugite and potassium alum strongly suggested the high concentration of Al^{3+} at this site, which was consistent with the very high toxicity classification result for this site (Figure 8.8).

Table 8.1: Potential toxicity categories interpreted from the presence of aluminosilicates (kaolinite) and Al hydroxides (gibbsite) and soil pH

Potential toxicity category	**pH range**	**Al-bearing**	**Image**
Very high	< 2.8	Kaolin, gibbsite	Red
High	2.8 – 4.5	Kaolin, gibbsite	Orange
Medium	4.5 – 6	Kaolin, gibbsite	Yellow
Low	> 6	Kaolin, gibbsite	Green

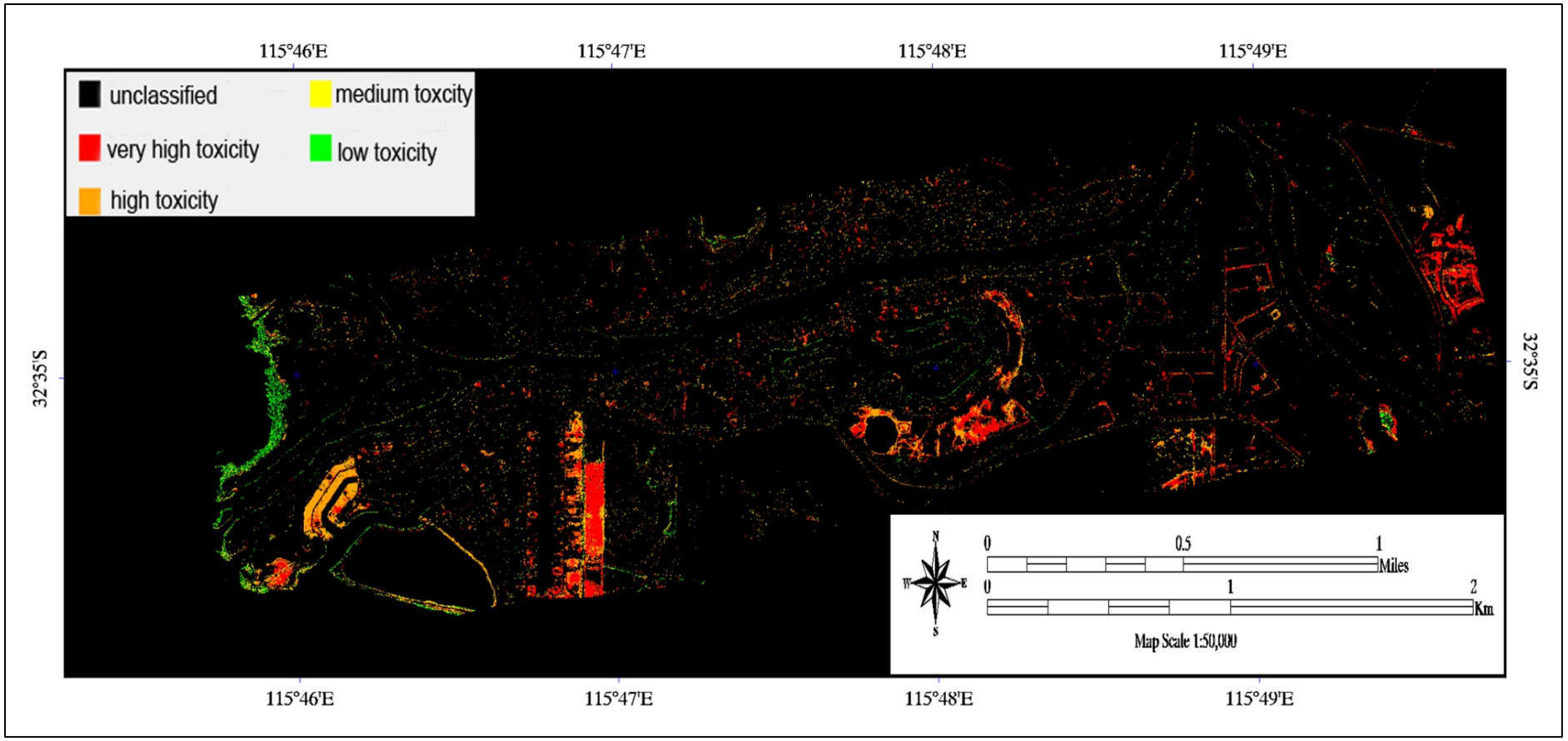

Figure 8.8: Potential aluminium toxicity map as constructed from soil from the distribution of soil pH and main aluminium silicate and aluminium hydroxide-bearing minerals in the area (some soluble aluminium sulphates were found in site Y-005).

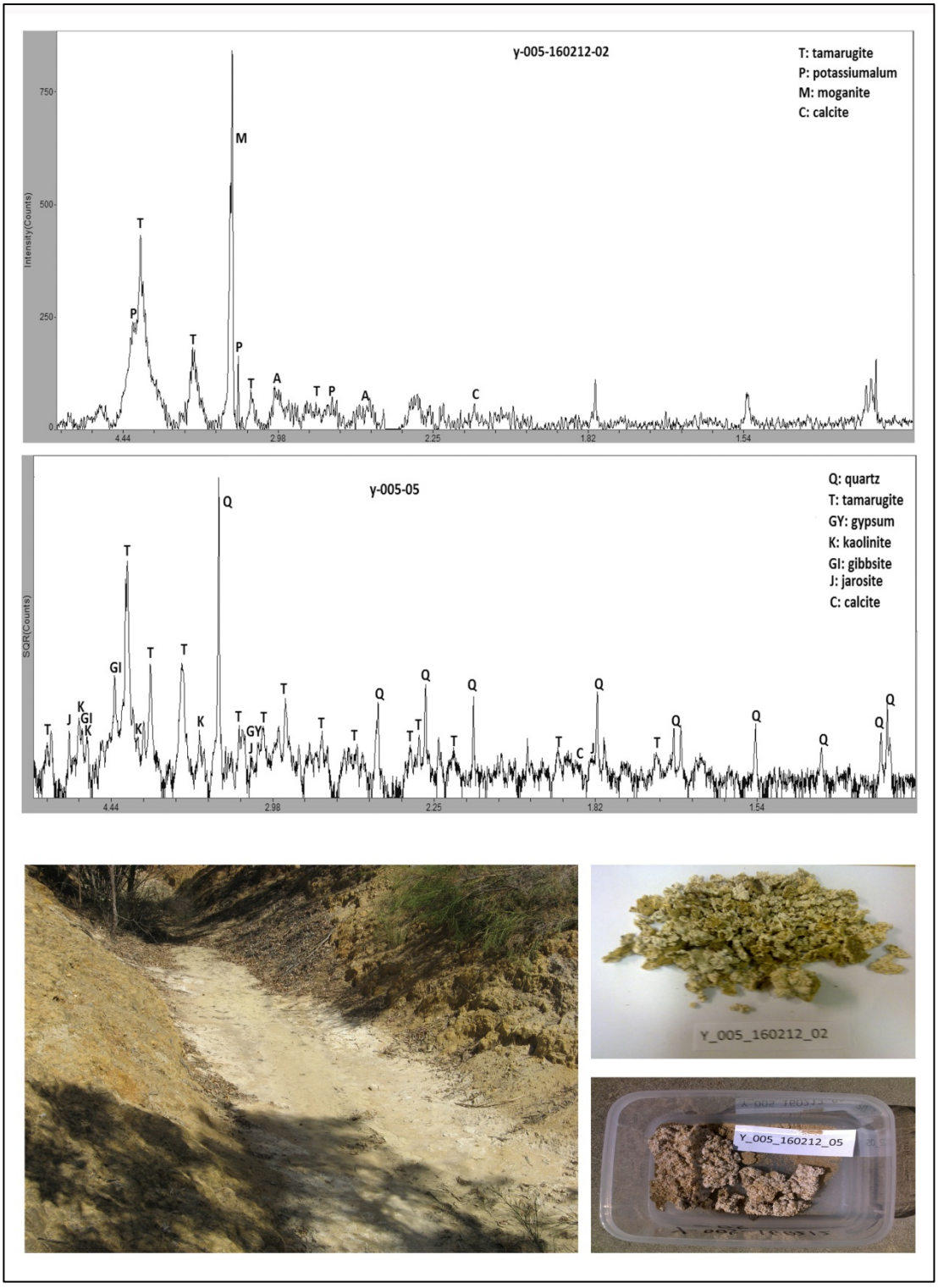

Figure 8.9 Two samples collected from the bed of a creek in site Y-005 were identified by XRD that contain soluble aluminium sulphate namely tamarugite and potasiumalum.

Chapter 9 Assessment of Acid Sulphate Soils in the Subsurface by Proximal Hyperspectral Sensing

9.1 Introduction

Acid sulphate soils can be grouped into two kinds: AASS, where iron sulphides have oxidised to produce acidic conditions; and PASS, where iron sulphides are present but have not been oxidised to produce acidity (Fitzpatrick, et al., 2003; Fitzpatrick et al., 2008; Sullivan et al., 2002; 2004; 2006). These two types of ASS often occur vertically in the same site, containing a sulphuric horizon (AASS) in the top layers because of oxidation near the surface, and sulphidic materials in deeper parts of the profile where reducing conditions still exist (Fitzpatrick et al., 2008). The conversion of PASS to AASS is largely due to the oxidation of the iron sulphides in the PASS, and much of this oxidation occurs due to exposure of the submerged sulphidic material to oxidative conditions. The oxidative conditions are facilitated either due to drying of the soil profiles (lowering of water tables) or exposure of the sulphidic material to the surface via physical disturbance (e.g., dredging, earth movements) or draining of waters.

Similar to the surface mineralogy of ASS, as has been documented and explained in Chapters 6-8, an understanding of the mineralogy and chemical properties of soil at varying depths is important to assess the occurrence and severity of ASS. A sound knowledge of mineralogical and chemical properties in three dimensions in these soils could greatly assist in predicting the changes and evolution of ASS in the foreseeable future. Firstly, the surface ASS and low pH conditions could make some metals more soluble, and these soluble metals and resulting sulphate could leach from the top soil to the lower horizons of the soils, thereby impacting the conditions in the subsoil. Secondly, layers of soil on the surface may be eroded by wind or surface flows and new layers of soils may be exposed to the atmosphere, resulting in the new oxidation of newly exposed pyrite and subsequent chemical and biochemical reactions. In addition, changes in climatic conditions such as precipitation and infiltration rates may affect groundwater levels, resulting in exposure to oxidising conditions if the water table falls. Therefore, knowing the mineralogy and chemical properties of soil to some depth beneath could greatly assist us to assess ASS more comprehensively and to predict the changes and evolution of ASS. Furthermore, it is

important to note that understanding the chemistry and mineralogy in the subsurface of soils is necessary in order to predict the negative effects or potential hazards, such as acidity and toxicity of trace metals to plants, because the roots of plants usually exist in certain depths under the surface.

Most remote sensing instruments in the solar reflection region have the ability to sense and acquire data from the top 50 μm or less of the Earth's surface, and even in the thermal infrared region, the detectable thickness of the top zone is less than 10 cm (Gupta, 2003). Conventional methods for subsurface soil mineralogical and geochemical investigations (e.g., chemical analysis and XRD) have been proved to be time-consuming and costly. Thus, a rapid mineralogical detection and soil property estimation method would greatly aid in interpreting, monitoring and predicting ASS evolution. Furthermore, it has been established that ASS properties change rapidly and seasonally (Sommer, 2006; Fitzpatrick et al., 2008), and although airborne hyperspectral studies on acid drainages have aided in estimating the temporal changes of acid spread (Swayze et al., 2000; Riaza and Muller, 2010), rapid measurements of the subsurface of acid-bearing soils have not been conducted. Translating knowledge of the surface mineralogy linkages with acid conditions to the subsurface would greatly benefit in: i) assessing the subsurface environment for prevailing acid conditions and the potential to convert to acid conditions, thereby aiding the prediction of its subsequent adverse effects over a selected area; and ii) being able to link surface conditions with those of the immediate subsurface so as to assess whether the surface acid conditions are correctly indicative of the subsurface.

To address the need for rapidly mapping the subsurface mineralogy in a manner similar to the surface mapping conducted via hyperspectral sensing, the newly established proximal hyperspectral technology of the HyLogger^{TM} system was employed in this investigation. The HyLogger system has been widely used in the mineral exploration industry to rapidly identify and map VNIR-SWIR-sensitive minerals (clay minerals, iron oxides, sulphate, carbonates). Its ability to quickly and effectively map large amounts of subsurface material from drill core, which was previously impossible, has aided in the interpretation of the genesis of ore deposits (Haest et al., 2012). Based on the growing success of the HyLogger system in mineralogically characterising the subsurface, it was employed in this study to investigate the mineralogy of the subsurface around the study area via soil cores. In addition, to add and validate interpretations from the HyLogger data, specific

physical (pH, EC) and chemical properties (major and trace metals) of the core samples were also examined so the relationships between the ASS properties and the mineralogy interpreted via the HyLogger could be established. Accordingly, the specific aims of the research presented in this chapter were: (1) to identify the near continuous distribution of the secondary mineralogy in cores taken through AASS and PASS using reflectance spectroscopy acquired via the HyLogger; (2) to measure the distribution of pH and EC in different depths of soil; (3) to determine the possible relationship between reflectance spectral features and soil properties by PLS modelling to see whether it was possible to predict the soil properties by spectral features.

9.2. Data Acquisition

9.2.1 Soil coring

Shallow soil cores (up to 1.2 m depth) were collected using the push coring method whereby a PVC pipe was pushed into the soil and extracted. Initially, sampling stations (locations) were selected and highlighted on the base map before the field work according to the principles that: (1) the stations would be distributed as evenly as possible in the study area; and (2) the study would focus on selected areas where ASS-related environmental issues appeared to be severe as interpreted from the hyperspectral data and from ground visual observations. In the selection of sites, an attempt was made to select soil coring sites that reflected average environmental conditions and to concentrate on selected landforms.

Most of the landform settings were chosen in order to get a representation across the study area. The sampled landform sites were the wetlands and adjoining marshy areas, excavated drains and adjoining weathered spoils (Table 9.1). The wetlands are permanently submerged, but much of the perimeters dry out during the summer months. Cores were taken from the oxidised dredged sediment which was rich in sulphidic material. The sediment has been piled on adjacent banks and either left undisturbed for natural regrowth or manually flattened for construction activity. The sulphidic piles on the banks have since oxidised and weathered to form profile materials showing typical properties of ASS such as brown-yellow jarosite and goethite mottles and red mottles in a grey matrix.

Figure 9.1: The location soil coring sites on HyMap image

Table 9.1: Geographical data and landform location of the soil cores

Core No.	Easting	Northing	Landform
Core 1	384167	6393326	Wetland adjoining inlet
Core 2	384307	6393411	Weathered dredge spoil flattened for construction
Core 3	385765	6393196	Weathered dredge spoil undisturbed since dredging
Core 4	386115	6393714	Ephemeral wetland (dry)
Core 5	389782	6394911	Marshy lowland adjoining constructed wetland
Core 6	389782	6394960	Weathered dredge spoil adjoining marshy
Core 7	386503	6394886	Intensely weathered dredge spoil adjacent drain
Core 8	384167	6393326	Edge of large wetland

9.2.2 HyLogger scanning

The cores were cut in half. One half of the core surface was carefully cleaned with a brush and then subjected to measurement with the reflectance spectra using the HyLogger system developed by the CSIRO. The HyLogger system provides rapid non-destructive spectral collection and imaging from drill core and chips (rock or soil cuttings); the instrument used in this study was the second generation HyLogger-2 which was equipped with an in-house assembled spectroscopic instrument that combines a Control Development Incorporated (CDI) silicon charge-coupled device(CCD) array grating spectrometer for measuring VNIR wavelengths and a Designs and Prototypes-developed Fourier transform infrared spectrometer for the SWIR wavelength. The sensors collect spectra at a resolution of 4 nm. Both the spectrometers measure the radiance that is converted to reflectance according to a National Institute of Standards and Technology traceable Spectralon. The core is scanned as it continuously moves under the sensor driven by a computer-controlled X-Y plane table at a rate of approximately one metre every 20 seconds. The sensor collects spectra every 4 mm and averages over a pair to enhance the signal-to-noise ratio, but due to the table motion when scanning, the actual spatial resolution is about 18 mm along and 10 mm across the core. In addition to the spectral sensor, a high spatial resolution imaging camera takes a three channel image every 0.1 mm thereby composing a continuous high resolution image of the core as it moves on the table.

The HyLogger operates continuously with 8 mm intervals spatially on a sample in the range of VNIR and SWIR.

9.3 Results and Discussion

9.3.1 Soil profile characteristics

Core 1 was sandy to loam in texture and had a relatively low pH average value of 4.25 but a high average EC value of 4749 μS/cm, indicating saline conditions throughout the core. The high salinity was expected considering the location of the wetland adjacent to the inlet and the likely hydrological connection of the wetland with the estuarine waters.

Core 2, taken from oxidised, flattened dredge spoil, had a distinct texture contrast in the profile that coincided with pH and total S content changes. The upper texture in the upper 50 cm of the profile was sandy-clay to clay loam, while in the lower part of the profile it was sandy-loam with a low average EC value of 261 μS/cm. The pH varied considerably through the core. The top 50 cm had a pH between 4-4.30 while the deeper parts had neutral to alkaline pH of above 6.7, and the pH was correlated to the total S contents (Table 9.1). The top parts with low pH and clay-loam textures had higher total S contents (942-1486 ppm), while the lower neutral to alkaline pH zones and sandy-loam textures had significantly lower S contents (<150 ppm).

Core 3, taken from an abandoned oxidised dredge spoil, was sandy-clay to loamy-sand in texture, with an average pH value of 4.12 and average EC value of 78 μS/cm. The pH throughout the core had uniformly acute acidic values between 3.94 and 4.3, and the total S contents were also uniform throughout the depth of the core.

Core 4 was mainly loamy sand in texture, with acidic pH ranging from 4.28 to 4.65 while the EC values were high at the surface and decreased deeper. The total S values were also higher near the surface and decreased lower.

Core 5 had a fine sand grain size with a loamy sand texture. In comparison to the other collected soil cores, the soil profile in this core had higher pH values falling in the neutral range, varying between 5.45 and 6.75, with comparatively low EC values (<40 μS/cm).

Core 6 was dominated by fine sand and a loamy sand texture. The pH values were comparatively higher towards neutral, ranging from 6.24 to 4.84, with a gradual increase towards the bottom of the soil profile. This soil profile had negligible total S, which indicated it did not possess acid generation capacity.

Core 7 was dominantly clay to silt in grain size and sandy clay in texture. Compared to the other soil cores, it had the lowest pH values ranging from 2.88 to 3.29. The EC values were relatively high, ranging between 232 and 1600 μS/cm, with a gradual increase in EC going downwards. The total S was also comparatively high, ranging between 1600 to 4500 ppm. The acute acidic nature of the entire soil core with high total S content was consistent with the material being ASS and having been taken from an intensely oxidised sulphidic material (dredge spoil).

Core 8, taken from the edge of a large natural wetland, showed a texture contrast in the profile. The upper section had a loam texture, whereas the lower section had a loamy sand texture. The pH range was acidic, ranging from 3.85-4.48, with very high salinity (1600-15560 μS/cm). The total S contents were also high in the surface horizon (14100 ppm) but decreased significantly at the 70 cm depth (500 ppm). The higher S content at the surface suggested that sulphidic material only formed in the upper layers of the wetlands.

The pH, EC and total S variations within the individual soil profiles and across the collected soil profiles allowed some interesting deductions. The variations in properties were grouped into soils from wetlands and those from oxidised sulphidic material piles.

Wetland Soils

Core 1 and core 8, which were collected from the two permanently saturated wetland sites, had the highest concentration in total sulphur contents, with average values of 13477 and 4495 ppm, respectively. Core 7 also bore high S, while core 2, core 4, core 3 and core 5 had significantly less sulphur contents, and the sulphur content of core 6 was negligible. The distribution of dark hues through the soil profile for cores 1 and 8 corresponded with the S contents, but in reverse. For core 1, the S content increased with depth and so did the dark hues, with pH values increasing with depth. The pH values and S content indicated much of the vertical profile to be PASS with only the near surface being ASS. In core 8, the S content was highest at the surface and decreased significantly with depth, matching the colour change from black to pale grey (Table 9.1 and Figure 9.1). These physical and chemical variations for the wetland cores were explained by the progress of sulphidisation and oxidation in the wetland profiles. For core 1 from wetlands adjacent to an inlet, the active sulphidisation occurred through much of the vertical soil column, with oxidation occurring at the surface only with the onset of semi-drying conditions. For core 8,

situated at the edge of an inland wetland, sulphidisation was only occurring near the surface due to the availability of organic matter and soluble S, while at depth, theoriginal sandy sediment of the Bassendean sand prevailed. The textures of the soils also reflected the sulphidisation active horizons, with sulphidic materials being loam rich and non-sulphidic materials being sandy loams.

Soil profiles on oxidised sulphidic piles

For the soils formed on dredged and oxidised sulphidic materials, the pH and S content were likely a reflection of the original S content of the sulphidic material and the intensity of the oxidation. The soil profiles of cores 3 and 7 were from highly oxidised sulphidic material piles and therefore the pH was acidic throughout, with the S contents having no systematic pattern. The difference in S contents was likely due to original S content variation within the two sulphidic materials or due to leaching on oxidation. The soil profile from core 2 was made up of two distinct materials: the upper 50 cm was made up of clay loams and represented by the oxidised sulphidic materials with acidic pH, and the lower profile material was composed of the original deltaic sands (sandy-loam texture) with a lower total S content and neutral pH. The profile was interpreted as sulphidic material deposited over the original deltaic sands, with subsequent oxidisation of the sulphidic materials.

Regarding the distribution patterns of the sulphur contents, core 1, core 3 and core 7 displayed a similar increasing tendency as the depth increased, which suggested that the sulphides (mainly pyrite and MBO) from the sulphidic materials

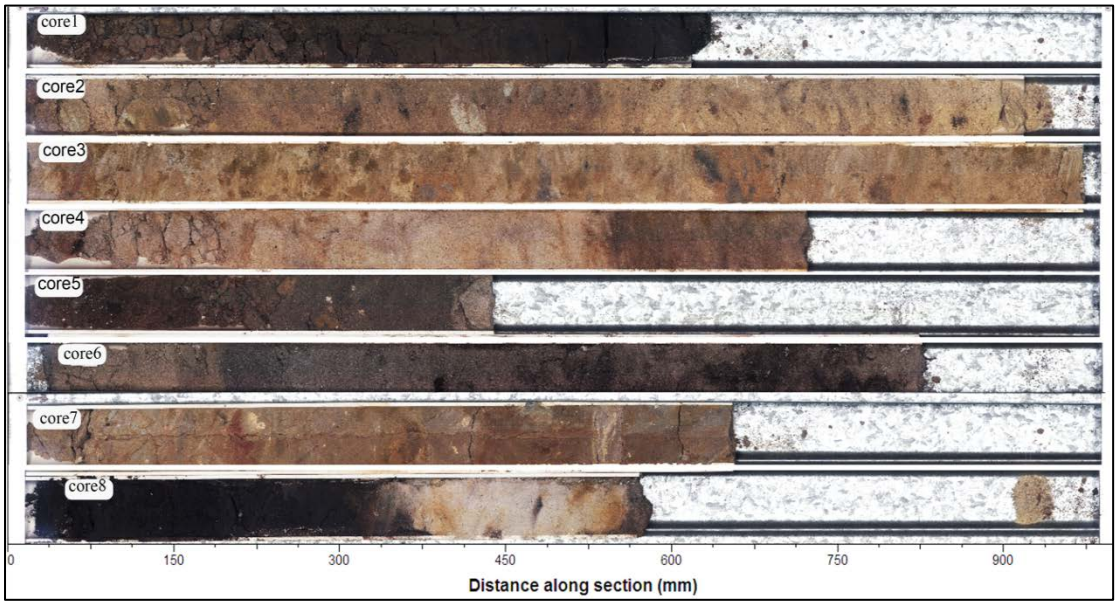

Figure 9.2: Images of 8 soil cores collected from the study area

were oxidised and the sulphur mobilised and removed (leached) from the upper soil layers as soluble sulphur (Sohlenius and Obor, 2004); while in other cores, the profile variations of the sulphur contents were complicated. Detailed descriptions of the soil cores are presented in Table 9.2 and Figure 9.1.

Table 9.2: Selected physical and chemical properties of the soil profiles in the cores

	Depth	**Grain size**	**Texture**	**pH**	**EC**	**Total S**
Core 1	14-16	Silt	Sandy-clay	3.81	9740	5809
	26-28	Clay	Loam	3.45	6250	6119
	34-36	Clay	Loam	3.48	3840	6884
	44-46	Silt	Sandy-clay	3.56	3320	6500
	53-55	Clay	Loam	5.06	3440	25486
	60-63	Clay	Loam	6.19	1906	30069
Core 2	4.0-7.0	Very fine	Sandy-clay	4.30	40.1	1486
	24-26	Fine sand	Sandy-clay-	4.20	108.1	572
	44-46	Fine sand	Sandy-clay-	4.09	770	942
	64-66	Medium sand	Sandy-loam	8.52	302	149
	84-86	Medium sand	Sandy-loam	6.70	85	53
Core 3	0-5	Silt	Sandy clay	4.30	135.5	281
	19-21	Silt	Sandy clay	4.26	71.3	344
	39-41	Silt	Sandy clay	3.98	54	295
	59-61	Fine sand	Loamy sand	4.13	67.5	289
	79-81	Fine sand	Loamy sand	3.94	76.5	283
	97-99	Clay	Loam	4.13	63.9	373
Core 4	4-6			4.65	1774	549
	24-26	Fine sand	Loamy sand	4.28	644	209
	44-46	Fine sand	Loamy sand	4.34	897	505
	64-66	Fine sand	Loamy sand	4.60	509	240
Core 5	0-5	Fine sand	Loamy sand	5.47	19	173
	9-11	Fine sand	Loamy sand	5.45	39.6	182
	19-21	Fine sand	Loamy sand	6.21	27.5	112
	29-31	Fine sand	Sandy loam	6.45	24.8	66
	39-41	Fine sand	Sandy loam	6.75	32.2	BDL
Core 6	0-4	Fine sand	Loamy sand	4.84	16.9	BDL
	19-21	Fine sand	Loamy sand	5.04	12.3	BDL
	39-41	Fine sand	Loamy sand	5.27	10.1	BDL
	59-61	Fine sand	Loamy sand	6.39	20.3	54
	78-79	Fine sand	Loamy sand	6.15	23.6	BDL
Core 7	0-5	Silt	Sandy-clay	3.29	202	1881
	15-17	Silt	Sandy-clay	2.98	391	3239
	30-33	Silt	Sandy-clay	2.88	621	1686
	44-46	Silt	Sandy-clay	2.93	685	4273
	58-60	Fine sand	Sandy	3.07	586	4222
	65-69	Clay	Loam	2.68	1632	2791
Core 8	4-6	Clay	Loam	4.02	5130	14122
	24-16	Clay	Loam	3.85	3250	2228
	44-46	Fine sand	Loamy sand	4.48	7930	672
	54-56	Fine sand	Loamy sand	3.92	15560	959

Note: The BDL in the cell means no value because it was beyond the detectable limitation

9.3.2 Spectral characteristics in the subsurface

Eight soil cores were scanned and the resulting spectral data initially processed via the software of TSG Core version 7. The spectra were processed to remove the hull and then a snapshot of each depth slice was taken to rapidly visualise the main variations in the subsurface spectra. In the depth slice, the depths of the absorptions were illustrated by different rainbow colour systems with warm colours of red indicative of greater depth while the cold colours closing to blue and greens were indicative of high reflectance. The spectra of the soil in core 1 to core 3 are shown in Figure 9.2, the spectra of the soil in core 4 to core 6 are shown in Figure 9.3 and the spectra of the soil in core 7 to core 8 are shown in Figure 9.4.

The spectra for all cores showed absorption features occurring near 0.45-0.5 μm, near 0.9 μm, near 1.4 μm, near 1.9 μm and near 2.2 μm (Figures 9.2 to 9.4). In addition, at some depths in some cores, the absorption features were also apparent near 2.265 (i.e., at the depth of about 60 cm of core 6, with the soils having strong absorption near 2.265 μm) and 2.268 μm (i.e., at the depth of 29-40 cm in core 5 and at the depth above 20 cm in core 6, with the soils having strong absorptions near 2.268 μm). An absorption near 0.45-0.5 μm is commonly related to the crystal effect of ferric iron; an absorption near 0.9 μm commonly suggests the abundance of ferric iron content; the absorption near 1.9 μm relates to hydroxyl and water; an absorption near 1.4 μm is related to water content; and an absorption near 2.2 μm is relevant to the hydroxyl ion occurring in combination with Al which can be described as Al-OH, and it commonly relates to the kaolin group (Clark, 1999). The absorption at 2.265 μm is a diagnostic feature indicative of the presence of jarosite (Crowley et al., 2003; Cloutis et al., 2006) and the depth of this absorption suggested the abundance of jarosite; the absorption at 2.268 μm was considered indicative of the presence of gibbsite and the depth at this position suggested the abundance of gibbsite. The absorption features recorded and identified were only from those minerals that were spectrally responsive and the dominant mineral quartz present in most of the profiles did not show any absorption features in the wavelength region scanned.

The abundance (or intensity) of Al-OH and iron oxides was regarded as the main focus of the observation in the soil profiles. The variations in the occurrence and depth of the absorption features at 2.22 μm (for Al-OH) and 0.9 μm for iron oxides at particular depths were represented as horizontal bar widths adjacent to the depths (Figures 9.2-9.4). The wider the bar, the greater the depth of the absorption feature

was, and this indicated a higher abundance of the minerals causing the respective absorption.

The results showed that for core 1 both the Al-OH and iron oxide-related absorptions were minor, with 2.2 μm absorption only showing in minor to moderate amounts in the upper half of the core. Both of the absorption features displayed a gradually decreasing tendency with the increasing depth.

For soil profile 2 (core 2), the spectrum slice showed a semi-continuous broad absorption around 0.9 μm and a continuous sharp absorption at 2.2 μm. These features were indicative of relatively moderate to high contents of Al-OH and semi-continuous presence of iron oxides through the soil profile.

For soil profile 3 (core 3), the distribution of the spectrum slice showed a continuous absorption around 0.9 μm which became deeper from around 30 cm depth and above, thereby indicating a greater proportion of iron oxides towards the surface. The absorption at 2.2 μm was also moderate from 30 cm to deeper; from 0-30 cm, the depth of this absorption became comparatively deeper, thereby suggesting the greater presence of Al-OH-bearing minerals in the upper part of the core, similar to iron oxides.

The soil profile in core 4 showed a low abundance of Al-OH and moderate content in iron oxides with both features exhibiting a decreasing tendency in abundance with depth. The soil profile in core 5 had a very apparent upright green stripe near 2.2 μm mixed with some brown mottles at some depth. At near 0.9 μm, the spectra of core 5 also showed apparent stripes although they appeared to discontinue in some depth. These two features suggested that the Al-OH and iron oxides were abundant and evenly distributed in core 5. It was notable that below 30 cm, there was a continuous absorption strip at 2.268 μm, suggesting the continual presence of gibbsite below 30 cm in core 5.

In the soil profile in core 6, the 2.2 μm feature was dominantly present above 20 cm, and gradually disappeared downward, indicating Al-OH minerals were present only in the upper 20 cm of the soil. It was noteworthy that below 50 cm in core 6, the spectrum had a continuous absorption strip near 2.268 μm which suggested the continual presence of gibbsite below 50 cm.

The soil profile in core 7 had stronger absorptions near 0.45 μm and near 0.9 μm which suggested a high abundance of ferric iron throughout the profile. The moderate depth features near 2.2 μm also suggested the relatively moderate

abundance of Al-OH throughout the core. Around 27 cm, the absorption feature at 0.9 μm became intense, indicating a strong presence of iron at these depths. Another absorption near 2.265 μm was also present around 27 cm and suggested the presence of jarosite, but the intensity of the iron oxides was not very strong; this means the ferric iron content was mainly from jarosite but not from iron oxides. Interestingly, the stripe related to the absorption feature near 1.9 μm was interrupted at this depth which suggested this part of the soil was dry. In the depth of 35-38cm, the stripe related to the absorption near 0.9 μm also displayed orange to red colours which suggested the existence of very abundant ferric iron, while the lack the absorption near 2.265 μm suggested that the ferric iron content was mainly from iron oxides.

For the soil profile in core 8, the absorption feature at 2.2 μm was weak to moderate in the upper 30 cm and negligible in the bottom part of the profile. The iron-bearing absorption at around 0.45 μm was also moderate in the top half of the core and negligible in the bottom half. This spectral data correspond to the distinct texture contrast in this profile, with clay loams in the upper part and sands in the lower part.

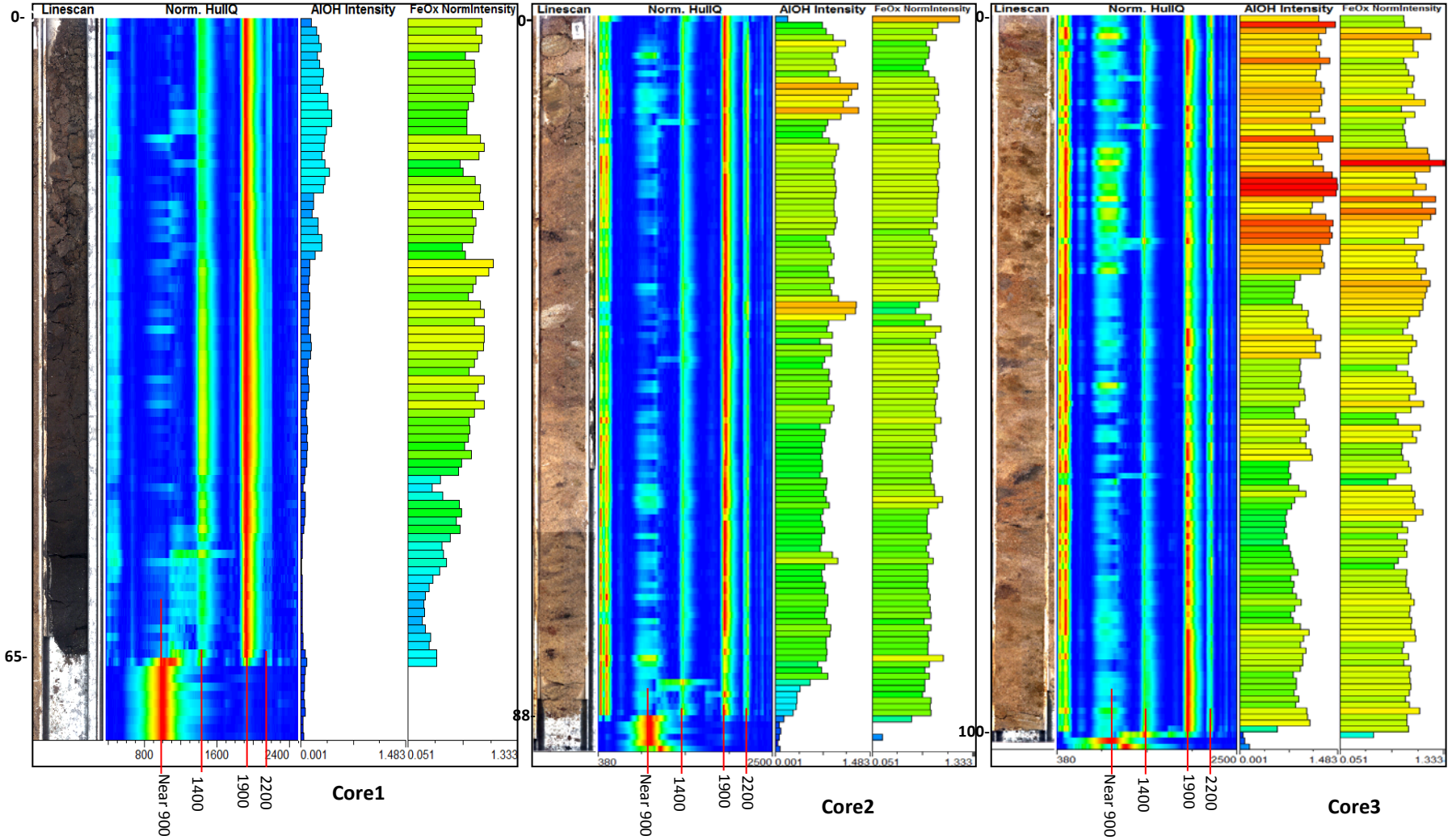

Figure 9.3: Slice spectrum with corresponding intensity of 900, 1400, 1900 and 2200 nm absorption and abundance of Al-OH and FeO_x for core 1 to core 3

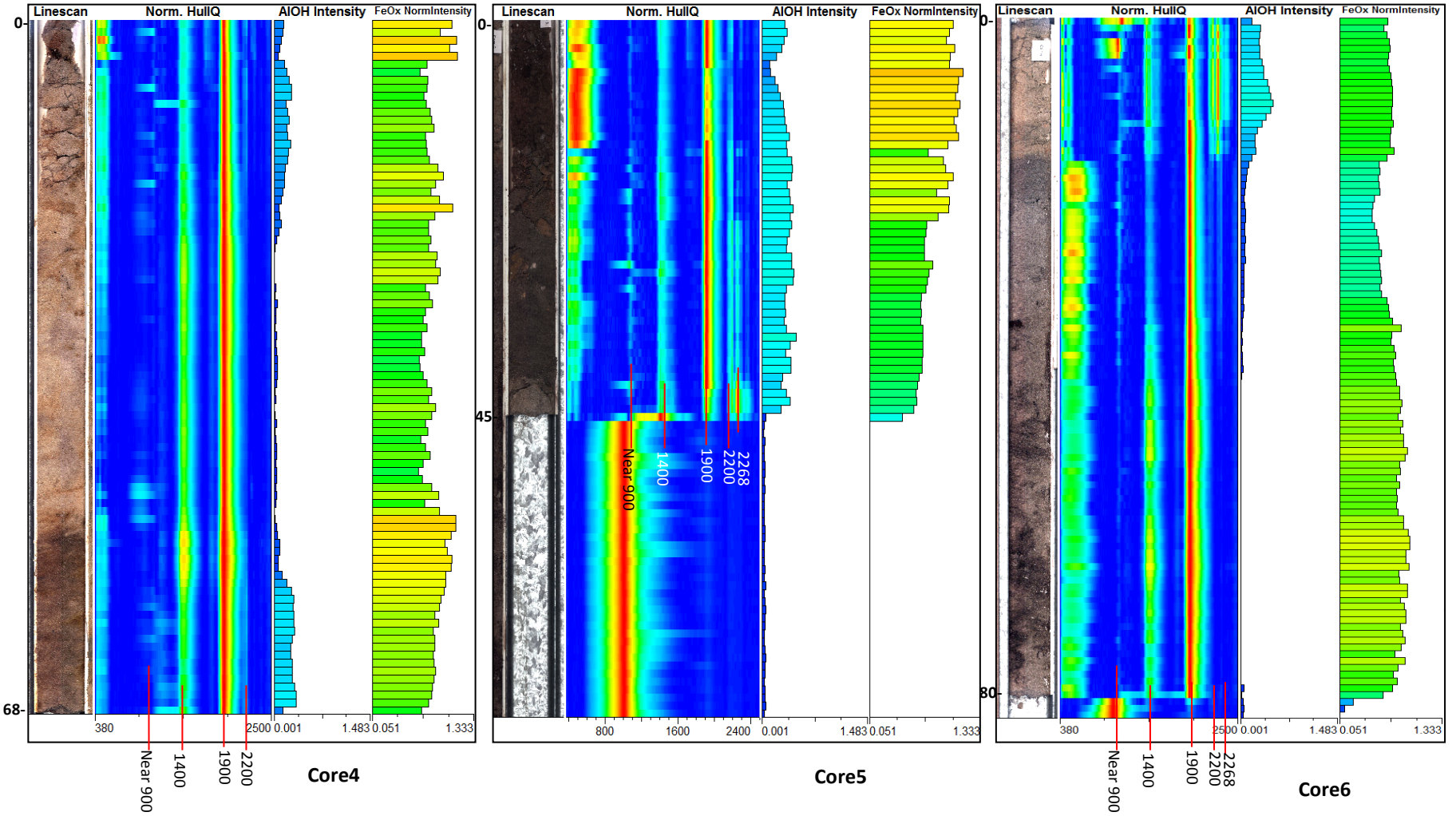

Figure 9.4: Slice spectrum with corresponding intensity of 900, 1400, 1900, 2200 and 2268 nm absorption and abundance of Al-OH and FeO_x for core 4 to core 6(notice: the top and bottom of core 6 was upside down when scanned)

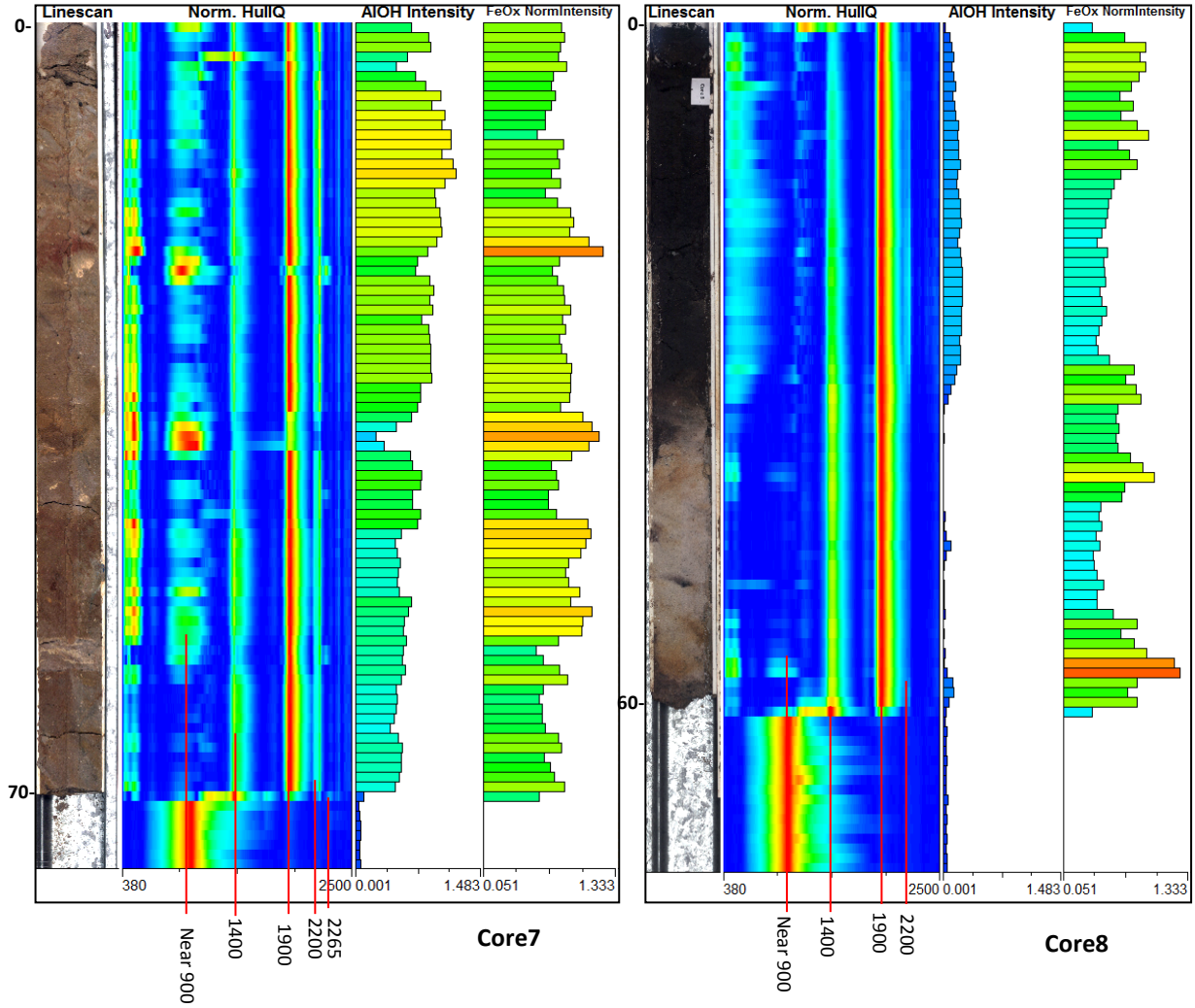

Figure 9.5: Slice spectrum with corresponding intensity of 900, 1400, 1900, 2200 and 2265 nm absorption and abundance of Al-OH and FeO_x for core 7 to core 8

9.3.3 Mineral identification

To identify the secondary mineralogy in the soil profiles (core 1 to core 8), the reflectance spectra acquired from the HyLogger scanning of the eight soil cores were processed to check for the diagnostic absorption features of specific electronic and molecular combinations of ions specific to minerals or mineral assemblages typical of ASS, and subsequently confirmed by matching the mineral or mineral assemblage to the spectra in the USGS Spectral Library (Clark et al., 2007). In the first instance, a reflectance spectra study of selected parts of the soil profiles was conducted to identify the secondary minerals based on diagnostic absorption features. The zones within the

profiles were selected based on morphological properties – mainly colour and texture – the former being indicative of the main iron oxide and hydroxide secondary minerals (Bigham et al., 2002). Subsequently, the data for the entire profile were processed to construct a mineral or mineral assemblage map of the soil core.

In many soil cores, bright red-coloured regions were present, suggestive of the presence of hematite. The reflectance spectra from the red-coloured zones of the soil cores were investigated and these zones showed absorption features with a strong and broad absorption centred at 0.89 μm, a broad shallow absorption at 0.67 μm and a strong absorption at 0.53 μm, all of which are features matching those of hematite (e.g., sample C7-07C; Figure 9.5). In the reflectance spectra of C7-07C, the doublet absorption features at 2.162 and 2.207 μm were diagnostic of kaolinite, while a smaller absorption feature at 1.78 μm was indicative of the possible presence of gypsum.

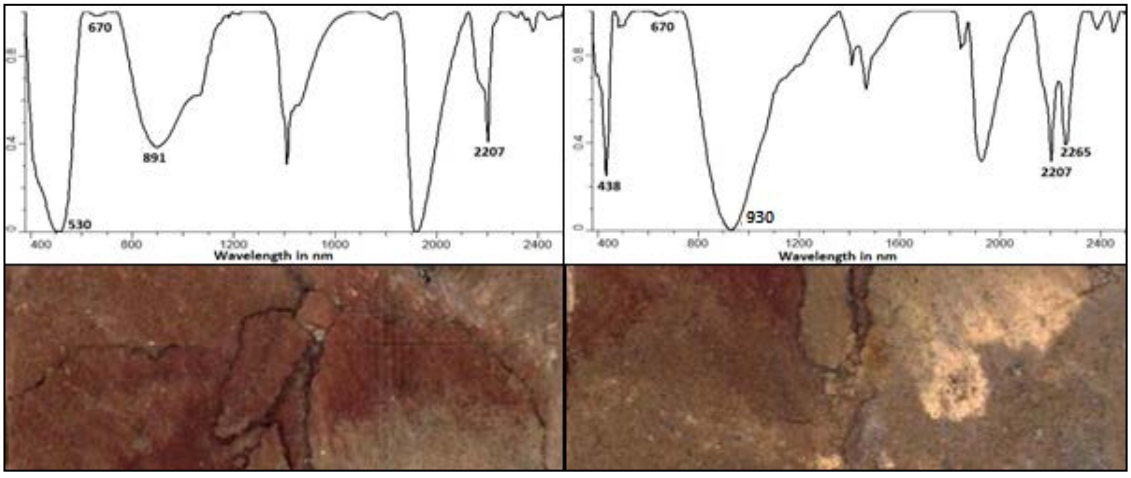

Figure 9.6: Reflectance spectra of soil cores; (Left) Image of core from 30 cm (below) showing reddish hues in a pale grey matrix with minor pale yellow fine mottles and spectra from same depth (Core 7, sample C7-07C) – the absorption features indicated the presence of kaolinite and hematite; (Right) Image of core from 60 cm (below) showing pale yellow mottles in brownish and grey matrix, and spectra from the same depth (above) (sample c7-05c) – the absorption features indicated kaolinite, jarosite and goethite (The reflectance spectra were collected from the centre line from top to bottom of the soil pictures and were continuum removed hull corrected)

The reflectance spectra for the parts of soil cores displaying yellow and straw-coloured mottles (soil colour), surrounded by reddish brown mottling (soil colour), showed absorption features typical of the kaolinite doublet absorption at 2.162 and 2.207 μm, and jarosite absorption features at 0.438, 1.85 and 2.265 μm (e.g., sample C7-05C; Figure 9.5). The broad absorption feature centred near 0.93 μm and the less strong absorption at 0.67 μm were indicative of the presence of goethite. The absorption was likely the result of the superimposition of the spectral feature of jarosite at 0.92 μm and the spectral features of goethite at 0.94 μm. Some other samples had similar striking yellow and straw-coloured mottles (e.g., sample C7-03C; Figure 9.6); however, the reflectance spectra just displayed the diagnostic features of jarosite with a strong absorption at 2.265 μm and a strong but broad absorption centred near 0.913 μm, and a doublet of absorption of kaolinite near 2.205 μm, but no apparent features of goethite (broad absorption near 0.93 μm). A few zones in the highly oxidised sulphidic material profiles showed medium (1-3 cm) pale yellow/straw-coloured irregular mottles (2.5YR8/4) in a pale grey matrix (Figure 9.6). The reflectance spectra of these zones

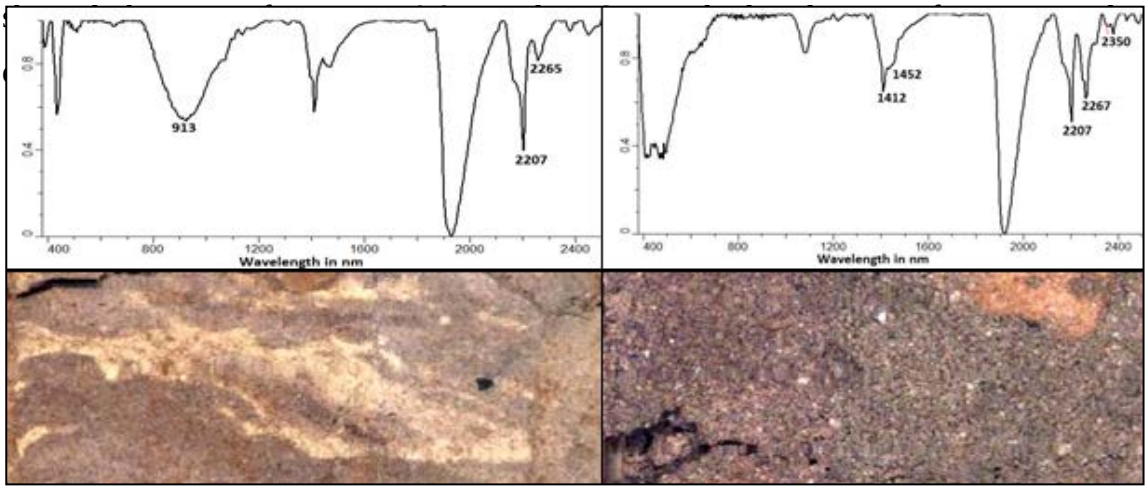

Figure 9.7: Reflectance spectra of soil cores (Left) Image of core from 65 cm (below) showing pale yellow/straw-coloured fine mottles and spectra from same depth (Core 7, sample C7-03C) – the spectral absorption features indicated jarosite and kaolinite (Right) Image of core from ~30 cm depth with reflectance spectra (above) showing features diagnostic of kaolinite and likely gibbsite (sample equivalent to C5-04C) (The reflectance spectra were collected from the centre line from the top to bottom of the soil pictures and were continuum-removed hull corrected)

Light grey parts of the soils were common although the grey colours differed. The light grey (2.5Y6/2) areas with sandy-clay texture showed the kaolinite diagnostic doublet near 2.205 μm, and also displayed the spectra with strong diagnostic absorption at 2.267 μm, a lesser absorption at 2.35 μm, and a doublet absorption at 1.412 and 1.452 μm (e.g., sample C5-04C; Figure 9.6). These features were indicative of gibbsite.

The soil profile samples with sandy-clay texture and with light brown colours (7.5YR4/4) showed spectra similar to that of smectites, in this case that of Ca-smectite montmorillonite. The spectra showed diagnostic but not strong absorption at 2.205 μm, and two deep water absorptions at 1.411 and 1.904 μm, both with an asymmetric shape (e.g., sample C4-06C; Figure 9.7). The spectra also exhibited the feature at 1.78 μm which was possibly assigned to gypsum. It was noteworthy that the absorption of montmorillonite at 2.205 μm is very close to the absorption of kaolinite at 2.207 μm, but kaolinite usually has a doublet absorption in this range at 2.207 and 2.162 μm, and this was not present. The 2.205 μm absorption could be assigned to illite which is a secondary mineral in soils, but the relative depth of the water feature was significant to the 2.205 μm feature, unlike that of illite.

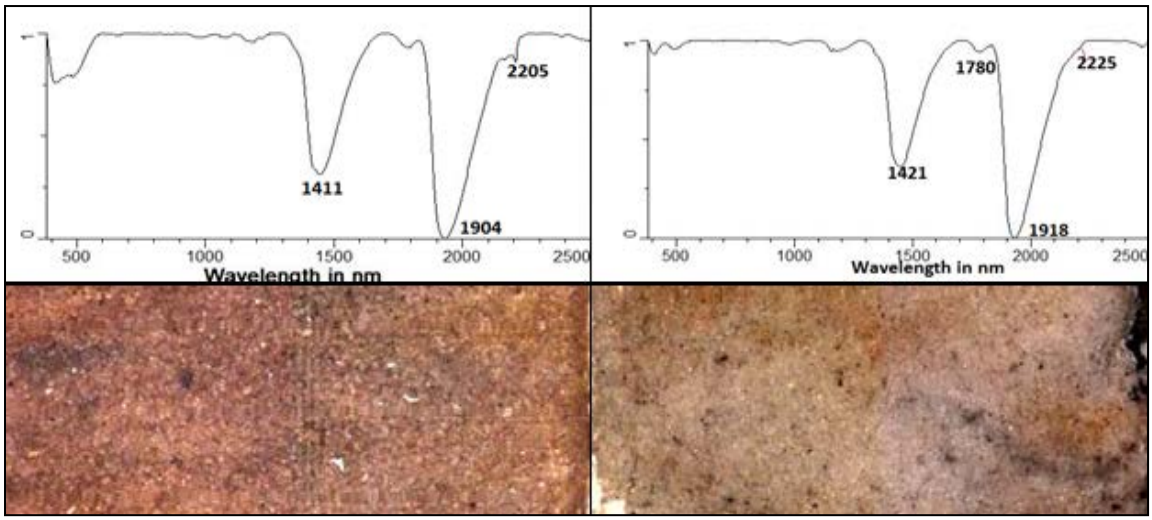

Figure 9.8: Reflectance spectra of soil cores (Left) Image of the core (below) of loam texture with spectra (above) (sample C4-06C) – the spectra indicate montmorillonite and gypsum (Right) Image of core ~ 35 cm depth with spectra (above) showing presence of gypsum and deep water feature (sample equivalent C8-04C) (The reflectance spectra were collected from the centre line from top to bottom of the soil pictures and were continuum-removed hull corrected)

To validate the mineralogical identification from the HyLogger spectra of the soil cores, both XRD and SEM were conducted. XRD confirms the presence of minerals only when present in major amounts. Several samples were examined by SEM to check the mineral composition. Examination of the sample C7-05C showed aggregates of Al-Si rich 0.5-2 μm plates, which are typical of kaolinite (Figure 9.8a). The kaolinite plate aggregates were mixed with an aggregate 0.2-.5μm equant to slight tubular iron-rich particles, which are goethite (Figure 9.8a). The composition of the kaolinite and goethite aggregates was determined by EDXA. Sample C7-03, which represented the pale yellow mottles, showed 1-3 μm, euhedral orthorhombic crystals (Figure 9.8b and c). The crystal forms were typical of jarosite and the EDXA data displayed K, Na, Fe and S concentrations in the orthorhombic forms. These jarosite crystals were present on a dense aggregate of Al-Si dominated plates which were consistent with kaolinite (Figure 9.8c). The reddish part of sample C7-07C showed iron-rich very fine grain aggregates (< 0.2 μm individual grains) which resembled hematite. These iron-rich grain aggregates were over dense coarser (>2μm) plates of kaolinite (Figure 9.8d).

9.3.4 Mineral distribution in the subsurface

The results of the spectral processing indicated that the following spectrally identifiable secondary minerals were present in the soil cores: the aluminosilicates, kaolinite and smectite (montmorillonite), iron oxides and hydroxides (goethite, hematite), iron sulphates (jarosite) and sulphates (gypsum) and minor Al hydroxides (gibbsite). The secondary minerals, however, were not singly present, but mostly present in mixtures of two or three minerals as revealed by spectral identification, SEM mages and XRD. Based on the mixtures of the secondary minerals as identifiable from the spectra data collected by the HyLogger, several separate mineral and mineral assemblages were distinguished. The main spectrally responsive minerals and mineral assemblages in the major parts of the cores included kaolinite + goethite, kaolinite + goethite + hematite, kaolinite + goethite + jarosite, kaolinite + goethite, kaolinite + gibbsite, and montmorillonite as well. The common ASS-bearing minerals such as ferrihydrite, copiapite and schwertmannite, had been identified on the surface of the soils but were

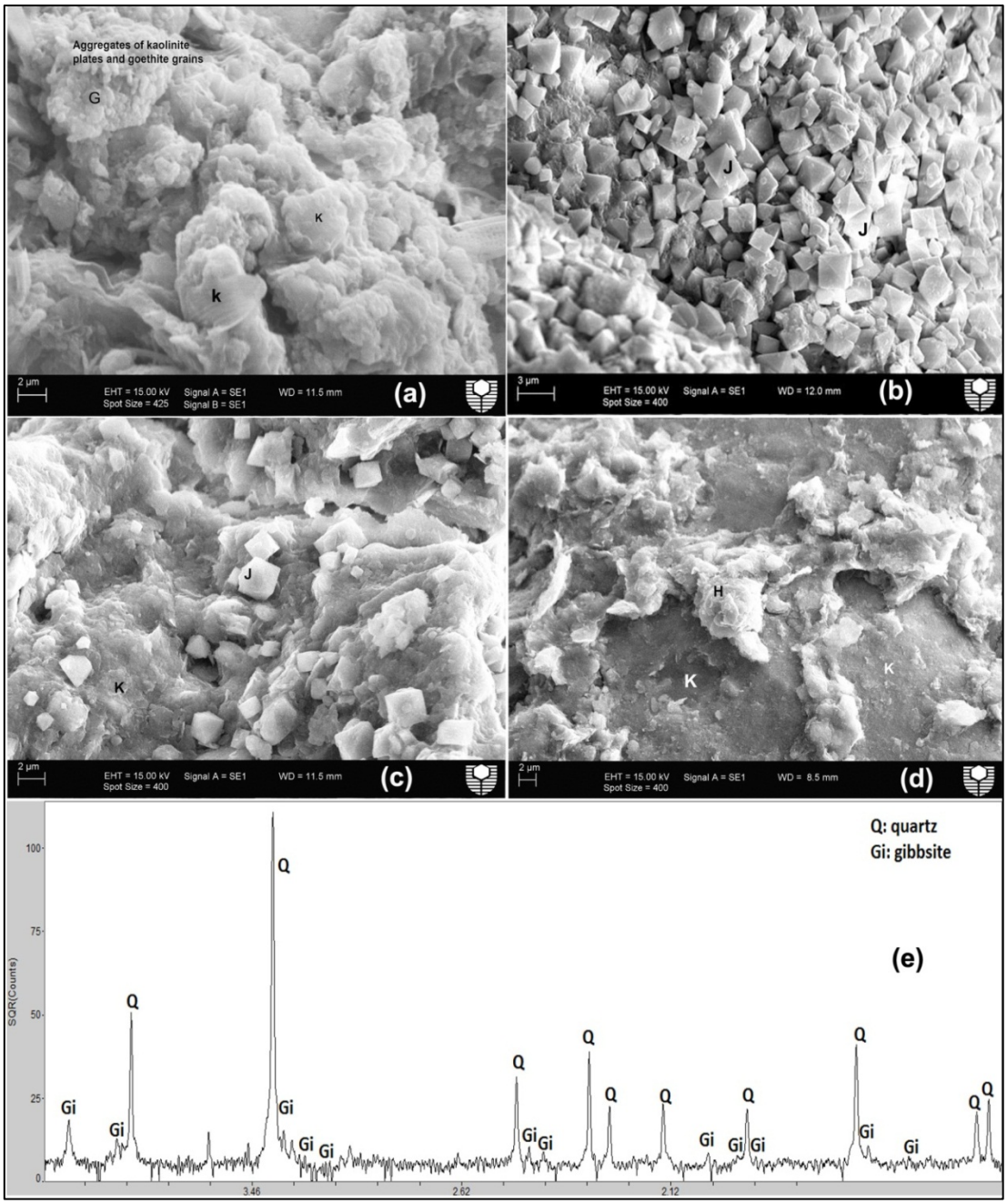

Figure 9.9: Minerals confirmed by SEM and XRD. (a) SEM image of yellow-grey parts of the core (C7-05C) showing aggregates of kaolinite plates and goethite grains; (b) SEM image of yellow parts of core (C7-03C) showing euhedral rhomboidal crystal morphologies typical of jarosite; (c) SEM image of yellow part of core (C7-03C) showing typical euhedral rhomboidal individual jarosite grains on a matrix of fine-grained kaolinite; (d) SEM image of the red parts of core (C7-07C) showing aggregates of hematite grains over a dense matrix of grey kaolinite (Re the letters in the image – K represents kaolinite, J represents jarosite, H represents hematite, G represents goethite); (e) XRD plot indicate the existence of gibbsite and kaolinite in sample C6-01C.

not identified by the soil profile reflectance data and were not likely to exist in the studied profiles.

Using knowledge of the diagnostic spectral properties of each mineral or mineral group, the entire spectra from each core were processed to make a down-hole mineral assemblage map of the core. The results of this processing are shown in Figure 9.9.

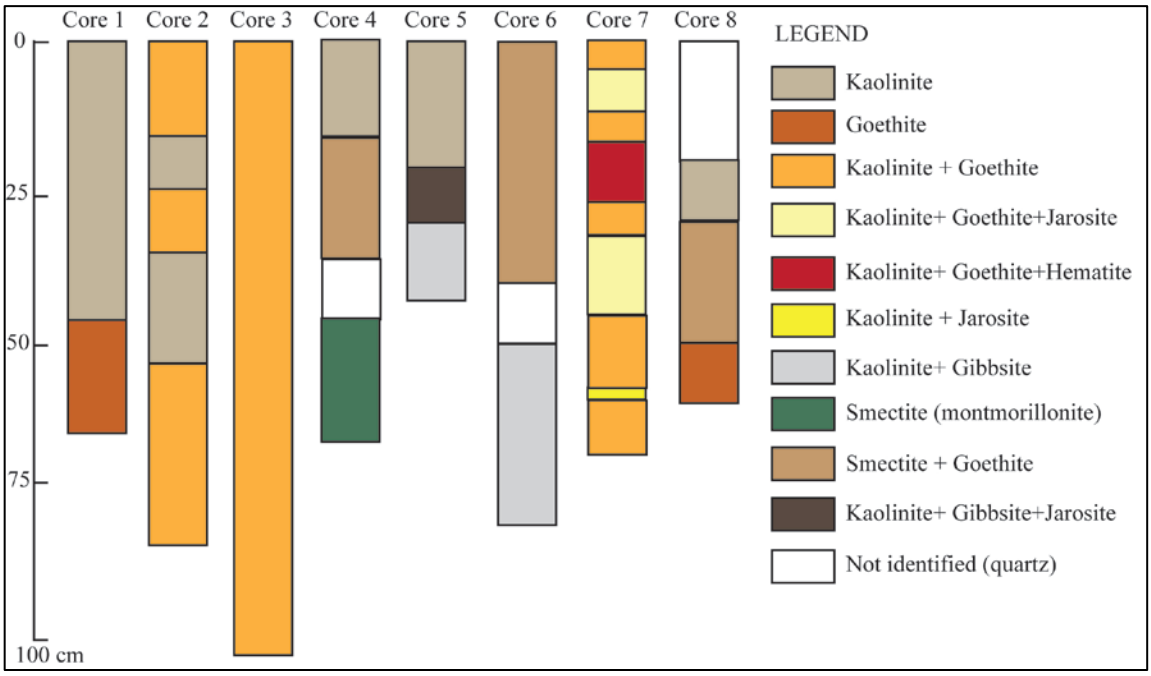

Figure 9.10: Distribution of main secondary minerals and mineral assemblages as interpreted from the HyLogger data of the studied soil profiles

The results of the mineral distribution showed that kaolinite was present in all the cores and at various depths and therefore was the most common aluminosilicate mineral in the ASS in the area. Based on the secondary mineral distribution of the soil profiles, there appeared to be some general links between the presence of specific mineral assemblages and the pH of the soil. Core 3, which was collected from an ASS area (oxidised sulphidic material), was dominated by kaolinite + goethite, and the pH values of this core varied between 3.98 and 4.3. Core 7, which was collected from a highly oxidised sulphidic material pile exhibiting the most intense features of ASS and acidic pH, had the mineral assemblages of kaolinite + goethite, kaolinite + goethite + jarosite, kaolinite + jarosite and kaolinite + goethite + hematite, and these mineral assemblages were linked to the intensity of the yellow-brown and red mottling through the core. The

pH values of this core were in the range of 2.68-3.35. Kaolinite + gibbsite was found in core 5 and core 6, and the pH values of these cores varied between 5 to 6.8. Smectite was observed in core 4, core 6 and core 8, and the pH values for these soils varied between 4.2 and 5.5.

The mineralogical and pH data from the cores allowed the construction of some empirical links between the presence of mineral and mineral assemblages and pH ranges. Kaolinite was found in all the cores and as such was not indicative of any acidic (pH) or neutral conditions in the soil profiles. The presence of specific and iron (goethite) and iron sulphate minerals (jarosite) was linked to the most acidic soil samples (pH <3.5), while the presence of goethite with kaolinite was indicative of less severe acidic conditions (3.5 to 4.2). The presence of gibbsite and kaolinite either singly or mixed was indicative of neutral conditions (5 to 6.8).

The absence or presence of trace amounts of other ASS-associated minerals such as ferrihydrite and schwertmannite in the subsurface was interesting. The cores represented the subsurface ASS profiles and not the surface of the ASS. Both ferrihydrite and schwertmannite have been widely detected in surface precipitates that arise from acid drainages (Bigham, 1994; Fitzpatrick, 1998; Sullivan and Bush, 2004). In comparison, not much research has been done on subsurface ASS mineralogy and the distribution of schwertmannite in the soil profiles (subsurface). The main iron sulphate mineral that has been identified in the subsurface is jarosite (or natrojarosite) (Fitzpatrick et al., 2008), and jarosite was identified in the soil profiles with intense oxidation in this study. It is likely that the formation of schwertmannite requires specific sulphate-rich oxidising conditions that were not common in the ASS subsurface under investigation in this study.

9.3.5 Separation of AASS and PASS

In core 1, the soil pH values above 45 cm were less than 4; thus, this part of the soils undoubtedly belonged to AASS. The soil below 45 cm had pH values in the range of 5-6.2 with relatively higher total sulphur contents and therefore the lower soil was classified as PASS. The mineralogy of this soil profile, however, was not clearly indicative of the AASS and PASS.

In core 2, goethite was distributed across most parts of the core from top to bottom, and the pH values of the soil above 65 cm depth were less than 4.3; thus, this part of the

soils could be grouped into AASS, while the remains which were below 65cm, containing goethite, with high pH values in the range of 6-8.52 and low sulphur contents, could be classified as PASS. However, there was a texture contrast separating the acid soil from the neutral to alkaline soil layer below. As suggested earlier (Section 9.3.1), the acidic soil above 65 cm had formed in sulphidic material excavated from the inlet and dumped over the existing deltaic sands (which started at 65 cm in the profile). Subsequent oxidation of the near surface sulphidic material had resulted in acidic conditions in the upper part of the soil with much of the original content of S being solubilised and leached, while the lower original sandy soil was still unaffected. Therefore, the upper soil was AASS, but the lower soil could not be classified as PASS as it was likely to not contain sulphides.

In core 3, which represented a soil profile developed in an oxidised sulphidic material pile, goethite and kaolinite dominated the entire core, with goethite present as brown mottles. The core pH varied between 3.94 and 4.3. The soil was accordingly classified as AASS. Although the total sulphur concentrations were relatively low, the reason was likely to be the leaching of the sulphur from the profiles due to intense oxidation. Oxidation and solubilisation of the sulphidic material has been found to result in the loss of S (Sohlenius and Ahern, 2004). For core 4 and core 8, both had relatively low average pH values of near 4, although the total sulphur contents were relatively low due to the consumption of pyrite when oxidising, so these could also be grouped into the AASS category.

In the soil profile from core 5, jarosite was observed at the depth of about 30 cm, and the pH of the soil above 30 cm was relatively low comparing the soil below; thus, the soils above 30 cm were grouped into AASS. The remainder had pH values of 6.47 on average, no secondary iron-bearing minerals but kaolinite and gibbsite were observed by the HyLogger detection, so they probably belonged to PASS or non-ASS, depending on the presence and absence of pyrite which could not be identified in the reflection spectral range and has not confirmed by SEM or XRD so far. However, usually, the sediments or soils which are located below a 5 metre elevation could be regarded as PASS (Degens, 2009), and the elevation of the site from which core 5 was collected was

below 5 metres; thus, the part of the soils below 30 cm in core 5 could be grouped into PASS.

Core 6 was collected from a site which was just 50 metres away from the site of core 5. The existence of an assemblage of kaolinite + goethite and relatively lower pH values (about 5 on average) of the soil above 35 cm suggested this part of the soils belonged to AASS, while the high pH (6.16 average) and lack of any iron-bearing minerals observed in the remains implied this part of the soils belonged to PASS. The soils across core 7 undoubtedly belonged to AASS because the whole core contained iron oxides or iron hydroxyl sulphates and had low pH values in the range from 2.68 to 3.29. The distributions of AASS and PASS in the 8 cores are illustrated in Figure 9.10, and the soil profiles of core 5 and core 6 are shown in Figure 9.11.

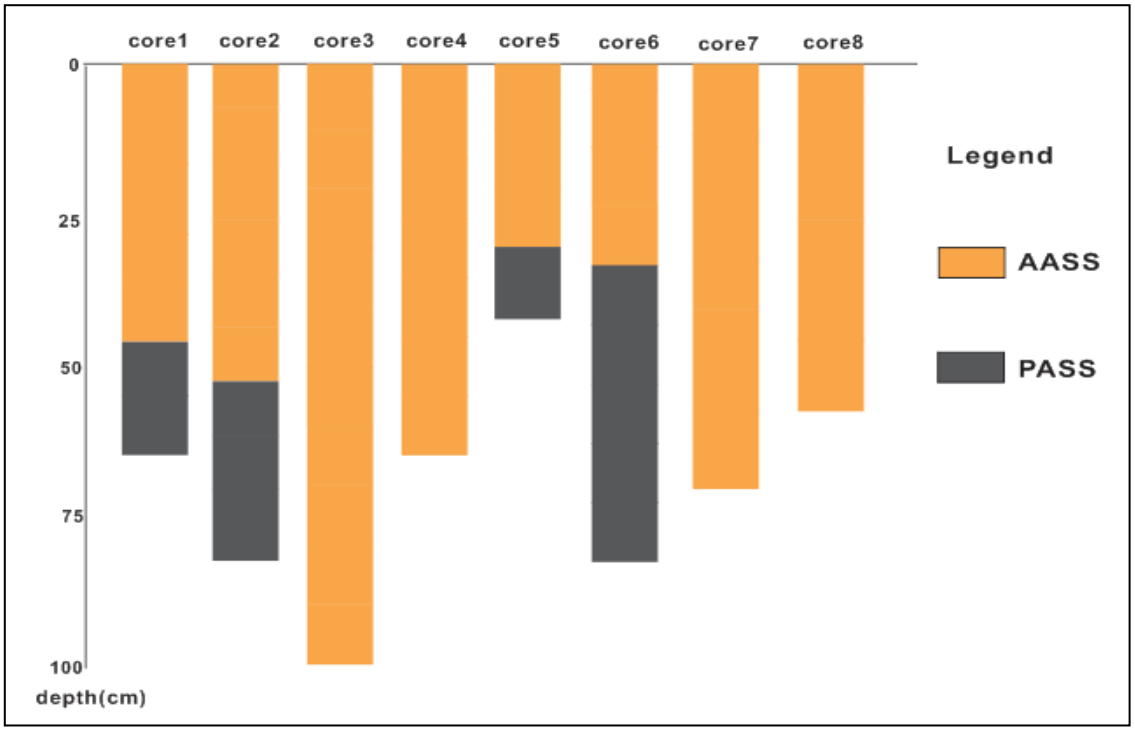

Figure 9.11: Separation of AASS and PASS in 8 cores

Figure 9.12: Soil profile of core 5 (left) and core 6 (right)

9.3.6 Correlation between soil pH and reflectance spectra by PLSR modelling

Given the empirical observations of the mineralogy and pH of soil profiles, a study to assess the relationship between the spectral properties and pH of the soil profiles was conducted. As for the surface samples (Chapter 7), the PLSR method was employed to examine the correlation between the soil profile pH and the reflectance spectra.

Sixty-four samples extracted from the 8 soil cores were used as a training dataset to establish the predictive model. The training dataset included the spectral data and corresponding pH values for each sample. Normalisation was applied for the spectral processing by utilising its own mean value, with the aim to remove unwanted spectral variability. As the values of the PRESS had a minimum value when factor number is 11, Eleven was taken as the optimum number of factors for establishing a robust PLS model. The R^2 of the relation between the actual pH and predicted pH reached 0.9515; this suggested that the model acquired via PLSR was very robust (Figure 9.12).

The final regression coefficient shows the influential weight in different spectral predictor variables. For example, a positive coefficient influences the response variable pH positively, while a negative coefficient affects pH negatively, and the bigger the absolute coefficient value of the predictor, the more significant impact on the pH value.

The final regression coefficient (FRC) (Figure 9.13) showed significant troughs which negatively influenced the pH value, including the bands (features) near 2.266, 0.69, 0.509 and 2.343 μm. Among these negative absorption features, 2.266 μm was the most influential feature which was very likely related to the diagnostic absorption feature of jarosite at 2.265 μm. The lesser influential feature at 0.509 μm was likely

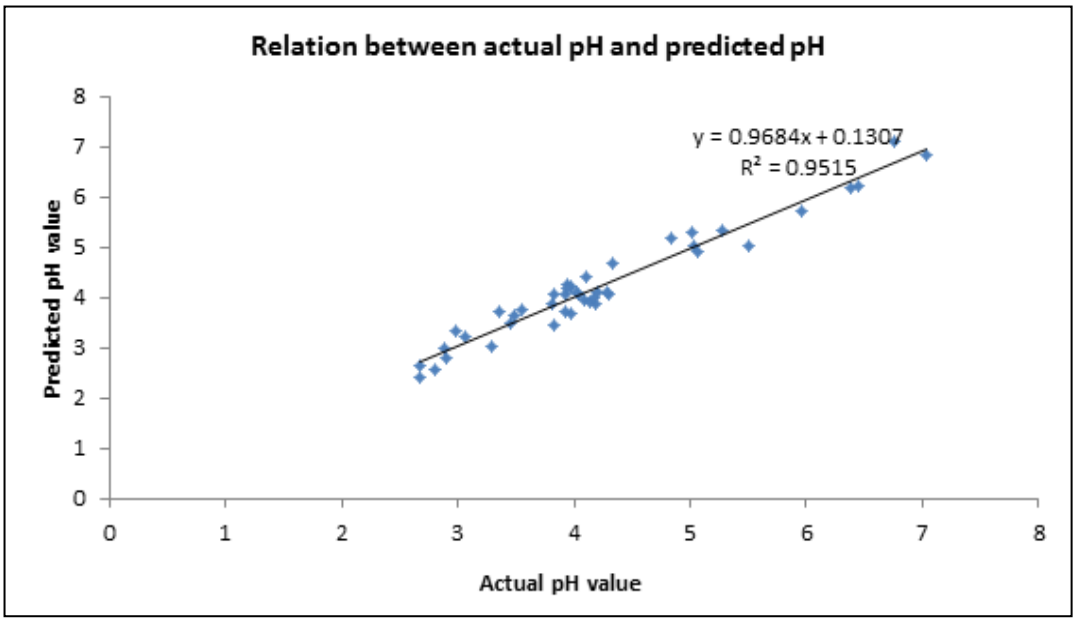

Figure 9.13: Relation between actual pH and predicted pH for soil profiles

related to the ferric absorption due to crystal effects, involving some iron-bearing minerals such as goethite and jarosite. Another less influential feature near 0.69 µm was likely related to the feature of goethite commonly observed at 0.66-0.7 µm, while the bands near 2.343 µm looked to be related to the absorption of gibbsite at 2.35 µm, or more likely related to the reflectance peak feature of jarosite at 2.345 µm.

There were some less significant features in the FRC plot which also negatively influenced the pH. The bands between 0.8-0.9 µm and the bands near 1.1 µm were possibly related to the ferric iron and ferrous iron crystal absorption of goethite. The feature near 1.9 µm was close to the absorption of jarosite at 1.85 µm. The reason why the features between 1.4 to 1.5 µm and between 1.6 to 1.7 µm negatively influenced the pH was unclear.

There were also significant positive peak points in the final regression coefficient plot which were indicative of positively influencing the pH. The main features were at 2.204, 0.395, 0.581, 1.868 and 2.467 µm, and less significant features were near 0.777, 1.077 and 1.248 µm. The feature at 2.204 µm may have been related to the absorption of kaolinite at 2.207 µm or it may likely be related to the absorption feature of gibbsite at 2.205 µm because kaolinite is commonly distributed in wide ranges of pH conditions.

The features near 0.395 and 0.581um were probably related to the reflectance peaks of gibbsite at 0.4 and 0.567 μm, and the features near 1.868 μm were likely related to the absorption of gibbsite in the range from 1.75 to 2.0 μm, while the feature near 2.467 μm was probably related to the absorption of gibbsite near 2.496 μm. The absorptions near 1.077 and 1.248 μm in the FRC plot were also possibly related to the absorptions of gibbsite near the range of 0.998-1.012 μm and the range of 1.24-1.28 μm, respectively. The reason for the features near 0.777 μm being linked positively to pH was unclear.

9.3.7 Application of the model to predict the pH distribution in soil profiles

The prediction model can be described as the sum of the FRC of certain wavelengths multiplied by the reflectance value at that wavelength after the normalisation operation. The pH prediction model was applied to the spectral measurements from the cores; the result of which provided the predicted pH and the distribution of the predicted pH (Figure 9.14). A comparison of the soil core pH measurements with that of the pH predicted via the PLSR model found that nearly 76% of the predicted pH values were very close to the real pH values, with the error less than 0.5 units. These high matches implied the relative robustness of the PLSR model. A detailed comparison of the pH measurements and pH predictions is shown in Figure 9.14. The comparison showed the predicted pH values to be slightly higher than the actual pH values for specific parts of the soil profile.

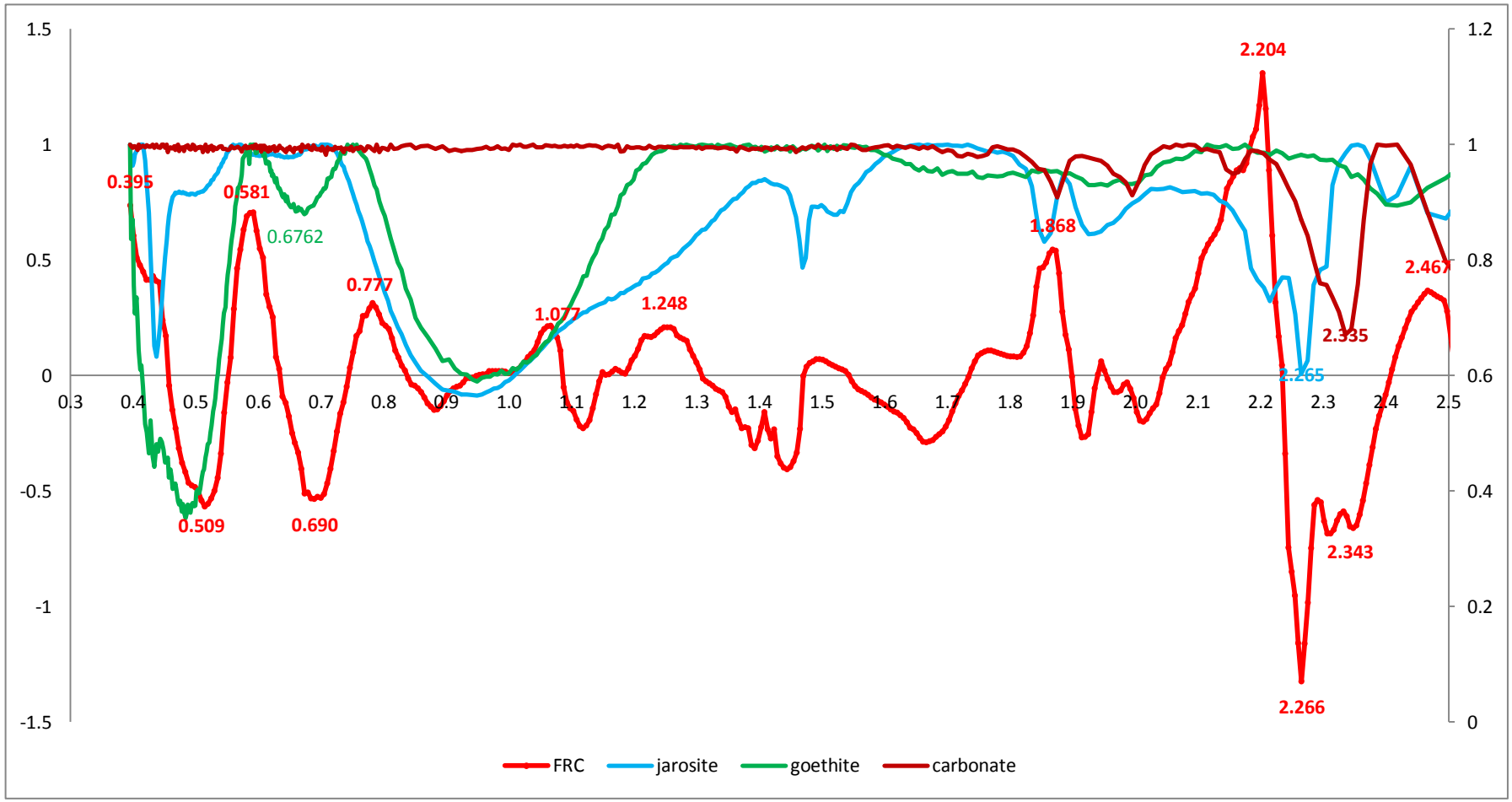

Figure 9.14: Final regression coefficient compared to continuum-removed spectra of ASS-related minerals; the X axis is the spectral wavelength in micrometers, the Y axis on the left is the FRC; the Y axis on the right is the reflectance response for the mineral spectra

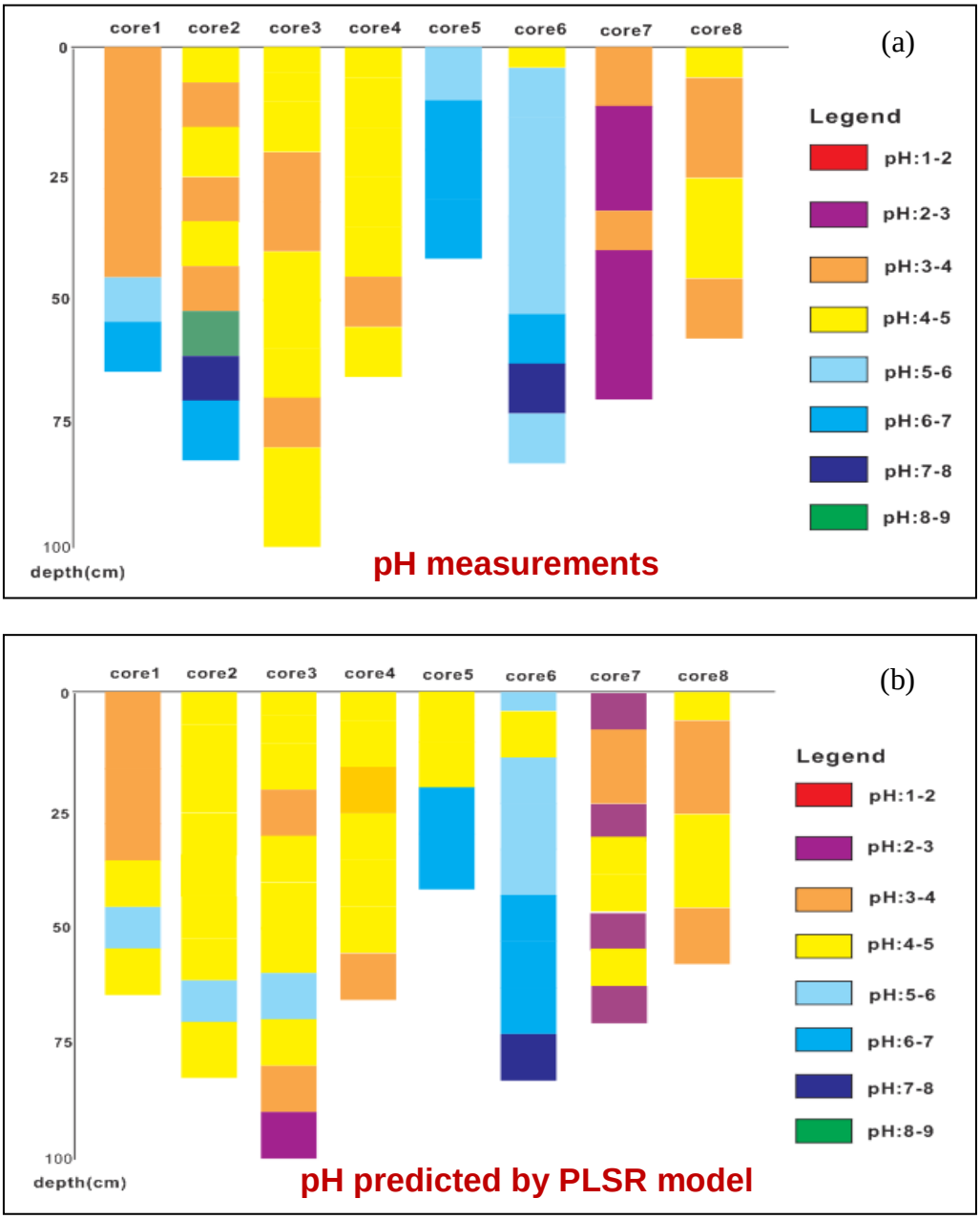

Figure 9.15: Comparison of the pH measurements and pH values predicted by the PLSR model. (a) Measured pH values for core samples; (b) pH values of the cores predicted by the PLSR model

9.3.8 Comparison of the pH at the top of the cores with the pH on the surface soil

In order to examine the relationship between the pH in the soil cores (subsurface) and the pH distributed on the surface of study area, the pH of the top layer soil of the cores was compared with the surface soil pH at the same location in the map deduced from the PLSR model (Chapter 7). The comparison showed that differences of a

single unit of pH were present; for some cores, the difference was less (core 7) and for some cores it was more (core 5). The details of the comparison are presented in Table 9.3 and Figure 9.15.

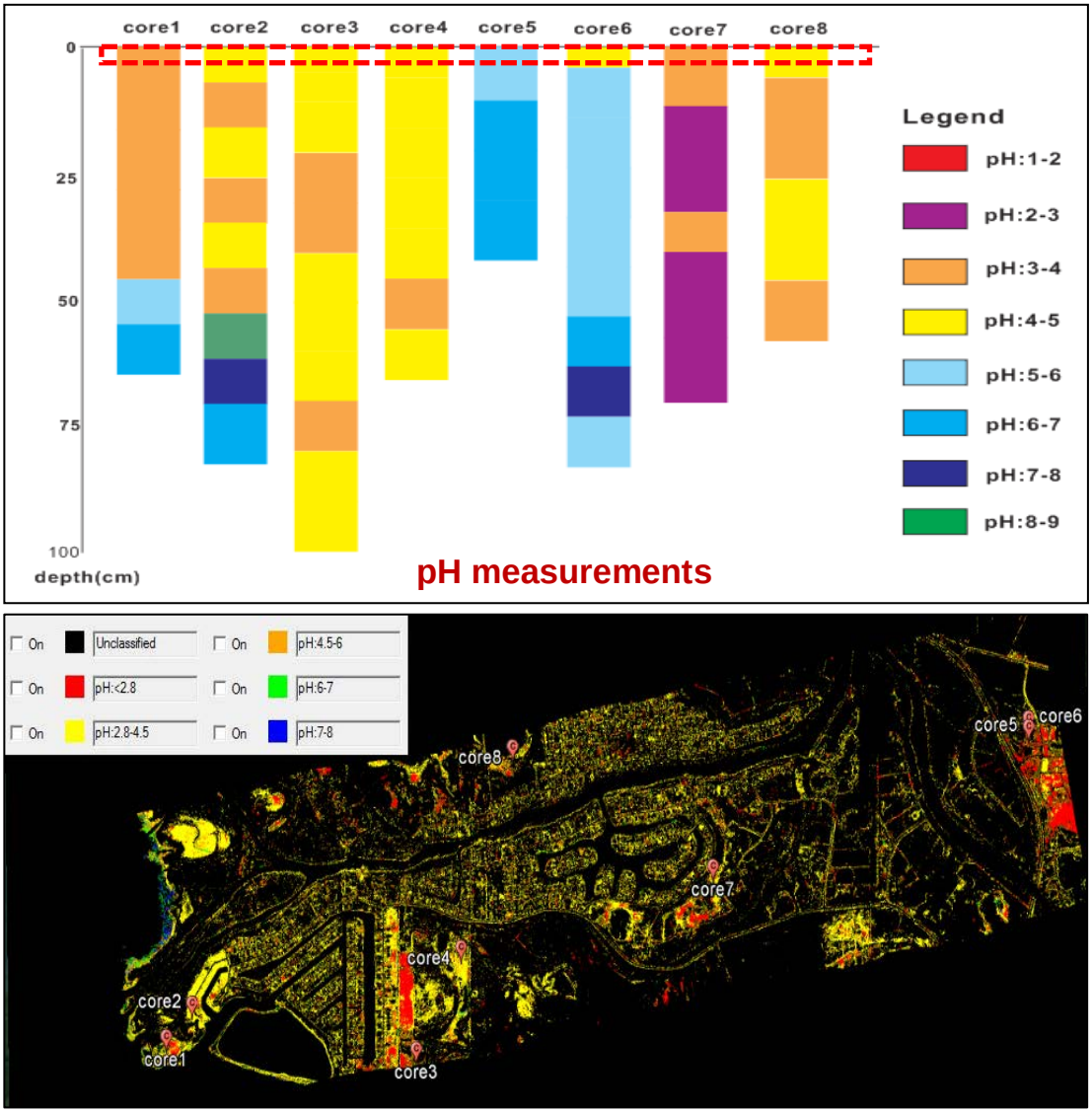

Figure 9.16: Comparison of the pH measurement of the soil in the top 5 cm of cores (marked by red dashed line) and pH map of the soil surface in the study area with core locations (reproduced from Figure 7.7)

Table 9.3: Comparison of the pH ranges of the soil in the top layer of the cores with the surface soil at the same location

Core	pH range in the pH map of the surface soil in the study area	pH range of the top layer soil in the cores
Core 1	4.5-6	3.4-4.0
Core 2	2.8-4.5	4.0-5.0
Core 3	2.8-4.5	4.0-5.0
Core 4	2.8-4.5	4.0-5.0
Core 5	2.8-4.5	5.0-6.0
Core 6	2.8-4.5	4.0-5.0
Core 7	2.8-4.5	3.0-4.0
Core 8	4.5-6	4.0-5.0

9.4 Conclusion

The mineralogy of ASS in the subsurface in the study area was identified via soil HyLogger scanning of 8 soil cores followed by spectral matching. The most common minerals included kaolinite and goethite which existed in most cores and at most depths of soils, while jarosite, hematite, gibbsite and montmorillonite were present in certain cores. SEM confirmation verified the effectiveness and reliability of the mineral identification using the combined method of HyLogger scanning and spectral matching. The map of the main iron-bearing minerals and aluminosilicates distributed in the cores, together with the pH and EC distribution in the subsurface, gave us a basis upon which to further separate the harmful actual acid sulphate soils and the harmless potential acid sulphate soils in the profiles, and thus provided a relatively comprehensive base for the assessment of ASS in the study area. The high value of R^2 in the model between the pH and the reflectance spectra, and the reasonable explanation of the final regression coefficient, proved the robustness of the model. The spectral features of jarosite, including absorption features and peak features, were the primary negative factors responsible for the pH changes. The absorption features of goethite were the second-most contributing factors negatively affecting the prediction of the pH values. The spectral features of gibbsite were the main factors impacting positively on the pH changes.

In conclusion, the ASS in the subsurface were characterised spectrally and the mineralogy was mapped by introducing the HyLogger instrument, and more importantly, the harmful AASS and the harmless PASS were separated based on the mineralogy information and pH measurements. Furthermore, due to the

establishment of the relationship between pH values and spectral features, the soil pH could be predicted for a continuous soil core in the future by applying the model instead of measuring soil pH; thus, it could improve the assessment of ASS in the subsurface. The next chapter presents the conclusions drawn from the main aims of the study.

Chapter 10 Conclusions

The research reported in this thesis used hyperspectral remote sensing to characterise, map and monitor acid sulphate soils and their environmental effects in a rapidly urbanising township located within a coastal zone in south-western Australia. The specific aims were to investigate the spectral changes occurring during the mineralogical and geochemical evolution of the oxidation of sulphidic materials, identify ASS-specific secondary minerals via proximal and airborne hyperspectral remote sensing, establish the link between indicative minerals and soil pH, and model the direct relationship between the spectral features and soil pH on the surface and subsurface; and more importantly, to map the environmental impacts, especially soil acidity and Al toxicity. These objectives were successfully achieved. This chapter summarises the main results and novelties of this study and recommends directions for future work.

10.1 Main Results and Findings

The main results and findings of this study fell in six categories:

1. the chemical and mineralogical changes, and related environmental impacts occurring during the controlled oxidation of sulphidic material under naturally simulated conditions;
2. the surface mineralogical changes accompanying oxidation of sulphidic material as detected via reflectance spectra;
3. the main mineral composition and spectral characterization of ASS;
4. the mapping of surface soil acidity using the link between indicator minerals and pH values and comparing it to pH mapped via the PLS method;
5. the mapping of potential toxicity using the pH map and aluminosilicate mineral maps; and finally,
6. examining the application of hyperspectral data to mapping the subsurface soil mineralogy and pH.

Incubation experiments were conducted to observe the change of chemical properties, mineral transformation and reflectance spectral variations during the simulated formation and evolution of the AAS (Chapter 4 and Chapter 5). The results presented in Chapter 4 revealed the mineral transformation and accompanying

chemical changes in variable duration wetting and drying conditions that mimicked some natural conditions. The findings reiterated that the importance of the presence of water and oxygen to the occurrence of pyrite oxidation and the formation of acid sulphate soils, and the supply of water and oxygen is usually influenced by the wetting and drying conditions. The repeated flushing of the sulphidic material greatly facilitated the development of ASS and produced stable iron oxide minerals, while the material subjected to lesser flushing, and therefore lower water interaction, showed comparatively less oxidation and produced mainly intermediary to meta-stable iron hydroxysulphate minerals. The incubation results suggested that surface sulphidic soils or sediments that were exposed to high rainfall conditions could be more rapidly oxidised and transformed to ASS than those in drier semi-arid conditions or on landforms that were less subject to wetting-drying cycles. Long-term drying, however, may promote desiccation cracks, facilitating pyrite oxidation deeper in the soil or sediment, which is dependent on grain size and depositional facies of the sediment, and may also promote oxidation over a larger surface area. The results also suggested the sulphate release rate could be used as a proxy for the sulphidic material oxidation rate. The oxidation rate, together with the thickness of the oxidised layer within the sulphidic material measured after experiment, could be used to assess the evolution and changes of the acid sulphate soils in different weather conditions, as well as the negative environmental impacts due to trace metal release during oxidation.

The investigation of the surface mineralogical evolution of ASS during the controlled oxidation of the sulphidic material via the reflectance spectra (Chapter 5) showed that the sulphidic material, on oxidation and drying developed and evolved three distinct micro-reliefs or micro-landforms. The surface of these micro-landforms was characterised by specific secondary iron sulphate and iron oxyhydroxide minerals, as revealed by the proximal spectral measurements, and the mineral evolution for each micro-landform was governed largely by evolving drainage conditions (differences in drying immediately below the micro-landform). The micro-landform that oxidised rapidly and dried rapidly promoted rapid evaporation, and the evaporation favoured the formation of ferrous-ferric sulphate salts, namely, copiapite. The mineralogy remained consistent as the oxidation progressed, because the micro-landform consistently experienced high evaporation and thereby a very low pH (<2) in the surface soil. In the micro-landform with moderate saturation,

copiapite developed initially, but gradually the comparatively poorer drainage resulted in lesser evaporation and greater saturation, leading to the oxidation of Fe and S, followed by ferric iron hydrolysis and precipitation of jarosite and goethite. In the landform with moderate drainage, and high oxidation and saturation, the hydrolysis of the ferric iron resulted in goethite being the dominant mineral together with lesser jarosite, but negligible copiapite, which was indicative of greater oxidation and higher pH (pH >4). The findings of the saturation state or drainage-based changes in the surface mineralogy were consistent with those found at acid drainage sites. The characterisation of the mineralogical changes on the surface of the oxidising sulphidic material via the proximal spectral measurements and the interpreted underlying pH range and saturation states provided a framework through which to test and apply airborne hyperspectral sensing to map similar surface mineralogy across the study area.

Chapter 6 presented the examination of the mineralogy and the spectral characterization of the ASS in the study area. The examination revealed the overall mineral composition of the soil/sediments in the study area. The dominant minerals in the ASS samples studied were the inherited minerals, quartz, kaolinite, halite and calcite, and the minerals formed as a result of ASS oxidative formation such as goethite, jarosite, schwertmannite, gypsum and copiapite. The reflectance spectral features of the ASS minerals were investigated and characterised. A variety of different subtypes of ASS were grouped by pH ranges and mineral compositions, and their spectral characterisations were presented. These relatively systematic spectral characterisations of the acid sulphate soils were very helpful to understand the characteristics of different AAS and choose proper end-members to further identify and map the distribution of the AAS, and also aided to confirm the link among the pH values, indicative mineral composition and spectral features.

An investigation was conducted into the applicability of the HyMap dataset over a known ASS affected area to map soil surface pH values via two different methods. The soil pH map deduced from the distribution of the pH indicative minerals showed that jarosite, or a mixture of jarosite and another iron oxide/oxyhydroxide or iron oxysulphate (like schwertmannite), indicated the presence of low pH surface conditions, while goethite and ferrihydrite appeared as indicators of higher soil pH conditions (closer to neutral). In contrast, the soil surface pH map deduced from the PLSR model (as pH ranges) was consistent with the final regression coefficients in

the PLSR model derived from the laboratory spectral and pH measurements on the field samples. The PLSR model showed high negative coefficients for the wavelengths related to the absorption features of jarosite, which forms and persists largely in low pH conditions (pH <4.5). The PLSR model showed high positive coefficients for the wavelengths related to the absorption features of ferrihydrite, which usually forms at higher pH conditions and also in the absorption features related to carbonates, which have the acidity buffering capability. A comparison between the two methods that were used to map the surface acid ranges found that approximately 94% of the pixels in the pH classification maps deduced from the two different methods to be highly similar. The high correlation suggested that the PLSR model established in this study was robust and suitable for predicting soil surface acidity arising in response to ASS in the study area, and the relationships between indicative iron oxide/oxyhydroxide and iron sulphate-bearing minerals and pH values were reliable. More importantly, the high correlation between the two methods indicated the high accuracy of the mapping results of the distribution soil pH and indicative iron-bearing minerals.

Much of the work on using hyperspectral remote sensing for acid environments has been to map acidity or pH ranges, largely in acid mine drainage environments. The negative issues created by the low pH such as major and trace metal release and spread have as yet not been investigated via remote sensing methods. One of the main negative issues linked to ASS is the release of mobile Al in the soil pore waters and hydrologically connected waterways, thereby causing Al toxicity and damaging ecosystems. The reason for Al release in acid environments is the reaction of aluminosilicates with acid pore waters to buffer the acid, with kaolinite dissolving only at pH <4.5. A map of soil Al bearing minerals, mainly kaolinite and to a lesser extent gibbsite, was constructed using HyMap data. The secondary aluminosilicate mineral map was combined with the pH map generated by the PLSR modelling methods (Chapter 6) to construct five potential categories of Al toxicity across the area, with the highest toxicity level being represented by very low pH (<4) and an abundance of kaolinite and gibbsite and the negligible toxicity category represented by neutral pH and low kaolinite presence.

The mineralogy of ASS in the subsurface in the study area was identified and mapped via soil coring, HyLogger scanning and spectral matching. The common secondary soil minerals that could be detected and mapped were kaolinite, goethite

and gypsum which existed through most depths of the soil profiles. The other secondary minerals that were detected, namely, jarosite, hematite, gibbsite and montmorillonite, were only observed in some cores, with the oxidised sulphidic material soils showing the presence of an acid indicator mineral, jarosite, and the neutral pH soils being composed mainly of kaolinite and montmorillonite. The harmful AASS and harmless PASS were separated in the profiles based on the distribution of the secondary iron-bearing minerals and pH distribution on the subsurface.

10.2 Correlations among the Results

Among the results and findings listed above, there were some correlations. The observations of the incubation experiments suggested the relatively quick changes in mineral transformation during the evolution of ASS, and these changes may have been responsible for the differences between the ground truths and mapping results. From the mapping results, including the mineral mapping and soil pH mapping results, merely 65-70% of the ground truths were consistent with the mapping results; this was very possibly because the relatively high rate of changes occurred during the period after the acquisition of the HyMap image. The relatively low pH measurements of the solution from the incubation experiment were consistent with the pH map which suggested most that most of the area was in low pH conditions. Furthermore, the high concentration of Al^{3+} of the solution observed during the whole incubation experiment, highlighted the importance of the assessment of Al^{3+} in Chapter 8, which assessed the Al toxicity in study area. It verified also the result of the severity of Al toxicity in study area to some extent. The link between the spectral variations and the mineral transformation with the micro-landforms and oxidation stages observed in the incubation experiment also helped us to understand the mapping result of the mineral and soil pH in the different landforms, as well as to interpret the distribution of the minerals, total sulphur contents and the separation of the PASS and AASS in the subsurface.

The results of the soil pH distribution of the surface soil were deduced from two methods which were consistent with each other, and more importantly, the pH values in the resulting map (deduced from the PLSR model) were consistent with the pH measurements of the top layer soil of the cores collected from the corresponding

location; this further proved the relatively high accuracy of the results both on the surface and in the subsurface.

Spectral characterization of different subtypes of ASS conducted in Chapter 6, and the linkage between mineral species or mineral assemblages presented in Chapter 6, provided good understanding to select end-members for mapping ASS in Chapter 7.

The difference between the two predictive models (a model for the surface and a model for the subsurface) was most likely due to the variation of the mineral distribution between the surface and subsurface. The PLSR model acquired for the prediction of the soil pH on the surface soil was mainly negatively related to the spectral features of jarosite and copiapite which usually form in low pH conditions; it was positively related to the spectral features of ferrihydrite which usually forms in high pH conditions, positively related to the spectral features of carbonate which has the acidity buffering capability, and positively related to the spectral features of goethite which could form in a wide range of pH conditions. The PLSR model for the prediction of the soil pH in the subsurface was mainly positively related to the spectral features of gibbsite, although still negatively related to the spectral features of jarosite, but also negatively related to goethite. The difference between two models was because they were based on different training datasets. The training datasets collected from the surface soil were mostly from the actual acid sulphate soils and therefore contained most iron oxides/oxyhydroxides or iron sulphates, and importantly, were found to contain gibbsite. In contrast, the datasets collected from the subsurface were from both the actual acid sulphate soils which contained iron oxides/oxyhydroxides or iron sulphates, and the potential acid sulphate soils which had not been oxidised and therefore did not contain oxides/ oxyhydroxides or iron sulphates, and more importantly, gibbsite was found in these subsurface samples.

The difference between the two models in the same study area suggested the pH mapping result by the predictive model was training dataset-dependent, while the result via the indicative minerals was more universal. Although the result of the pH of the surface soil deduced from the PLSR model was more consistent with the ground truth data, the method may be constrained to a specific area and may have been dependent on the specific training data. Meanwhile, the method via the mapping of the indicative mineral was more universal because the link between the

pH values and minerals has been proved by numerous previous studies and applications in other areas.

10.3 Novelties of the Study

There were some novelties in the results of this study. Firstly, with respect to the methodology, this study involved multiple hyperspectral instruments, together with conventional methods, to map the extent and severity of acid sulphate soils. Most of the previous studies usually used one or two hyperspectral instruments, such as airborne or spaceborne hyperspectral sensors, and a proximal sensor such as an ASD for ground truth. This study applied the airborne sensor HyMap, proximal spectrometer ASD, and also the HyLogger system. The combination of these different instruments which were used for different purposes made the assessment of the acid sulphate soils and environmental effects more comprehensive, overcoming the limitation of detecting the surface of the Earth by conventional remote sensing and the constraints in merely detecting the subsurface by traditional chemical methods or by proximal sensing.

Secondly, this study continued to trace the changes in chemical properties, mineral transformation and spectral variations during the formation and evolution of acid sulphate soils by setting up an incubation experiment with natural sulphidic materials. This study found that the different changes in mineral transformation, sulphate release rate and trace metal release occurred in the different drying and rewetting weather conditions, and the changes were related to the landform, water supply and stage of oxidation. The link observed between the changes in chemical properties, mineral compositions and spectral characteristics suggested an alternative way to assess the changes in acid sulphate soil by measuring the reflectance spectra.

Thirdly, most of the previous studies on acid sulphate soils have mainly focused on mineral identification and mapping or on the chemical properties in this soil. No previous study had combined the use of mapped surface pH with the presence of buffering aluminosilicate minerals in the soil as a proxy for potential Al toxicity. This study used the HyMap constructed surface pH map of the soil together with the aluminosilicate occurrence map of the area to provide a potential toxicity index. Low pH with moderate to high kaolinite-bearing soils was likely to result in the

dissolution of kaolinite, releasing mobile Al to the immediate environment and thereby increasing the chances of Al toxicity.

Fourthly, this study attained a robust predict model and applied it to successfully produce a relatively accurate soil pH map. The established model was reasonably interpreted and the prediction results were proved by the ground truths.

Fifthly, this study relatively systematically characterized the different subtypes of ASS in reflectance spectra and linked the mineral composition, soil pH values and spectral features together. The spectral characterization and the linkage could be useful to characterize, identify and map ASS by hyperspectral sensing, both by proximal or remote method.

10.4 Future Works

This study assessed the AAS and their environmental impacts both on the surface and in the subsurface of the study area so far. The results attained suggested the possibility of predicting the evolution and environmental changes in the future because this study identified the oxidation rate of the iron sulphides, the mineral composition and the distribution of the actual and potential acid sulphate soils in the subsurface. While, the oxidation rate would not keep constant as the oxidation further deepen in the subsurface because the soil on the top could prevent the oxygen. Furthermore, this study merely conducted the separation of the actual acid sulphate soils and potential acid sulphate soils in 8 soil cores, and this study did not identify the boundary between these two types of ASS across much of the study area. Therefore, the dataset collected was not sufficient to predict the further evolution of acid sulphate soils and their environmental impacts quantitatively. In order to make a better assessment and prediction of the spread and severity of acid sulphate soils in this area, further work is required and proposed as follows:

1. To update the current assessment of the surface soil which was based on the HyMap data acquired 7 years ago by applying new remotely sensed imagery. Some new and improved sulphidic hyperspectral sensors could be employed, such as the German Environmental Mapping and Analysis Program, which has a spectral resolution of at least 10 nm in the spectral range from 0.42 μm to 2.45 μm and a spatial resolution of 30 m×30 m with a swath width of 30 km, and the Japanese hyperspectral image suite (HISUI) which has 185 bands in the range of 0.4-2.5 μm with 30 metre spatial resolution. Both these instruments have much

coarser spatial resolution, but based on the methodology and results from the present study, they could be employed to map and monitor ASS over larger areas along coastal plains around Australia.

2. To further observe the oxidation of the iron sulphide material to attain more information about the oxidation rate in the different development phases of ASS.
3. To enhance the use of the HyLogger^{TM} system to map the subsurface soils affected by ASS. This study used the HyLogger on only 8 soil cores; a more robust dataset of more cores is required to map the subsurface accurately and produce a 3-D map of the distribution of the mineral composition, chemical properties and the separation of the two types of ASS.
4. To expand the research into the relationship between the growth and distribution of vegetation and the spatial spread of acid sulphate soils, particularly with respect to the environmental impacts of ASS. Hyperspectral remote sensing can be used to study and map vegetation affected by acid sulphate soils, which is a critical environmental aspect not considered in this thesis. Another critical environmental issue that can be potentially mapped and monitored via hyperspectral imagery is the quality of the surface waters affected by ASS. Litle research has been done on the relation between water quality and the distribution of flocs and water colour affected by acid sulphate soils.

References

Ahern, C.R., McElnea, A.E., Sullivan, L.A., 2004. Acid Sulphate Soils Laboratory Methods Guidelines. Queensland Department of Natural Resources, Mines and Energy, Indooroopilly, Queensland, Australia.

Alpers, C. N., Blowes, D. W., Nordstrom, D. K., and Jambor, J. L., 1994. Secondary minerals and acid mine-water chemistry. In Environmental Geochemistry of Sulphide Mine-Wastes, edited by Jambor, J. L. and Blowes, D. W. Mineral. Assoc. Canada Short Course Handbook, vol. 22, pp.247-270.

Anderson, J.H., and Robbins, E.L., 1998. Spectral reflectance and detection of iron-oxide precipitation associated with acid mine drainage. *Photogrammietric Engineering & Remote Sensing*, vol.64 (12), pp.1201-1208

Anderson, J.H., Flohr, M., Nord, G., Podwysocki, M., Prugh, B., Stanton, M., Sweet, P., 1995. Application of the microbial and spectral reflectance technique (MAST) to the identification of acid mine drainage at contrary creek, louisa county,Viginia. U.S department of the interior- U.S. Geology Survey

Anderson, J.E., 1994. Spectral Characterization of Acid-Mine and Neutral-drainage Bacterial Precipitates and Their Relationship to water Quality in a Piedmont Watershed. *Virginia Journal of Science*, vol. 45, 175-185.

Andrew, R., 2011. SODA: A new method of in-scene atmospheric water vapor estimation and post-flight spectral recalibration for hyperspectral sensors Application to the HyMap sensor at two locations. *Remote Sensing of Environment*, Vol. 115, pp. 536–547.

Baptista, G.M.M., Martins, E.S., Madeira Netto, J.S., Carvalho, O.A., Meneses, P.R., 1998. Use of AVIRIS Data for Mineralogical Mapping in Tropical Soils in the District of SoJoo D'Aliana, GoisÓ. Proceedings of the Seventh Airborne Visible/Infrared Imaging Spectrometer (AVIRIS) Workshop, JPL Publications 97-21, vol.1, pp.33-42.

Basciano, L.C., 2008. Crystal Chemistry of the Jarosite Group of Minerals: Solid-solution and atomic structures. Thesis of Doctor of Philosophy in Queen's University, Canada.

Bastian, L.V., 1996. Residual soil mineralogy and dune subdivision, Swan Coastal Plain, West Australia. *Australian Journal of Earth Science,* Vol. 43, pp. 31-44.

Baumgardner, M.F., Silva, L.F., Biehl, L.L., & Stoner, E.R., 1985. Reflectance properties of soil. *Advances in Agronomy,* Vol. 38, pp. 2-44.

Ben-Dor, E., 2002. Quantitative remote sensing of soil properties. *Advances in Agronomy*, Vol. 75, pp.173-243.

Berman, M., Bischof, L., and Huntington, J., 1999. Algorithms and software for the automated identification of minerals using field spectra or hyperspectral imagery. Paper presented at the International Conference on Applied Geologic Remote Sensing, 13th, Vancouver, BC, Canada, Ann Arbor, Environmental Research Institute of Michigan, Proceedings, pp. 222–232.

Berner, R.A., 1984. Sedimentary pyrite formation: an update. *Geochemica. Cosmochimica Acta,* Vol. 48, pp. 605-615.

Berner, R.A., 1970. Sedimentary pyrite formation. *American Journal of Science,* vol.268, pp.1-23.

Bigham, J.M., 1994. Mineralogy of ochre deposits formed by sulphide oxidation. In: Jambor, J.L., Blowes, D.W. (Eds.), Environmental Geochemistry of Sulphide Mine-Wastes, Mineral. Assoc. Can. Short Course 22.

Bigham, J.M., and Nordstrom, D.K., 2000. Iron and Aluminium hydroxysulphates from acid sulphate waters. In: Alpers,C.N.; Jambor, J.L. & Nordstrom, D.K. (Eds.) sulphate minerals: crystallography, geochemistry and environmental significance.Washingto,D.C., Rev. Mineral geochem., Min, Soc. Am. And Geochem. Soc., Vol.40, pp.351-403

Bigham,J.M., Fitzpatrick,R.W., Schulze, D.G., 2002. Iron oxides. Soil science society of America, 677 south segoe Road, Madison,WI 53711,USA. Soil mineralogy with environmental applications. SSSA book series, No.7.

Bigham, J.M., Schwertmann, U., Carlson, L., and Murad, E., 1990. A poorly crystallized oxyhydroxysulphate of iron formed by bacterial oxidation of Fe(II) in acid mine water. *Geochimica Cosmochimica Acta*, Vol.54, pp. 2743-2758

Bigham, J.M., Carlson, L., and Murad, E., 1994. Schwertmannite, a new iron oxyhydroxysulphate from Pyhasalmi, Finland, and other localities. *Mineralogical Magazine*, Vol. 58, pp. 641-648

Blowes, D.W., Ptacek, C.J., Jambor, J.L., Weisener, C.G., 2003. The geochemistry of acid mine drainage. In Holland, H.D and Turekian, K.K (eds). Treatise on Geochemistry, Vol. 9, pp. 149-204.

Boardman, J.W., Kruse, F.A., 1994, Automated spectral analysis: a geological example using AVIRIS data, north Grapevine Mountains, Nevada. In Proceedings, ERIM Tenth Thematic Conference on Geologic Remote Sensing, Environmental Research Institute of Michigan, Ann Arbor, I-407 - I-418.Bolland M.,1998. Soils of the Swan Coastal Plain, Agriculture Western Australia, Bunbury

Borengasser, M., Hungate, W.S., 2008. Watkins R.S., Hyerpsetral remote sensing principles and applications , CRC press , Taylor &Francis Group

Buckby, T., Black, S., Coleman, M. L., and Hodson, M. E., 2003. Fe-sulphate-rich evaporative mineral precipitates from the R|¨o Tinto, southwest Spain. *Mineralogical Magazine*, Vol. 67(2), pp. 263–278

Burns, R.G., 1993. Origin of electronic spectral of minerals in the visible to near-infrared region. In: Pieters, C.M., Englert, P.A.J.(Eds.), Remote Geochemical Analysis: Elemental and Mineralogical Composition, vol. 4. Cambridge University Press, Cambridge, UK, pp. 3-29.

Burton, E., Bush, R., Sullivan, L., 2006. Acid-volatile sulphide oxidation in coastal flood plain drains: Iron-sulphur cycling and effects on water quality. *Environmental Science & Technology*, Vol. 40, pp. 1217-1222.

Bush, R.T., Sullivan, L.A., 1997. Morphology and behaviour of greigite from a Holocene sediment in eastern Australia. *Australian Journal of Soil Research*, Vol.35, pp.853-861.

Campbell, J.B., 2007. Introduction to remote sensing-fourth edition, the Guillford press, ISBN-13-978-1-59385-319-8, ISBN-10 1-59385-319-X.

Carroll, S. A. and Walther, J. V., 1990. Kaolinite dissolution at 25, 60 and 80°C. *American Journal of Science*, Vol. 290, pp. 797-810.

Cama, J., Metz, V., and Ganor, J., 2002. The effect of pH and temperature on kaolinite dissolution rate under acidic conditions. *Geochim. Cosmochim. Acta*, Vol. 66, pp. 3913-3926.

Chang, C.I., 2003. Hyperspectral imaging techniques for spectral detection and classification, ISBN 0-306-47483-2.

Chen, J. Y., and Reed, I. S., 1987. A detection algorithm for optical targets in clutter. *IEEE Trans. on Aerosp. Electron. Syst.*, vol. 23(1).

Clark, R. N., 1999. Spectroscopy of Rocks and Minerals, and Principles of Spectroscopy, in Manual of Remote Sensing, Volume 3, Remote Sensing for the Earth Sciences, (A.N. Rencz, ed.) John Wiley and Sons, New York, pp. 3- 58.

Clark, R.N., & Swayze, G.A., 1991. Mapping with imaging spectrometer data simultaneously fit to multiple spectral features from multiple materials: in Proceedings of the Third Airborne Visible/Infrared Imaging Spectrometer (AVIRIS) Workshop, JPL Publication 91-28, pp. 2-3.

Clark, R.N., Gallagher, A.J. and Swayze, G.A. 1990. Material absorption band depth mapping of imaging spectrometer data using the complete band shape least-squares algorithm simultaneously fit to multiple spectral features from multiple materials. Paper presented at the Third Airborne Visible/Infrared Imaging Spectrometer (AVIRIS) workshop, JPL Publication 90-54, pp. 176-186.

Clark, R.N., Swayze, G.A., Wise, R., Livo, E., Hoefen, T., Kokaly, R., Sutley, S.J. 2007. USGS digital spectral library splib06a: U.S. Geological Survey, Digital Data Series 231.

Cloutis, E.A., Hawthorne,F.C., Mertzman,S.A., Krenn,K., Craig, M.A., Marcino,D., Methot, M., Strong, J., Mustard, J.F., laney, D.L., Bell III,J.F., and Vilas, F.,

2006. Detection and discrimination of sulphate minerals using reflectance spectroscopy. *Icarus* 184, pp. 121–157

Cocks, T., Jenssen, R., Stewart, A., Wilson, I., and Shields, T., 1998. The HyMap^{TM} airborne hyperspectral sensor: The system, calibration and peformance. Presented at 1st EARSEL Workshop on Imaging Spectroscopy, Zurich, October 1998.

Cornell, R.M., and Schwertmann, U., 2003. The iron oxides: structure, properties, reactions, occurrences and uses, second edition, Weinheim ; [Cambridge] : Wiley-VCH, 2003.

Cowardin, L.M., Carter, V., Golet, F.C., and La Roe, E.T., 1979. Classification of wetlands and deepwater habitats in the United States. U.S. Dept. Interior, Fish & Wildlife Service, FWS/OBS-79/31.

Cozzolino, D., Moroe´n, A., 2006. Potential of near-infrared reflectance spectroscopy and chemometrics to predict soil organic carbon fractions. *Soil & Tillage Research*, Vol. 85, pp. 78–85.

Crowley, J.K., Williams, D.E., Hammarstrom, J.M., Piatak, N., and Chou, I.M., 2003. Spectral reflectance properties (0.4–2.5 μm) of secondary Fe-oxide, Fe-hydroxide, and Fe-sulphate-hydrate minerals associated with sulphide-bearing mine wastes. *Geochemistry: Exploration, Environment, Analysis*, Vol..3, pp..219-228.

CSIRO, 2009. Groundwater yields in south-west Western Australia. A report to the Australian Government from the CSIRO South-West Western Australia Sustainable Yields Project. CSIRO Water for a Healthy Country Flagship, Australia.

Cudahy, T.J., and Ramanaidou, E.R., 1997. Measurement of the hematite:goethite ratio using field visible and near-infrared reflectance spectrometry in channel iron deposits, Western Australia. *Australian Journal of Earth Science,* Vol.44, pp.411-420

Cudahy,T.J., Caccetta, M., Cornelius, A., Hewson, R.D., Wells, M., Skwarnecki, M., Halley, S., Hausknecht, P., Mason, P. and Quigley, M., 2005. Regolith geology and ateration mineral maps from new generation airborne and satellite remote

sensing technologies; and Explanatory Notes for the Kalgoorlie-kanwna 1:100,000 scale map sheet, remote sensing mineral maps. Perth, MERIWA Report No.252, pp.114

Davidson, W.A., 1995. Hydrogeology and groundwater resources of the Perth Region, Western Australia. *Western Australia Geological Survey, Bulletin,* Vol.142.

Deer, W.A., Howie, R.A., and Zussman, J., 1992. An Introduction to the Rock-Forming Minerals, second edition. Halsted Press

Degens, B.P., 2006. Metadata Statement for the Acid Sulphate Soil Risk Map, Swan Coastal Plain, Western Australia. Department of Enviroment and Conservation, Western Australia.

Degens, B.P., 2009. Acid sulphate soil survey of superficial geological sediments adjacent to the Peel-Harvey Estuary. Report from Department of Environment and Conservation, Government of Western Australia. pp.105.

Degens, B. P., Fitzpatrick, R., George, R.W., Rogers, S., and Smith, M., 2008. Ch10. Avon Basin, WA Wheatbelt: An Overview of Geochemical Risks of Saline Acidic Discharge from Deep Drains Used to Manage Dryland Salinity in Western Australia. In Inland Acid Sulphate Soil Systems Across Australia (Eds. Rob Fitzpatrick and Paul Shand). pp 169-175. CRC LEME Open File Report No. 249. (Thematic Volume) CRC LEME, Perth, Australia.

Demattê, J.A.M., Sousa, A. A., Alves, M.C., Nanni, M.R., Fiorio, P.R., Campos, R.C., 2006.Determining soil water status and other soil characteristics by spectral proximal sensing. *Geoderma,* Vol. 135, pp. 179-195.

Dent, D., 1986. Acid sulphate soils: a baseline for research and development. International Institute for Land Reclamation and Improvement: Wageninen, The Netherlands.

Department of Environment, 2004. Acid Sulphate Soils Guideline Series: Identification and investigation of acid sulphate soils. October 2004. http:\\acidsulphatesoils.environment.wa.gov.au).

Department of Environment and Conservation, 2011. Treatment and management of soils and water in acid sulphate soil landscapes. Contaminated Sites Branch Environmental Regulation Division

Dold, B., 2000. Basic concepts in environmental geochemistry of sulphide mine-waste. In: Memorias de XIX Curso International de Postgrado en Metalogenia. International UNESCO & SEG Short course in Metalogenesis., Quito, Ecuador, pp. 113-151

Doner, H.E, Lynn, W.C., 1989. Carbonate, Halide, sulphate and sulphide minerals, mineral in soil environments. Pp.279-330. In Dixon,J.B., and Weed,S.B.,(eds). Mineral in soil environments, 2nd edition. Soils science society of America, Madison, WI.

Drake, N.A., Mackin, S., and Settle, J.J., 1999. Mapping vegetation, soils, and geology in semiarid shrublands using spectral matching and mixture modelling of SWIR AVIRIS imagery. *Remote Sensing of Environment*, Vol. 67, pp. 12-25.

Eggleton, R.A., Aspandiar, M., 2007. Environmental Mineralogy: Honours Shortcourse, 18-22June 2007. CRC LEME Open File Report 206. pp.159.

Environmental Protection Authority, 1993a. A Guide to Wetland Management in the Perth and Near Perth Swan Coastal Plain Area: EPA Bulletin 686, Perth.

Environmental Protection Authority, 1993b. A Strategy for the Protection of Lakes and Wetlands of the Swan Coastal Plain: EPA Bulletin 685, Perth.

Environmental Protection Authority, 2004. Environmental protection of wetlands. Position Statement No. 4 , Environmental Protection Authority, November 2004.

Essential Environmental Services, 2010. Stirling City Centre District Water Management Strategy, report Prepared for the Department of Planning

Evangelou, V.P., 1995. Pyrite oxidation and its control, P 77, ISBN 0-8493-4732-7,@1995 by CRC Press, Inc Western Australian Planning Commission, 2008, Acid Sulphate Soils Planning Guidelines, published by Western Australian Planning Commission,. ISBN 0 7309 9875 4

Fanfani, L., Nunzi, A., Zanzzi, P.F., Zanzari,A.R., 1973. The Gopiapite Problem: The Crystal Structure of a Ferrian Copiapite. *American Mineralogist*, Vol. 58, pp. 314-322.

Fanning, D.S., Fanning, M.C.B., 1989. Soil morphology, genesis, and classification. John Wiley and Sons, New York, ISBN: 978-0-471-89248-9.

Farifteh, J., Van der Meer, F., Atzberger, C., Carranza, E.J.M., 2006. Quantitative analysis of salt-affected soil reflectance spectra: A comparison of two adaptive methods (PLSR and ANN). *Remote Sensing of Environment*, vol. 110, pp. 59-78.

Farrand, W.H., 1997. Identificatgion and mapping of ferric oxide and oxyhydroxide minerals in imaging spectrometer data of Summitville, Colorado,U.S.A., and the surrounding San Juan Moountains, Int.j. *Remote Sensing*, Vol.18, No7, pp. 1543-1552.

Fitzpatrick, R.W., 2003. Overview of Acid Sulphate Soil Properties, Environmental Hazards, Risk Mapping and Policy Development. In Roach I (Ed), Advances in Regolith, pp, 122-125, CRC LEME.

Fitzpatrick, R.W., Shand, P., Thomas, M., Merry, R.H., Raven, M.D., & Simpson, S.L., 2008. Acid sulphate soils in subaqueous, waterlogged and drained soil environments of nine wetlands below Blanchetown (Lock 1),South Australia: properties, genesis, risks and Management. CSIRO Land and Water Science Report 42/08.

Fitzpatrick, R.W., Shand, P., and Merry,R.H., 2009. Acid sulphate soils. In: Jennings J.T (Ed.) 'Natural history of the riverland and murraylands'. Royal society of South Australia(Inc.) Adelaide, South Australia, pp. 65-111

Fitzpatrick, R.W., Merry, R.H., Williams, J., White, I., Bowman, G., and Taylor, G., 1998. Acid Sulphate soil Assessment: Coastal, Inland and Minespoil Conditions. National Land and Water Resources Audit Methods Paper, pp.18.

Fitzpatrick, R.W., Fritsch, E., Self, P.G., 1996. Interpretation of soil features produced by ancient and modem processes in degraded landscapes: V. Development of saline sulphidic features in non-tidal seepage areas. *Geoderma*, Vol.69, pp. 1-29.

Fraser, R.S., and Curran, R.J., 1976. Effects of the atmosphere on remote sensing. Chapter 2 in Remote sensing of environment (lintz, C.C. and Simonett, D.S., eds.). Reading, M.A: Addison-Wesley, pp. 34-84)

Gaffey, S.J., 1986. Spectral reflectance of carbonate minerals in the visible and near infrared (0.35-2.55 microns): Calcite, aragonite, and dolomite. *American Mineralogist*, Vol.71, pp.151-162.

Garcia, I., Diez, M., Marti, N, F., Simon, M., and Dorronsoro, C., 2009. Mobility of Arsenic and Heavy Metals in a Sandy-Loam Textured and Carbonated Soil. *Pedosphere* 19: 1, 2009, ISSN 1002-0160/CN 32-1315/P.

GMEX, 2008. Spectral Analysis Guides for Mineral Exploration. Spectral Interpretation Field Manual 1. Ausspec International Ltd.

Goetz, A. F. H., and Davis, C. O., 1991. The High Spectral Resolution Imaging Spectrometer (HIRIS): science and instrument. *J. Imaging Syst. Technol*, Vol.3, pp.131-143.

Goetz, A. F. H., Vane, G., Solomon, J. E., and Rock, B. N., 1985. Imaging spectrometry for earth remote sensing. *Science*. Vol.228, pp.1147-1153.

Gozzard, J.R., 2007. Geology and landform of the Perth region. Western Australia Geological Survey. pp.126.

Gray, D.J., 2001. Hydrogeochemistry in the Yilgarn Craton. *Geochemistry: Exploration, Environment, Analysis*, Vol. 1, pp.253-264.

Gupta, R.P., 2003. Remote Sensing Geology, ISBN 3-540-43185-3 Spring-Verlag Berlin Heidelberg New York

Haaland, D. M., and Thomas, E. V., 1988. Partial least-squares methods for spectral analyses. 1. Relation to other quantitative calibration methods and the extraction of qualitative information. *Analytical Chemistry*, Vol.60, pp. 1193–1202.

Haest,H., Cudahy,T., Laukamp,C., and Gregory,S., 2012. Quantitative Mineralogy from Infrared Spectroscopic Data.I. Validation of Mineral Abundance and Composition Scripts at the Rocklea Channel Iron Deposit in Western Australia. *Economic Geology*, v. 107, pp. 209–228.

Hammarstrom, J.M., Seal II, R.R., Meier, A.L., Kornfeld, J,M., 2005. Secondary sulphate minerals associated with acid drainage in the eastern US: recycling of metals and acidity in surficial environments. *Chemical Geology*, Vol.215, pp.407-431.

Harsanyi, J. C., and Chang, C. I., 1994, Hyperspectral image classification and dimensionality reduction:An orthogonal subspace projection approach. *IEEE Trans. Geosci. and Remote Sens.*, vol. 32, pp. 779-785.

Harries, J., 1997. Acid mine drainage in Australia: its extent and potential future liability. Supervising scientist report 125, supervising scientist, Canberra.

Haubrock, S., Chabrillat, S., Lemmnitz, C., & Kaufmann, H., 2008. Surface soil moisture quantification models from reflectance data under field conditions. *International Journal of Remote Sensing*, Vol.29, pp.3-29.

Hecker, C., Dilles, J. H., van der Meijde, M., and van der Meer, F. D., 2012. Thermal infrared spectroscopy and partial least squares regression to determine mineral modes of granitoid rocks. In Geochemistry, Geophysics, Geosystems G3, 13(2012)15 p.

Hewson, R.D., and Cudahy, T.J., 2010. 'Geological mapping accuracy issues using ASTER in Australia' Applications in ASTER. Land Remote Sensing and Global Environmental Change: NASA's Earth Observing System and the Science of ASTER and MODIS. Eds. Ramachandran, B, Justice, C, and Abrams M., Springer, New York.

Hunt, G.R., & Ashley, R.P., 1979. Spectra of altered rocks in the visible and near infrared. *Economic Geology*, Vol.74, pp.1613–1629.

Hunt, G.R., 1977. Spectral signatures of particulate minerals, in the visible and near-infrared. *Geophysics,* Vol.42, pp.501-513.

Hunt, G.R., Salisbury, J.W., & Lenhff, C.J., 1971. Visible and near-infrared spectra of minerals and rocks: IV. Sulphides and sulphates. *Modern Geology*, Vol.3, pp.1–14

Huntington, J.F., Whitbourn, L.B., Quigley, M.A., Yang, K., Mason, P., Cudahy, T.J., Connor, P., Coward, D., Hewson, R and Phillips, R., 2007. Development and implementation of advanced automated core logging technology for enhanced mine feasibility and development in Western Australia: final report — Project M373: CSIRO, Exploration and Mining Report P2007/958, pp.62.

Hurtgen, M.T., Lyons, T.W., Ingall, E.D., Cruse, A.M., 1999. Anomalous enrichments of iron monosulphide in euxinic marine sediments and the role of H_2S in iron sulphide transformation: examples from Effinghan Inlet, Orca Basin, and the Black Sea. *American journal of science*, Vol. 299, pp. 556–588.

Jambor, J.L., Nordstrom, D.K., and Alpers, C.N., 2000. Metal sulphate salts from sulphide mineral oxidation. In: Sulphate Minerals – Crystallography, Geochemistry, and Environmental Significance (P.H. Ribbe, ed). Reviews in Mineralogy and Geochemistry 40, pp. 305-340. Mineralogy of Society of America.

Jamieson, H.E., Robinson, C., Alpers, C.N., McClesky, R.B., Nordstrom, D.K., Peterson, R.C., 2005. Major and trace element composition of copiapite-group minerals and coexisting water from Richmond mine, Iron Mountain, California. *Chemical Geology*, Vol.215, pp.387-405.

Johnston, S.J., Keene, A., Burton, E.D., Bush, R.T., and Sullivan, L.A., 2011. *Environmental science and Technology,* Vol. 45 (6), pp. 2179-85.

Kim, J.J., Kim, S.J. and Choo, C.O., 2003. Seasonal change of mineral precipitates from the coal mine drainage in the Taebaek coal field, South Korea. *Geochemical Journal*, Vol. 37, pp. 109 - 121.

Kruse, F. A., Lefkoff, A. B., Boardman, J. B., Heidebrecht, K. B., Shapiro, A. T., Barloon, P. J., and Goetz, A. F. H., 1993. The Spectral Image Processing System (SIPS) - Interactive Visualization and Analysis of Imaging spectrometer Data. *Remote Sensing of Environment*, Vol. 44, pp. 145 - 163.

Kruse, F.A., Calvin, W.M., Seznec, O., 1988. Automated extraction of absorption features from airborne visible/infrared imaging spectrometer(AVIRIS) and Geophysical environmental research imaging spectrometer(GERIS) data. In:Pro

AVIRIS Performance evaluation workshop, JPL pub88-38, Jet propulsion laboratory, California Inst Tech, Pasadena, CA,pp 62-75.

Lamongtagne, S., Hicks, W.S., Fitzpatrick, R.W., Rogers, S., 2004. Survey and description of sulphidic materials in wetlands of the lower river Murray floodplains: Implication for floodplain salinity management. CRC LEME Open File Report 165, pp.65.

Lau , I. C., 2008. Report to the DEC on Hyperspectral Imagery of South Yunderup for mapping the effects of Acid Sulphate Soils. CSIRO Exploration and Mining Open File Report No: P2008/1086 July 2008.

Leeuw, N.H.D., and Parker, S.C., 1998. Surface Structure and Morphology of Calcium Carbonate Polymorphs Calcite, Aragonite, and Vaterite: An Atomistic Approach. *J. Phys. Chem*. Vol. 102, pp. 2914-2922.

Li, L., 2006. Partial least squares modelling to quantify the lunar soil composition with hyperspectral reflectance measurement. *Journal of Geophysical Research*, Vol.111, pp. E04002.

Ljung, K., Maley, F., Cook, A., & Weinstein, P., 2009. Acid sulphate soils and human health – A Millennium Ecosystem Assessment. *Environmental International*, Vol.35, pp.1234-1242.

Mamindy-Pajany,Y., Hurel, C., Marmier, N., Rome´o, M., 2009,Arsenic adsorption onto hematite and goethite. *C. R. Chimie,* Vol. 12, pp. 876-881.

Márquez, R., García, J.M.M., Delgado, G., Bech, J., and Delgado, R., 2010. Genesis of the quartz in Spanish Mediterranean soils. © 2010 19the World Congress of Soil Science, Soil Solutions for a Changing World 1 – 6 August 2010, Brisbane, Australia

McArthur, W.M., and Bettenay, E., 1974, the development and distribution of the soils of the Swan Coastal Plain, Western Australia. Soil publication No.16, second printing June 1974

McArthur, W.M., and Bettenay, E., 1960. Development and distribution of soils of the Swan Coastal Plain, Western Australia. CSIRO Division of Soils, Soil Publication No. 35.

McArthur, W.M., 1991. Reference soils of south-western Australia. Australian Society of Soil Science (WA Branch Inc.).

Meer, F.V.D., 2004. Analysis of spectral absorption features in hyperspectral imagery. *International Journal of Applied Earth Observation and Geoinformation*, Vol. 5, pp.55-68.

Montero, I.C.S., Brimhall, G.H., Alpersb, C.N., Swayze, G.A., 2005. Characterization of waste rock associated with acid drainage at the Penn Mine, California, by ground-based visible to short-wave infrared reflectance spectroscopy assisted by digital mapping. *Chemical Geology*, Vol.215, pp.453–472.

Morgan, B., Burton, E.D., & Rate, A.W., 2012. Iron monosulfide enrichment and the presence of organosulfur in eutrophic estuarine sediments. *Chemical Geology*, Vol. 296-297, pp. 119-130.

Morse J.W., Millero, F.J., Cornwell, J.C., and Rickard, D., 1987. The chemistry of the hydrogen sulphide and iron sulphide systems in natural waters. Earth-Science Reviews 24(1), 1-42.Morgan, B., Buron, E.D, and Rate, A.W, 2012. Iron monosulphide enrichment and the presence of organosulfur in eutrophic estuarine sediments. *Chemical Geology*, 296-297, 119-130.

Mira, E., and Rojík, P., 2004. Jarosite, schwertmannite, goethite, ferrihydrite and lepidocrocite: the legacy of coal and sulphide ore mining. 2004. SuperSoil 2004: 3rd Australian New Zealand Soils Conference, 5 – 9 December 2004, University of Sydney, Australia

Murad, E., and Rojiak, P., 2005. Iron mineralogy of mine-drainage precipitates as environmental indicators:review of current concepts and a case study from the Sokolov Basin, Czech Republic. *Clay Minerals*, Vol. 40, pp.427-440

Murray, I., 1986. The NIR spectra of homologous series of organic compounds. In: Hollo, J., Kaffka, K.J., Gonczy, J.L.(Eds.), Proceedings of the International NIR/NIT Conference, Akademiai Kiado, Budapest, pp. 13–28.

Nickel, E. H., 1995. The definition of a mineral. *The Canadian Mineralogist*, Vol. 33 (3), pp. 689–690

Nordstrom, D.K., and Alpers, C.N., 1999. Geochemistry of acid mine waters. In Reviews in Economic Geology, vol. 6A, The Environmental Geochemistry of Mineral Deposits. Part A. Processes, Methods and Health Issues, G.S.Plumlee and M.J. Logsdon, eds., Soc. Econ. Geol., Littleton, CO. 133-160.

Ong, C., Cudahy, T.J., and Swayze, G., 2003. Predicting acid drainage related physicochemical, measurements using hyperspectral data. Paper presented at the 3rd EARSel Workshop on Imaging Spectroscopy (pp. 363-373), Herrsching, May 13-16, 2003.

Pearce, A., Feng, M., 2007. Observations of warming on the Western Australian continental shelf. *Marine and Freshwater Research*, Vol.58, pp. 914-920.

Pedro, G., 1997. Clay minerals in weathered rock materials and in soils mineralogy and chemistry, soils and sediments,p1, ISBN 3-540-61599-7 Spring-Verlag Berlin Heidelberge New York

Poleo, A.B.S., 1995. Al polymerization—a mechanism of acute toxicity of Ponnamperuma, F. N., 1972. The chemistry of submerged soils. *Advances in Agronomy*, Vol.24, pp.29-96.

Pontural, S., Mery, N., and Gamson, P., 1997. Spectral interpretation field manual , G-MEX , version 1.0, Auspec international pty. Ltd,1997

Powell, B., and Martens, M., 2005. A review of acid sulphate soil impacts, actions and policies that impact on water quality in the Great Barrier Reef catchments, including a case study on remediation at East Trinity. *Marine Pollution Bulletin*, Vol.51, pp.149–164

Prakongkep,N., Gilkes, R.J., Singh, B., and Wong, S., 2011. Mineralogy and chemistry of sandy acid sulphate soils in the Perth metropolitan area of the Swan Coastal Plain. Report to Department of Environment and Conservation. 177pp.

Rayment, G.E., and Lyons, D.J., 2010. Soil Chemical Methods – Australasia. Publisher: CSIRO PUBLISHING, ISBN: 9780643067684

Riaza, A., Buzzi, J., Garcia-Melendez, E., Carrere, V., Muller, A., 2011. Monitoring the extent of contamination from acid mine drainage in the Iberian Pyrite Belt (SW Spain) using hyperspectral imagery. *Remote Sensing*, Vol. 3(10), pp. 2166-2186

Riaza，A., and Muller, A., 2010. Hyperspectral remote sensing monitoring of pyrite mine wastes: a record of climate variability (Pyrite Belt, Spain). *Environ. Earth Sci*. Vol.61, pp. 575-594.

Richter, N., 2009. Pedogenic iron oxide determination of soil surfaces from laboratory pectroscopy and HyMap image data, doctor thesis from Humboldt Universität zu Berlin – Geographisches Institut

Richter, N., Jarmer, T., Chabrillt, S., Oyonarte, C., Hostert, P., Kaufmann, H., 2008. Free iron oxide determination in Mediterranean soils using difference reflectance spectroscopy. *Soil science society of America*, Vol.73, pp.72-81

Richter, N., 2010. Pedogenic iron oxide determination of soil surfaces from laboratory spectroscopy and HyMap image data: A case study in Cabo de Gata-Níjar Natural Park, SE Spain. Doctoral dissertation Humboldt Universität zu Berlin – Geographisches Institut

Rivers, M., 2009. Overview of the Peel Inlet and Harvey Estuary – genesis to water quality, ARWA Centre for Ecohydrology. *Australian Journal of earth science*, Vol.43, pp.31-44

Robbins, E.I., Aderson, J.E., Cravotta, C.A., Bilger, M.D., 1997. AMD flocculates and precipitates: potential for habitat destruction by sediment of a different colour, proceedings of the U.S. Geological Survey (USGS) sediment workshop, February 4-7,1997

Rockwell, B.W., 2004, Spectral variations in rocks and soils containing ferric iron hydroxide and(or) sulphate minerals as seen by AVRIS and laboratory spectroscopy. USGS open-file report 2004-1431

Rodger, A., 2011. SODA: A new method of in-scene atmospheric water vapor estimation and post-flight spectral recalibration for hyperspectral sensors Application to the HyMap sensor at two locations. *Remote Sensing of Environment*. Vol.115(2), pp. 536-547.

Sammut, J., Lines-Kelly, R., Natural Heritage Trust (Australia), Australian Seafood Industry Council. & Australia. Environment Australia. 2000, An introduction to acid sulphate soils. 2nd edition, Environment Australia, Canberra.

Smith, J., 2004. Chemical changes during oxidation of iron monosulphide-rich sediments. *Aust. Journal of Soil Research*. Vol.42, pp. 659-666.

Suave, S., Martı´nez, C.E., McBride, M., & Hendershot, W., 2000. Adsorption of Free Lead (Pb21) by Pedogenic Oxides, Ferrihydrite, and Leaf Compost. *Soil Science Society of America Journal*, Vol. 64, pp.595–599

Scheinost, A.C., Schulze, D.G., & Schwertmann, U., 1999. Diffuse reflectance spectra of Al substituted goethite: A ligand field approach. *Clays and Clay Minerals*, Vol.47, pp. 156–164.

Schwertmann, U., Fitzpatrick, R.W., 1977. Occurrence of lepidocrocite and its association with goethite in Natal soils. *Soil Science Society of America Journal* Vol.41, pp. 1013-1018.

Schwertmann, U., and Cornell, R.M., 2000. Iron oxides in the laboratory: preparation and characterization, second edition, VCH, Weinheim, Germany, 2000.

Schwertmann,U., and Murad, E., 1983. Effect of pH on the formation of goethite and hematite from ferrihydrite. *Clays and Clay Minerals*, Vol. 31(4), pp. 277-284.

Semeniuk, C.A, and Semeniuk, V., 1990. The coastal landforms and peripheral wetlands of the Peel-Harvey estuarine system. *Journal of the Royal Society of Western Australia*, Vol.73, pp.9-21.

Shand,P., Merry, R.H., Thomas, B.,P., Thomas, T., and Fitzpatrick, R.W., 2009. Acid sulphate soil assessment of the Pike River system, CSIRO Land and Water Science Report series ISSN: 1834-6618

Sherman, D.M., and Waite, T.D., 1985. Electronic spectra of Fe3+ oxides and oxide ydroxides in the near IR to near UV. *American Mineralogist*, Vol.70, pp.1262–1269

Sherman, D.M., Burns, R.G., Burns, V.M., 1982. Spectral characteristics of the iron oxides with applications to the Martian BrightRegion mineralogy. *Journal of Geophysical Research*, Vol.87, pp. 10169–10180.

Singh, B., and Wong, S., 2010.Acid sulphate soils in the Perth metropolitan area of Western Australia. 2010 19th World Congress of Soil Science, Soil Solutions for a Changing World 1 – 6 August 2010, Brisbane, Australia

Smith, J., Melville, M.D., 2004. Iron monosulphide formation and oxidation in drain-bottom sediments of an acid sulphate soil environment. *Applied Geochemistry*, Vol.19, pp.1837-1853

Sommer, B., 2006. Drying and re-wetting of organic sediments: iogeochemistry and implication for wetland management, thesis for the degree of doctor of philosophy in Edith Cowan University.

Stephens, D., Denby, C., Evans, F., Leeming, T., Goulding P., 2009. The changing crop growing season of the southwest of Western Australia. Climate 21, Perth, Western Australia, 27 March.

Stocker, A. D., Reed, I. S., and Yu, X., 1990. Mulitdimensional signal processing for electrooptical target detection. Proc, SPIE Int. Soc. Opt. Eng., vol. 1305.

Sullivan, L.A., Ward, N.J., Bush, R.T., Burton, E.D., 2009. Improved identification of sulphidic soil materials by a modified incubation method. *Geoderma*. Vol.149, pp. 33–38

Sullivan, L.A., Bush, R.T., & Burton, E., 2006. Acid sulphate soil development issues in the Peel Region. Report to the Department of Environment November 2006.

Sullivan, L.A., Bush, R.T., & Fyfe, D., 2002. Acid sulphate soil drain ooze: distribution, behaviour and implications for acidification and deoxygenation of waterways. In: Lin,C., Melville, M. D., & Sullivan, L. A., (Eds), Acid Sulphate Soils in Australia and China, Science Press, Beijing, pp. 91-99.

Sullivan, L.A., & Bush, R.T., 2004. Iron precipitate accumulations associated with waterways in drained coastal acid sulphate landscapes of eastern Australia. *Marine and Freshwater Research*, Vol. 55, pp. 727-736

Sullivan, L. A., Bush, R. T., 2000. The behaviour of drain sludge in acid sulphate soil areas: Someimplications for acidification and waterways management. In 'Proceedings of Workshop on Remediation and Assessment of Broadacre Acid Sulphate Soils'. (Ed. P Slavich) pp. 43–48. (ASSMAC: Australia).

Swayze G.A., Smith K.S., Clark R.N., Sutley S.J., Pearson R.M., Vance J.S., Hageman, P., Briggs P.H., Meier A.L., Singleton M.J., Roth S., 2000.Using imaging spectroscopy to map Acidic Mine Waste. *Environmental Science and Technology*, Vol.34, pp.47-54.

Thomas, E. V., and Haaland, D. M., 1990. Comparison of multivariate calibration methods for quantitative spectral analysis. *Analytical Chemistry*, Vol.62, pp.1091– 1099.

Ward, N.J., Sullivan, L.A., Fyfe, D.M., Bush, R.T., and Ferguson, A.J.P., 2004. The process of sulphide oxidation in some acid sulphate soil materials. *Australia journal of soil research*. Vol.42, pp.449-458

Water & Rivers Commission, Department of Environmental Protection, 2002. Navigation of soil and groundwater acidity, Stirling, Department of Environmental Protection Western Australian planning commission, 2008. Acid sulphates soils Guidelines.

Western Australian Planning Commission, 2003. Planning Bulletin 64. Acid Sulphate Soils. ISSN 1324-9142.

West Australia Planning Commission, 2008. Acid Sulphate Soils Planning Guidelines.

White, I., Melville, M.D., 1993. Treament and containment of potential acid sulphates soils. CSIRO centre for environmental mechanics, Technical report No.53

Wold, H., 1966a, Nonlinear estimation by iterative least squares procedure, in Research Papers in Statistics, edited by F. David, pp. 441– 444

Wold, H., 1966b, Estimation of principal components and related models by iterative least squares, in Multivariate Analysis, edited by P. R. Krishnaiah, pp. 391– 420, Elsevier, New York.

Wold, S., Sjöström, M., and Eriksson, L., 2001. PLS-regression: A basic tool of chemometrics, Chemom. Intell. Lab. Syst., 58(2), 109–130, doi:10.1016/S0169-7439(01)00155-1.

Yu, X., Reed, I. S., and Stocker, A. D., 1993. Comparative performance analysis of adaptive multispectral detectors. *IEEE Trans. on Signal Processing*, vol. 41(8).

Appendix 1. XRD plot of the soil samples collected from the surface of the study area

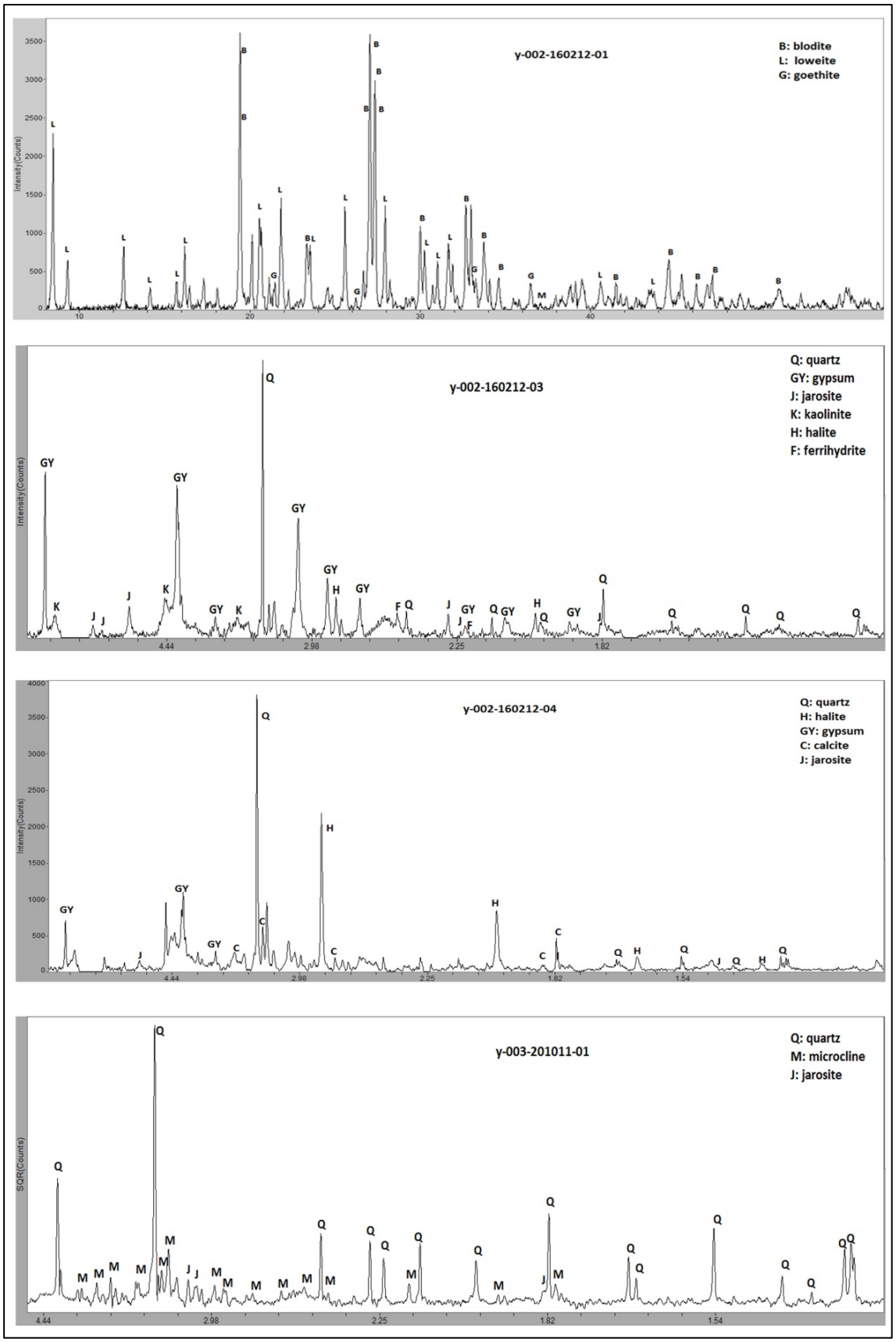

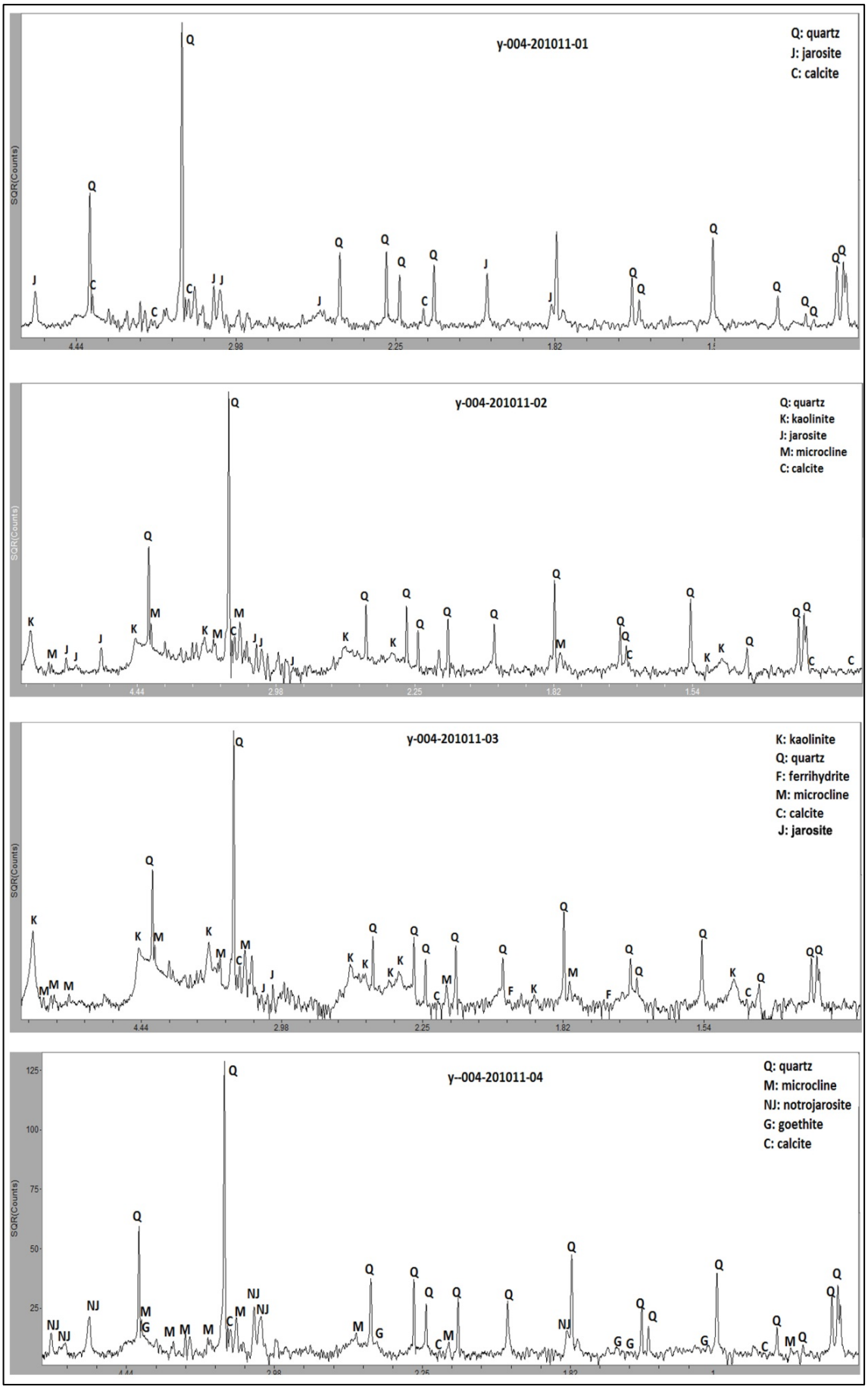
y-004-201011-01
Q: quartz
J: jarosite
C: calcite
SQR(Counts)
y-004-201011-02
Q: quartz
K: kaolinite
J: jarosite
M: microcline
C: calcite
SQR(Counts)
y-004-201011-03
K: kaolinite
Q: quartz
F: ferrihydrite
M: microcline
C: calcite
J: jarosite
SQR(Counts)
y--004-201011-04
Q: quartz
M: microcline
NJ: notrojarosite
G: goethite
C: calcite
SQR(Counts)

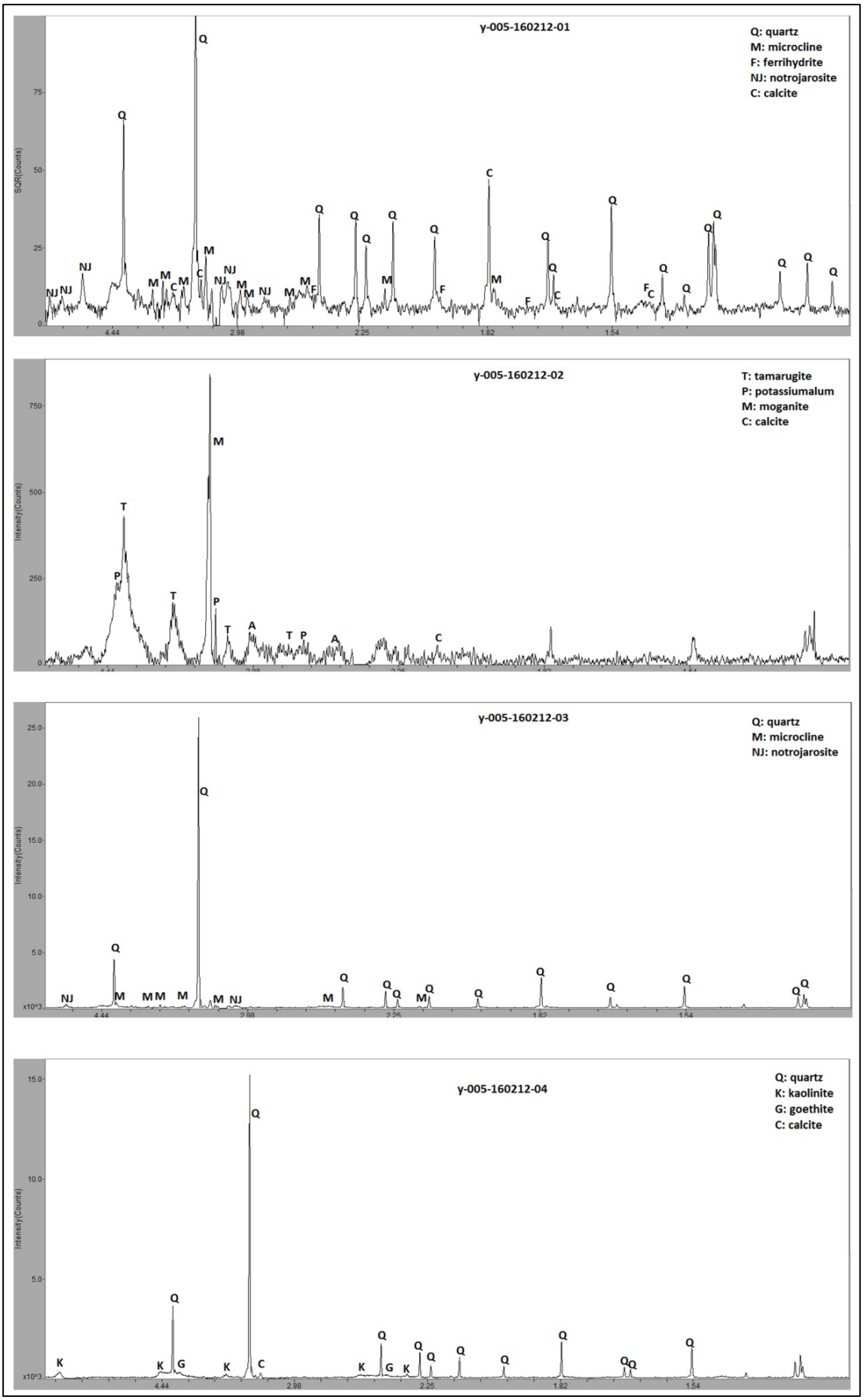
y-005-160212-01
Q: quartz
M: microcline
F: ferrihydrite
NJ: notrojarosite
C: calcite
SQR(Counts)
y-005-160212-02
T: tamarugite
P: potassiumalum
M: moganite
C: calcite
Intensity(Counts)
y-005-160212-03
Q: quartz
M: microcline
NJ: notrojarosite
Intensity(Counts)
y-005-160212-04
Q: quartz
K: kaolinite
G: goethite
C: calcite
Intensity(Counts)

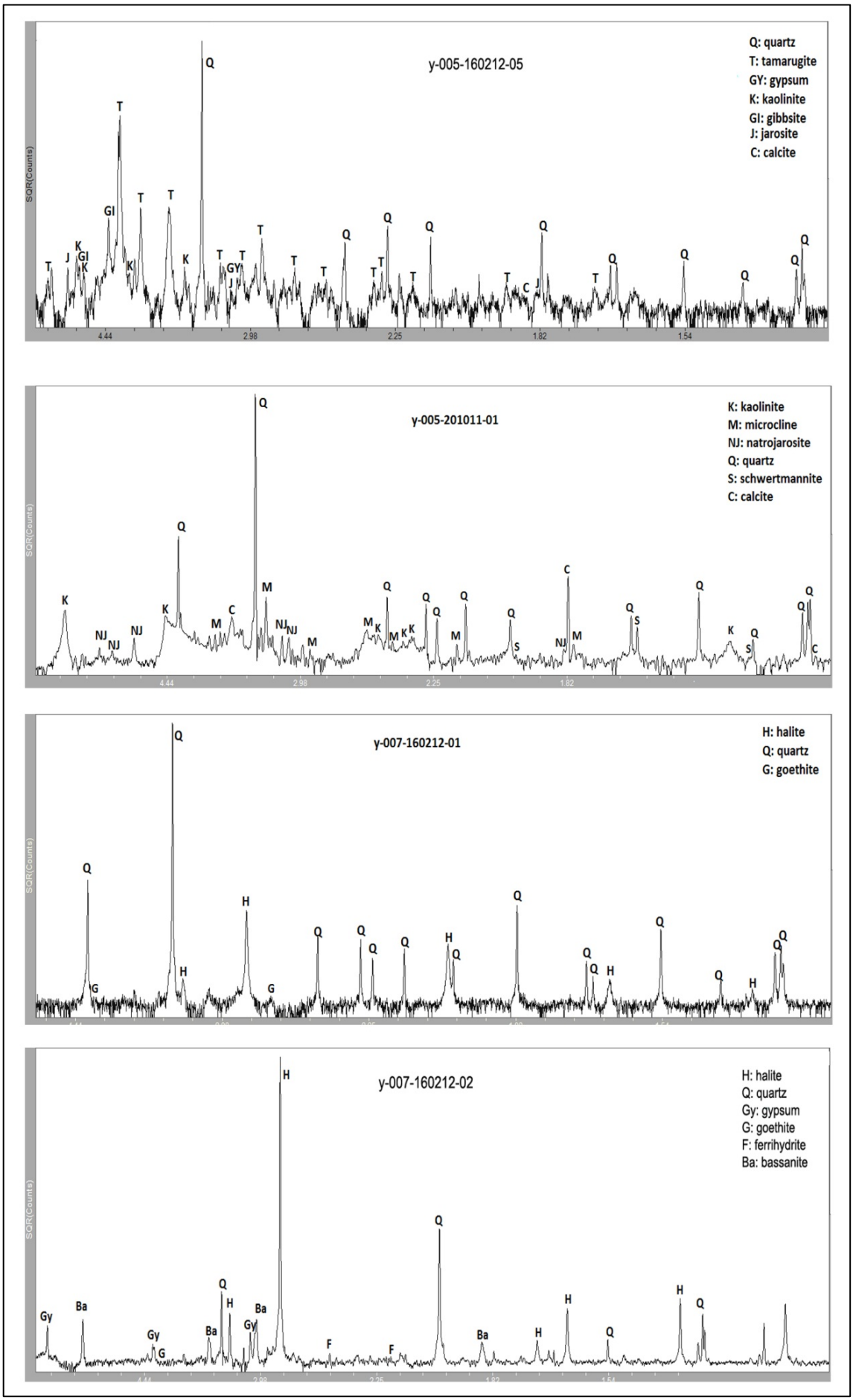
y-005-160212-05
Q: quartz
T: tamarugite
GY: gypsum
K: kaolinite
GI: gibbsite
J: jarosite
C: calcite
SQR(Counts)
4.44
2.98
2.25
1.82
1.54
y-005-201011-01
K: kaolinite
M: microcline
NJ: natrojarosite
Q: quartz
S: schwertmannite
C: calcite
SQR(Counts)
4.44
2.98
2.25
1.82
y-007-160212-01
H: halite
Q: quartz
G: goethite
SQR(Counts)
y-007-160212-02
H: halite
Q: quartz
Gy: gypsum
G: goethite
F: ferrihydrite
Ba: bassanite
SQR(Counts)

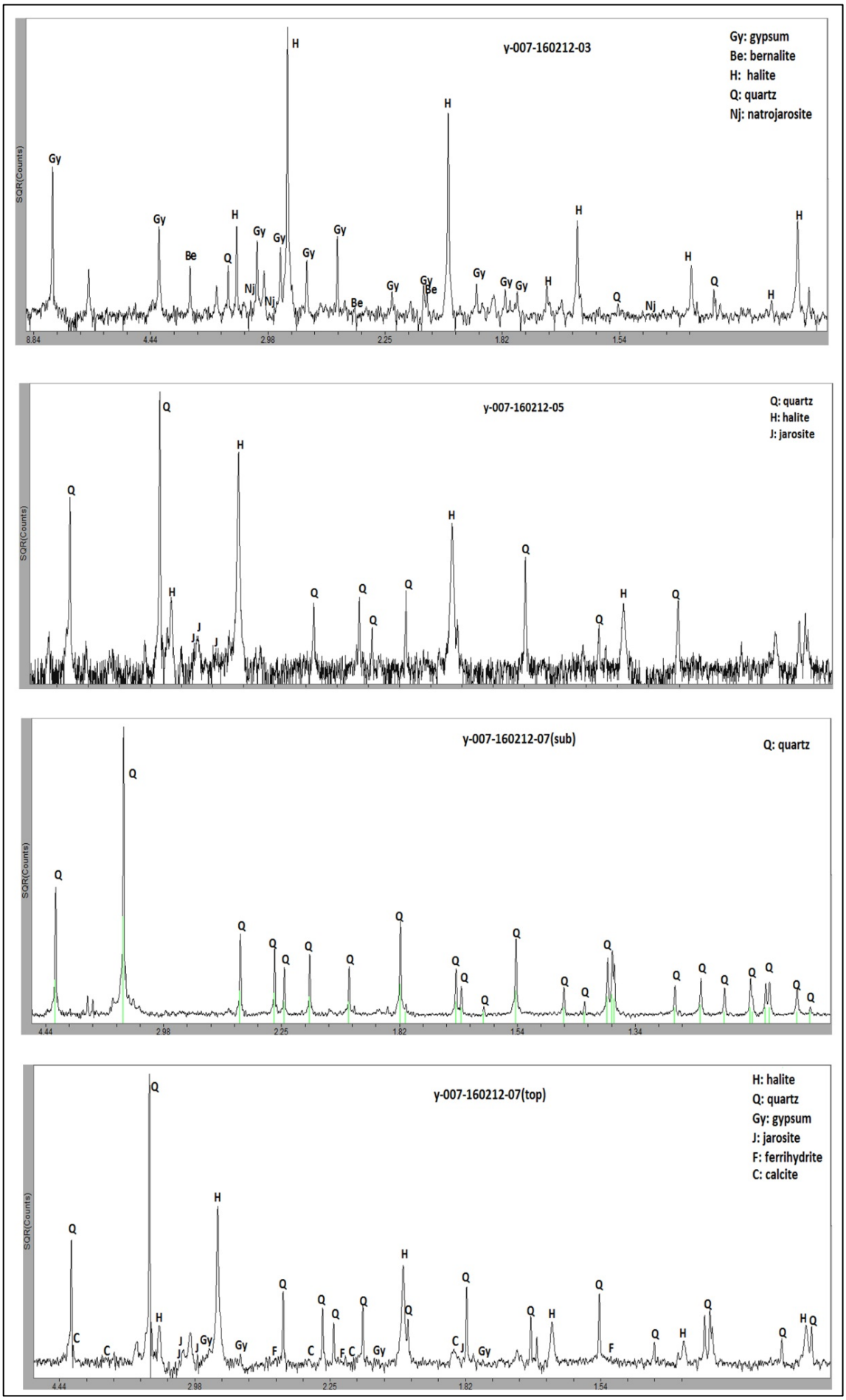
y-007-160212-03
Gy: gypsum
Be: bernalite
H: halite
Q: quartz
Nj: natrojarosite
SQR(Counts)
y-007-160212-05
Q: quartz
H: halite
J: jarosite
SQR(Counts)
y-007-160212-07(sub)
Q: quartz
SQR(Counts)
y-007-160212-07(top)
H: halite
Q: quartz
Gy: gypsum
J: jarosite
F: ferrihydrite
C: calcite
SQR(Counts)

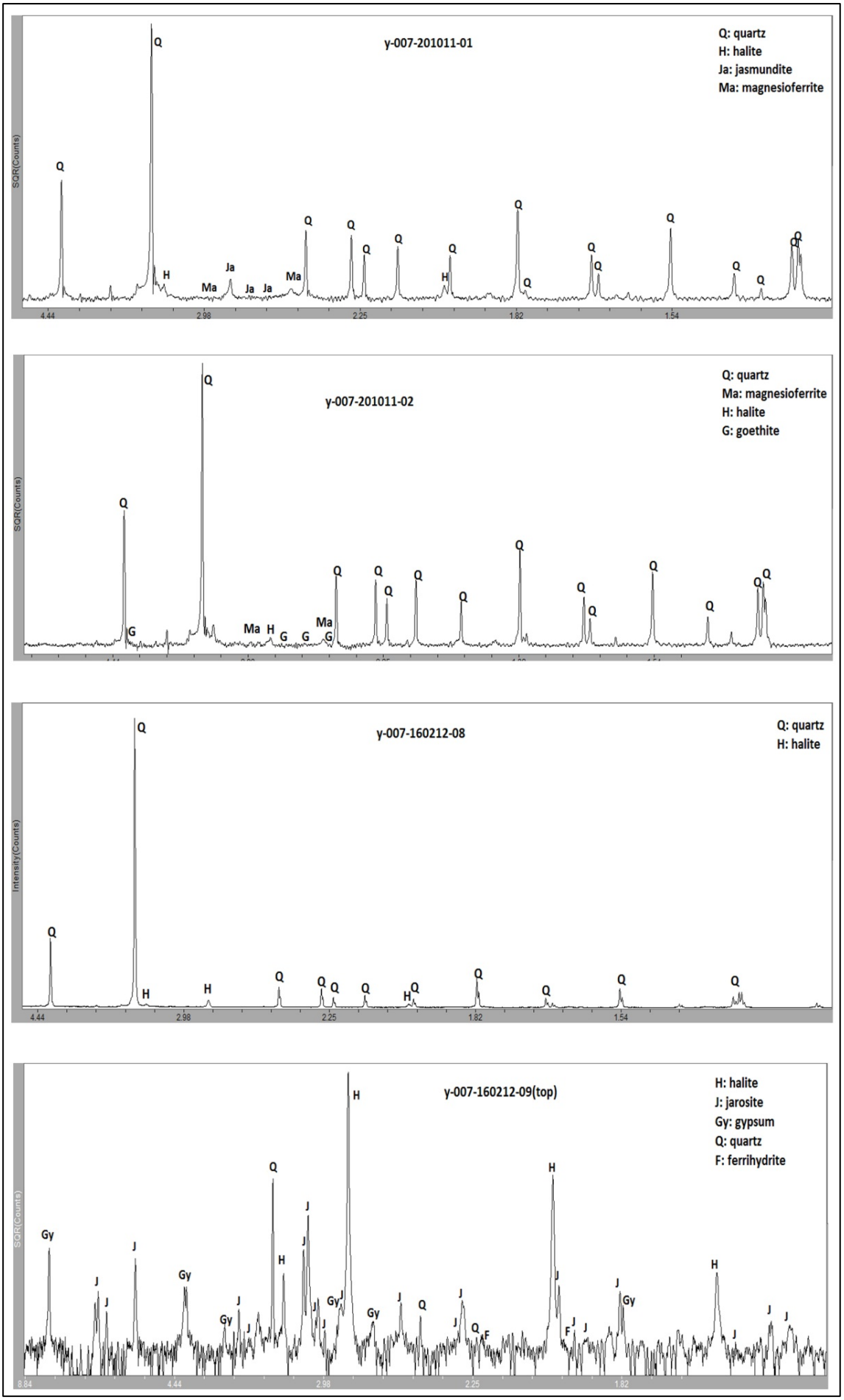
y-007-201011-01
Q: quartz
H: halite
Ja: jasmundite
Ma: magnesioferrite
SQR(Counts)
y-007-201011-02
Q: quartz
Ma: magnesioferrite
H: halite
G: goethite
SQR(Counts)
y-007-160212-08
Q: quartz
H: halite
Intensity(Counts)
y-007-160212-09(top)
H: halite
J: jarosite
Gy: gypsum
Q: quartz
F: ferrihydrite
SQR(Counts)

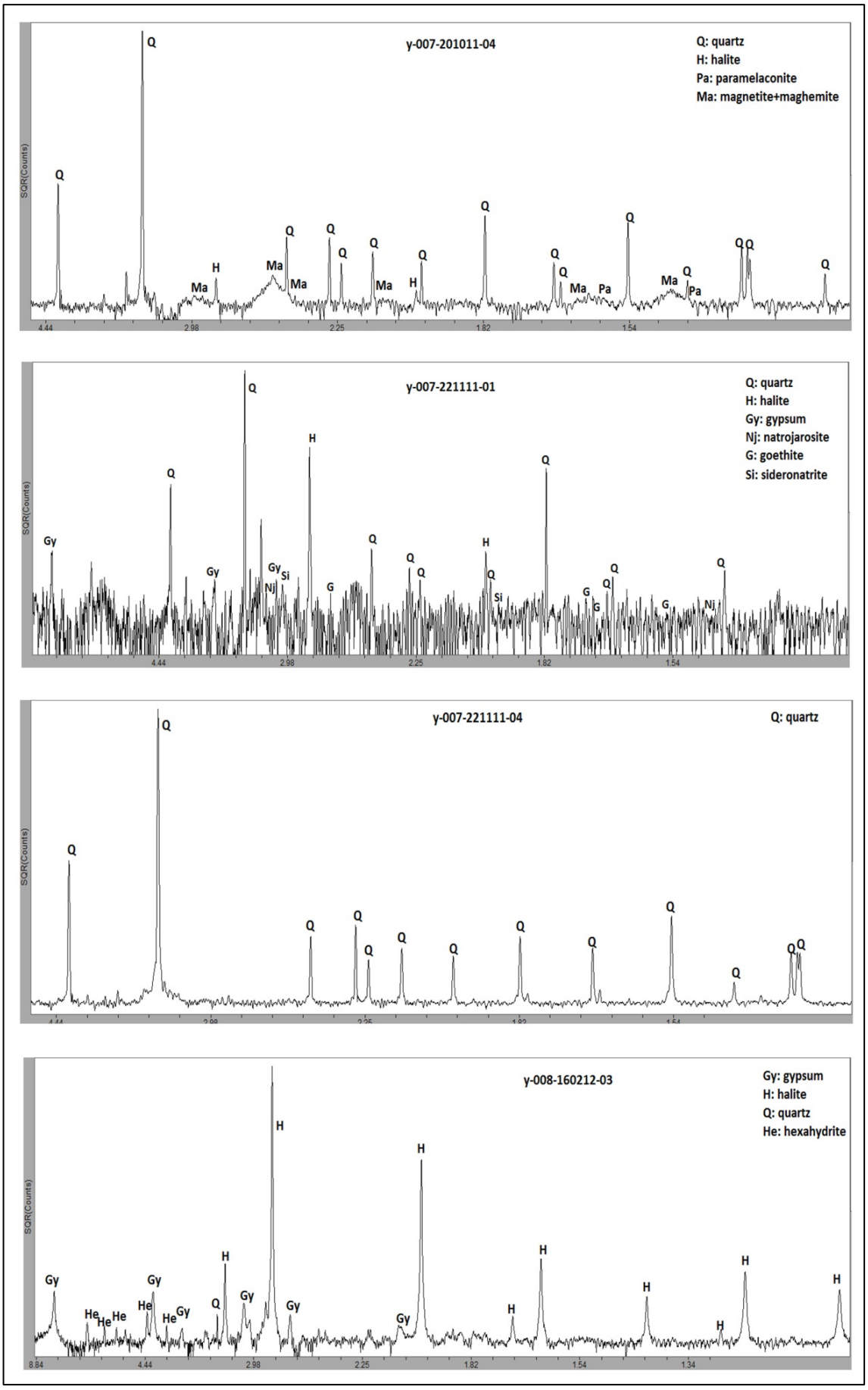
y-007-201011-04
Q: quartz
H: halite
Pa: paramelaconite
Ma: magnetite+maghemite
SQR(Counts)
y-007-221111-01
Q: quartz
H: halite
Gy: gypsum
Nj: natrojarosite
G: goethite
Si: sideronatrite
SQR(Counts)
y-007-221111-04
Q: quartz
SQR(Counts)
y-008-160212-03
Gy: gypsum
H: halite
Q: quartz
He: hexahydrite
SQR(Counts)

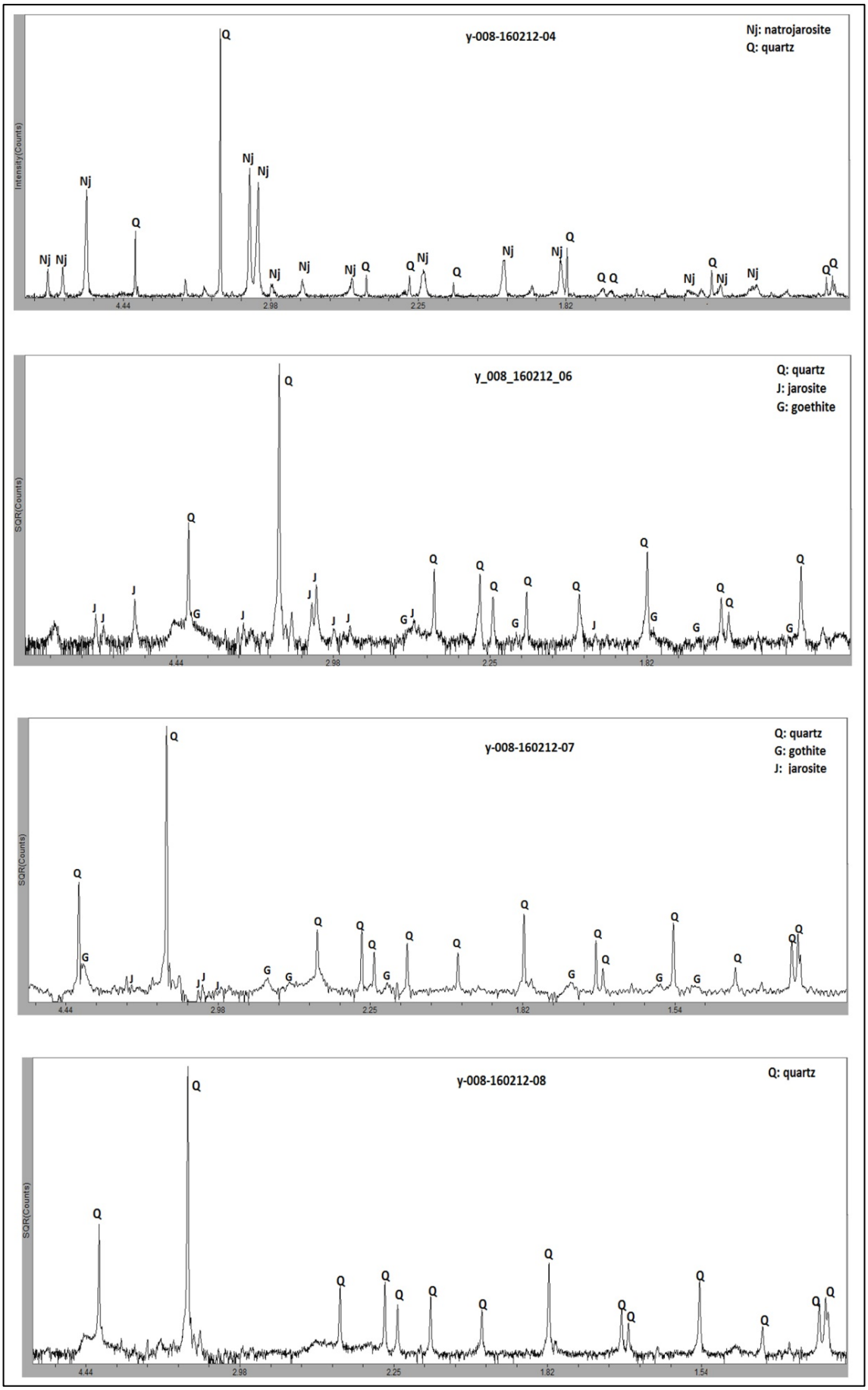
y-008-160212-04
Nj: natrojarosite
Q: quartz
Intensity(Counts)
y_008_160212_06
Q: quartz
J: jarosite
G: goethite
SQR(Counts)
y-008-160212-07
Q: quartz
G: gothite
J: jarosite
SQR(Counts)
y-008-160212-08
Q: quartz
SQR(Counts)

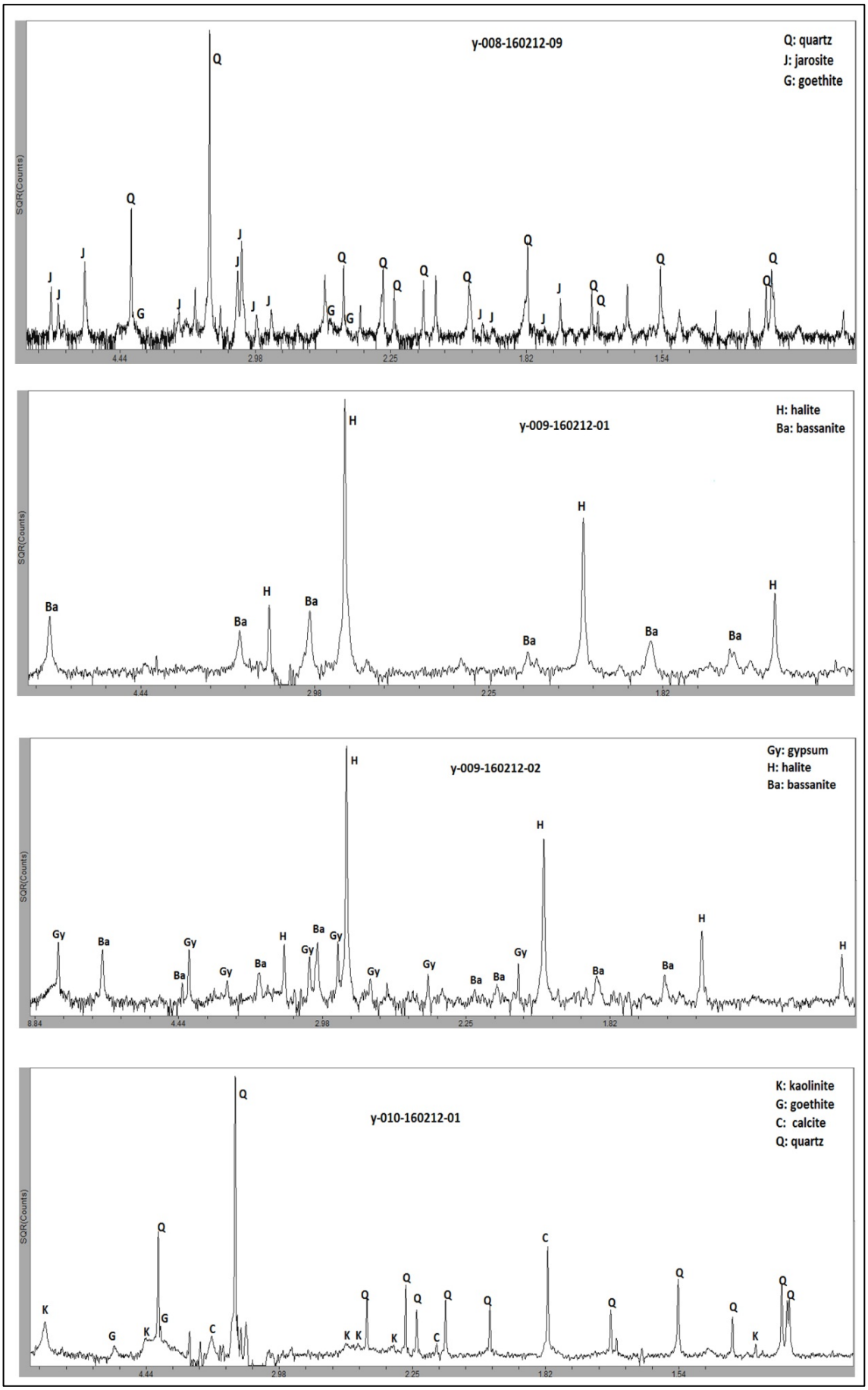
y-008-160212-09
Q: quartz
J: jarosite
G: goethite
SQR(Counts)
4.44
2.98
2.25
1.82
1.54
y-009-160212-01
H: halite
Ba: bassanite
SQR(Counts)
4.44
2.98
2.25
1.82
y-009-160212-02
Gy: gypsum
H: halite
Ba: bassanite
SQR(Counts)
8.84
4.44
2.98
2.25
1.82
y-010-160212-01
K: kaolinite
G: goethite
C: calcite
Q: quartz
SQR(Counts)
4.44
2.98
2.25
1.82
1.54

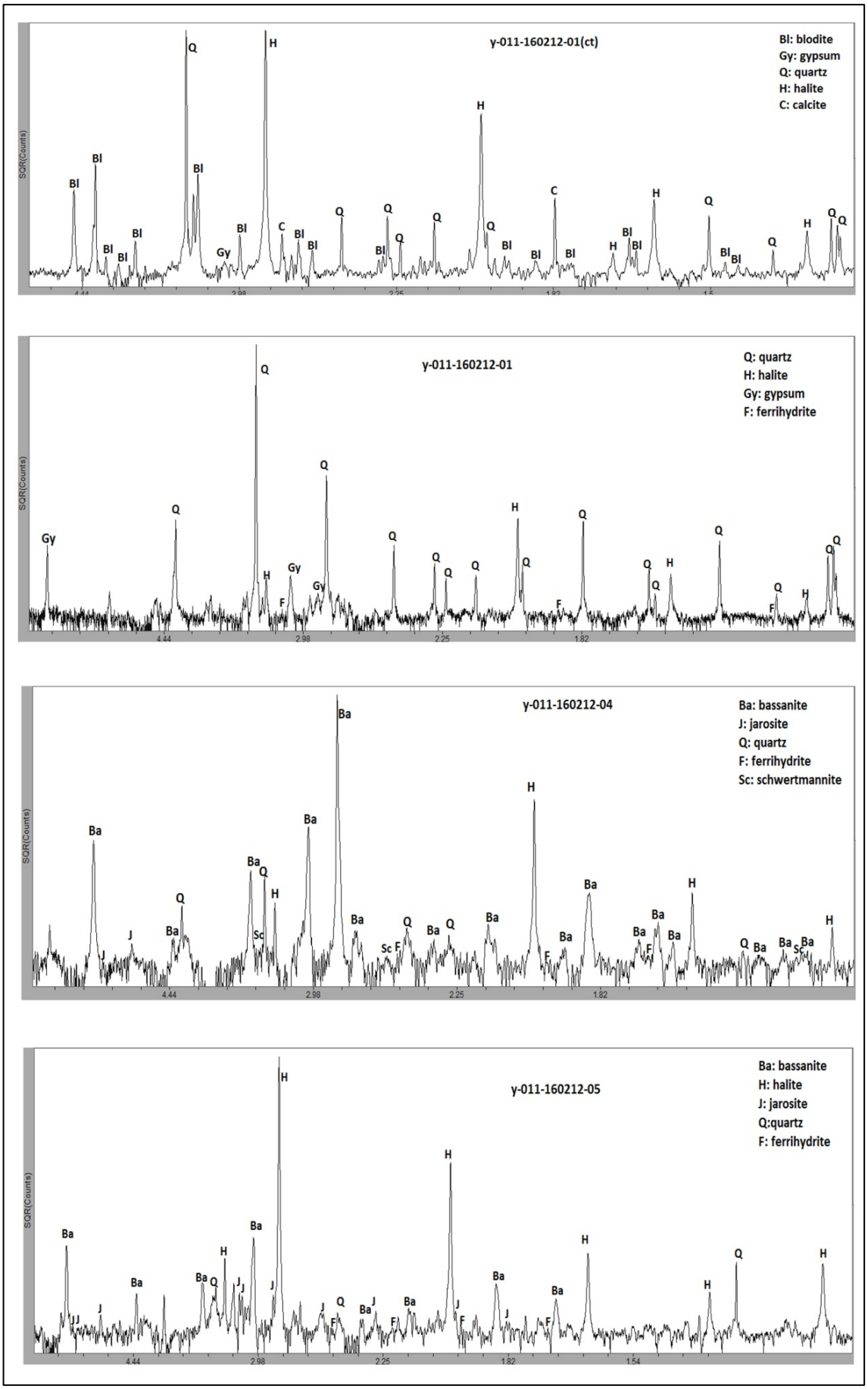
y-011-160212-01(ct)
Bl: blodite
Gy: gypsum
Q: quartz
H: halite
C: calcite
SQR(Counts)
y-011-160212-01
Q: quartz
H: halite
Gy: gypsum
F: ferrihydrite
SQR(Counts)
4.44
2.98
2.25
1.82
y-011-160212-04
Ba: bassanite
J: jarosite
Q: quartz
F: ferrihydrite
Sc: schwertmannite
SQR(Counts)
4.44
2.98
2.25
1.82
y-011-160212-05
Ba: bassanite
H: halite
J: jarosite
Q:quartz
F: ferrihydrite
SQR(Counts)
4.44
2.98
2.25
1.82
1.54

Appendix 2: Reflectance Spectral measurements of the soil samples collected from the surface of study area

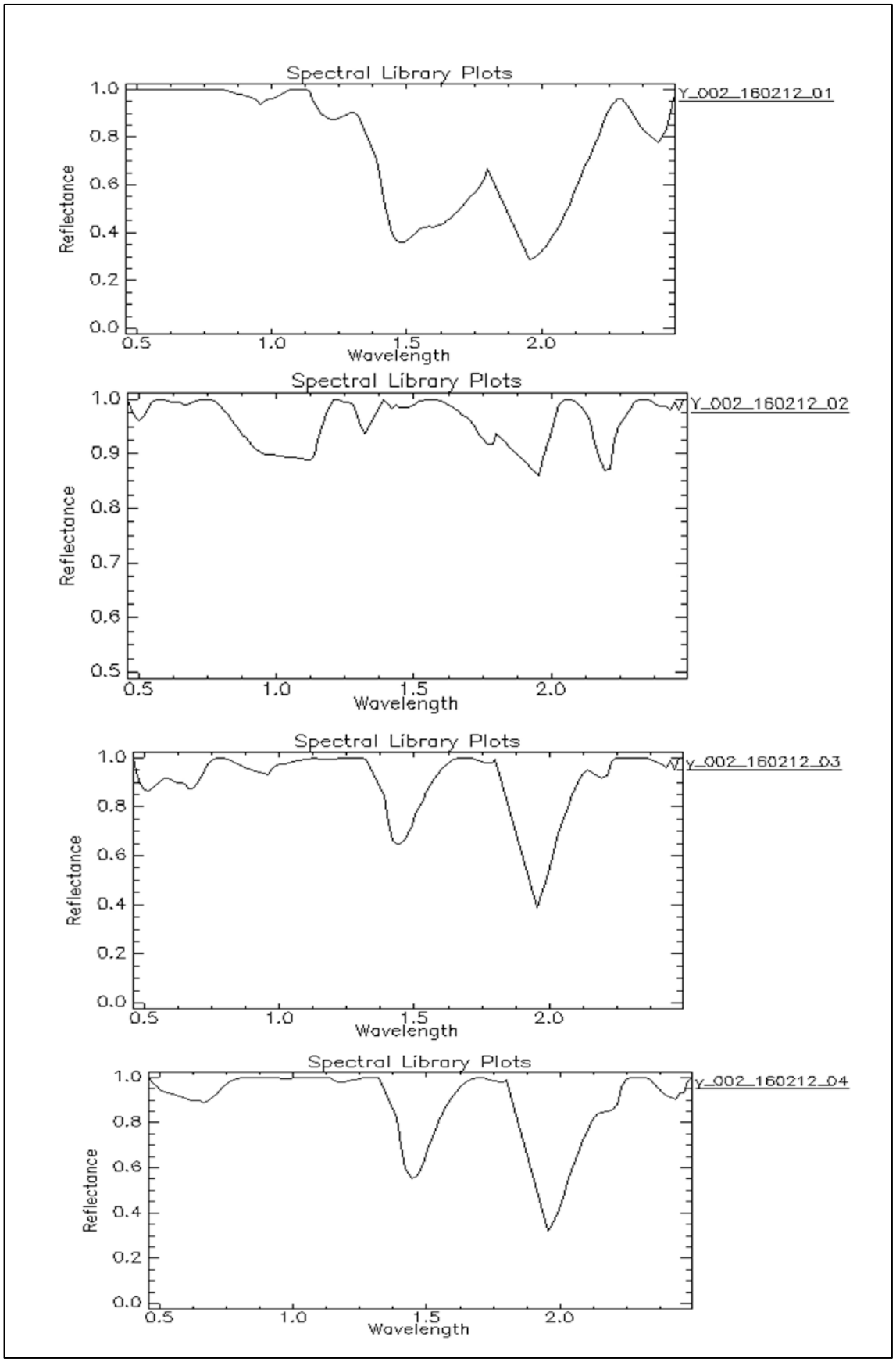

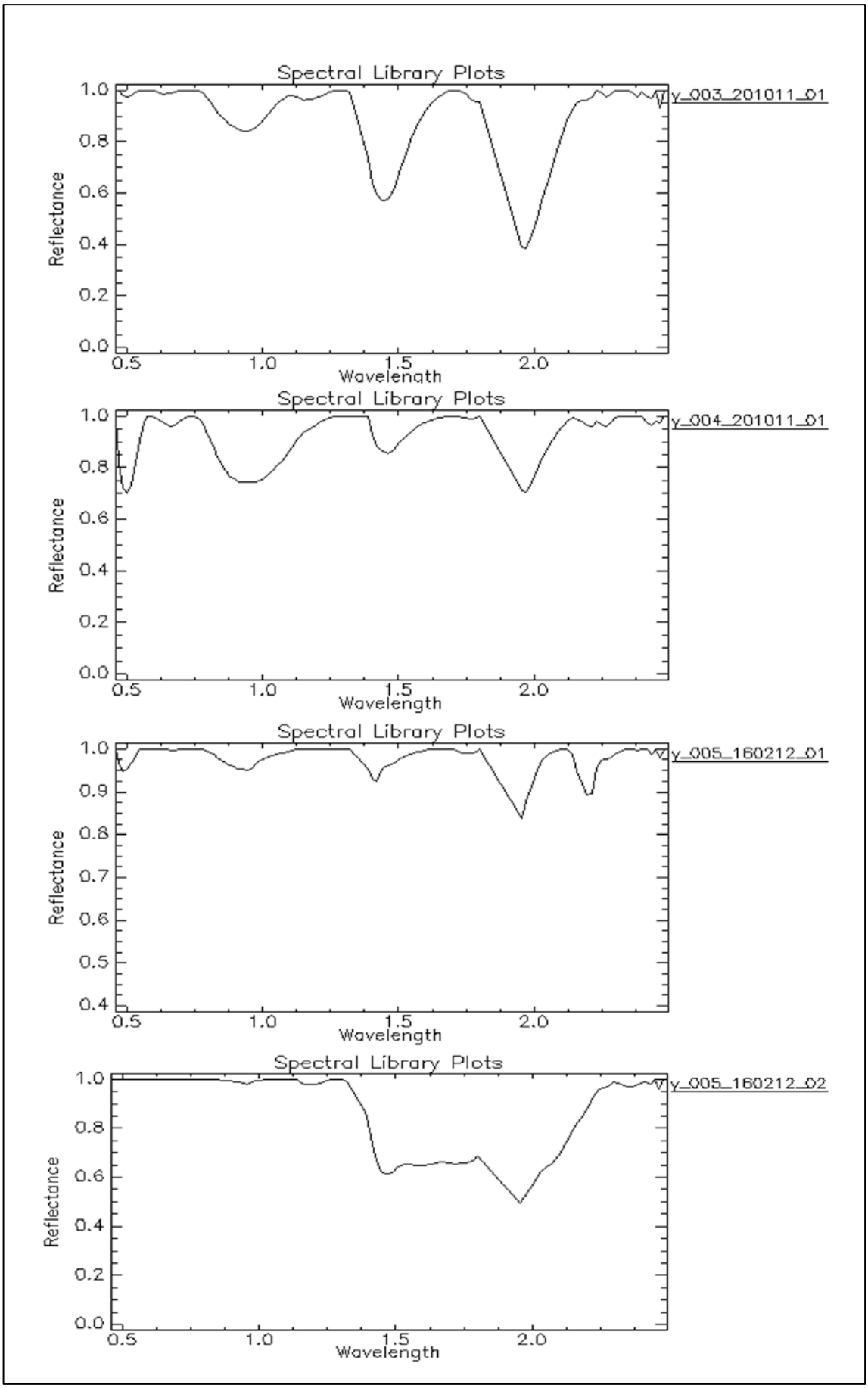
Spectral Library Plots
y_003_201011_01
Reflectance
Wavelength
Spectral Library Plots
y_004_201011_01
Reflectance
Wavelength
Spectral Library Plots
y_005_160212_01
Reflectance
Wavelength
Spectral Library Plots
y_005_160212_02
Reflectance
Wavelength

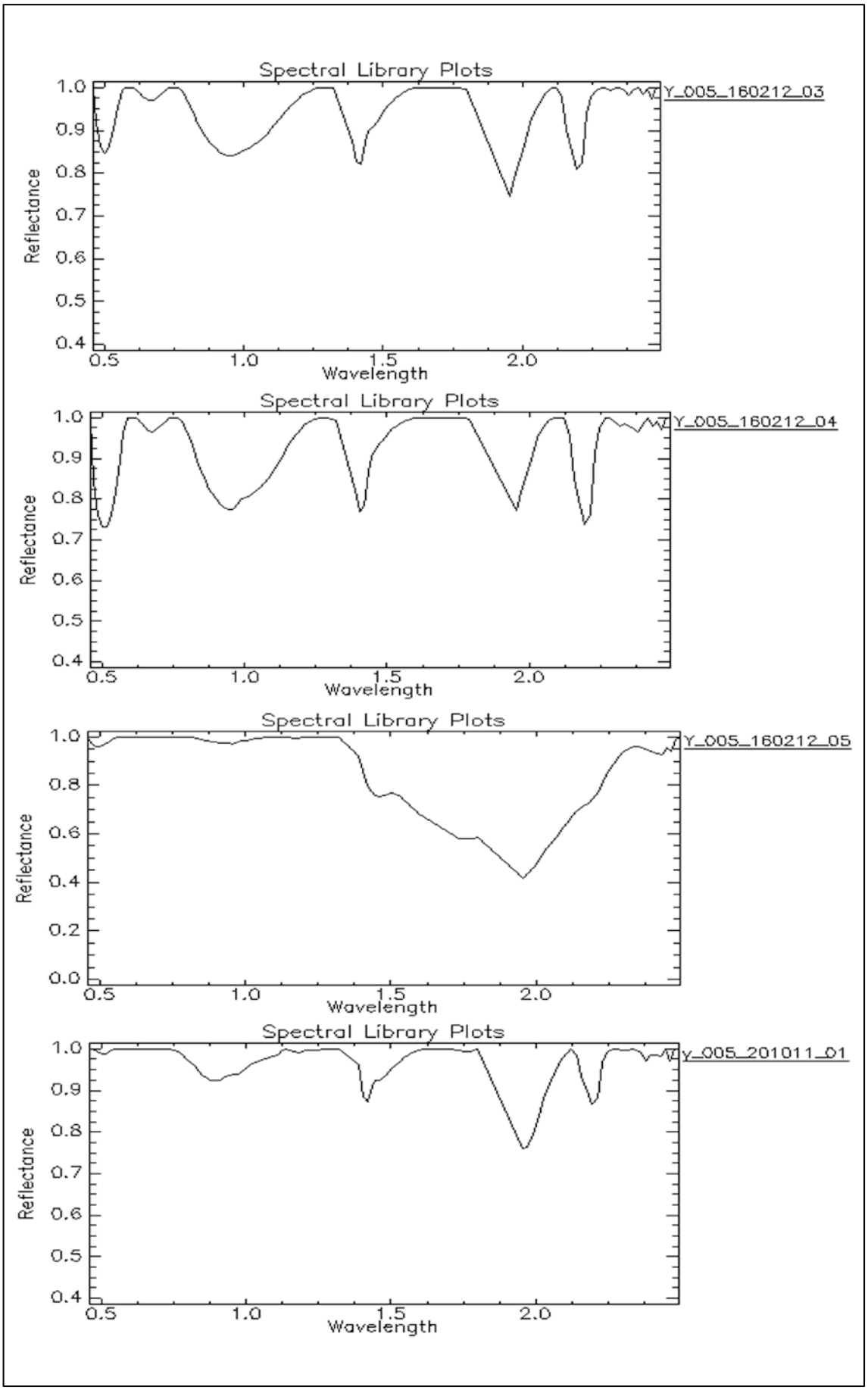
Spectral Library Plots
Reflectance
Wavelength
Y_005_160212_03
Spectral Library Plots
Reflectance
Wavelength
Y_005_160212_04
Spectral Library Plots
Reflectance
Wavelength
Y_005_160212_05
Spectral Library Plots
Reflectance
Wavelength
Y_005_201011_01

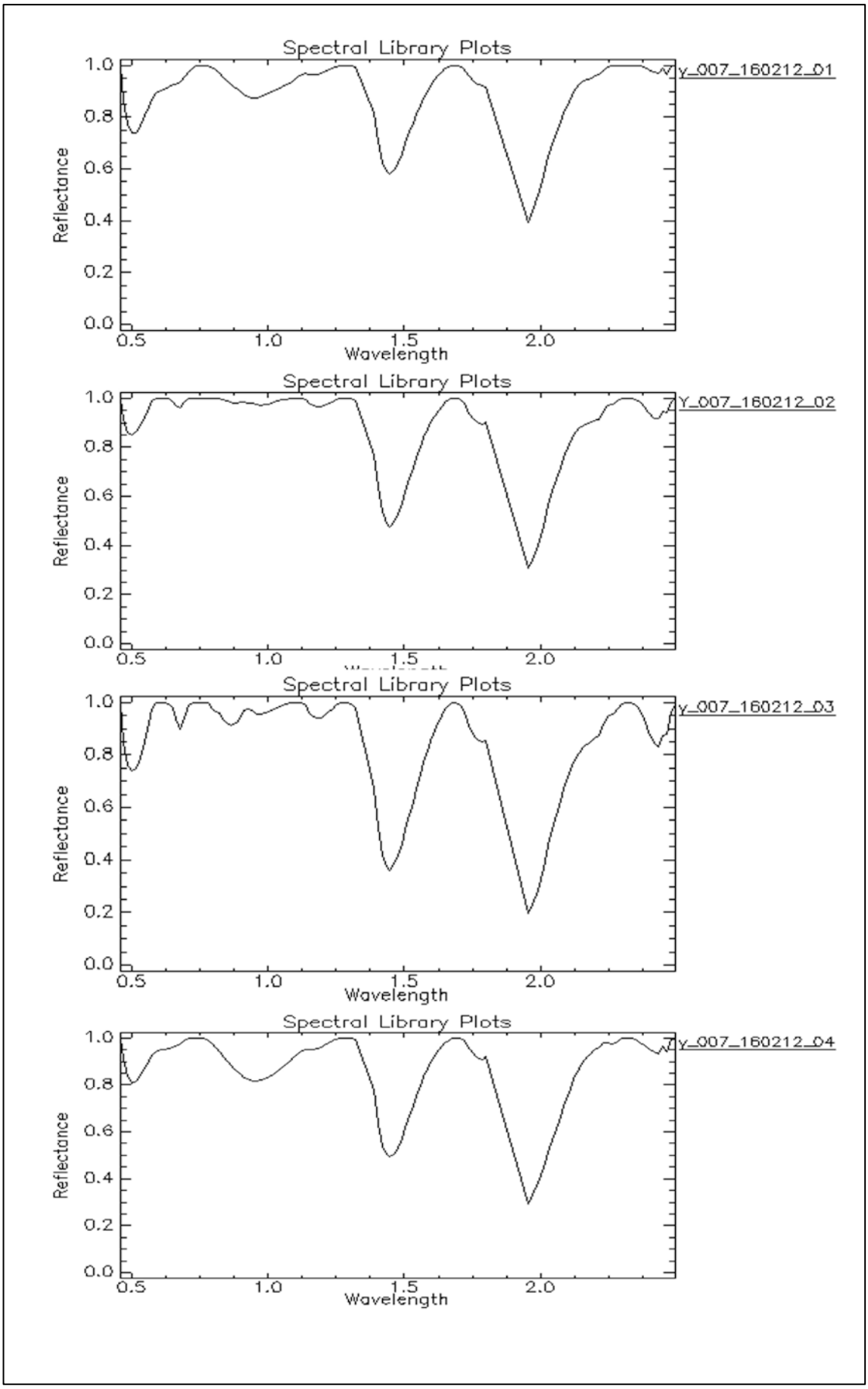
Spectral Library Plots
Reflectance
Wavelength
Y_007_160212_01
Spectral Library Plots
Reflectance
Wavelength
Y_007_160212_02
Spectral Library Plots
Reflectance
Wavelength
Y_007_160212_03
Spectral Library Plots
Reflectance
Wavelength
Y_007_160212_04

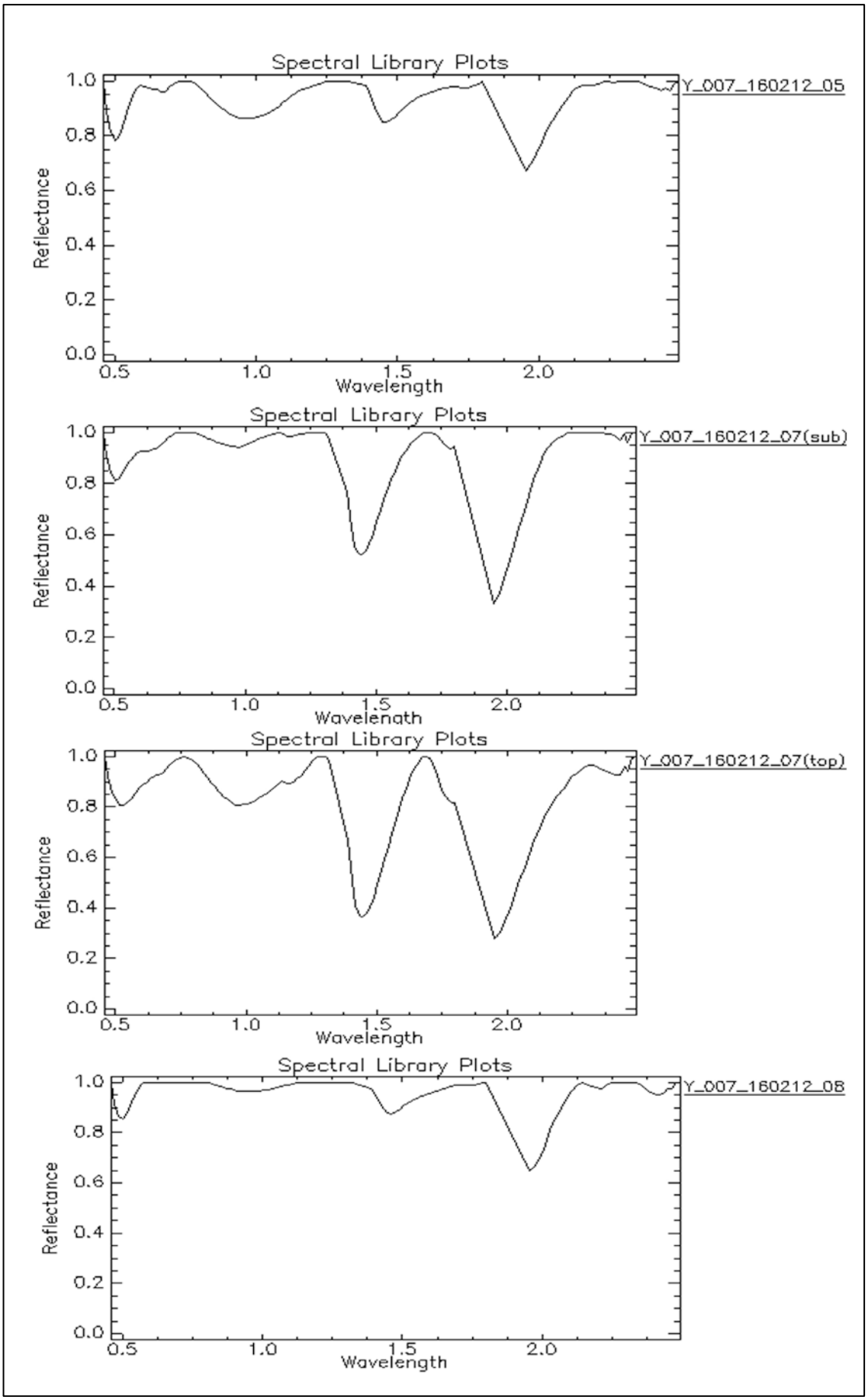
Spectral Library Plots
Y_007_160212_05
Reflectance
Wavelength
Spectral Library Plots
Y_007_160212_07(sub)
Reflectance
Wavelength
Spectral Library Plots
Y_007_160212_07(top)
Reflectance
Wavelength
Spectral Library Plots
Y_007_160212_08
Reflectance
Wavelength

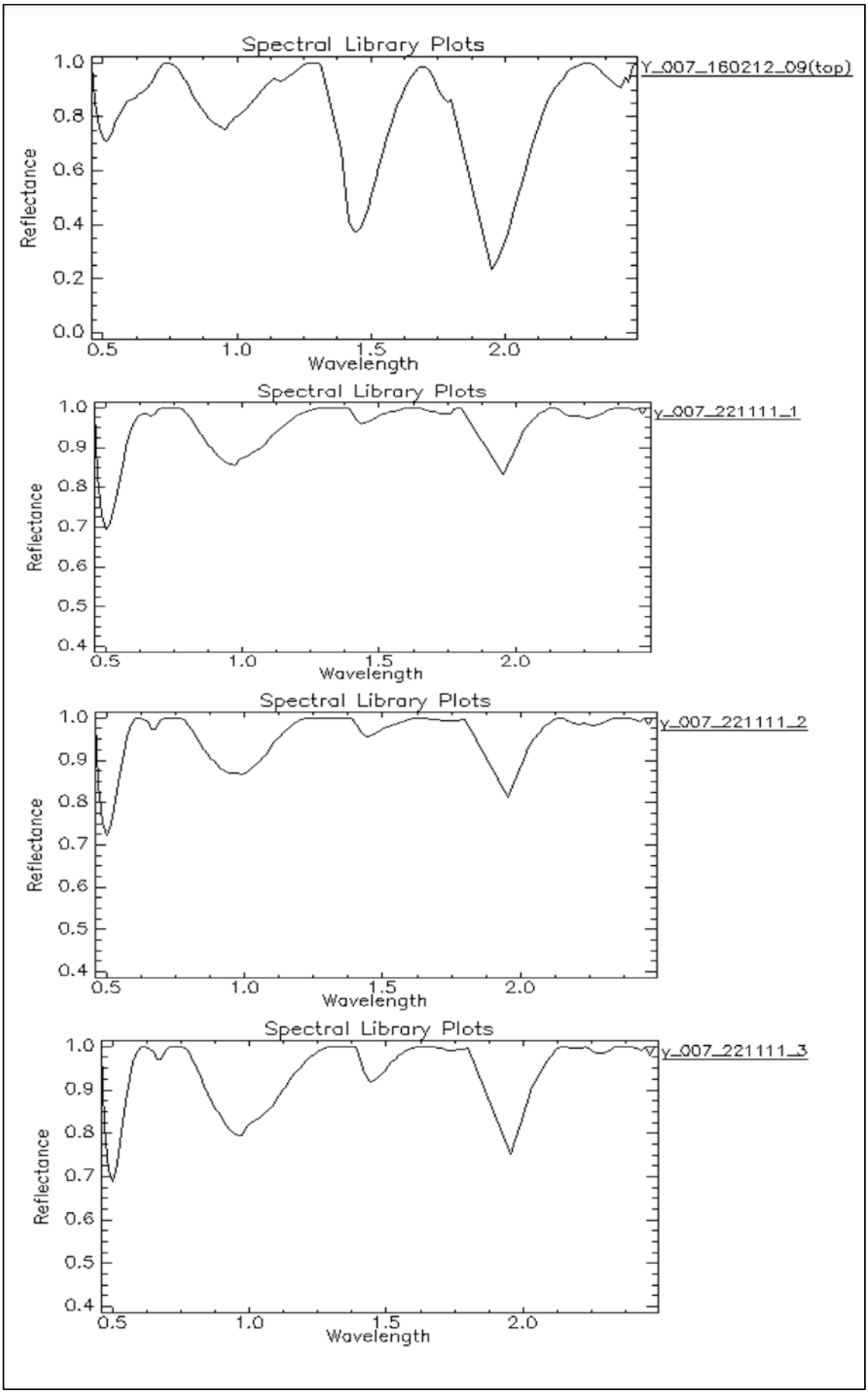
Spectral Library Plots
Y_007_160212_09(top)
Reflectance
Wavelength
Spectral Library Plots
y_007_221111_1
Reflectance
Wavelength
Spectral Library Plots
y_007_221111_2
Reflectance
Wavelength
Spectral Library Plots
y_007_221111_3
Reflectance
Wavelength

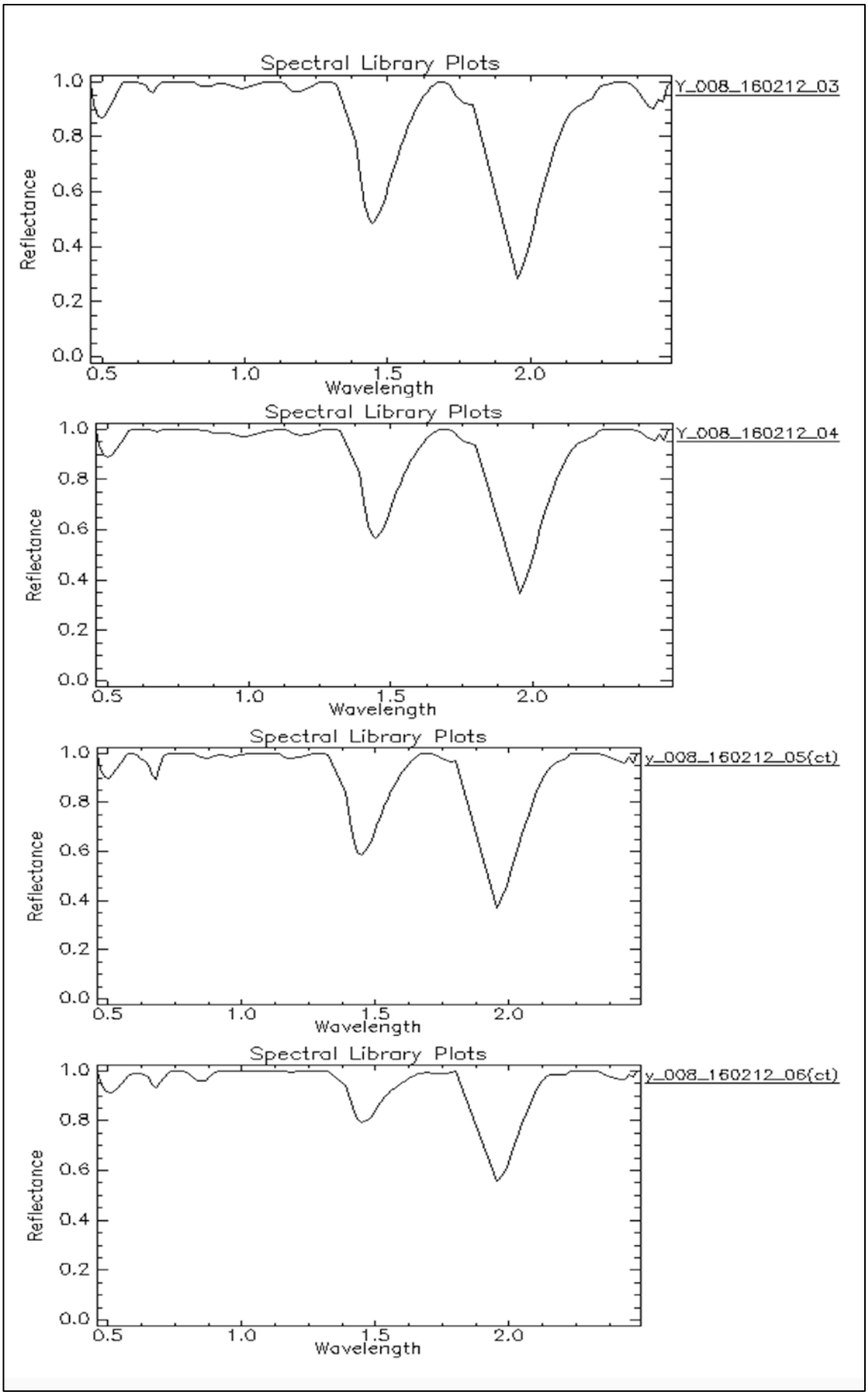
Spectral Library Plots
Reflectance
Wavelength
Y_008_160212_03
Spectral Library Plots
Reflectance
Wavelength
Y_008_160212_04
Spectral Library Plots
Reflectance
Wavelength
y_008_160212_05(ct)
Spectral Library Plots
Reflectance
Wavelength
y_008_160212_06(ct)

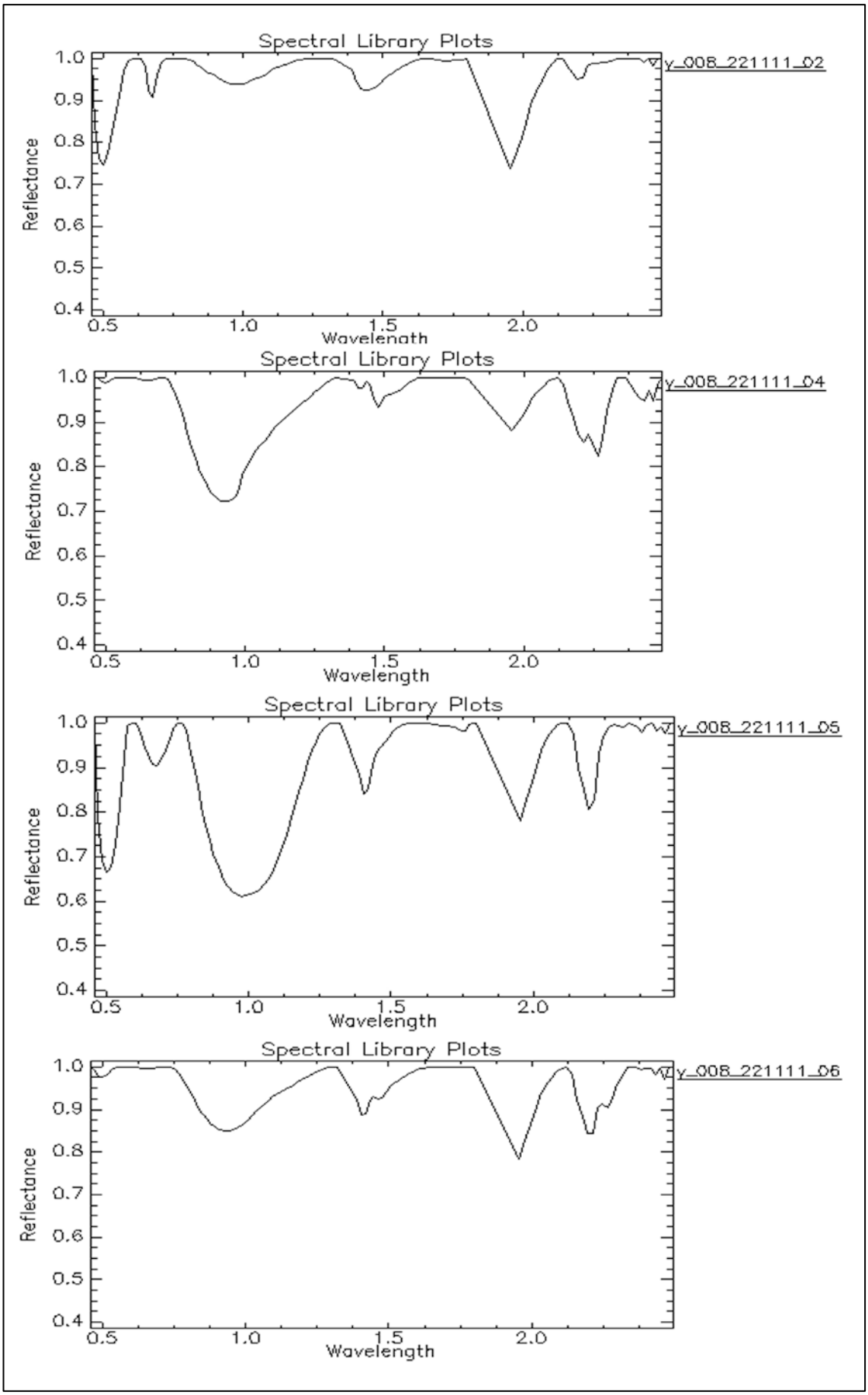
Spectral Library Plots
y_008_221111_02
Reflectance
Wavelength
Spectral Library Plots
y_008_221111_04
Reflectance
Wavelength
Spectral Library Plots
y_008_221111_05
Reflectance
Wavelength
Spectral Library Plots
y_008_221111_06
Reflectance
Wavelength

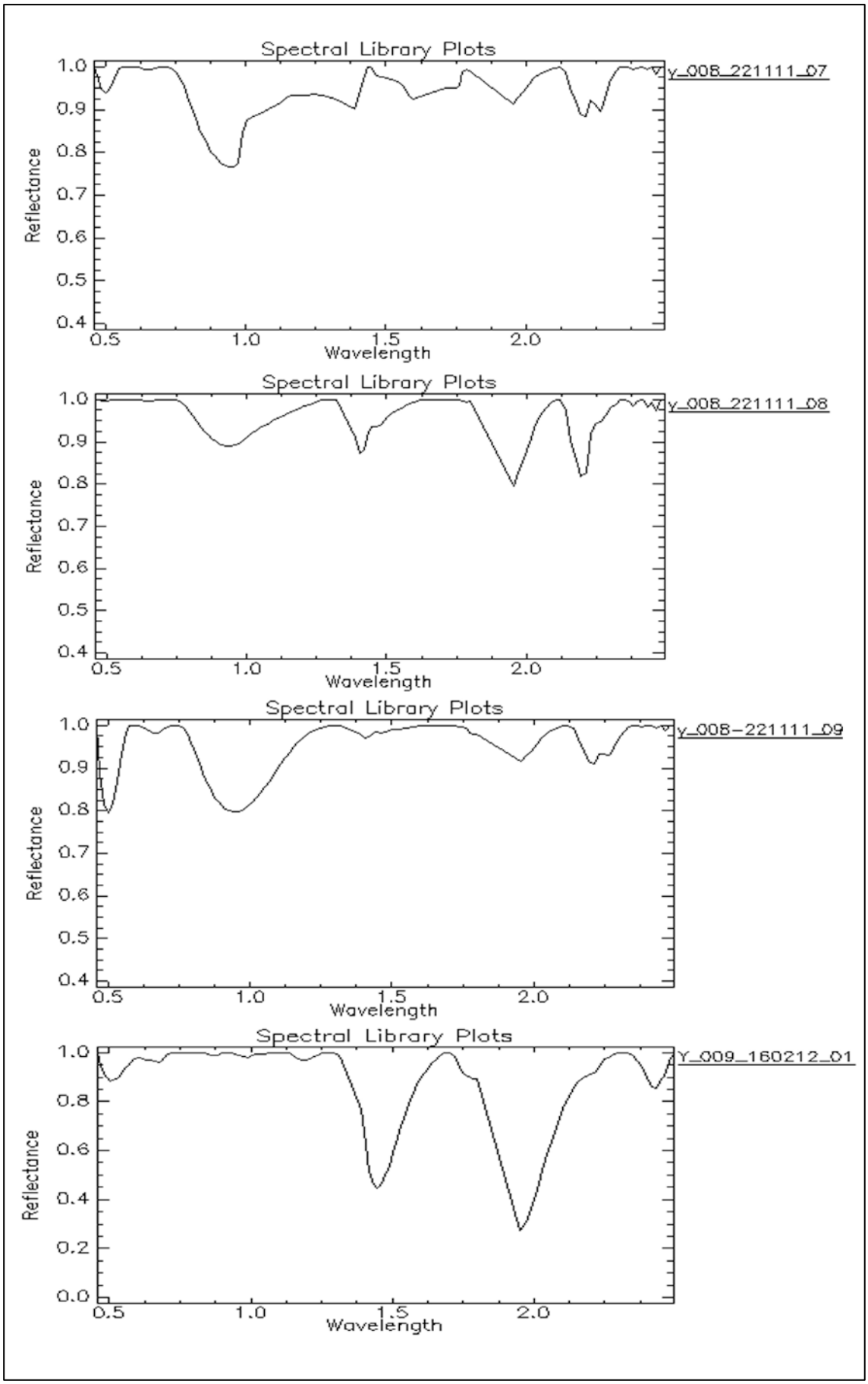
Spectral Library Plots
Reflectance
Wavelength
y_008_221111_07
Spectral Library Plots
Reflectance
Wavelength
y_008_221111_08
Spectral Library Plots
Reflectance
Wavelength
y_008-221111_09
Spectral Library Plots
Reflectance
Wavelength
Y_009_160212_01

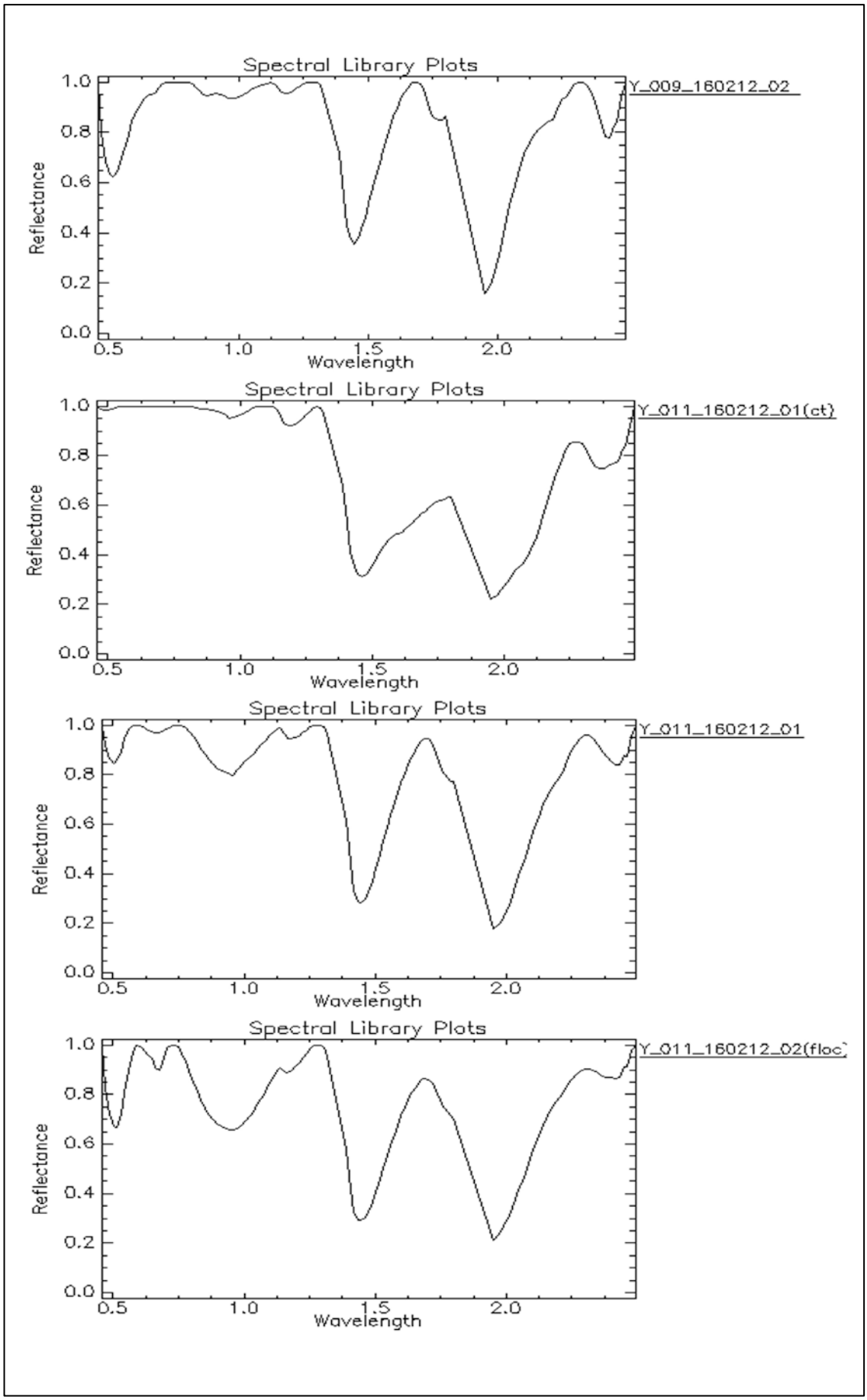
Spectral Library Plots
Y_009_160212_02
Reflectance
Wavelength
Spectral Library Plots
Y_011_160212_01(ct)
Reflectance
Wavelength
Spectral Library Plots
Y_011_160212_01
Reflectance
Wavelength
Spectral Library Plots
Y_011_160212_02(floc)
Reflectance
Wavelength

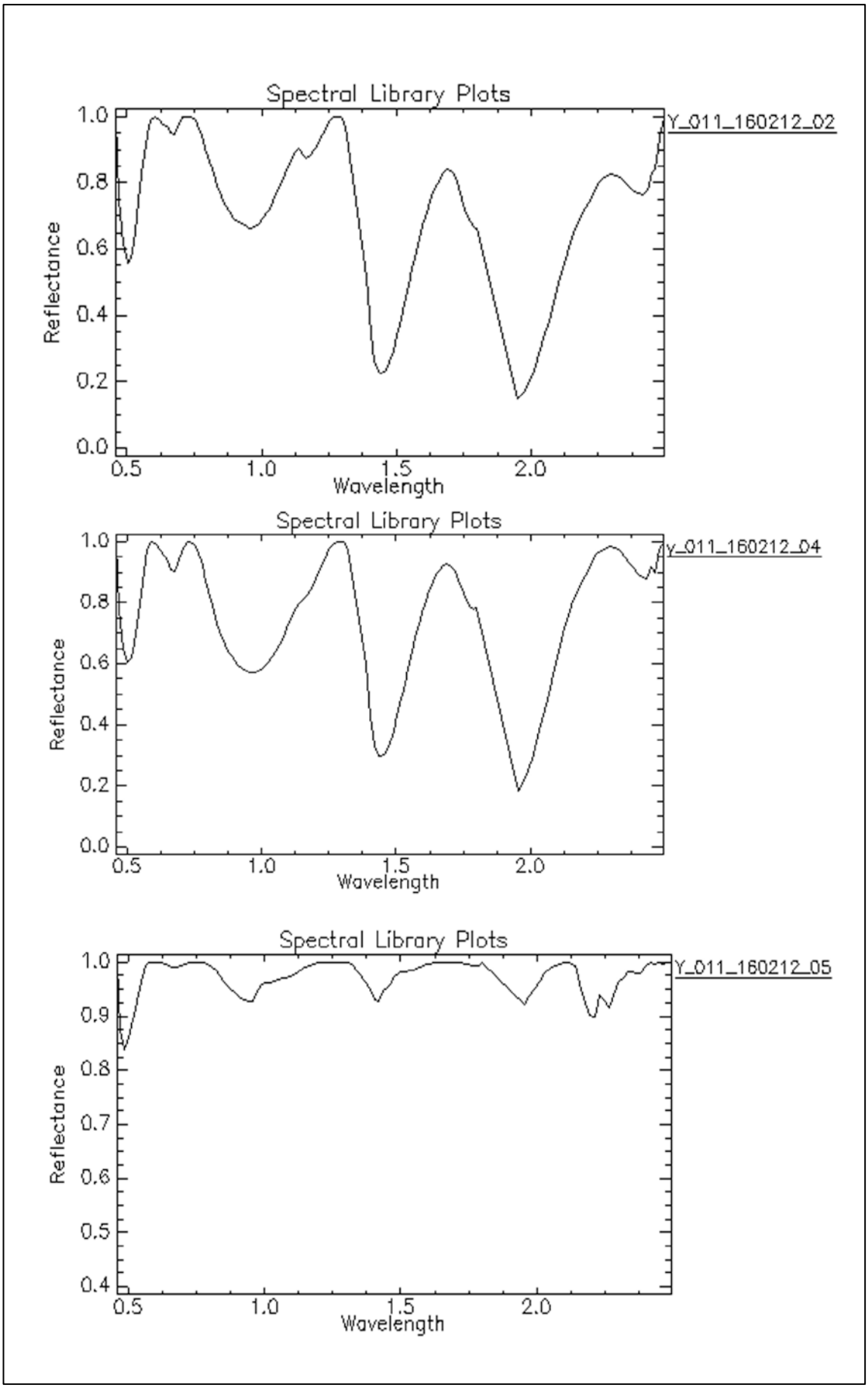
Spectral Library Plots
Reflectance
Wavelength
Y_011_160212_02
Spectral Library Plots
Reflectance
Wavelength
y_011_160212_04
Spectral Library Plots
Reflectance
Wavelength
Y_011_160212_05

Appendix 3: Field images of the sample sites in the study area

Field images in the first field work on 20-10-2011

Site y-001

Site y-002

Site y-004

Site y-005

Site y-006

Site y-007

Field images in the second field work on 22-11-2012


Scene of site y-011


Scene of site y-008


Scene of site y-007

Field images in the third field work on 16-02-2012

Site y-005

Site y-007

Site y-009

Site y-011

Site y-012

Field images in the fourth field work on 24-05-2012

Site y-008(soil undisturbed, covered by vegetation)

Site y-008(soil disturbed,near the road)

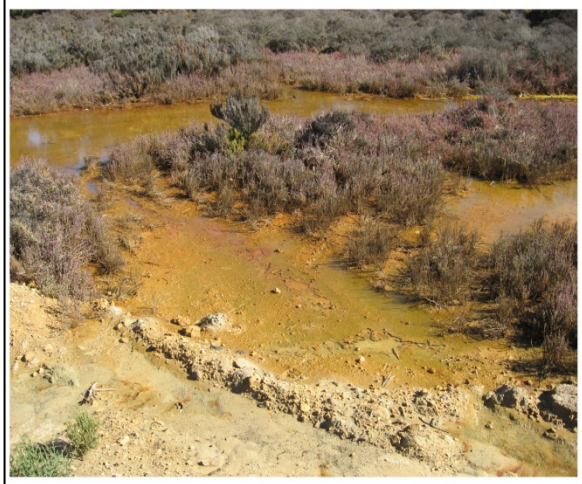

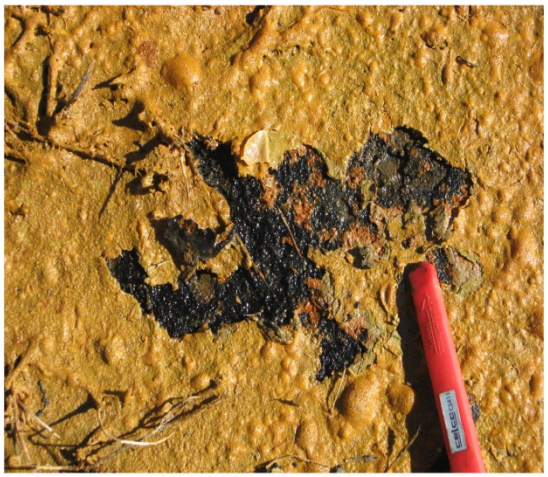

Site y-012(wetland, containing MBO)

Appendix 4: Parts of photos of soils samples collected from the surface of the study area


y-008-160212-06(ct)
y-002-160212-02
y-005-160212-01
Y_005_160212_03
Y_002_160212_01
Y_008_160212_03


Y_008_160212_04


y-005-160212-04


y-011-160212-05


y-011-160212-01


y-002-1602120-4


y-002-160212-02


Y_011_160212_02
Y_007_160212_04
Y_007_160212_02
Y_007_160212_03
Y_007_160212_04
Y_007_160212_01


Y_007_160212_02


Y_009_160212_02

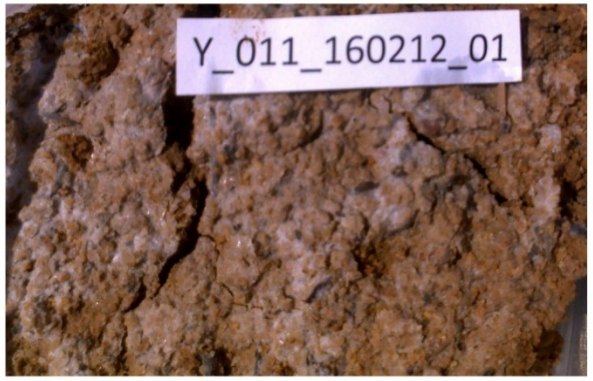
Y_011_160212_01

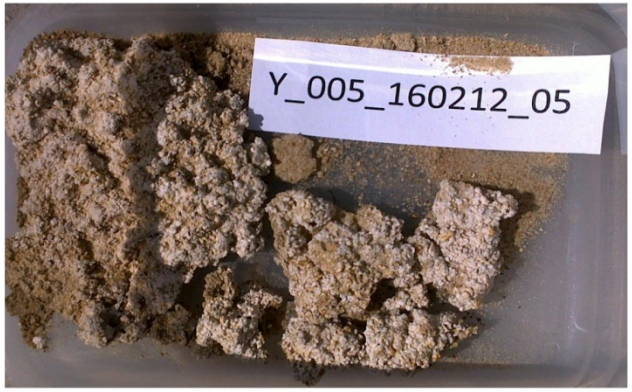
Y_005_160212_05


Y_005_160212_02

Appendix 5: The measurements of the solution from the incubation experiment described in Chapter 4

Sample id	EC (ms/cm)	Ph	Al	As	Ba	Co	Fe-Sol	Mn	Pb	Si	U	F	Cl	Br	NO3	PO4	SO4
G1-1(23-10-2012)	6.88	3.81	2.7	DBL	20.7	0.01	0.3	1.1	0.012	8.1	0.89	0.44	1830	6.657			1008.66
G1-1(30-10-2012)	6.64	3.6	0.8	0.001	20.2	0.004	0.2	1.3	DBL	7.4	0.51	0.22	1685	5.875			1029.98
G1-1(06-11-2012)	7.41	3.39	1.1	DBL	24.9	0.006	0.4	1.8	0.005	12.1	0.72	0.373	1807	6.305			1305.48
G1-1(13-11-2012)	5	3.64	1.1	DBL	17.2	0.003	0.2	1.4	DBL	11.5	0.46	0.372	1182	3.936			963.12
G1-1(19-11-2012)	4.51	3.64	0.8	DBL	13.3	0.002	0.2	1.3	DBL	12.1	0.35	0.333	1017	3.015			857.144
G1-1(27-11-2012)	3.98	3.8	1.6	DBL	11.4	0.002	0.2	1.2	DBL	13.3	0.38	0.501	760.3	2.372	5.694		850.387
G1-1(04-12-2012)	3.33	3.79	2	DBL	8.6	0.003	0.2	1.1	0.006	12.6	0.41	0.926	562.4	1.793			763.494
G1-1(11-12-2012)	2.91	3.87	3.1	DBL	9.1	0.004	0.3	1.1	DBL	13.8	0.54	0.845	459.9	1.614			760.424
G1-1(18-12-2012)	3.13	3.73	3.9	DBL	10.9	0.005	DBL	1	DBL	12.6	0.61	0.748	410.3	1.381			700.604
G1-1(27-12-2012)	3.04	3.47	5.6	DBL	8.8	0.008	2.1	1.2	0.005	16.1	0.9	0.99	428.8	1.496			1062.09
G1-1(03-01-2013)	2.87	3.5	6.7	DBL	8.7	0.009	1.4	1.1	0.008	16	1.01	1.667	253.6	1.585		6.32	794.78
G1-1(10-01-2013)	2.32	3.65	5.3	DBL	6.2	0.009	0.1	0.9	0.006	13	0.83	0.751	173.7	0.888			632.557
G1-1(18-01-2013)	2.71	3.45	8.6	DBL	13.2	0.017	0.3	1.2	0.009	23.6	1.82	1.252	171.2	0.641			791.503
G1-1(25-01-2013)	1.571	3.6										0.605	83.18				487.461
G1-1(31-01-2013)	1.634	3.52										0.636	68.72	0.327	2.857		520.075
G1-2(23-10-2012)	9.82	3.62	3.1	DBL	27.9	0.01	2	1.3	0.026	9.3	2.71	0.535	2493	9.506			1411.63
G1-2(30-10-2012)	8.72	3.73	1.1	DBL	27.8	0.006	DBL	1.7	0.007	11.5	0.63	0.678	2424	8.276			1351.65
G1-2(06-11-2012)	7.07	3.46	3.1	DBL	23	0.007	0.2	1.6	0.009	14	1.57	1.247	1913	8.614			1201.11
G1-2(13-11-2012)	5.43	3.57	2.6	DBL	17	0.005	DBL	1.4	0.009	15.2	1.47	0.701	1392	4.599		3.529	988.075
G1-2(19-11-2012)	4.1	3.71	1.7	DBL	12.4	0.002	DBL	1	DBL	13.8	0.96		909.8	5.092			723.644
G1-2(27-11-2012)	3.97	3.7	1.4	DBL	11.5	0.001	DBL	0.9	DBL	16	0.56	0.597	334	1.266	7.237		689.946
G1-2(04-12-2012)	3.02	3.72	0.7	DBL	9	0.001	DBL	0.7	DBL	13.2	0.37	0.267	562	1.711			571.86

G1-2(11-12-2012)	2.74	3.81	0.7	DBL	9.9	0.002	DBL	0.7	0.005	15.2	0.37	0.343	500.1	1.764			606.785
G1-2(18-12-2012)	3.1	3.68	1	DBL	11.6	0.003	0.1	0.8	DBL	15.7	0.4	0.401	397.5	1.302			607.574
G1-2(27-12-2012)	3.07	3.43	1.7	DBL	11.4	0.003	0.2	1	0.006	21.3	0.65	1.594	885.6	2.848			786.396
G1-2(03-01-2013)	3.3	3.5	1.4	DBL	9.3	0.003	DBL	0.8	DBL	19	0.56	0.652	198.6	0.811			528.249
G1-2(10-01-2013)	1.87	3.64	1.2	DBL	8.6	0.004	DBL	0.7	0.005	17.1	0.58	0.433	159.7	0.56			479.923
G1-2(18-01-2013)	1.95	3.69	1.9	DBL	10.2	0.003	DBL	0.8	DBL	21.8	0.61	0.75	149.6				513.768
G1-2(25-01-2013)	1.228	3.62										0.769	86.4	0.49	2.974	8.087	344.512
G1-2(31-01-2013)	1.458	3.57										0.418	80.87	0.27	2.652		376.6
G1-2(27-02-2013)	1.204	3.54										1.03	56.26	0.233	2.679		655.641
G2-1(13-11-2012)	9.91	3.76	5.4	DBL	20.9	0.013	0.7	2.7	0.006	11.4	1.18	0.72	2367	8.868			1817.11
G2-1(11-12-2012)	10.97	3.36	13.6	0.002	31.4	0.026	0.6	2.7	DBL	14.2	4.57	2.752	2665	13.26		1.69	1815.97
G2-1(10-01-2013)	16.26	3.79	6.6	0.005	22.3	0.105	42	4.1	0.026	13.6	1.94	1.094	3362	11			2263.11
G2-2(13-11-2012)	11.82	3.63	8.6	DBL	27.4	0.021	0.4	3.2	DBL	14.7	2.42	1.627	3167	14.03			2170.76
G2-2(11-12-2012)	11.05	3.5	6.4	DBL	17.3	0.007	0.3	2.8	0.007	13.4	2.27	0.922	2656	9.156			2055.99
G2-2(10-01-2013)	12.78	3.62	7	0.006	23.2	0.136	72.3	3.9	0.026	12.4	2.44	1.472	2339		8.032		1984.31
G2-2(27-02-2013)	14.86	3.35										12.595	2344	8.021	10.562		6461.02
G3-1(10-01-2013)	26.3	3.41	25.1	0.011	25.1	0.241	90.3	9.1	0.097	14.1	8.56	3.674	5453	17.55			3815.31
G3-2(10-01-2013)	21.8	3.46	23.4	0.011	17.7	0.231	78.4	8.5	0.11	13.2	7.9	3.066	4381	19.19	14.783		2902.87
G3-2(27-02-2013)	21.2	3.39										13.523	5108	18.12	18.173		6136.19
pore water1	34.5	6.68	DBL	0.005	111.2	0.004	DBL	3.3	DBL	9.8	0.26	2.251	10377	64.7	24.448		5780.09
pore water2	34.5	6.68	DBL	0.005	111.2	0.004	DBL	3.3	DBL	9.8	0.26	3.128	10175	60.06	26.438		5701.98
Pore water (average)			DBL	0.005	111.2	0.004	DBL	3.3	DBL	9.8	0.26	2.6895	10276	62.38	25.443		5741.03

Note: The BDL in the cell means no value because it beyond the detectable limitation.

Appendix 6: Photos and spectral measurements of the iron sulphides materials in the experiment described in Chapter 5.

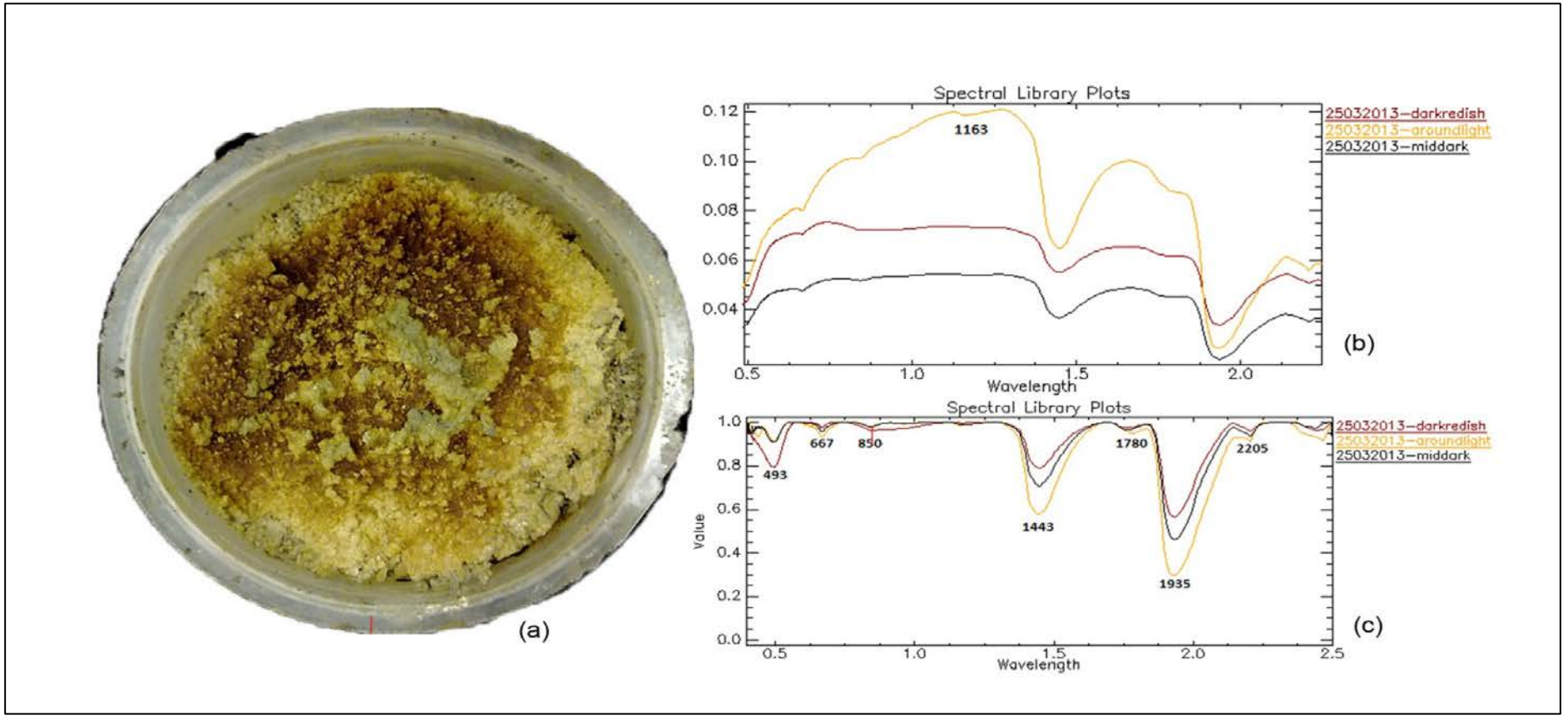

Spectra measured on 25th, March, 2013. (a) picture of the material;(b) spectra measured of the material;(d) continuum removed spectra of the material

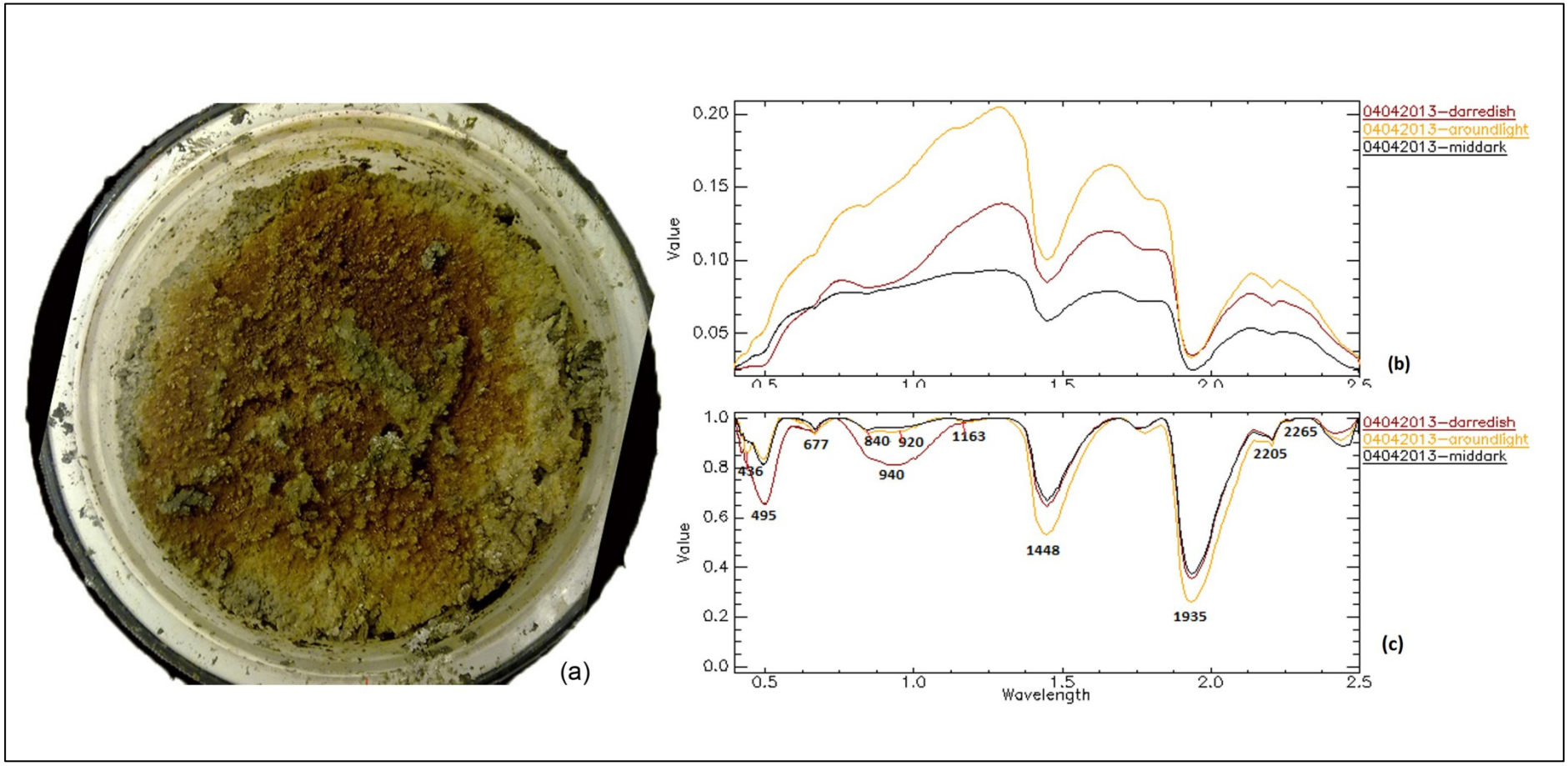

Spectra measured on 4th, Apr, 2013. (a) picture of the material;(b) spectra measured of the material;(d) continuum removed spectra of the material

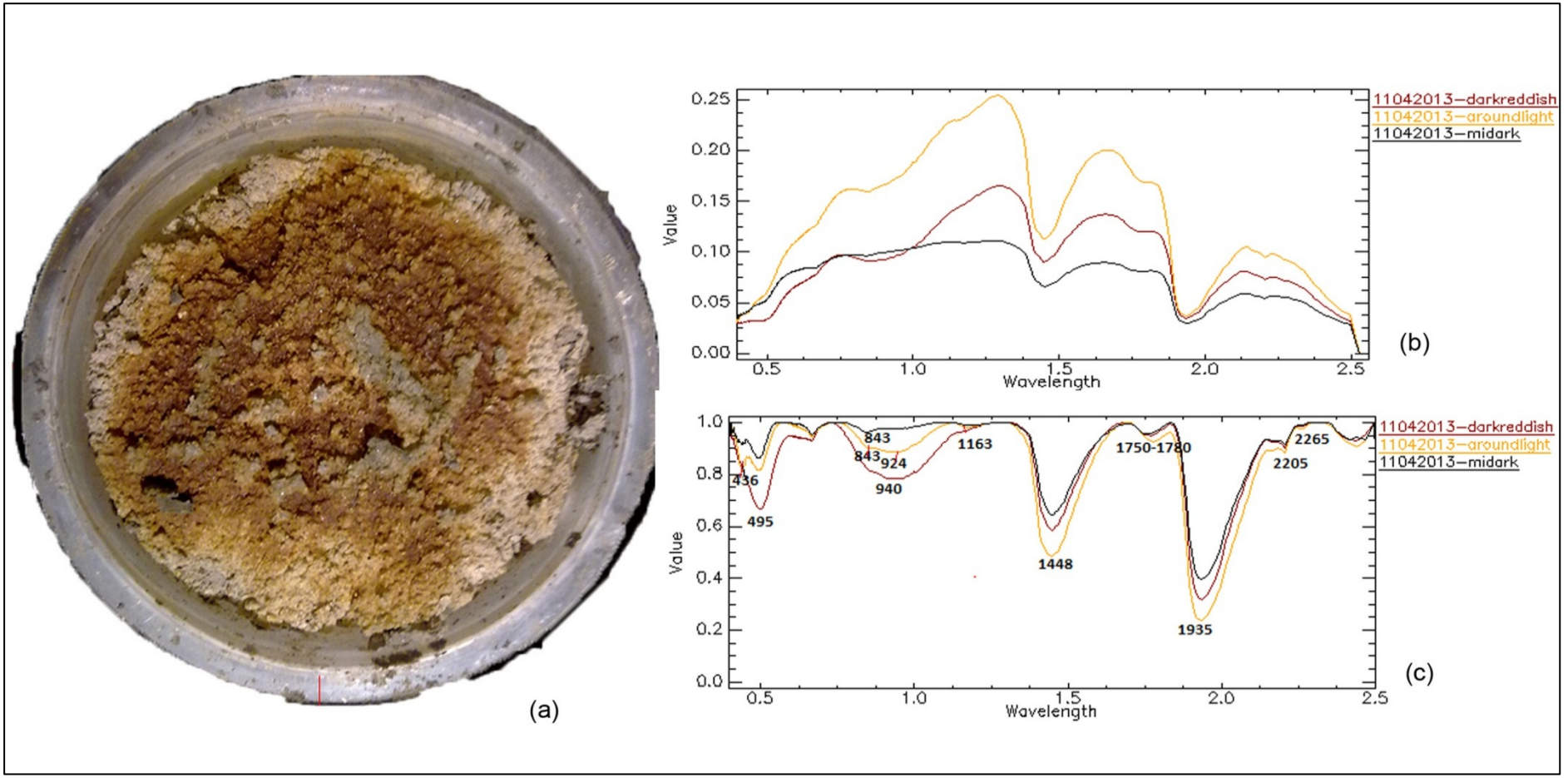

Spectra measured on 11th, Apr, 2013. (a) picture of the material;(b) spectra measured of the material;(d) continuum removed spectra of the material

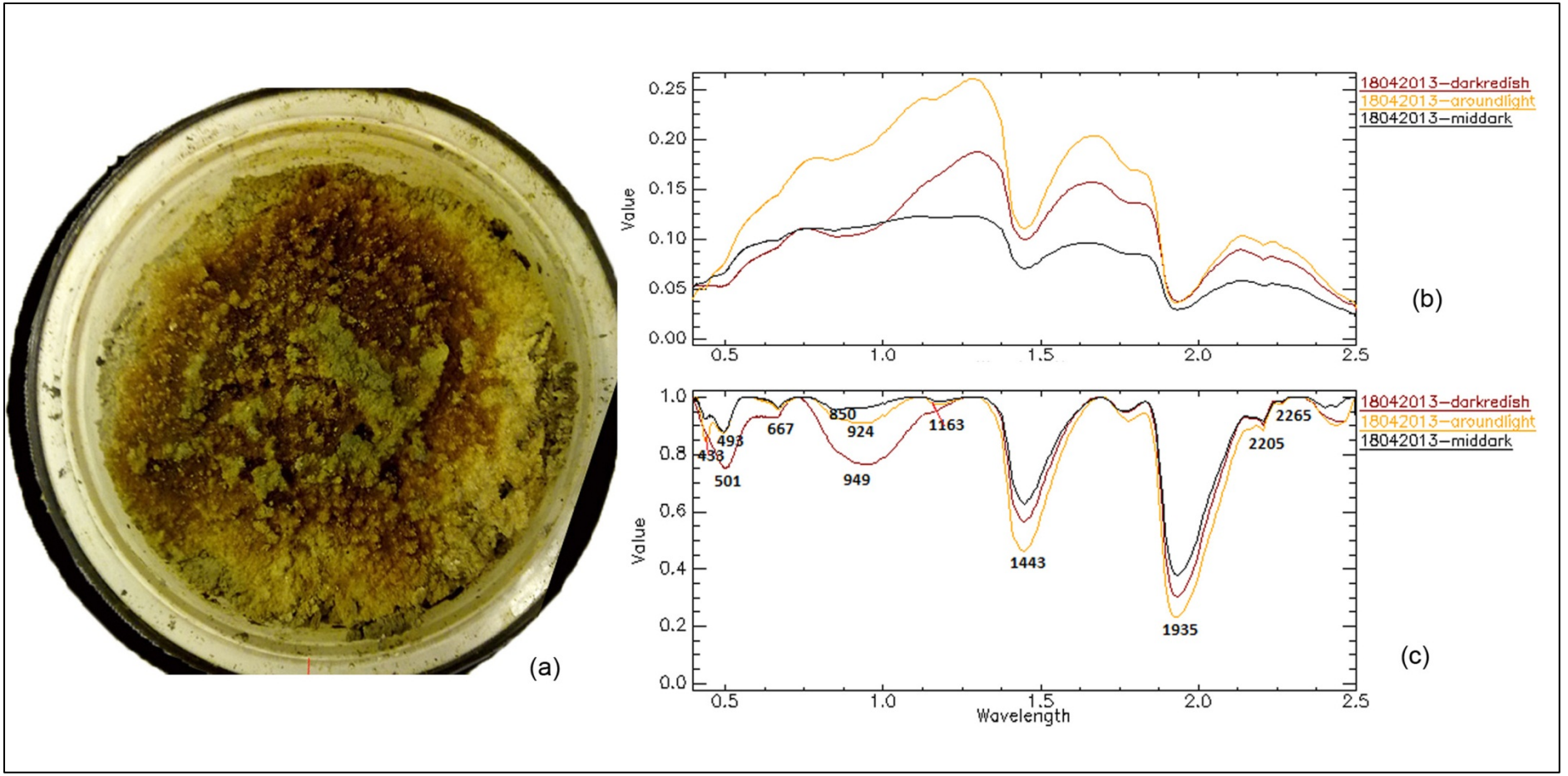

Spectra measured on 18th, Apr, 2013. (a) picture of the material;(b) spectra measured of the material;(d) continuum removed spectra of the material

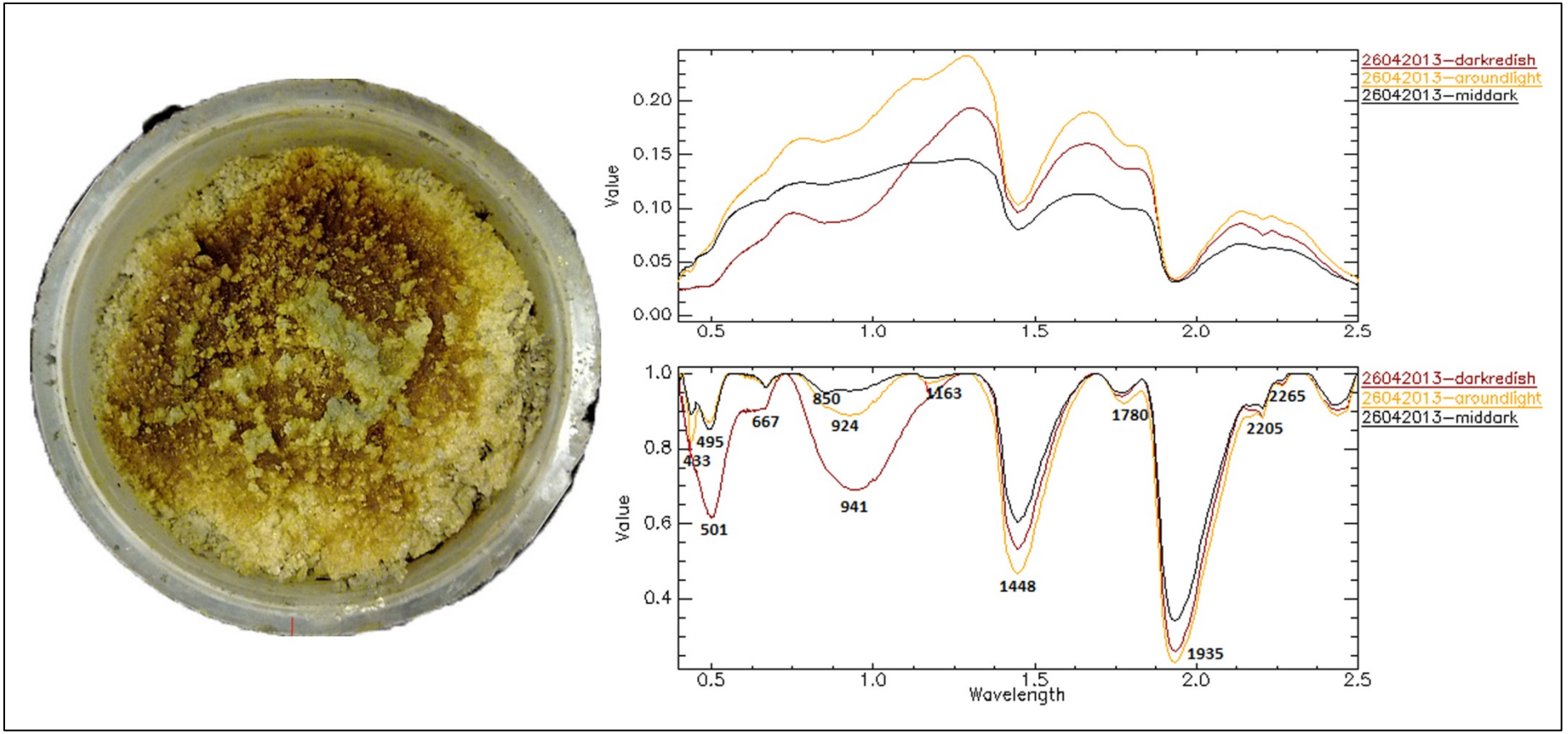

Spectra measured on 26th, Apr, 2013. (a) picture of the material;(b) spectra measured of the material;(d) continuum removed spectra of the material

Appendix 7: The reflectance spectral measurements of the samples extracted from soil cores

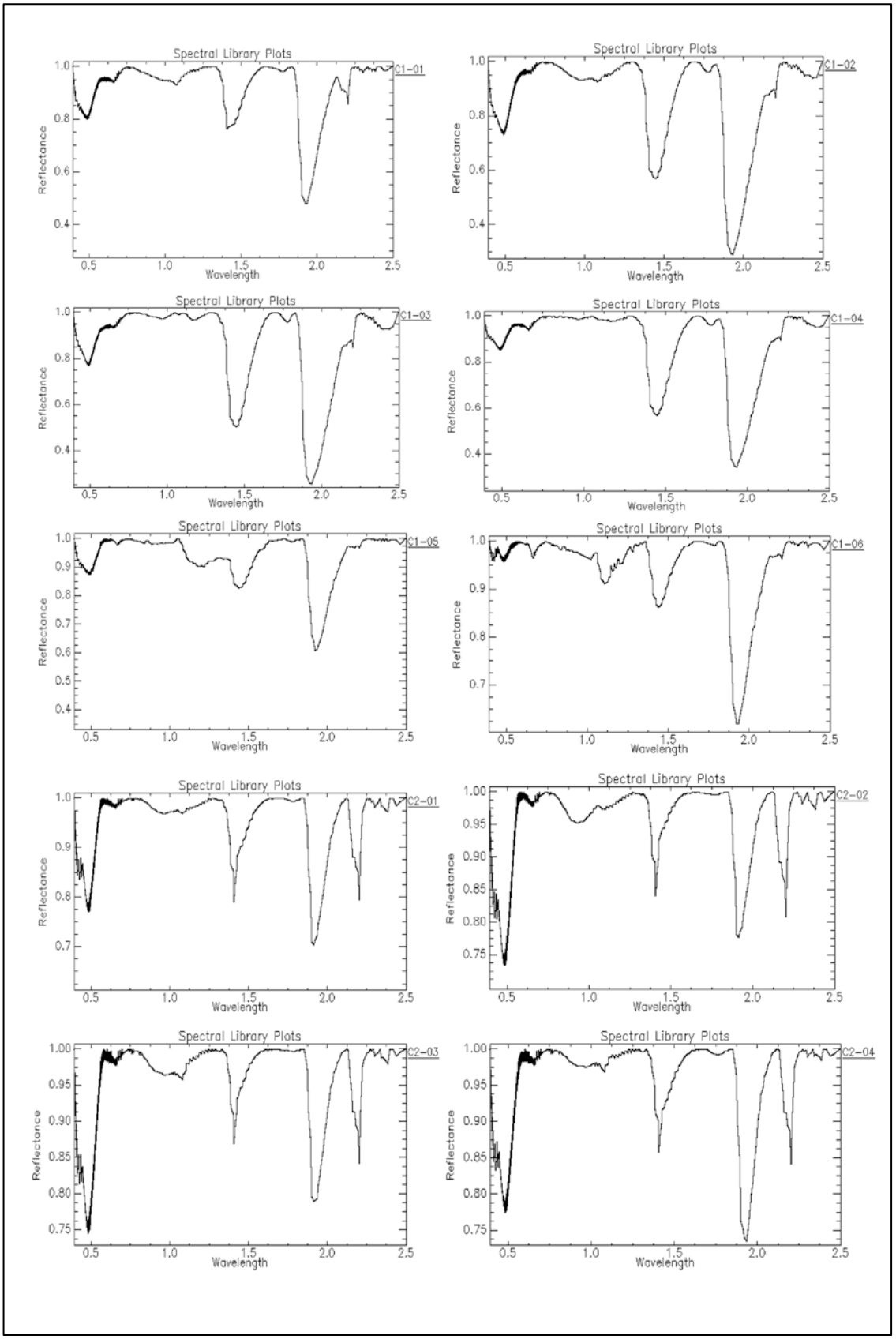

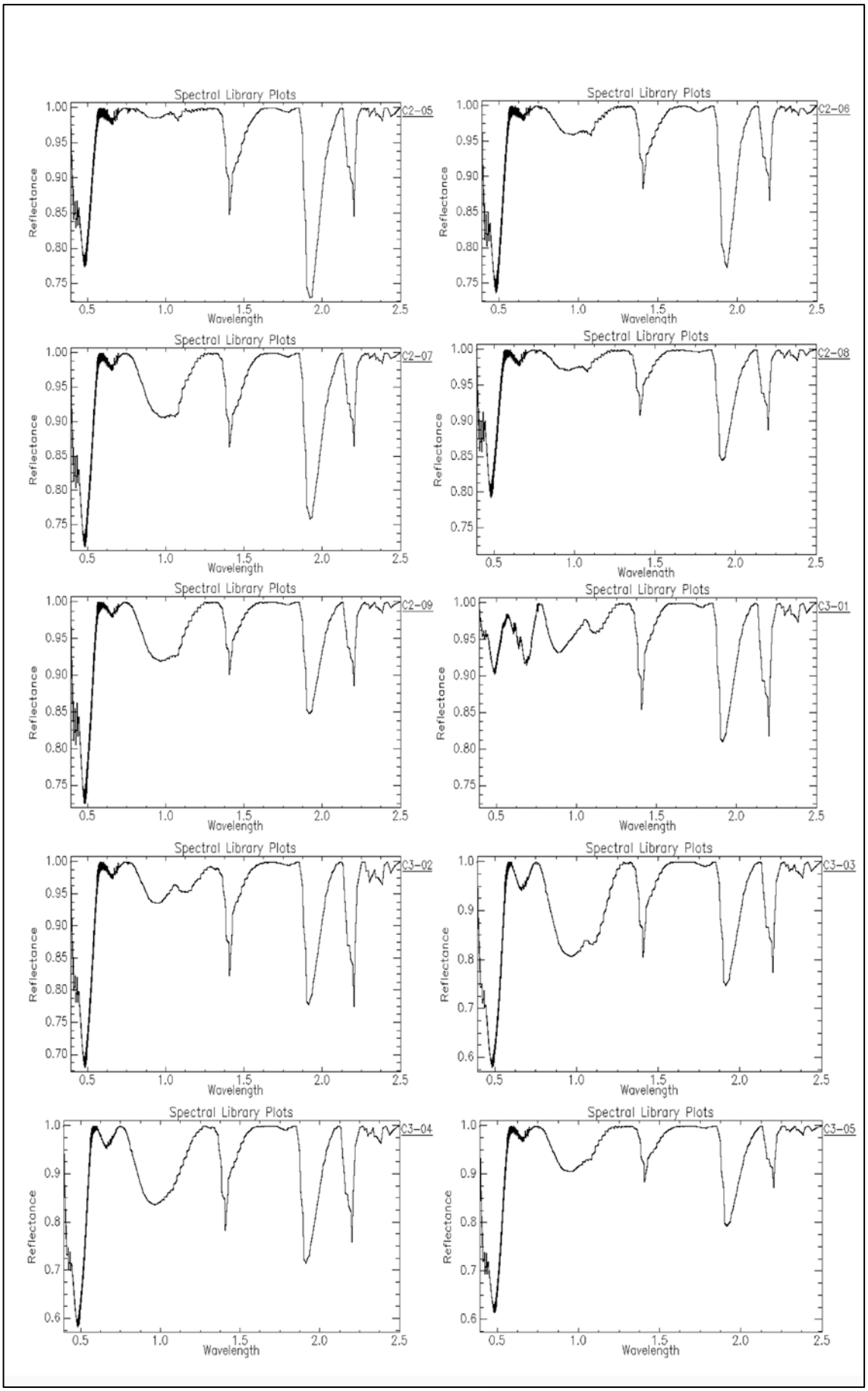
Spectral Library Plots
C2-05
Reflectance
Wavelength
Spectral Library Plots
C2-06
Reflectance
Wavelength
Spectral Library Plots
C2-07
Reflectance
Wavelength
Spectral Library Plots
C2-08
Reflectance
Wavelength
Spectral Library Plots
C2-09
Reflectance
Wavelength
Spectral Library Plots
C3-01
Reflectance
Wavelength
Spectral Library Plots
C3-02
Reflectance
Wavelength
Spectral Library Plots
C3-03
Reflectance
Wavelength
Spectral Library Plots
C3-04
Reflectance
Wavelength
Spectral Library Plots
C3-05
Reflectance
Wavelength

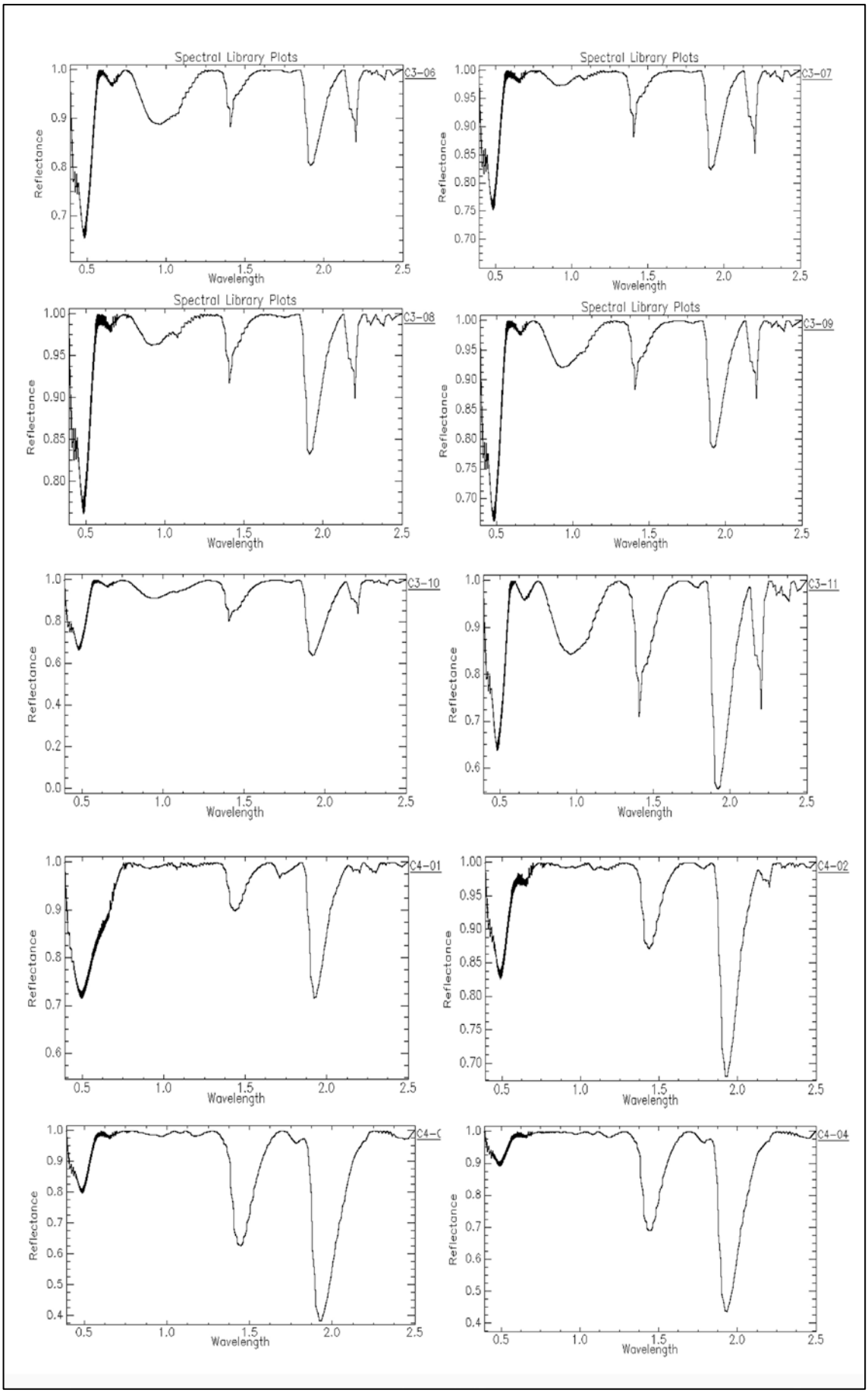
Spectral Library Plots
C3-06
Reflectance
Wavelength
Spectral Library Plots
C3-07
Reflectance
Wavelength
Spectral Library Plots
C3-08
Reflectance
Wavelength
Spectral Library Plots
C3-09
Reflectance
Wavelength
C3-10
Reflectance
Wavelength
C3-11
Reflectance
Wavelength
C4-01
Reflectance
Wavelength
C4-02
Reflectance
Wavelength
C4-04
Reflectance
Wavelength

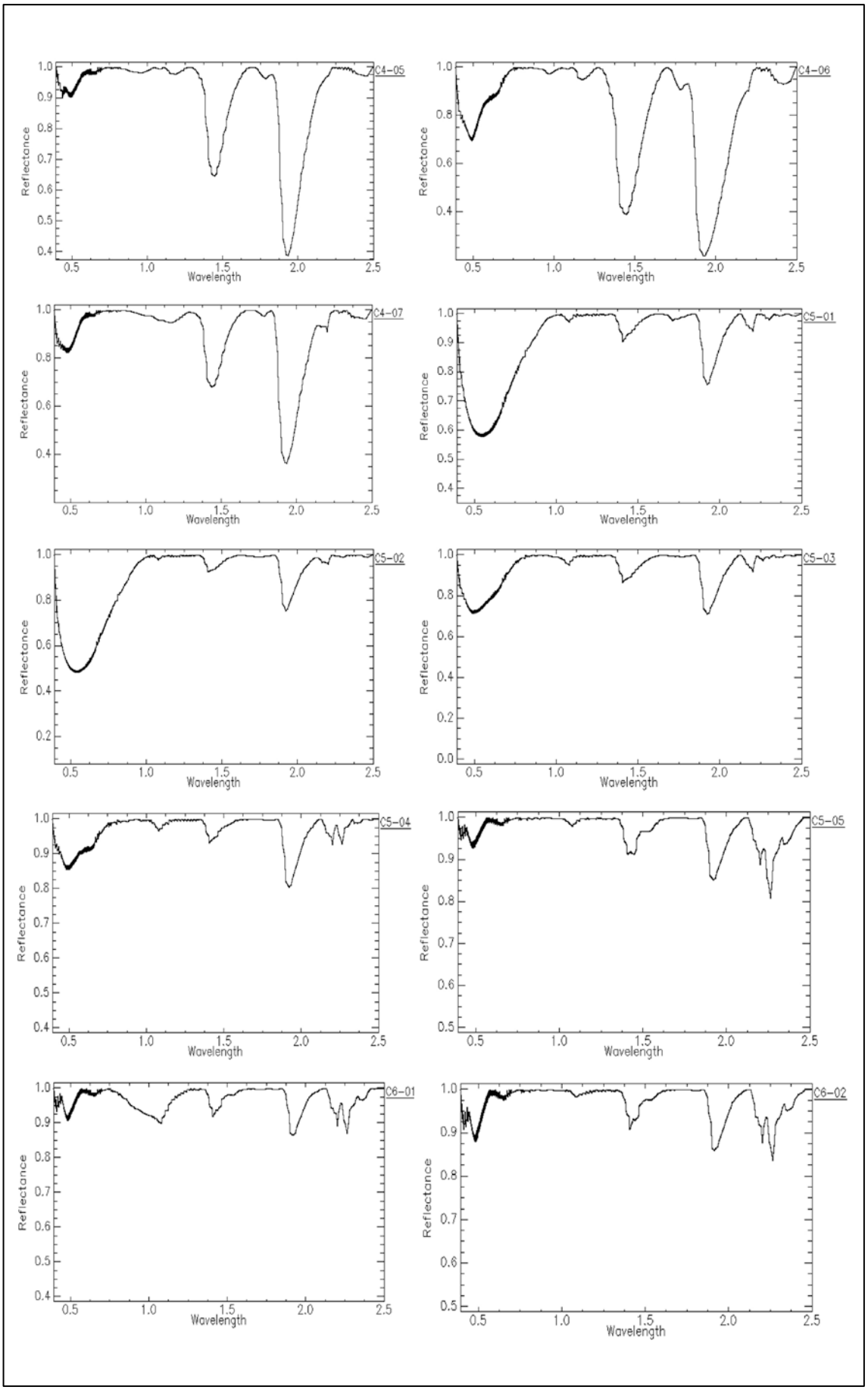
C4-05
C4-06
C4-07
C5-01
C5-02
C5-03
C5-04
C5-05
C6-01
C6-02
Reflectance
Wavelength

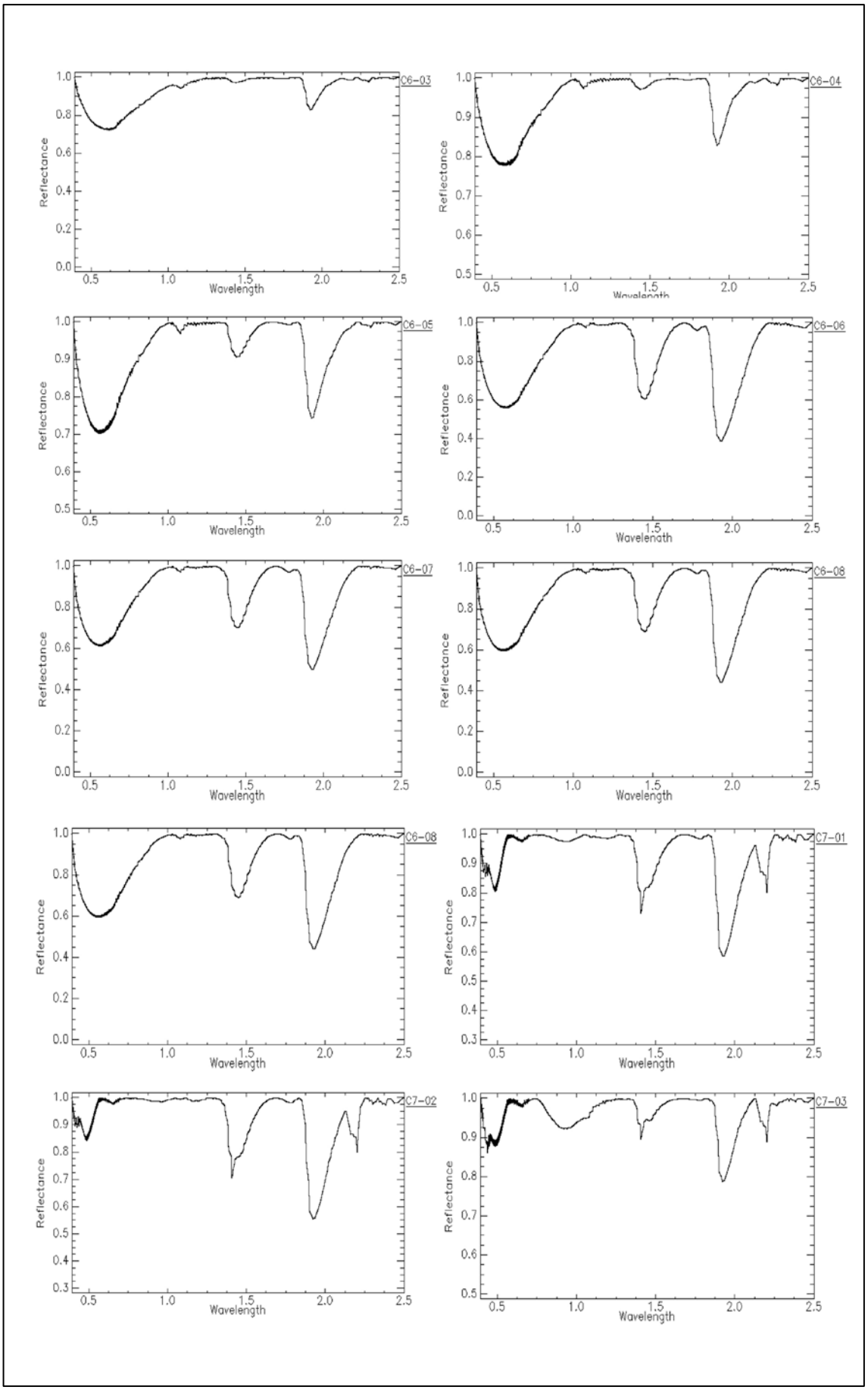
C6-03
C6-04
C6-05
C6-06
C6-07
C6-08
C6-08
C7-01
C7-02
C7-03
Reflectance
Wavelength

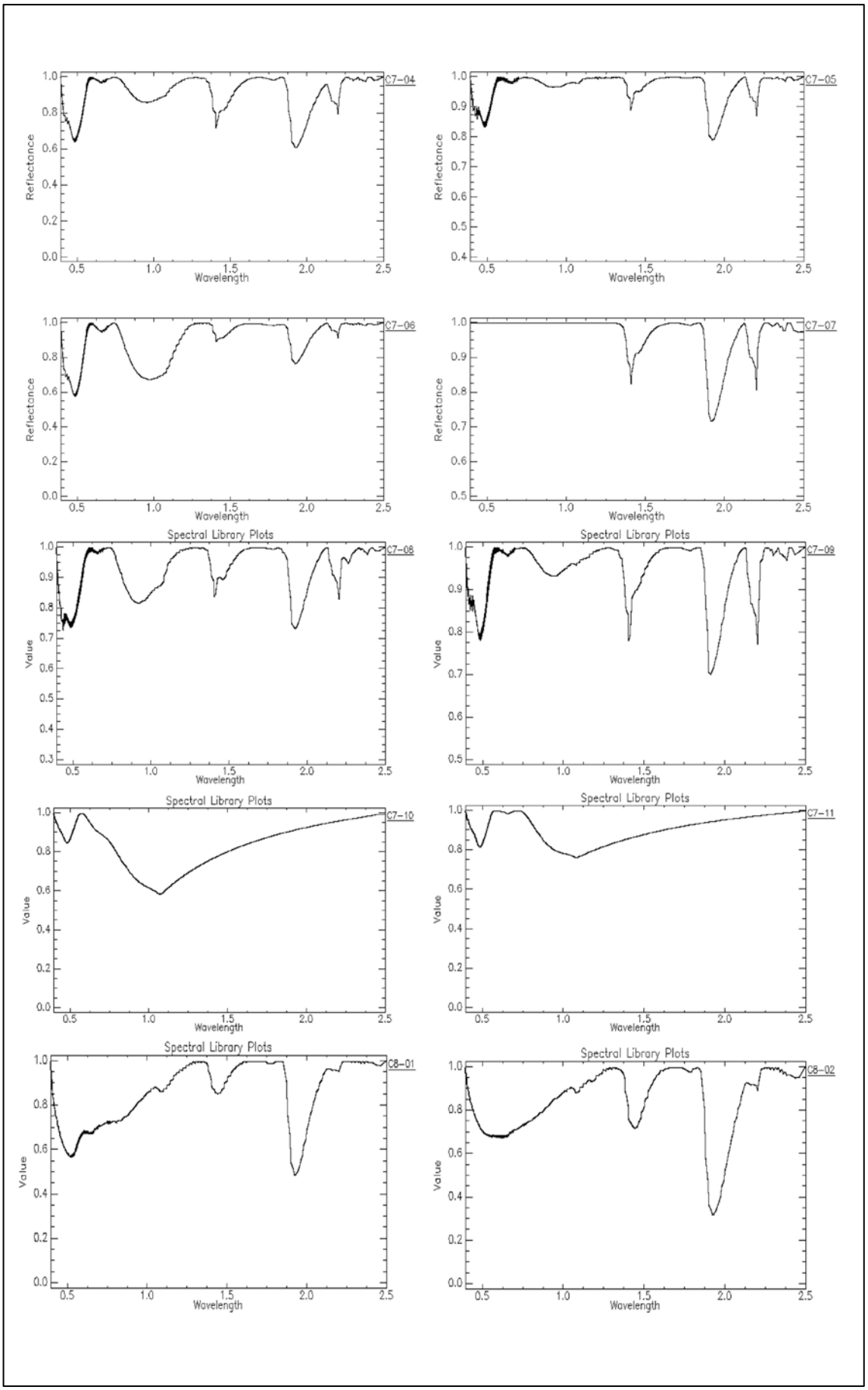
C7-04
Reflectance
Wavelength
C7-05
Reflectance
Wavelength
C7-06
Reflectance
Wavelength
C7-07
Reflectance
Wavelength
Spectral Library Plots
C7-08
Value
Wavelength
Spectral Library Plots
C7-09
Value
Wavelength
Spectral Library Plots
C7-10
Value
Wavelength
Spectral Library Plots
C7-11
Value
Wavelength
Spectral Library Plots
C8-01
Value
Wavelength
Spectral Library Plots
C8-02
Value
Wavelength

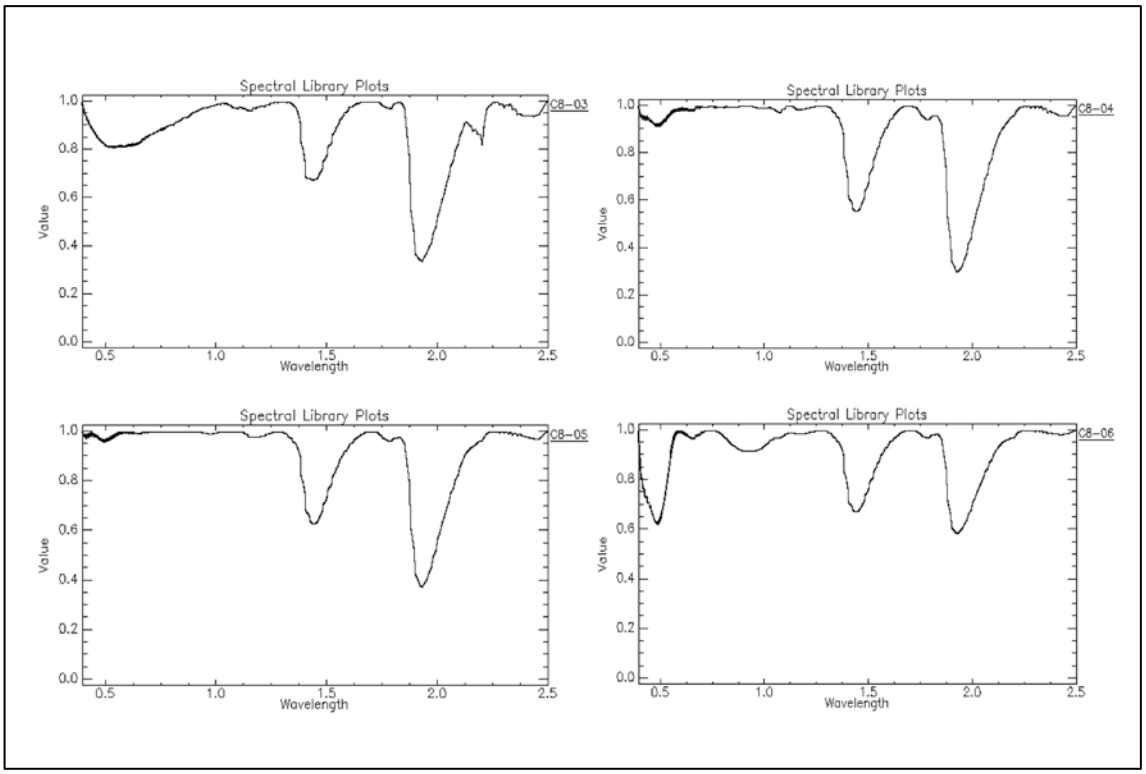
Spectral Library Plots
C8-03
Value
Wavelength
Spectral Library Plots
C8-04
Value
Wavelength
Spectral Library Plots
C8-05
Value
Wavelength
Spectral Library Plots
C8-06
Value
Wavelength

Appendix 8: The sample pictures extracted from soil cores

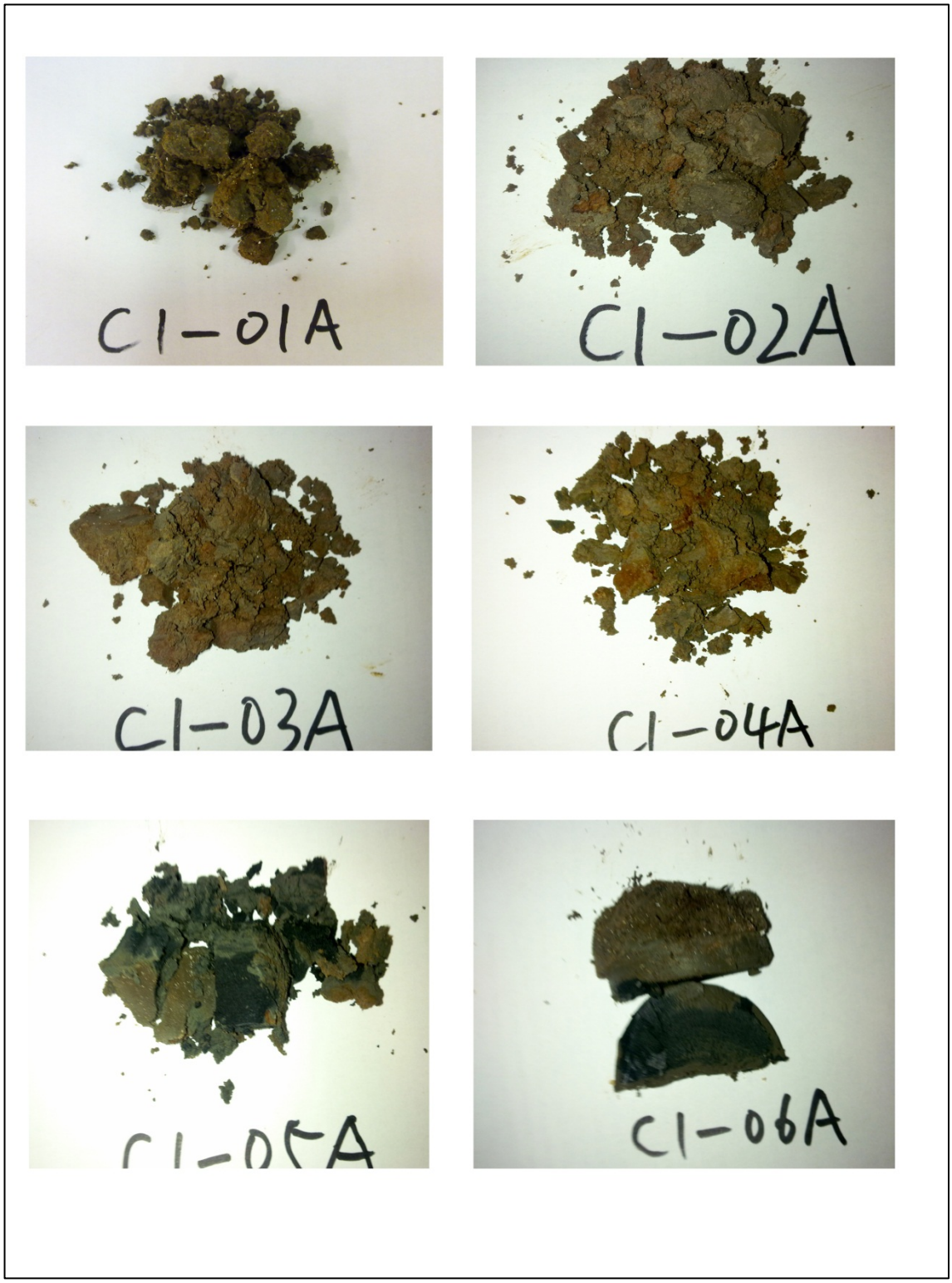

Pictures of parts of sample extracted from core 1, including C1-01, C1-02, C1-03, C1-04, C1-05, C1-06 with the sequence from left to right and from top to bottom. The label A means a backup of certain sample, i.e. C1-01A is a backup of the sample of C1-01.

Pictures of parts of sample extracted from core 2, including C2-01, C2-02, C2-03, C2-04, C2-05, C2-06 with the sequence from left to right and from top to bottom. The label A means a backup of certain sample, i.e. C2-05A is a backup of the sample of C2-05.

Pictures of parts of sample extracted from core 2, including C2-07, C2-08, C2-09, C2-10 with the sequence from left to right and from top to bottom. The label A means a backup of certain sample, i.e. C2-10A is a backup of the sample of C2-10.

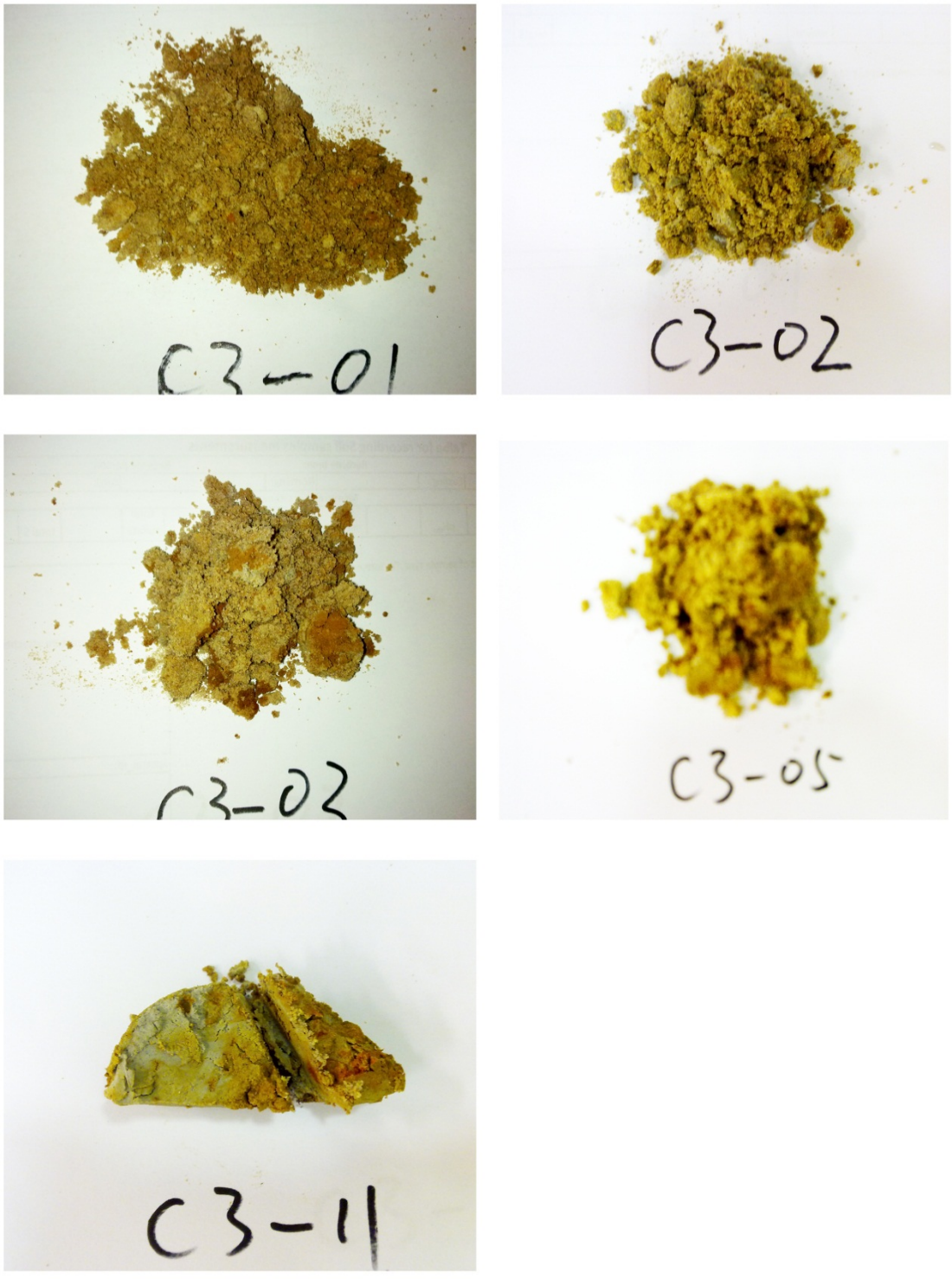

Pictures of Parts of Sample extracted from core 3, including C3-01, C3-02, C3-03, C3-04, C3-05, C3-11 with the sequence from left to right and from top to bottom.

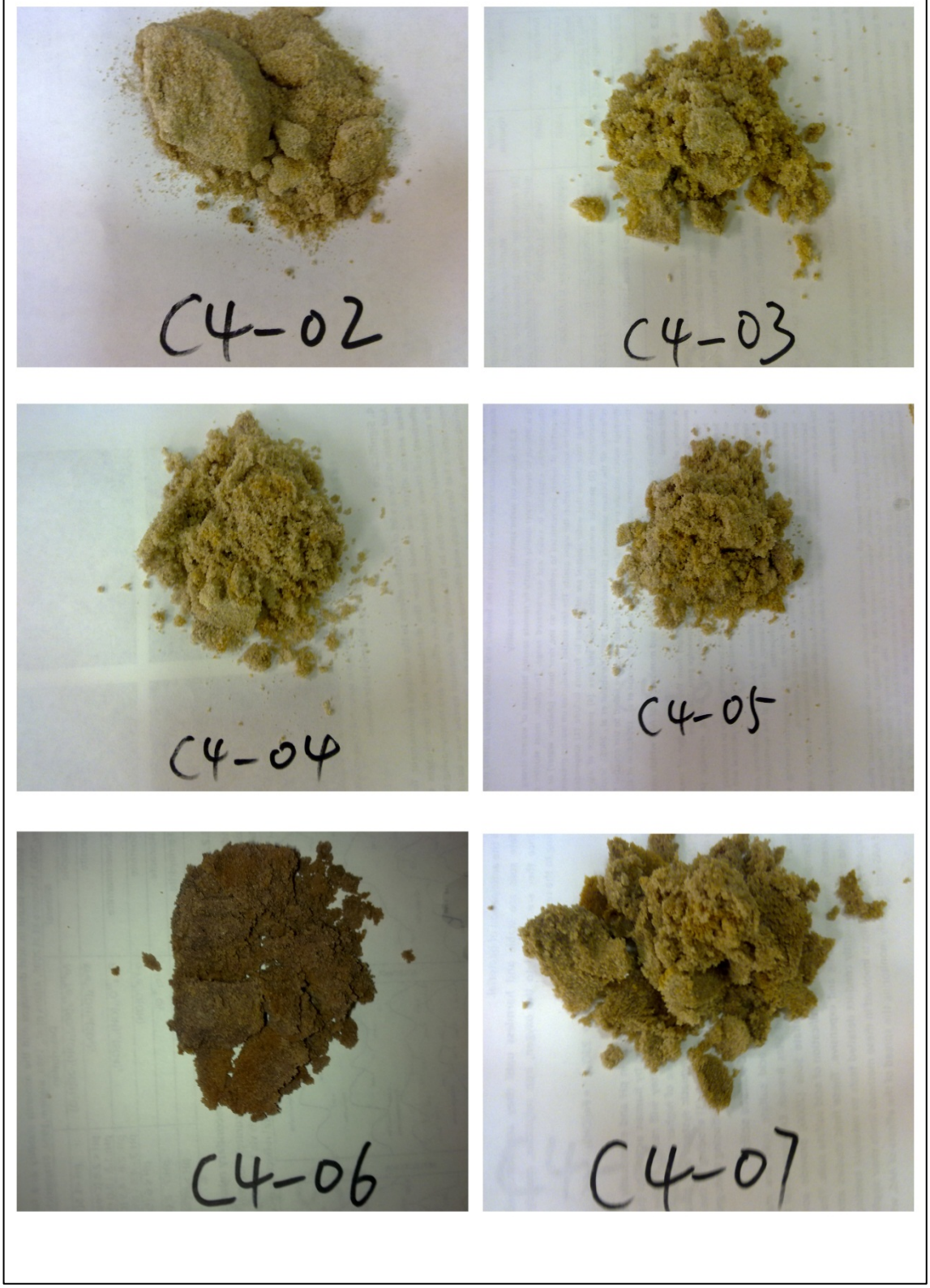

Pictures of parts of sample extracted from core 4, including C4-02, C4-03, C4-04, C4-05, C4-06, C4-07 with the sequence from left to right and from top to bottom.

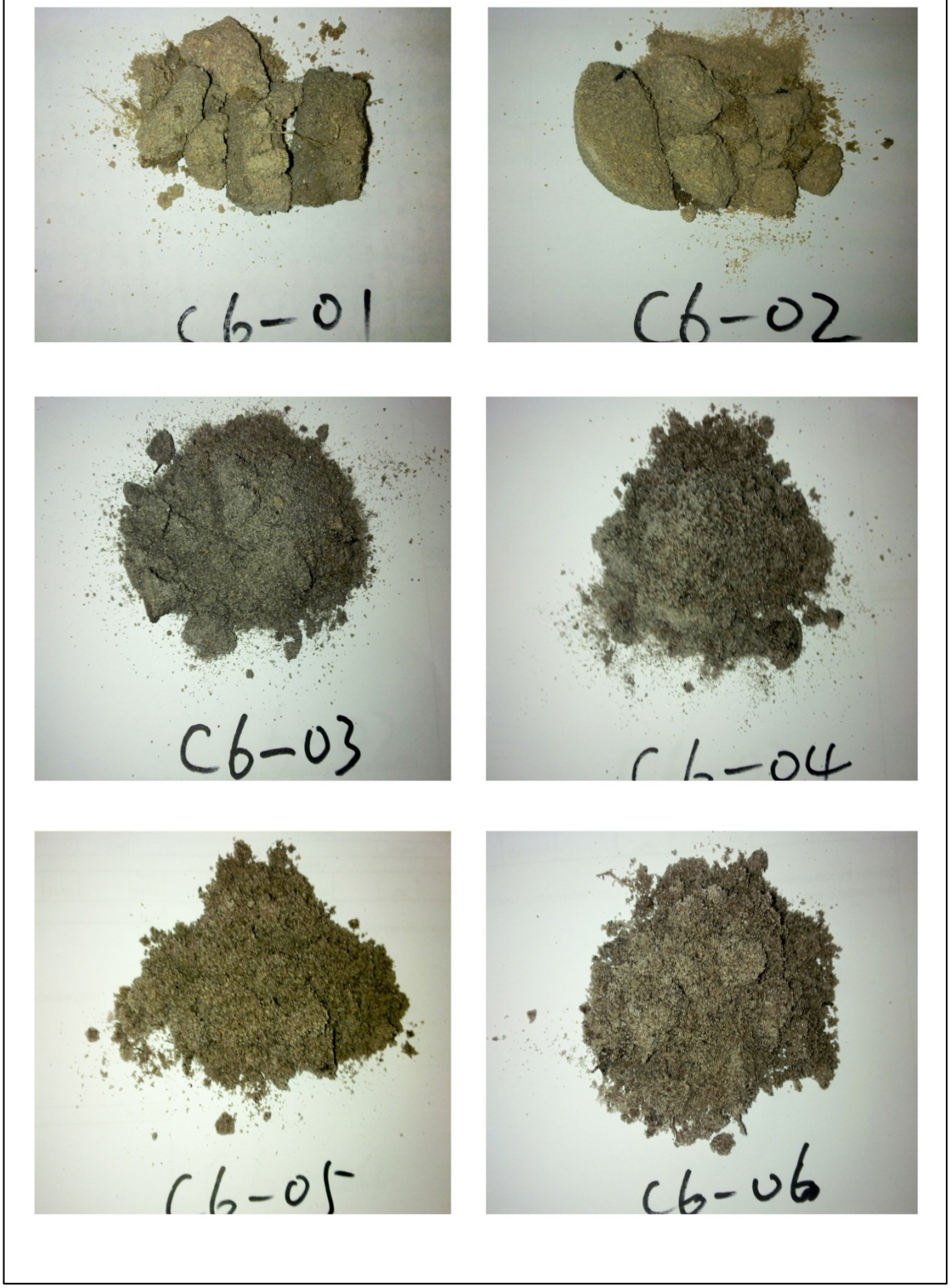

Pictures of parts of sample extracted from core 6, including C6-01, C6-02, C6-03, C6-03, C6-04, C6-05, C6-06 with the sequence from left to right and from top to bottom.

Pictures of parts of sample extracted from core 8, including C8-01, C8-02, C8-03, C8-03, C8-04, C8-05, C8-06 with the sequence from left to right and from top to bottom. The label A means a backup of certain sample, i.e. C8-06A is a backup of the sample of C8-06.

Appendix 9: The description of the soil cores and the measurements of pH and EC of the sample extracted from different depth of soil cores

	sample id	Depth(cm)	Colour	Grain size	Texture	pH value	EC
core 1	C1-01C	14-16	matrix:10yr 4/3; mottle: 7.5yr 3/3	silt	sandy-clay	3.81	9740
	C1-02C	26-28	matrix:7.5yr 5/2,motel:7.5y 4/4	clay	loam	3.45	6250
	C1-03C	34-36	matrix:7.5yr 5/2 ; mottle: 7.5 yr 4/4	clay	loam	3.48	3840
	C1-04C	44-46	7.5yr 5/2	silt	sandy-clay	3.56	3320
	C1-05C	53-55	gley1 2.5/N; mottle:10y 4/4	clay	loam	5.06	3440
	C1-06C	60-63	gley1 2.5/N; mottle:10y 4/4	clay	loam	6.19	1906
core 2	C2-01C	4.0-7.0	10yr 5/6,10yr 7/1	very fine sand	sandy-clay	4.3	40.1
	C2-03C	24-26	matrix:10yr 5/6,mottle:10yr 6/8	fine sand	sandy-clay-loam	4.2	108.1
	C2-05C	44-46	10yr 5/6	fine sand	sandy-clay-loam	4.09	770
	C2-07C	64-66	10yr 7/6	medium sand	sandy-loam	8.52	302
	C2-09C	84-86	10yr 7/6	medium sand	sandy-loam	6.7	85
core 3	C3-01C	0-5	matrix:2.5y 7/4; mottle: 2.5yr 6/6	silt	sandy clay	4.3	135.5
	C3-03C	19-21	matrix:2.5y 7/4; mottle: 2.5yr 6/6	silt	sandy clay	4.26	71.3
	C3-05C	39-41	matrix:2.5y 7/4; mottle: 2.5yr 6/6	silt	sandy clay	3.98	54
	C3-07C	59-61	matrix:2.5y 7/4; mottle: 2.5yr 6/6	fine sand	loamy sand	4.13	67.5
	C3-09C	79-81	matrix:2.5y 7/4; mottle: 2.5yr 6/6	fine sand	loamy sand	3.94	76.5
	C3-11C	97-99	gley:7/10g; mottle:5yr 4/6	clay	loam	4.13	63.9
core 4	C4-01C	4.0-6.0	7.5yr 8/2			4.65	1774
	C4-03C	24-26	matrix: 8/6; mottle:7.5yr 4/6	fine sand	loamy sand	4.28	644
	C4-05C	44-46	matrix: 8/6; mottle:7.5yr 4/6	fine sand	loamy sand	4.34	897
	C4-07C	64-66	matrix:7.5y 6/2; mottle:7.5yr 4/6	fine sand	loamy sand	4.6	509

	sample id	Depth(cm)	Colour	Grain size	Texture	pH value	EC
core 5	C5-01C	0-5	2.5y 5/2	fine sand	loamy sand	5.47	19
	C5-02C	9.0-11.0	2.5y 5/2	fine sand	loamy sand	5.45	39.6
	C5-03C	19-21	2.5y 6/3	fine sand	loamy sand	6.21	27.5
	C5-04C	29-31	matrix:2.5y 6/3;mottle:2.5y 6/6	fine sand	sandy loam	6.45	24.8
	C5-05C	39-41	10yr 7/2	fine sand	sandy loam	6.75	32.2
core 6	C6-09C	78-79	gley1 5/N	fine sand	loamy sand	4.84	16.9
	C6-07C	59-61	gley1 5/N	fine sand	loamy sand	5.04	12.3
	C6-05C	39-41	gley1 5/N	fine sand	loamy sand	5.27	10.1
	C6-03C	19-21	gley1 5/N	fine sand	loamy sand	6.39	20.3
	C6-01C	0-4	2.5y 7/3	fine sand	loamy sand	6.15	23.6
core 7	C7-01C	65-69	yellow:10yr 6/8	clay	loam	2.68	1632
	C7-03C	58-60	yellow:2.5yr 8/4	fine sand	sandy	3.07	586
	C7-05C	44-46	gray: 5y 5/1; brown 10yr 5/6	silt	sandy-clay	2.93	685
	C7-07C	30-33	10yr 6/8	silt	sandy-clay	2.88	621
	C7-09C	15-17	mottle:5y 8/6;matrix:7.5y 3/3	silt	sandy-clay	2.98	391
	C7-11C	0-5	mottle: 5y 8/6;matrix:2.5y 6/3	silt	sandy-clay	3.29	202
core 8	C8-01C	4.0-6.0	7.5yr 3/1	clay	loam	4.02	5130
	C8-03C	24-16	7.5yr 4/1	clay	loam	3.85	3250
	C8-05C	44-46	10yr 8/1	fine sand	loamy sand	4.48	7930
	C8-06C	54-56	7.5yr 8/1; 7.5yr 7/6	fine sand	loamy sand	3.92	15560

Appendix 10: The measurements of main elements interested of the samples extracted from different depth of soil cores

ELEMENTS	Fe	S	Ca	K	Mg	Na	Mn	Mo	Ni	Pb	Sb	Al	As	Ba	Cr	Cs	Cu	Zn
UNITS	%	ppm	ppm	ppm	ppm	ppm	ppm	ppm	ppm	ppm	ppm	ppm	ppm	ppm	ppm	ppm	ppm	ppm
DETECTION	0.01	50	50	20	20	20	1	0.1	0.5	0.5	0.05	50	0.5	0.1	1	0.05	0.5	1
METHOD	4A/OE	4A/OE	4A/OE	4A/OE	4A/OE	4A/OE	4A/OE	4A/MS	4A/OE	4A/MS	4A/MS	4A/OE	4A/MS	4A/MS	4A/OE	4A/MS	4A/OE	4A/OE
C1-01C	4.37	5809	1883	13700	3384	3325	116	16	20.5	40.6	0.86	91852	17.4	358.2	56	1.67	22	22
C1-02C	5.1	6119	2584	13444	3571	4035	127	14.1	20.4	39	1	91138	18.1	350.2	95	1.71	22.8	21
C1-03C	5.32	6884	2425	21149	3220	5312	135	19	20.3	43.3	1.18	85901	30.4	571.1	60	1.57	16.2	19
C1-04C	4.21	6500	2280	25194	2998	6106	171	12.8	19.4	38.7	1.07	79309	26.4	720	54	1.4	15.7	14
C1-05C	4.82	25486	3826	22625	6247	7993	292	14	25.9	38.1	1.04	77709	25.6	612.4	52	1.47	17.6	40
C1-06C	5.49	30069	4609	15413	8389	8941	324	12.3	25.6	37.8	1.06	85598	28.6	384	57	1.59	19.2	30
C2-01C	1.32	1486	373	8715	446	858	120	4.6	5.7	16.5	0.74	23927	6	241	39	0.48	6.3	6
C2-03C	1.48	572	446	8424	226	679	105	3.8	4.5	14.5	0.67	20524	7.5	237.3	36	0.38	4.4	5
C2-05C	0.98	942	966	8725	217	721	106	3.3	5.3	14.2	0.49	20079	4.4	244.6	22	0.37	3	6
C2-07C	1.18	149	918	4799	140	316	140	2.4	4.6	8.5	0.34	8506	3.6	129	11	0.16	5.2	3
C2-09C	1.21	53	171	4390	65	259	125	1.9	4.6	6.4	0.27	5914	2.1	118.8	9	0.13	5.6	5
C2-10C	1.2	316	396	14381	333	797	179	1.7	8.7	19.3	1.21	44840	3.9	392.9	71	0.89	6.2	8
C3-01C	1.79	281	195	6809	276	556	92	6.4	8.1	14.9	0.42	29423	5.5	185	28	0.52	7.9	7
C3-03C	3.91	344	152	8237	289	670	104	13.9	8.1	18.7	0.62	35889	21.4	231.9	38	0.59	7.6	5
C3-05C	1.74	295	103	5616	182	432	90	6.6	5.9	11.1	0.43	19719	8	160.7	21	0.34	4.5	5
C3-07C	1.34	289	101	5485	144	407	114	5.7	5.5	14.5	0.4	14131	5	155.9	16	0.29	5.9	5
C3-09C	1.32	283	99	5112	150	383	122	5.5	6.7	9.5	0.41	14484	4.5	145.8	16	0.28	6.8	4
C3-11C	2.75	373	300	15615	616	1516	141	12.6	14.9	29.8	0.76	73887	21.1	444.3	52	1.24	8.5	11
C4-01C	1.24	549	220	5088	179	990	95	3.5	5.5	7.5	0.27	13899	3.5	138.3	59	0.25	5.8	5
C4-03C	1.09	209	267	5107	136	1291	101	2.1	4.8	6.3	0.18	6662	1.6	137	9	0.13	8.7	4

ELEMENTS	Fe	S	Ca	K	Mg	Na	Mn	Mo	Ni	Pb	Sb	Al	As	Ba	Cr	Cs	Cu	Zn
UNITS	%	ppm	ppm	ppm	ppm	ppm	ppm	ppm	ppm	ppm	ppm	ppm	ppm	ppm	ppm	ppm	ppm	ppm
C4-05C	1.18	505	327	2540	172	783	112	1.8	6.2	4.2	0.18	3303	1	64.2	7	0.09	8.2	2
C4-07C	1.1	240	176	1885	356	1333	88	2.7	5.4	4.1	0.2	6547	1.1	51	8	0.14	6.2	4
C5-01C	1.14	173	303	1982	101	183	135	2.8	9	9	0.64	8935	3	55.1	13	0.13	8.5	8
C5-02C	1.62	182	216	1413	85	134	174	3.1	9.7	7.4	0.74	5832	3	40.5	19	0.09	12.6	6
C5-03C	2.37	112	322	1957	121	169	225	4.1	19.1	9.2	0.66	11631	3.8	56.7	23	0.14	19.4	6
C5-04C	2.17	66	468	1559	131	153	214	3	10.9	8.8	0.33	11147	3.2	45.6	19	0.14	13.4	6
C5-05C	2.05	DBL	269	1867	87	141	214	2.2	9.1	10.1	0.21	9739	2.1	50.9	15	0.09	10.7	5
C6-01C	1.14	DBL	354	1858	128	148	141	1.4	6.2	10.6	0.14	10240	1.2	51.1	16	0.11	6.2	7
C6-03C	0.98	54	416	124	55	51	94	1.8	5	2.6	0.19	1070	0.6	5.6	8	DBL	6.1	6
C6-05C	1	DBL	109	39	31	41	94	1.9	4.4	2.2	0.17	312	0.7	4.7	8	DBL	6.2	4
C6-07C	1.06	DBL	95	66	27	38	109	2	4.7	2.4	0.18	402	1.2	4.1	10	DBL	7.5	3
C6-09C	1.77	DBL	94	31	27	38	162	2.6	7.1	2.1	0.27	282	1.5	3.4	11	DBL	10.7	3
C7-01C	2.94	2791	243	8750	915	1663	95	4.7	14.3	39.9	0.48	81346	7.5	230.1	44	1.53	13.8	7
C7-03C	2.48	4222	1310	20235	377	4434	214	7.9	4.8	41	0.43	33962	4.6	525.6	26	0.59	9.8	6
C7-05C	2.94	4273	1269	21235	421	4726	195	11.1	5.6	38	0.45	45054	11.1	555.9	85	0.73	10.5	8
C7-07C	2.32	1686	753	14222	500	2992	134	5.2	7.6	24.1	0.33	48576	4.4	398.5	32	0.8	9.6	6
C7-09C	2.94	3239	637	13496	563	3168	128	5.5	8.5	31.6	0.34	59711	5.3	363.2	32	0.99	10.7	8
C7-11C	2.59	1881	676	13845	704	2962	140	5.3	7.9	24.8	0.36	48491	5	401.1	29	0.88	10.4	10
C8-01C	5.67	14122	4565	14283	3010	14238	135	8.9	16.9	32.3	0.32	72013	6.6	320.3	39	1.26	21.7	21
C8-03C	2.77	2228	2003	16409	3265	10728	121	11.5	15.7	28.3	0.3	89378	6.8	422.2	58	2.4	21.7	13
C8-05C	0.66	672	820	14795	556	4473	104	2.1	2.3	14.8	0.18	18412	1.1	400.8	11	0.38	2.7	3
C8-06C	0.98	959	1057	16366	656	5940	137	4.6	3.2	13.1	0.26	18731	1.6	458.6	8	0.35	3.8	7

Note: The BDL in the cell means no value because it beyond the detectable limitation.